Physiological functions of GABA$_B$ receptor-associated proteins

Inauguraldissertation

zur

Erlangung der Würde eines Doktors der Philosophie

vorgelegt der

Philosophisch-Naturwissenschaftlichen Fakultät

der Universität Basel

von

Pascal Dominic Rem

aus Laufen (BL), Schweiz

Basel, 2021

Genehmigt von der Philosophisch-Naturwissenschaftlichen Fakultät

auf Antrag von

Prof. Dr. Bernhard Bettler

Prof. Dr. Peter Scheiffele

Basel, den 25.05.2021

Prof. Dr. Marcel Mayor

Dekan der Philosophisch-Naturwissenschaftlichen Fakultät

Table of content

1   Summary

GABA$_B$ receptors (GBRs) play a crucial role in synaptic transmission (Gassmann and Bettler, 2012), and alterations of GBR levels and functions are associated with various neurological diseases (Evenseth et al., 2020; Heaney and Kinney, 2016; Kumar et al., 2013). The GBR is an obligate heterodimer composed of GB1 and GB2 subunits, comprising the core subunits of GBRs (Kaupmann et al., 1998; Schwenk et al., 2010). The GB1 subunit exists in two isoforms, GB1a and GB1b, localizing at pre-or postsynaptic sites, respectively (Vigot et al., 2006). The sole difference between the two isoforms is two sushi domains (SDs) located exclusively at the N-terminus of GB1a (Hawrot et al., 1998; Kaupmann et al., 1997). SDs are required for axonal localization and stabilization at the cell surface of GB1a/2 receptors (Biermann et al., 2010; Hannan et al., 2012). At the presynapse, GB1a/2 receptors inhibit neurotransmitter release by blocking voltage-gated Ca^{2+} (Cav) channels, and at the postsynapse, GB1b/2 receptors induce hyperpolarization of neurons through activating inward-rectifier K$^+$ (Kir3) channels (Gassmann and Bettler, 2012). Native GBRs form macromolecular complexes with auxiliary subunits and various constituents, which impart distinct functional properties to GBRs (Schwenk et al., 2010; Schwenk et al., 2016).

Cytosolic potassium channel tetramerization domain (KCTD)-containing protein 8, 12, 12b, and 16 (hereafter collectively designated KCTDs) are auxiliary GBR subunits, influencing the GBR response (Schwenk et al., 2010). KCTDs comprise a T1 and an H1 domain with KCTD8 and -16 containing an additional C-terminal H2 domain (Schwenk et al., 2010). Homopentameric KCTDs interact through their T1 domain with the C-terminus of GB2 and accelerate GBR-mediated Kir3 channel responses (Schwenk et al., 2010). However, solely KCTD12 and 12b induce pronounced desensitization of GBR-mediated Kir3 currents and Cav channel inhibition by uncoupling G$\beta\gamma$ from the effector channel, suggesting that GBR/KCTD complexes can generate distinct functional properties (Schwenk et al., 2010; Turecek et al., 2014). Because of their overlapping expression patterns (Metz et al., 2011), it is conceivable that KCTDs also form hetero-oligomers interacting with GBRs and G proteins. In co-immunoprecipitation experiments, my colleagues identified KCTD12/KCTD16 hetero-oligomers in brain tissue that form a complex with GBRs. They further demonstrated that KCTD12 and KCTD16 retained their distinct regulatory properties in KCTD12/KCTD16 hetero-oligomers, resulting in intermediate GBR-mediated Kir3 current desensitization. They also revealed that KCTD12/KCTD16 hetero-oligomers produce slow deactivation kinetics of Kir3 currents that lead to an increase in the duration of GBR-mediated slow inhibitory postsynaptic currents (sIPSCs). However, it was yet unknown whether KCTD hetero-oligomers can interact with G proteins. My data showed that KCTD homo-and hetero-oligomers bind to the G protein in living cells, which contributed to the understanding of distinct functional properties of KCTD12/KCTD16 hetero-oligomers. Thus, my data complemented the findings of my colleagues and resulted in a co-authorship publication (Fritzius et al., 2017). Together our data show that KCTD12/KCTD16 hetero-oligomers regulate the fine-tuning of GBR-mediated Kir3 currents and enrich the molecular and functional repertoire of native GBRs.

β-amyloid precursor protein (APP), adherens junction-associated protein 1 (AJAP1), and PILRα-associated neural protein (PIANP) are single-spanning membrane proteins that interact with the N-terminal SD1 of GB1a (Dinamarca et al., 2019; Schwenk et al., 2016). Axonal GB1a/2 receptor trafficking is dependent on kinesin-1 (Valdes et al., 2012), but the SD1 required for axonal transport reside within the lumen of transport vesicles (Biermann et al., 2010; Vigot et al., 2006). Due to the interaction with the SD1, APP, AJAP1, and PIANP represent promising candidates for linking GB1a/2 receptors in transport vesicles to the kinesin motor. While APP, AJAP1, and PIANP share the ability to bind SD1 of presynaptic GB1a/2 receptors, only APP linked GB1a/2 receptors to the kinesin motor and mediated axonal trafficking of GB1a/2 receptors, as demonstrated by my colleagues. They further showed that the interaction of APP with GB1a/2 receptors resulted in mutual stabilization at the cell surface, which prevented GB1a/2 receptor internalization and reduced the proteolytic processing of APP in endosomes. However, whether the APP/GB1a/2 receptor complex formation is altered

upon GB1a/2 receptor activation and whether APP modulates GB1a/2 receptor signaling remained unclear. I showed that the GB1a/2 receptor activation did not regulate the association or dissociation between APP and GB1a/2 receptors. My data further demonstrated that the co-expression of APP did not modulate GB1a/2 receptor signaling in heterologous cells. Thus, my data contributed to the characterization of the interaction of APP and GB1a/2 receptors and were integrated into a publication with me as a co-author (Dinamarca et al., 2019). Since proteolytic APP processing in the amyloidogenic pathway yields Aβ fragments, a hallmark of Alzheimer's disease (AD) (Huang and Mucke, 2012; Muller et al., 2017; Selkoe and Hardy, 2016), and alterations in GB1 surface levels are observed in AD patients (Chu et al., 1987a, b; Iwakiri et al., 2005) and a mouse model of AD (Martin-Belmonte et al., 2020), our data reveal that APP/GB1a/2 receptor complex formation links presynaptic GB1a/2 trafficking to Aβ generation.

Proteolytic APP processing in the non-amyloidogenic pathway generates soluble APPα (sAPPα) fragments (Muller et al., 2017). sAPPα binds to SD1 of presynaptic GB1a/2 receptors (Dinamarca et al., 2019; Rice et al., 2019) and signals through G proteins (Fogel et al., 2014; Pasciuto et al., 2015). A recent publication reported that sAPPα induced presynaptic GB1a/2 receptor-mediated inhibition of neurotransmitter release *in vivo* (Rice et al., 2019). Likewise, a 17 residue long peptide composed of the APP sequence containing the SD1 binding motif, termed APP17, suppressed neurotransmitter release and neuronal transmission by activating endogenous GB1a/2 receptors at presynaptic sites (Rice et al., 2019). In contrast, my colleagues showed that sAPPα does not modulate GB1a/2 receptor-mediated G protein activation in heterologous cells (Dinamarca et al., 2019). Due to the controversial findings and the lack of data explaining the mechanism of GB1a/2 receptor modulation by sAPPα, I studied whether APP17 modulates recombinant GB1a/2 receptors. I confirmed binding of APP17 to GB1a/2 receptors expressed in HEK293T cells by displacing fluorescent APP17 peptides from receptors. However, my data demonstrated that APP17 does not modulate GB1a/2 receptor-mediated G protein activation or Gα signaling in heterologous cells. Using a very sensitive GB1a/2 receptor-induced firefly luciferase (FLuc) accumulation assay, my data further evidenced that APP17 does not exert subtle modulatory properties at recombinant GB1a/2 receptors. I further confirmed the absence of allosteric modulatory properties of co-expressed full-length APP at recombinant GB1a/2 receptors in G protein activation, Ga signaling and sensitive FLuc accumulation assays, confirming earlier data published in Dinamarca et al. (2019). My data further showed that the displacement of full-length APP by APP17 did not induce modulatory effects at recombinant GB1a/2 receptors. In addition, my colleagues observed that APP17 neither influenced GB1a/2 receptor-mediated Gβγ signaling *in vitro* nor changed GB1a/2 receptor-mediated inhibition of neurotransmitter release or neuronal transmission *in vivo*, using electrophysiological recordings. Hence, neither sAPPα nor APP17 modulates recombinant or native GB1a/2 receptor signaling. A manuscript reporting these findings with me as the first author is in preparation.

AJAP1 and PIANP form distinct complexes with GB1a/2 receptors and are not involved in axonal trafficking of GB1a/2 receptors (Dinamarca et al., 2019). I demonstrated that the formation of AJAP1/GB1a/2 receptor and PIANP/GB1a/2 receptor complexes *in cis* neither stabilized GB1a/2 receptors at the cell surface nor modulated GB1a/2 receptor-mediated G protein activation in heterologous cells. The observation of my colleagues that AJAP1 and PIANP are located in the somatodendritic compartment, together with their observation that mice genetically lacking AJAP1 or PIANP showed a deficit in presynaptic GB1a/2 receptor-mediated inhibition of neurotransmitter release (S. Früh and T. Lalanne, personal communications) (Winkler et al., 2019), suggested a trans-synaptic interaction between GB1a/2 receptors and AJAP1 or PIANP. Indeed, I demonstrated that AJAP1 and PIANP recruit and cluster transcellular GB1a/2 receptors. I further showed that the formation of AJAP1/GB1a/2 receptor and PIANP/GB1a/2 receptor complexes *in trans* resulted in a stabilization and negative allosteric modulation of GB1a/2 receptors. However, the maximum efficacy of transcellular GB1a/2 receptor signaling was not affected by the interaction with AJAP1 or PIANP, resulting in an increased dynamic range of receptor activity. My data further demonstrated that the negative allosteric properties exerted by AJAP1 and PIANP at transcellular GB1a/2 receptors required anchorage into the cell membrane because soluble

AJAP1 (sAJAP1), which is composed exclusively of the extracellular domain of AJAP1, did not allosterically modulate GB1a/2 receptors. Earlier my colleagues identified different affinities for SD1 binding in the rank order AJAP1>PIANP>>APP (Dinamarca et al., 2019). Thus, my data support a model in which APP traffics GB1a/2 receptors to axon terminals, where they are transferred to postsynaptic AJAP1 or PIANP that precisely localize the receptor and increase its dynamic range. My data will be part of a future publication from the lab with me as a co-author.

Elucidating the physiological functions of PIANP necessitates the analysis of mice genetically lacking PIANP and compare them to WT littermates. Since no PIANP-KO mice were available at the beginning of my Ph.D., I generated PIANP-KO mice using the clustered regularly interspaced short palindromic repeats (CRISPR) / CRISPR-associated (Cas) 9 system in collaboration with the Centre for Transgenic Models (CTM) of the University of Basel. Generating PIANP-KO mice using the CRISPR/Cas9 system requires the electroporation of one-cell embryos with ribonucleoprotein (RNP) that consist of the specific guide ribonucleic acid (RNA), the trans-activating RNA, and the CRISPR/Cas9. In the first step, I identified two guide RNAs. The CTM team pre-validated the two guide RNAs, electroporated CL57B/6 one-cell embryos with the RNP, transferred the surviving embryos into pseudopregnant females, and sampled biopsies of the offspring. The biopsies were transferred to me, and I validated the genomic alterations induced by the CRISPR/Cas9 system and used the PIANP-KO offspring to establish the PIANP-KO mouse line in the lab. I further confirmed the loss of endogenous PIANP protein in the PIANP-KO mouse line that my colleagues used for electrophysiological recordings published in Dinamarca et al. (2019) and Winkler et al. (2019), publications on which I am a co-author. In the Winkler et al. (2019) publication, the electrophysiological recordings of my colleagues showed that PIANP-KO mice exerted deficits in presynaptic GB1a/2 receptor-mediated inhibition of glutamate release. Thus, these data support that PIANP deficiency results in incorrect localization and function of presynaptic GB1a/2 receptors (Winkler et al., 2019).

2   Abbreviations

7TMD	heptahelical transmembrane domain
AC	adenylyl cyclase
AcD	acidic domain
ADAM10	metalloproteinase domain-containing protein 10
AICD	APP intracellular domain
AJAP1	Adherens junction-associated protein 1
AJAP1-SDBM	AJAP1-sushi domain binding mutant
ALICD	APLP intracellular domain
a-NHEJ	alternative NHEJ
APLP	APP-like protein
APP	β-amyloid precursor protein
APP17	synthetic APP peptide containing 17 residues including SD1 binding motif
AD	Alzheimer's disease
ASD	autism spectrum disorder
Aβ	amyloid-β
BACE	β-secretase
BRET	bioluminescence resonance energy transfer
Cas	CRISPR-associated
CaSR	Calcium-sensing receptor
Cav	voltage-gated clacium channel
CD	cytosolic domain
c-NHEJ	canonical NHEJ
CRISPR	Clustered regularly interspaced short palindromic repeats
crRNA	CRISPR RNA
CTD	C-terminal domain
CTF	C-terminal fragment
CTM	Centre for transgenic models
DIV	day *in vitro*
D-loops	displacement loops
DNA-PK	DNA-dependent kinase
DNA-PK$_{CS}$	DNA protein kinase catalytic subunit
DSB	double-strand break
EC50	half maximal effective concentration
ECD	extracellular domain
ELFN	extracellular leucin-rich repeat and fibronectin type-III domain-containing
EMax	maximum efficacy
ER	endoplasmatic reticulum
FLuc	firefly-Luciferase
GABA	γ-aminobutyric acid
GBR	GABA$_B$ receptor
GDP	guanosine diphosphate
GHB	γ-hyydroxybutyrate
GP	globus pallidus

GPC4	glypican 4
GPCR	G protein-coupled receptor
GTP	guanosine triphosphate
HCC	hepatocellular carcinoma
HD	Huntington disease
HDR	homology-directed repair
HSQC	heteronuclear single quantum coherence
ICD	intracellular domains
indels	insertions/deletions
KCTD	potassium channel tetramerization domain
Kir3	inward-rectifier potassium channel
LB	lobe
LTP	long-term potentiation
MAGE	melanoma-associated antigen
MAGEA2	MAGE family member A2
mEPSC	miniature excitatory postsynaptic current
mGluR	metabotropic glutamate receptor
mIPSC	miniature inhibitory postsynaptic current
MMP	metalloproteinase
mRNA	messenger RNA
NAM	negative allosteric modulator
NHEJ	non-homologous end-joining
NMDA	N-methyl-D-aspartate
PAM	positive allosteric modulator
PAM	proto-space adjacent motif
PD	Parkinson's disease
PIANP	PILRα-associated neural protein
PIANP-SDBM	PIANP-sushi domain binding mutant
PKA	protein kinase A
PLC	phospholipase C
RGS	regulator of G protein signaling
RLuc	renilla luciferase
RNA	ribonucleic acid
RNP	ribonucleoprotein
RPA	replication protein A
sAJAP1	soluble AJAP1
sAJAP1-SDBM	soluble AJAP1-SDBM
sAPPα	soluble APPα
sAPPβ	soluble APPβ
sc-APP17	scrambled APP17
SD	Sushi domain
sgRNA	single guid RNA
sIPSC	slow inhibitory postsynaptic current
SNAP	N-ethylmaleimide-sensitive factor attachment protein
SNARE	SNAP receptor
sPIANP	soluble PIANP

SRE	serum response element
SRS	spontaneous recurrent seizures
ssDNA	single-stranded DNA
TALEN	transcription activator-like effector nuclease
TLE	temporal lobe epilepsy
TMD	Transmembrane domain
TMR	tetramethylrhodamine
tracrRNA	trans-activating CRISPR RNA
VFTD	Venus fly-trap domain
ZEB1	zinc-finger E-box binding homeobox 1
ZFN	zing-finger nuclease

3   Introduction

G protein-coupled receptors (GPCRs) are involved in a variety of physiological processes, including but not limited to the visual system, the immune system, and the nervous system. The GPCR family comprises over 800 members in humans (Fredriksson et al., 2003), with 400 members being non-olfactory GPCRs (Bjarnadottir et al., 2006). GPCRs comprise the most prominent drug targets, with about 35% of approved drugs targeting GPCRs (Sriram and Insel, 2018). All GPCRs share a general structure containing an extracellular domain (ECD), a heptahelical transmembrane domain (7TMD), and an intracellular C-terminal domain (CTD). Despite the general similarities, variabilities of the ECDs and ligand binding locations exist, classifying the GPCRs (Ellaithy et al., 2020; Foord et al., 2005; Hu et al., 2017). Two characteristics for the class C GPCRs are the large structurally defined ECD called the venus fly-trap domain (VFTD) and the constitutive dimerization. Class C GPCRs comprise metabotropic glutamate receptors (mGluRs), γ-aminobutyric acid (GABA) B receptors (GBRs), calcium-sensing receptors (CaSRs), taste receptors, and orphan receptors (GPR156, GPR158, GPR179, GPRC5A, GPRC5B, GPRC5C, GPRC5D, and GPRC6a) (Alexander et al., 2019; Ellaithy et al., 2020). Integrated into cell membranes, GPCRs convert extracellular signals into an intracellular response through heterotrimeric G proteins. Heterotrimeric G proteins are composed of the Gα, Gβ, and Gγ subunits. The heterogeneity of Gα subunits groups heterotrimeric G proteins into four main classes: the Gαs, Gαi/o, Gαq, and Gα12 (Neves et al., 2002; Oldham and Hamm, 2008). Gαs and Gαi/o regulate adenylyl cyclase (AC) activity, whereas Gαq stimulates the phospholipase C (PLC), and Gα12 activates small GTPases (Neves et al., 2002).

3.1   GBR structure and mechanism of activation

GBRs represent the metabotropic receptors for GABA, the primary inhibitory neurotransmitter in the brain. GBRs are obligate heterodimers composed of a GB1 and GB2 subunit that share structural homology and contain an extracellular VFTD, a 7TMD, and a CTD (Evenseth et al., 2020). The CTD of GB1 contains an endoplasmatic reticulum (ER) retention signal, which is shielded by the coiled-coil interaction with the CTD of GB2, enabling trafficking of the assembled complex to the cell surface (Margeta-Mitrovic et al., 2000; Pagano et al., 2001). Despite structural homology, GB1 and GB2 exert different functions. Endogenous ligands bind within the VFTD of GB1, while GB2 pre-couples with intracellular heterotrimeric G proteins of the Gαi/o type (Evenseth et al., 2020). Even though the VFTD of GB2 is not involved in ligand binding, it increases agonist affinity at GB1 (Liu et al., 2004).

In the heterodimeric state, the VFTD of GB1 and GB2 face in opposite directions (Park et al., 2020). Both VFTDs are composed of two opposing lobes (LB1 and LB2) separated by a cleft (Geng et al., 2013). Compared to the cysteine-rich domain typical for class C GPCRs, a peptide linker of about 20 residues connects the LB2 with the 7TMD in GB1 and GB2 (Geng et al., 2012). This linker ensures strong pairing of the LB2 and the 7TMD, transmitting conformational changes in the VFTD to the 7TMD (Park et al., 2020). In the inactive GBR conformation, the VFTDs are in an open-state, the LB1 of GB1 and GB2 are in contact with one another, and the TMD3 and TMD5 form a heterodimer interface (Park et al., 2020). TMD3 and TMD6 are further tethered by a pair of basic and acidic amino acids forming the "ionic lock", stabilizing the inactive conformation of individual 7TMDs (Park et al., 2020).

Upon GBR activation by the endogenous ligand, the GB1 VFTD closes 29° resulting in the contact of the LB2 of GB1 and GB2, a hallmark of active VFTDs (Geng et al., 2013; Park et al., 2020). The conformational change within the VFTDs propagates to the 7TMDs, triggering direct contact of the TMD6 of both subunits, resulting in G protein activation (Geng et al., 2013; Shaye et al., 2020). In contrast to agonists and antagonists, allosteric modulators bind within the 7TMD, stabilizing the active or inactive conformation of GBRs (Evenseth et al., 2020). The stabilization of the active GBR conformation by positive allosteric modulators (PAMs) depends on fastening the TMD6 interface between GB1 and GB2 (Kim et al., 2020; Shaye et al., 2020). Up to date, only one negative allosteric modulator (NAM) for GBRs has been identified, namely CLH304a (Chen et al., 2014). CLH304a acts on the 7TMD of GB2, favoring the inactive GBR

conformation (Sun et al., 2016). However, the precise structural changes of GBRs induced by CLH304a are yet unknown.

Activation of heterotrimeric G proteins requires the replacement of guanosine diphosphate (GDP) tethered to the Gα with guanosine triphosphate (GTP) (Oldham and Hamm, 2008). Gα-GTP dissociates from Gβγ, enabling the regulation of distinct downstream effectors (McCudden et al., 2005; Smrcka, 2008). The intrinsic GTPase activity of Gα eventually hydrolyzes the GTP to GDP, inducing the re-association with the Gβγ complex, inactivating the G protein. Regulators of G protein signaling (RGS) proteins can induce the intrinsic GTPase activity of Gα, terminating the transduced signal (McCudden et al., 2005).

3.2 GB1 isoforms: distribution and effector systems

GB1 gene transcription is regulated by different promoters, resulting in two GB1 isoforms, namely GB1a and GB1b (Steiger et al., 2004). The two isoforms differ in their N-terminus by two sushi domains (SDs) exclusively present in GB1a (Hawrot et al., 1998; Kaupmann et al., 1997). The SDs are decisive for axonal localization and stabilization of GB1a/2 receptors at the cell surface (Biermann et al., 2010; Hannan et al., 2012). As a result, heterodimeric GB1a/2 receptors are present at pre- and postsynaptic sites, whereas heterodimeric GB1b/2 receptors are exclusively located in the somatodendritic compartment (Vigot et al., 2006). At the presynapse, GB1a/2 receptor activation prevents evoked neurotransmitter release by inhibiting voltage-gated calcium (Cav) channels through Gβγ and spontaneous neurotransmitter release by suppressing adenylyl cyclase (AC) activity through Gαi/o (Gassmann and Bettler, 2012). Dissociated Gβγ further binds directly to the soluble N-ethylmaleimide-sensitive factor attachment protein (SNAP) receptor (SNARE) complex (Wells et al., 2012), preventing neurotransmitter release downstream of Ca^{2+} entry. Due to the expression of GB1a in inhibitory and excitatory neurons, GB1a/2 receptors act as autoreceptors or heteroreceptors inhibiting the release of GABA or other neurotransmitters, respectively. Stimulation of heterodimeric GB1b/2 receptors at the postsynaptic site activates inward rectifying K^+ (Kir3) channels through Gβγ, thereby shunting excitatory currents (Bettler et al., 2004; Mott and Lewis, 1994). Released Gβγ further inhibits Cav channels, which prevents dendritic Ca^{2+} spikes (Chalifoux and Carter, 2011; Gassmann and Bettler, 2012). The GB1b/2 receptor-activated Gα suppresses AC activity resulting in a reduction of protein kinase A (PKA) activation. The GB1b/2 receptor-mediated reduction in PKA activity has been shown to influence the regulation of gene expression (Fukui et al., 2008; Schwirtlich et al., 2010), to alleviate tonic inhibition of TREK2 channels (Deng et al., 2009), and suppresses the Ca^{2+} permeability of N-methyl-D-aspartate receptor (NMDA)-type glutamate receptors (Chalifoux and Carter, 2010).

3.3 GBRs in disease

Altered GBR levels and functions are associated with various neurological and psychiatric diseases, including epilepsy, addiction, depression, anxiety, schizophrenia, autism spectrum disorder (ASD), Parkinson's disease (PD), Huntington disease (HD), and Alzheimer's disease (AD) (Reviewed by (Evenseth et al., 2020; Heaney and Kinney, 2016; Kumar et al., 2013)).

3.3.1 Alterations in GBR levels and functions in patients and animal models

Postmortem tissue analysis revealed decreased GB1 and GB2 levels in patients suffering from major depressive disorder (Fatemi et al., 2011), bipolar disorder (Fatemi et al., 2011; Ishikawa et al., 2005), schizophrenia (Fatemi et al., 2011; Ishikawa et al., 2005), and ASD (Fatemi et al., 2009; Oblak et al., 2010). Besides reduced GB1 and GB2 levels, a decrease in GBR density was observed in ASD patients (Fatemi et al., 2009; Oblak et al., 2010). In contrast, GB1 protein levels are upregulated in the globus pallidus (GP) in postmortem HD brains, most likely to increase the sensitivity to decreased GABA levels (Kumar et al., 2013). Instead of a general up- or downregulation, a region-specific increment or decrement of GB1 and GBR levels and functions were found in patients suffering from PD

(Calon et al., 2000; Johnston and Duty, 2003), temporal lobe epilepsy (TLE) (Billinton et al., 2001), and AD (Chu et al., 1987a, b; Iwakiri et al., 2005). Besides postmortem tissue analysis, animal models sharing features with human disease are widely used to study disease processes. Changes in localization and activity of GBRs in animal models have also been linked to the pathophysiology of PD (Galvan et al., 2011), mood disorders (Mokrushin et al., 2009), and Schizophrenia (Balla et al., 2009; Javitt et al., 2005; Roenker et al., 2012). In an animal model of absence seizures, GB1 expression and distribution were reduced, and the presynaptic GBR function was diminished (Inaba et al., 2009; Merlo et al., 2007). A decrease of pre- and postsynaptic GB1 surface localization is observed in an AD animal model, emphasizing the importance of accurately regulated GBR levels and functions (Martin-Belmonte et al., 2020).

3.3.2 GBR knock out animals

Genetic ablation of GB1, GB2, and individual GB1 isoforms helps to understand the physiological role of GBRs and advances our knowledge of various pathophysiological conditions. Mice genetically lacking GB1 or GB2 develop anxiety in several behavior paradigms (Mombereau et al., 2005) and exert antidepressant phenotypes (Cryan and Slattery, 2010). Deletion of GB1 in mice promotes seizures, memory impairments, hyperalgesia, anxiety, an increase in locomotor activity, and a decreased immobility in the forced swim test, attest for depression (Enna and Bowery, 2004). Due to the different localization of GB1a and GB1b, distinct phenotypes of GB1a-KO and GB1b-KO mice were expected. Interestingly, GB1a-KO mice display a vaster number of phenotypes than GB1b-KO mice (Gassmann and Bettler, 2012). Kasten and Böhm analyzed the published behavioral reports of GB1 isoform KO animals (Kasten and Boehm, 2015). They concluded that GB1a is crucial for hyperactivity, seizure activity, susceptibility to stress, protection of depressive phenotypes, and memory maintenance. GB1b is involved in susceptibility to depression-like phenotypes and impaired memory formation.

3.3.3 Orthosteric and allosteric ligands of GBR and clinical applications

Drugs of abuse induce dopamine release that appears to be suppressed by GBR activity (Bettler et al., 2004). Several reports have shown that GBR agonists and PAMs attenuate self-administration and prevent the reinforcing effects of drugs of abuse, including cocaine, amphetamine, nicotine, ethanol, and opiates (Vlachou and Markou, 2010). However, the effectiveness of baclofen as a treatment for alcohol abuse is still controversial (Agabio and Leggio, 2018). GBR agonists and PAMs have further shown beneficial effects in animal models for PD (Kumar et al., 2013), ASD (Silverman et al., 2015), fragile X syndrome (Henderson et al., 2012), and schizophrenia (Wieronska and Pilc, 2019).

GBR antagonists have shown promising results in animal models of depression (Evenseth et al., 2020; Slattery et al., 2005) and epilepsy (Bettler et al., 2004; Kumar et al., 2013). Despite the beneficial effects of GBR antagonists for treating epilepsy, the therapeutic window is critical because high doses of antagonists induce seizures (Enna and Bowery, 2004). The beneficial effects of GBR agonists or antagonists on cognitive functions are unclear and controversially discussed (Enna and Bowery, 2004; Kumar et al., 2013). However, especially GBR antagonists appear to be promising candidates to overcome cognitive disabilities associated with AD because these compounds have been reported to improve memory retention (Getova and Bowery, 2001) and enhance cognitive functions in a wide range of tasks and species (Heaney and Kinney, 2016; Kumar et al., 2017; Kumar et al., 2013). Interestingly, the GBR antagonist CGP36741 proceeded to clinical Phase II trials to treat AD and showed improved working memory and attention compared to placebo (Froestl et al., 2004) but has since failed to progress to Phase III trials (Sabbagh, 2009).

So far, the prototypic agonist baclofen and the GABA metabolite, γ-hydroxybutyrate (GHB) are the only GBR drugs on the market. Although the mechanism of action for GHB is unknown, its therapeutic effects to treat narcolepsy presumably rely on GBR activation (Fritzius and Bettler, 2019). Baclofen is prescribed for the treatment of spasticity. However, side effects limit its usefulness for psychiatric indications (Kumar et al., 2013; Mugnaini and Corelli, 2016). Pharmaceutical companies like Novartis, Roche, Addex, and AstraZeneca have identified

PAMs, which however did not yet reach the market (Mugnaini and Corelli, 2016). Problematical pharmacokinetics and toxicological profiles were observed for the NAM CLH304a and its derivatives (Mugnaini and Corelli, 2016). The distinct roles of pre-and postsynaptic GBRs in the pathophysiology of various diseases and the lack of discrimination between pre- and postsynaptic GBRs by current compounds highlight the demand for GB1 isoform-specific drugs.

3.4 Auxiliary GBR subunits – the KCTD proteins

Native GBRs exert different kinetic characteristics and responses than cloned GBRs in heterologous expression systems. In heterologous expression systems, GBRs exert longer rise-times of K^+ currents and little K^+ current desensitization (Gassmann and Bettler, 2012; Kaupmann et al., 1998). Proteomics analysis of native GBRs from mouse brains identified the K^+ channel tetramerization domain (KCTD)-containing proteins 8, 12, 12b, and 16 (hereafter collectively called KCTDs) as auxiliary subunits of native GBRs (Schwenk et al., 2010). KCTDs are cytosolic proteins and comprise the clade F within a larger KCTD protein family (Skoblov et al., 2013). KCTD12 and 16 are expressed throughout the brain, whereas KCTD8 and 12b show a restricted localization pattern, with KCTD12b only being detected in the medial habenula (Metz et al., 2011).

KCTDs share a conserved T1 domain and H1 domain, whereas only KCTD8 and 16 contain an additional conserved H2 domain (Schwenk et al., 2010). The T1 domain is homologous to the T1 domain of voltage-gated K^+ channels that mediates subunit tetramerization (Liu et al., 2013; Skoblov et al., 2013). In contrast, the T1 domain of KCTDs assembles into pentamers (Pinkas et al., 2017; Smaldone et al., 2016; Zheng et al., 2019; Zuo et al., 2019) and interacts with the C-terminus of GB2, of which Y902 is mandatory for interaction (Schwenk et al., 2010; Zheng et al., 2019; Zuo et al., 2019). The interaction of KCTDs and GBRs takes place in the ER and does not influence the trafficking of GBRs to plasma membranes (Ivankova et al., 2013). At the cell surface, KCTD12 reduces constitutive GBR internalization, increasing the availability of functional GBRs (Ivankova et al., 2013). The presence of KCTD12 further induces pronounced desensitization of GBR-mediated Kir3 currents and Cav inhibition. Desensitization is mediated by the H1 domain, which uncouples Gβγ from effector channels (Schwenk et al., 2010; Turecek et al., 2014; Zheng et al., 2019). In contrast, KCTD8 and 16 lack desensitizing properties that depend on two characteristics (Schwenk et al., 2010; Seddik et al., 2012). First, the T/NFLEQ motif present in the H1 domain of KCTD12 that is absent in the H1 domain of KCTD8 and 16 (Seddik et al., 2012). Second, KCTD8 and 16 contain a H2 domain that inhibits desensitization by steric hindrance (Seddik et al., 2012). However, all GBR-associated KCTDs accelerate the GBR response (Schwenk et al., 2010). In general, KCTDs do not exert allosteric properties at the principal GBR subunits with exception of KCTD8 that reduces constitutive GBR activity (Rajalu et al., 2015). KCTD12 and 16 increase the agonist potency of GBRs without changing agonist affinity (Rajalu et al., 2015; Schwenk et al., 2010). Hence, the 10 fold increased agonist affinity of native GBRs compared to recombinant GBRs suggest the involvement of other factors, like additional GBR binding partners (Rajalu et al., 2015).

Clinically, KCTD12 has been associated with bipolar I disorder (Lee et al., 2011), depressive disorders (Sibille et al., 2009), and schizophrenia (Benes, 2010), whereas KCTD16 is a candidate disease gene for a congenital partial epilepsy syndrome (Angelicheva et al., 2009). Mice lacking either KCTD12 or 16 show a reduction in fear memory, further supporting the contribution of auxiliary KCTDs to the pathophysiology of neuropsychiatric disorders involving GBRs (Cathomas et al., 2017; Cathomas et al., 2015).

3.5 SD1 binding proteins

Native GBRs are macromolecular complexes of a defined architecture but with diverse subunit compositions. Besides the principal GB1 and GB2 subunits forming the core receptor and the auxiliary KCTD subunits, several additional proteins associate with native GBRs (Schwenk et al., 2016). These proteins include signaling effectors, elements of the presynaptic

release machinery, adhesion proteins, and SD-interacting proteins (Schwenk et al., 2016). β-amyloid precursor protein (APP), adherens junction-associated protein 1 (AJAP1) and PILRα-associated neural protein (PIANP) bind to SDs of GB1a (Schwenk et al., 2016). PIANP shares sequence similarity with AJAP1 (Geraud et al., 2010).

3.5.1 APP

APP belongs to a small genetic family comprising APP and the APP-like proteins (APLP) 1 and 2 (Shariati and De Strooper, 2013). APP, APLP1, and APLP2 are single-spanning membrane proteins that are structurally homologous, share a large extracellular domain (ED), a juxtamembrane domain, a transmembrane domain (TMD), and a short intracellular cytoplasmic tail called APP intracellular domain (AICD) or APLP intracellular domain (ALICD) (Coburger et al., 2014; Muller et al., 2017). The extracellular domains are further subdivided into ED1 and ED2 that are linked by an unfolded and flexible acidic domain (AcD) mediating SD1 binding (Dinamarca et al., 2019; Rice et al., 2019). Different secretases target the juxtamembrane domain and the TMD. These secretases proteolytically process APP, yielding distinct biologically active fragments. Proteolytical processing of APP is very complex and occurs in canonical and non-canonical processing pathways (Muller et al., 2017). Dependent on the secretases cleaving APP, the canonical processing follows the amyloidogenic or non-amyloidogenic pathway. In the amyloidogenic pathway, β-secretase 1 (BACE1) and BACE2 cleave APP within the juxtamembrane domain, liberating soluble APP-β (sAPPβ). γ-secretases cleave the membrane-tethered C-terminal fragments (CTFs), generating AICDs and amyloid-β (Aβ) fragments. Aβ fragments are a hallmark of AD and occur only upon APP processing (Huang and Mucke, 2012; Muller et al., 2017; Selkoe and Hardy, 2016). In the competing and physiologically predominant non-amyloidogenic pathway, α-secretase, also known as disintegrin and metalloproteinase domain-containing protein 10 (ADAM10), cleaves APP within the Aβ region, preventing Aβ formation and liberating soluble APPα (sAPPα). Similar to the amyloidogenic pathway, γ-secretases cleave the membrane-tethered CTFs but generate AICDs and p3 fragments. Besides the canonical processing pathways, non-canonical processing pathways exist, yielding distinct N-terminal and C-terminal fragments (Muller et al., 2017). The non-canonical processing pathways include δ-, η-, meprin-β-, and caspase pathways. Besides the attenuating properties of Aη fragments on neuronal activity (Willem 2015), very little is known about the physiological roles of these cleavage products.

APP exists in three isoforms APP695, APP751, and APP770, due to differential splicing (Kitaguchi et al., 1988; Sandbrink et al., 1996; Tanzi et al., 1988). In the brain, APP695 represents the major isoform that is expressed ubiquitously and is found in somatodendritic and axonal compartments (Apelt et al., 1997; Back et al., 2007; Muller et al., 2017). APP and its fragments, mainly sAPPα, exert various physiological functions ranging from transcriptional regulation to synaptic functions (Muller et al., 2017). The AICD interacts with several proteins and is involved in clathrin-mediated endocytosis (Muller et al., 2017), regulating APP processing (Muller et al., 2017), inducing neurite outgrowth (Deyts et al., 2012), and regulating transcription (Cao and Sudhof, 2001). Heterodimer formation of APP and APLPs *in trans* functions as synaptic adhesion molecules (Baumkotter et al., 2014) and exerts synaptogenic activity in hemisynapse assays (Wang et al., 2009). APP and sAPPα are involved in the maintenance of spine density and dynamics (Muller et al., 2017). Despite the lack of knowledge of how APP and sAPPα act on spines, the involvement of NMDA receptors is conceivable. On the one hand, APP interacts with NMDA receptors increasing NMDA receptor localization at cell surfaces (Cousins et al., 2009), and on the other hand, APP-KO mice show reduced levels of extracellular D-serine (Zou et al., 2016), an essential endogenous cofactor of NMDA receptors. Hence, the reduced spine density observed in APP-KO mice could result from reduced levels or impaired functionality of NMDA receptors at spines (Muller et al., 2017). APP and sAPPα play a crucial role in synaptic plasticity, learning, and memory (Muller et al., 2017). APP-KO mice exhibited impaired long-term potentiation (LTP) and hippocampus-dependent behavior, such as spatial learning in the Morris water maze (Dawson et al., 1999; Ring et al., 2007). sAPPα facilitates NMDA receptor currents (Taylor et al., 2008), affects LTP (Taylor et al., 2008), and supports synaptic plasticity by initiating several signaling cascades, such as *de*

novo protein synthesis (Claasen et al., 2009) and transcriptional regulation (Aydin et al., 2011; Ryan et al., 2013). sAPPα has been reported to signal through G proteins (Fogel et al., 2014; Pasciuto et al., 2015) and binds SD1 of GB1a (Dinamarca et al., 2019; Rice et al., 2019). The interaction of sAPPα with SD1 activates presynaptic GB1a/2 receptors, thereby reducing the release probability of synaptic vesicles (Rice et al., 2019). A peptide composed of 17 amino acids corresponding to the SD1 binding site of APP, termed APP17, suppresses neuronal activity *in vivo* (Rice et al., 2019). However, data showing the modulatory properties of sAPPα and APP17 on GB1a/2 receptor signaling were not provided, and the GB1a/2 receptor-mediated G protein activation by sAPPα in the heterologous system could not be confirmed (Dinamarca et al., 2019), rendering GB1a/2 receptor modulation by sAPPα controversial.

3.5.2 AJAP1 and PIANP

AJAP1 and PIANP are single-spanning membrane proteins comprising an extracellular domain (ECD), a transmembrane domain (TMD), and a homologous cytosolic domain (CD) (Geraud et al., 2010). The CD mediates basolateral sorting in polarized epithelial cells, localizing AJAP1 and PIANP to E-cadherin positive adherens junctions (Bharti et al., 2004; Evdokimov et al., 2016; Jakob et al., 2006). At the adherens junction, AJAP1 interacts with the E-cadherin/β-catenin complex modulating the dynamics of adherens junctions (Gross et al., 2009). In contrast, PIANP does not interact with E-cadherin/β-catenin complexes but attenuates cleavage of E-cadherins by modulating γ-secretases (Evdokimov et al., 2016). Various proteases, including γ-secretase, proteolytically process PIANP during its maturation (Biswas et al., 2016; Evdokimov et al., 2013; Evdokimov et al., 2016). Before trafficking to cell surfaces, Furin-like proprotein convertase process PIANP (Evdokimov et al., 2013). Once inserted in the plasma membrane, matrix metalloproteinases (MMPs) and ADAM10/17 cleave PIANP generating CTFs that act as a substrate for γ-secretases generating intracellular domains (ICDs) (Biswas et al., 2016). Processing PIANP by various proteases further suggests the generation of soluble PIANP (sPIANP) fragments that could act as a ligand (Evdokimov et al., 2013). However, the function of ICDs and potential sPIANP fragments remain elusive. Besides being processed proteolytically, PIANP is subject to O-glycosylation and sialylation that is essential for PILRα interaction (Kogure et al., 2011).

In the brain, PIANP is expressed in neurons throughout all brain regions and is located in axons and somatodendritic compartments of neurons (Winkler et al., 2019), whereas AJAP1 is located exclusively in dendrites of cultured hippocampal neurons and is expressed in mossy cells in the hilus of the dentate gyrus (personal communication S. Früh). AJAP1 and GB1 were downregulated in patients suffering from TLE and in a mouse model of epilepsy (Zhang et al., 2020). The downregulated GB1 levels in the epileptic mouse model were rescued by lentiviral induced expression of AJAP1, resulting in a reduction of spontaneous recurrent seizures (SRSs) (Zhang et al., 2020). Frequent downregulation of AJAP1 is further observed in oligodendroglioma and neuroblastoma, which resulted in increased tumor cell migration and invasion, suggesting that AJAP1 acts as a tumor suppressor (Zeng et al., 2014a; Zeng et al., 2014b). The tumor-suppressive activity of AJAP1 in hepatocellular carcinoma (HCC) metastasis is based on AJAP1-mediated accumulation of β-catenin in the cytoplasm, preventing β-catenin's nuclear translocation and transcriptional activity (Han et al., 2017). By preventing the transcriptional activity of β-catenin, zinc finger E-box binding homeobox 1 (ZEB1) expression was repressed, preventing HCC metastasis (Han et al., 2017). Besides an indirect action, AJAP1 represses melanoma-associated antigen (MAGE) family member A2 (MAGEA2) expression by binding physically to the transcriptional promoter of MAGEA2 (Zeng et al., 2014b).

Figure 3.1 Overview of GBR-associated proteins. Principal GB1 (here shown GB1a) and GB2 subunits interact with G proteins and auxiliary KCTD subunits (inner purple circle). The interaction sites or partners (outer purple circle) mediating the complex formation of GBRs with various constituents (proteins listed in the square) are indicated. The constituents are grouped according to their known function. Proteins that failed the stringent significant criteria of Schwenk and colleagues (2016) but were purified with native GBR complexes are marked with a star (Schwenk et al., 2016). PRAF2 showed functional effects on GBR signaling but was not co-purified with native GBRs by Schwenk and colleagues (2016) (Pin and Bettler, 2016). Courtesy of Martin Gassmann.

4   Aim of the thesis

Native GBRs show a diversity in functional properties that are not reproduced by cloned GBRs, indicating the involvement of additional proteins in GBR signaling (Cruz et al., 2004; Deisz et al., 1997; Kaupmann et al., 1997; Kaupmann et al., 1998). Proteomic analysis revealed that native GBRs form macromolecular complexes with a variety of distinct proteins including auxiliary KCTD subunits (Schwenk et al., 2010; Schwenk et al., 2016). KCTDs differently influence the kinetic properties of GBRs and show overlapping expression patterns (Metz et al., 2011; Schwenk et al., 2010). Hence, KCTD hetero-oligomers may exist and impart distinct properties to GBRs. Besides the KCTDs, a group of transmembrane proteins binding to SD1 were identified (Dinamarca et al., 2019; Schwenk et al., 2016). SD1 is located at the N-terminus of GB1a in proximity to the orthosteric binding site and is required for axonal localization of GB1a/2 receptors (Biermann et al., 2010; Dinamarca et al., 2019; Hawrot et al., 1998; Kaupmann et al., 1997; Vigot et al., 2006). Hence, SD1 binding proteins potentially influence GBR localization and signaling. Recently, a synthetic APP peptide composed of 17 residues, termed APP17, was shown suppress neuronal transmission through binding SD1 (Rice et al., 2019). However, whether APP17 indeed induced GB1a/2 receptor-mediated G protein activation and signaling to effectors was not analyzed. The aim of my thesis was to study the influence of KCTD hetero-oligomers on GBR signaling and to address a possible role of APP, AJAP1, and PIANP on presynaptic GB1a/2 receptor trafficking and signaling. Furthermore, my thesis aimed at elucidating whether binding of APP17 to SD1 induces agonistic, allosteric, or antagonistic properties at GB1a/2 receptors.

In the first part of my thesis, I collaborated with my colleagues to address the possible existence of KCTD hetero-oligomers and their influence on GBR-mediated signaling (Section 5). My colleagues addressed the natural occurrence of KCTD hetero-oligomers, the ability of individual KCTDs to form hetero-oligomers, the interaction of KCTD hetero-oligomers with GBRs, and the influence of KCTD hetero-oligomers on GBR-mediated Kir3 currents, using biochemical approaches and electrophysiological recordings. Since KCTD homo-oligomers impart distinct properties on GBR responses (Schwenk et al., 2010) by interacting with G proteins (Turecek et al., 2014), I analyzed the interaction between KCTD hetero-oligomers and G proteins using bioluminescence resonance energy transfer (BRET) experiments (Section 5). My data were included in a publication with me as a co-author (Fritzius et al., 2017).

In the second part of my thesis, I collaborated with my colleagues to address the influence of APP on GB1a/2 receptor localization, trafficking, and signaling (Section 6). My colleagues addressed the influence of APP on GB1a/2 receptor localization and trafficking, the stability of APP/GB1a/2 receptor complexes with regards to proteolytic processing of APP, and the functionality of presynaptic GB1a/2 receptors in APP-KO mice, using proteomic analysis, imaging approaches, and electrophysiological recordings. Since APP binds to the SD1 that is linked to the VFTD of GB1a, which plays a crucial role in GB1a/2 receptor activity (Geng et al., 2013; Park et al., 2020; Shaye et al., 2020), I analyzed the influence of APP on GB1a/2 receptor signaling. Using the BRET sensor between Gα and Gγ, I monitored the influence of APP on constitutive, agonist-induced, and antagonist-inhibited GB1a/2 receptor activity. I further studied the influence of GB1a/2 receptor activation and inactivation on the assembly and disassembly of APP/GB1a/2 receptor complexes by measuring BRET between APP and GB1a. My data were included in a publication with me as a co-author (Dinamarca et al., 2019).

APP processing in the non-amyloidogenic pathway liberates sAPPα (Muller et al., 2017). Recently, sAPPα and APP17 were shown to modulate native GBR signaling through SD1 binding (Rice et al., 2019). These findings remained controversial, and Rice et al. (2019) provided no data explaining the mechanism for this modulation. Thus, I thoroughly analyzed the effect of APP17 on recombinant GB1a/2 receptors in the third part of my thesis (Section 7). First, I elucidated whether the commercially available APP17 used by Rice et al. (2019) binds to recombinant GB1a/2 receptors, using commercially available APP17 to displace APP17 labeled with tetramethylrhodamine (TMR) from GB1a/2 receptors. I then elucidated whether APP17 exerts agonistic, antagonistic, or allosteric properties at recombinant GB1a/2 receptors. Therefore, I analyzed GB1a/2 receptor-mediated G protein activation by measuring

BRET between Gα and Gγ, studied GB1a/2 receptor-mediated Gα signaling using a protein kinase A (PKA) renilla luciferase (RLuc) assay, and performed dose-response curves using a sensitive GB1a/2 receptor-induced firefly luciferase (FLuc) accumulation assay. It is conceivable that binding of full-length APP to GB1a/2 receptors influences the activity of GB1a/2 receptors and that APP17 could induce changes in GB1a/2 receptor activity by displacing full-length APP from the receptor. Therefore, I also elucidated whether APP17 influences GB1a/2 receptor activity by displacing full-length APP from GB1a/2 receptors by performing all experiments mentioned above in the presence and the absence of co-expressed full-length APP. Since Rice et al. (2019) analyzed the APP17 exclusively in neurons that may express GBR associated proteins not present in transfected HEK293T cells, my colleagues also addressed possible modulatory properties of APP17 at native GB1a/2 receptors using electrophysiological recordings and Ca^{2+} imaging. All these findings will be included in a manuscript with me as the first author (Rem et al., in preparation).

The group of SD1 binding proteins further include AJAP1 and PIANP (Dinamarca et al., 2019; Schwenk et al., 2016). SD1 is located proximal to the VFTD that undergoes conformational changes upon agonist binding, resulting in G protein activation (Geng et al., 2013; Park et al., 2020; Shaye et al., 2020). Thus, it is conceivable that binding to SD1 affects conformational changes of the VFTD. I studied the influence of AJAP1 and PIANP on GB1a/2 receptor signaling (Section 8). Earlier my colleagues identified the SD1 interaction motif within AJAP1, which is shared by PIANP (Dinamarca et al., 2019). In order to confirm the shared SD1 binding motif, I generated and characterized a SD1 binding deficient mutant of PIANP (PIANP-SDBM) by mutating the corresponding amino acids to alanine. Furthermore, I analyzed the effect of AJAP1 and PIANP on GB1a/2 receptor-mediated G protein activation *in cis*, using the BRET sensor between Gα and Gγ. I also used the sensitive GB1a/2 receptor-induced FLuc accumulation assay to perform GABA-induced dose-response curves of GB1a/2 receptors co-expressing AJAP1 or PIANP to elucidate possible subtle allosteric effects of AJAP1 or PIANP on GB1a/2 receptor signaling. Since the interaction of AJAP1 and PIANP with GB1a/2 receptors could also occur *in trans*, I further studied the ability of AJAP1 and PIANP to bind and cluster GB1a/2 receptors in HEK293 cell/neuron co-cultures. To elucidate potential modulatory properties of AJAP1 and PIANP on transcellular GB1a/2 receptors, I used both the BRET sensor between Gα and Gγ and the sensitive GB1a/2 receptor-induced FLuc accumulation assay. I also used the sensitive GB1a/2 receptor-induced FLuc accumulation system to analyze whether a soluble version of AJAP1, sAJAP, composed exclusively of the N-terminal extracellular domain of AJAP1, influences GB1a/2 receptor signaling. My data complement the work of my colleagues and will be published with me as a co-author.

In the last part of my thesis, I generated PIANP-KO mice using the CRISPR/Cas9 system (Section 9). In order to generate PIANP-KO mice, I collaborated with the Centre for Transgenic Models, University of Basel. I confirmed the loss of endogenous PIANP protein by Western blot analysis of membrane-enriched fractions of mouse brains and established the PIANP-KO mouse line in the lab. The mice were used for electrophysiological and immunocytochemical studies. I am a co-author of the publications reporting the findings of these studies (Dinamarca et al., 2019; Winkler et al., 2019).

5   KCTD hetero-oligomers confer unique kinetic properties on hippocampal GABA$_B$ receptor-induced K$^+$ currents

Thorsten Fritzius, Rostislav Turecek, Riad Seddik, Hiroyuki Kobayashi, Jim Tiao, <u>Pascal D. Rem</u>, Michaela Metz, Michaela Kralikova, Michel Bouvier, Martin Gassmann and Bernhard Bettler

Personal contribution

Cytosolic KCTDs are the auxiliary subunits of GBRs (Schwenk et al., 2010). Homo-oligomeric KCTDs accelerate GBR-mediated Kir3 and Cav responses (Schwenk et al., 2010). However, only KCTD12 and KCTD12b exhibited pronounced desensitization of Kir3 currents and Cav channel inhibition (Schwenk et al., 2010). Due to the overlapping expression patterns of KCTDs (Metz et al., 2011), hetero-oligomerization is conceivable. In this paper, my colleagues show that the KCTDs assemble hetero-oligomers in all dual combinations. Using bioluminescence resonance energy transfer (BRET) experiments in living cells, I demonstrate that KCTD homo- and hetero-oligomers bind to G proteins (Fig. 5b). These data complement similar BRET experiments of my colleagues showing that KCTD homo- and hetero-oligomers associate with GBRs and substantially contribute to the conclusion that simultaneous assembly of distinct KCTDs at the receptor increases the molecular and functional repertoire of GBRs.

Cellular/Molecular

KCTD Hetero-oligomers Confer Unique Kinetic Properties on Hippocampal GABA$_B$ Receptor-Induced K$^+$ Currents

Thorsten Fritzius,[1]* ⓘRostislav Turecek,[1,2]* Riad Seddik,[1]* ⓘHiroyuki Kobayashi,[3] Jim Tiao,[1] Pascal D. Rem,[1] ⓘMichaela Metz,[1] Michaela Kralikova,[2] ⓘMichel Bouvier,[3] Martin Gassmann,[1] and Bernhard Bettler[1]

[1]Department of Biomedicine, Institute of Physiology, University of Basel, 4056 Basel, Switzerland, [2]Institute of Experimental Medicine, ASCR, 14220 Prague 4-Krc, Czech Republic, and [3]Department of Biochemistry, Institute for Research in Immunology and Cancer, Université de Montréal, Montreal, Quebec H3C 3J7, Canada

GABA$_B$ receptors are the G-protein coupled receptors for the main inhibitory neurotransmitter in the brain, GABA. GABA$_B$ receptors were shown to associate with homo-oligomers of auxiliary KCTD8, KCTD12, KCTD12b, and KCTD16 subunits (named after their T1 K$^+$-channel tetramerization domain) that regulate G-protein signaling of the receptor. Here we provide evidence that GABA$_B$ receptors also associate with hetero-oligomers of KCTD subunits. Coimmunoprecipitation experiments indicate that two-thirds of the KCTD16 proteins in the hippocampus of adult mice associate with KCTD12. We show that the KCTD proteins hetero-oligomerize through self-interacting T1 and H1 homology domains. Bioluminescence resonance energy transfer measurements in live cells reveal that KCTD12/KCTD16 hetero-oligomers associate with both the receptor and the G-protein. Electrophysiological experiments demonstrate that KCTD12/KCTD16 hetero-oligomers impart unique kinetic properties on G-protein-activated Kir3 currents. During prolonged receptor activation (one min) KCTD12/KCTD16 hetero-oligomers produce moderately desensitizing fast deactivating K$^+$ currents, whereas KCTD12 and KCTD16 homo-oligomers produce strongly desensitizing fast deactivating currents and nondesensitizing slowly deactivating currents, respectively. During short activation (2 s) KCTD12/KCTD16 hetero-oligomers produce nondesensitizing slowly deactivating currents. Electrophysiological recordings from hippocampal neurons of KCTD knock-out mice are consistent with these findings and indicate that KCTD12/KCTD16 hetero-oligomers increase the duration of slow IPSCs. In summary, our data demonstrate that simultaneous assembly of distinct KCTDs at the receptor increases the molecular and functional repertoire of native GABA$_B$ receptors and modulates physiologically induced K$^+$ current responses in the hippocampus.

Key words: G-protein coupled receptor; GABA-B; GPCR; KCTD12; KCTD16; Kir3

Significance Statement

The KCTD proteins 8, 12, and 16 are auxiliary subunits of GABA$_B$ receptors that differentially regulate G-protein signaling of the receptor. The KCTD proteins are generally assumed to function as homo-oligomers. Here we show that the KCTD proteins also assemble hetero-oligomers in all possible dual combinations. Experiments in live cells demonstrate that KCTD hetero-oligomers form at least tetramers and that these tetramers directly interact with the receptor and the G-protein. KCTD12/KCTD16 hetero-oligomers impart unique kinetic properties to GABA$_B$ receptor-induced Kir3 currents in heterologous cells. KCTD12/KCTD16 hetero-oligomers are abundant in the hippocampus, where they prolong the duration of slow IPSCs in pyramidal cells. Our data therefore support that KCTD hetero-oligomers modulate physiologically induced K$^+$ current responses in the brain.

Introduction

GABA$_B$ receptors are the G-protein coupled receptors (GPCRs) for the inhibitory neurotransmitter GABA. GABA$_B$ receptors are expressed throughout the brain and influence synaptic transmission by regulating the activity of ion channels and adenylate cyclases (Couve et al., 2000; Chalifoux and Carter, 2011; Gassmann

and Bettler, 2012). Postsynaptic GABA$_B$ receptors activate inwardly rectifying K$^+$ channels (Kir3; also known as G-protein-activated inwardly rectifying K$^+$ channels [GIRK]) that generate slow IPSCs (sIPSCs) (De Koninck and Mody, 1997; Lüscher et al., 1997; Lüscher and Slesinger, 2010; Booker et al., 2013). GABA$_B$ receptors comprise principal and auxiliary subunits that assemble into molecularly and functionally distinct receptor subtypes (Schwenk et al., 2010, 2016; Gassmann and Bettler, 2012). The principal subunits GABA$_{B1a}$, GABA$_{B1b}$, and GABA$_{B2}$ are seven-transmembrane proteins and generate fully functional heterodimeric GABA$_{B(1a,2)}$ and GABA$_{B(1b,2)}$ receptors (Möhler and Fritschy, 1999; Pin et al., 2004; Monnier et al., 2011). The auxiliary subunits KCTD8, KCTD12, KCTD12b, and KCTD16 (herein collectively referred to as KCTDs) are cytosolic proteins that bind as homo-tetramers (Schwenk et al., 2010; Correale et al., 2013) or homo-pentamers (Smaldone et al., 2016) to the GABA$_{B2}$ subunit (Bartoi et al., 2010; Schwenk et al., 2010). KCTD8, KCTD12, KCTD12b, and KCTD16 comprise a clade of a larger family of KCTD proteins that all contain a T1 domain, which in voltage-gated K$^+$ channels mediates tetramerization (Liu et al., 2013; Skoblov et al., 2013). The T1 domain of the KCTDs interacts with the C-terminal intracellular domain of the GABA$_{B2}$ subunit, in which tyrosine-902 (Y902) is mandatory for interaction (Schwenk et al., 2010; Correale et al., 2013). The KCTDs additionally contain a conserved H1 homology domain, which in KCTD12 induces a pronounced desensitization of the GABA$_B$ receptor response by uncoupling the $\beta\gamma$ subunits of the activated G-protein from the effector channel (Seddik et al., 2012; Turecek et al., 2014). Selectively KCTD8 and KCTD16 feature a conserved H2 homology domain that prevents the receptor desensitization induced by the H1 domain (Seddik et al., 2012).

The KCTDs exhibit overlapping expression patterns in the brain (Schwenk et al., 2010; Metz et al., 2011; Hayasaki et al., 2012) and, in principle, could form hetero-oligomers in various neuronal populations. Here we demonstrate that KCTD12 and KCTD16 indeed form hetero-oligomers through self-association of their T1 and H1 domains. KCTD12/KCTD16 hetero-oligomers directly bind to the receptor-associated G-protein and confer unique desensitization and deactivation kinetics to GABA$_B$ receptor-induced K$^+$ currents. In hippocampal neurons, KCTD12/KCTD16 hetero-oligomers increase the duration of GABA$_B$ receptor-induced sIPSCs. In summary, our data show that KCTD hetero-oligomers contribute to functionally distinct GABA$_B$ receptor responses in the brain.

Materials and Methods

Mice. Kctd12$^{-/-}$ (RRID:MGI:5756048) and Kctd16$^{-/-}$ knock-out mice and control littermates of either sex were generated as described previously (Metz et al., 2011; Cathomas et al., 2015). Kctd12/16$^{-/-}$ double knock-out mice of either sex were obtained from mating of Kctd12$^{-/-}$ and Kctd16$^{-/-}$ mice. All experiments with mice were subjected to institutional review and approved by the Veterinary Office of Basel-Stadt.

Cell lines and cultured hippocampal neurons. Human Embryonic Kidney 293 (HEK293) cells were from ATCC (RRID: CVCL_0045) and maintained in DMEM supplemented with GlutaMAX (Invitrogen) and 10% FCS in a humidified atmosphere (5% CO$_2$) at 37°C. CHO-K1 cells (RRID: CVCL_0214), stably expressing human GABA$_{B1b}$ and rat GABA$_{B2}$ (Urwyler et al., 2001) were maintained in DMEM with 500 μM L-glutamine, 40 μg/ml L-proline, 0.5 mg/ml G418, 0.25 mg/ml zeocine, and 10% FCS. Cells were transfected at 70%–90% confluency in 6- or

R. Seddik's present address: Aix-Marseille Université, Physiologie et physiopathologie du système nerveux, 13013 Marseille, France.

J. Tiao's present address: Murdoch University, Murdoch, 6150 Western Australia, Australia.

24-well plates or in 10 cm dishes using Lipofectamine 2000 (Invitrogen), X-tremeGENE (Roche), or polyethylenimine (Sigma). Cultured hippocampal neurons were prepared as described previously (Brewer et al., 1993; Biermann et al., 2010). Briefly, embryonic day 16.5 mouse hippocampi were dissected, digested with 0.25% trypsin (Invitrogen) in 1 $\times$ PBS solution for 15 min at 37°C, dissociated by trituration, and plated on glass coverslips coated with 1 mg/ml poly-L-lysine hydrobromide (Sigma) in 0.1 M borate buffer (boric acid/sodium tetraborate). Neurons were seeded at a density of $\sim$550 cells/mm^2 in neurobasal medium (Invitrogen) supplemented with B27 (Invitrogen) and 0.5 mM L-glutamine and cultured in a humidified atmosphere (5% CO$_2$) at 37°C. Cultured hippocampal neurons were transfected at DIV7.

Biochemistry. Plasmids used for biochemistry experiments encoding FLAG- and Myc-tagged KCTD10, KCTD8, KCTD12, and KCTD16 constructs were described previously (Seddik et al., 2012). pCI-HA-GABA$_{B2}$-eYFP was a gift from Novartis.

Adult mouse brains were homogenized and lysed in 5 ml NETN buffer (100 mM NaCl, 1 mM EDTA, 0.5% Nonidet P-40, 20 mM Tris/HCl, pH 7.4) supplemented with complete EDTA-free protease inhibitor mixture (Roche) using a Dounce homogenizer. Following rotation for 3 h at 4°C, brain lysates were cleared by centrifugation at 15,000 $\times$ g for 30 min at 4°C. For affinity-depletion experiments, hippocampi of adult mouse brains were dissected and placed in 100 mg/ml of ice-cold homogenization medium (320 mM sucrose, 4 mM HEPES, pH 7.5, 1 mM EDTA, 1 mM EGTA, supplemented with complete EDTA-free protease inhibitor mixture) and homogenized using a glass-Teflon homogenizer with 20 passes on ice. After homogenization, the material was cleared by centrifugation at 1000 $\times$ g (4°C, 15 min). The membrane-enriched fraction was isolated by ultracentrifugation at 48,000 $\times$ g (4°C, 45 min) and solubilized for 3 h at 4°C in NETN buffer at 2 mg protein/ml. The solubilized fraction was cleared by ultracentrifugation at 10^5 $\times$ g (4°C, 45 min). Cultured HEK293 cells were lysed 48 h after transfection in NETN buffer or modified RIPA buffer (150 mM NaCl, 1% Nonidet P-40, 0.5% sodium deoxycholate, complete EDTA-free protease inhibitors, pH 7.4) by rotating for 30 min at 4°C. HEK293 cell lysates were then cleared by centrifugation at 10,000 $\times$ g for 20 min at 4°C. Brain and cell lysates were directly used for immunoblot analysis (input lanes) or immunoprecipitated with guinea-pig anti-KCTD12 (RRID:AB_2631051), guinea-pig anti-KCTD16 (RRID: AB_2631053), or mouse anti-Myc (9E10, Santa Cruz Biotechnology, RRID: AB_627268) antibodies coupled to a mixture of protein-A and protein-G Sepharose (GE Healthcare). Lysates and immunoprecipitates were resolved using SDS-PAGE and probed with the primary antibodies rabbit anti-KCTD12 (1:2500, RRID:AB_2631049), rabbit anti-KCTD16 (1:2500, RRID:AB_2631050), rabbit anti-Myc (C3956, Sigma, 1:2500, RRID:AB_439680), rabbit anti-FLAG (F7425, Sigma, 1:2500, RRID:AB_439687), rabbit anti-GABA$_{B2}$ (C44A4, #4819, Cell Signaling Technology, 1:1500, RRID:AB_2108339), and mouse β-tubulin III (T8660, Sigma, 1:2000, RRID:AB_477590) in combination with peroxidase-coupled secondary antibodies goat anti-guinea pig (A7289, Sigma, 1:10,000, RRID:AB_258337), sheep anti-mouse (NA931, GE Healthcare, 1:10,000, RRID:AB_772210), or donkey anti-rabbit (NA934, GE Healthcare, 1:10,000, RRID:AB_772206). Guinea-pig and rabbit KCTD12 and KCTD16 antibodies were raised against synthetic peptides of mouse KCTD12 (amino acid residues 145–167) or KCTD16 (residues 7–23) (Metz et al., 2011). Chemiluminescence was detected using the SuperSignal West kit (Thermo Scientific).

Bimolecular luminescence protein-fragment complementation (BiLC), bimolecular fluorescence complementation (BiFC), and bioluminescence resonance energy transfer (BRET) assays. The BiLC and BiFC template constructs were published previously (Héroux et al., 2007; Stefan et al., 2007). GATEWAY technology was used to insert the human KCTD cDNA C-terminal to Rluc and Venus fragments contained in a destination vector for eukaryotic expression based on pcDNA3.1(+)/Zeo (Invitrogen): N-terminal (amino acids 1–110, NTRluc) and C-terminal (amino acids 111–311, CTRluc) fragments of a bright *Renilla* luciferase mutant RlucII (A55T/C124A/M185V-Rluc) and N-terminal (amino acids 1–154, NTVen) and C-terminal (amino acids 146–239, CTVen) fragments of Venus. The construction of pcDNA3.1-Myc-GABA$_{B1}$ and pcDNA3.1-HA-GABA$_{B2}$-GFP was reported previously (Villemure et al.,

2005). The GFP used for HA-GABA$_{B2}$-GFP is a blue-shifted GFP known as GFP10 that is a preferred acceptor in BRET2 assays (Mercier et al., 2002). The HA and Myc tags were used to control for protein cell surface expression. The FLAG-Gβ2 and Venus-Gγ2 constructs used for BRET experiments were reported previously (Adelfinger et al., 2014; Turecek et al., 2014; Rajalu et al., 2015).

For BiLC, BiFC, and BRET assays, HEK293 cells were harvested 48 h after transfection, suspended in PBS, and distributed into 96-well microplates at $1–3 \times 10^5$ cells/well. To measure reconstituted luciferase activity from BiLC proteins, the luciferase substrate coelenterazine h (Nanolight Technology, final concentration 5 μM) was added to each well and luminescence signals were measured 2 min later using a Mithras LB940 multimode plate reader (Berthold Technologies). The expression levels of fluorescent proteins were measured using a FlexStation 2 fluorimeter (Molecular Devices) with excitation and emission wavelengths set at 410 and 510 nm (GFP10) or 518 and 570 nm (Venus), respectively. BRET2 between KCTD-BiLC and GABA$_{B2}$-GFP was measured 2 min after addition of the luciferase substrate DeepBlue C (coelenterazine 400A; Nanolight Technology; final concentration of 5 μM). BRET was calculated as the ratio of the light emitted by GFP10 (515 $\pm$ 20 nm) over the light emitted by RlucII (400 $\pm$ 70 nm) using a Mithras LB940 luminometer. The net BRET signal was defined as the difference between the total BRET and the signal obtained from samples expressing the RlucII-fusion constructs alone (background signal), and plotted against the ratio between the expression levels of the GFP10- and RlucII-fusion constructs as measured by the total fluorescence and luminescence signals, respectively, as previously described (Mercier et al., 2002). BRET between KCTD-BiLC and KCTD-BiFC was measured 2 min after the addition of the luciferase substrate, coelenterazine h (final concentration of 5 μM). BRET was calculated as the ratio of the light emitted by Venus (530 $\pm$ 20 nm) over the light emitted by RlucII (480 $\pm$ 20 nm) using a Mithras LB940 luminometer. BRET signals between KCTD-BiLC and Venus-Gγ2 were measured on an Infinite F500 microplate reader (Tecan) detecting Venus at 550 $\pm$ 25 nm and RlucII at <475 nm.

Electrophysiology. Whole-cell patch-clamp recordings of GABA$_B$-mediated Kir3 currents from CHO cells and cultured hippocampal neurons were performed 48–72 h and ~2 weeks (DIV18-DIV21) after transfection, respectively. EGFP-expressing cells were identified via epifluorescence using an FITC filter set and patched under infrared oblique illumination (BX61WI; Olympus). Kir3 currents were recorded at room temperature (22°C–23°C) in aCSF containing the following (in mM): 145 NaCl, 2.5 KCl, 1 MgCl$_2$, 2 CaCl$_2$, 10 HEPES, 25 glucose, pH 7.3. Neurons were superfused with aCSF supplemented with TTX (0.5 μM), DNQX (10 μM), and picrotoxin (100 μM). Patch electrodes were pulled from borosilicate glass capillaries (resistance of 3–5 MΩ) and filled with a solution containing the following (in mM): 107.5 K-gluconate, 32.5 KCl, 10 HEPES, 5 EGTA, 4 Mg-ATP, 10 phosphocreatine, 0.6 Na$_2$-GTP, at pH 7.2 (adjusted with KOH), 292 mOsm. GABA$_B$ receptor responses were evoked at −50 mV by fast application of baclofen (100 μM, 1–60 s) (Turecek et al., 2004; Dittert et al., 2006).

IPSCs were recorded in parasagittal hippocampal slices prepared from P25-P30 mice as follows. Animals were decapitated and the brains were excised in ice-cold extracellular solution containing the following (in mM): 130 NaCl, 3.5 KCl, 3.0 MgCl$_2$, 0.5 CaCl$_2$, 10 glucose, 1.25 NaH$_2$PO$_4$, 25 NaHCO$_2$, 0.5 ascorbic acid, 3 myo-inositol, and 3 sodium pyruvate; gassed with 5% CO$_2$/95% O$_2$ to pH 7.3. Slices (300 μm thick) were cut using a VT1200S vibratome (Leica), incubated at 35°C for 45 min and then stored at 31°C–32°C in the extracellular solution in which the concentrations of MgCl$_2$ and CaCl$_2$ were 1 and 2 mM, respectively. For recording, slices were superfused with aCSF containing the following
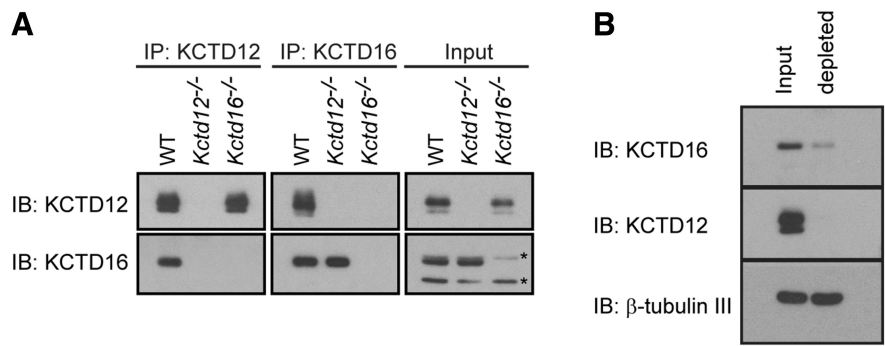

Figure 1. KCTD hetero-oligomers are abundant in the adult mouse brain. *A*, Anti-KCTD12 and anti-KCTD16 antibodies (Schwenk et al., 2010) copurify KCTD12 and KCTD16 proteins in immunoprecipitation (iP) experiments with brain lysates of WT mice, as shown on immunoblots (IB). Control IPs with brain lysates of Kctd12$^{-/-}$ and Kctd16$^{-/-}$ mice (Metz et al., 2011) show that the antibodies are specific for the KCTD12 and 16 proteins. Asterisks indicate cross-reactions of the anti-KCTD16 antibody in the Input samples. *B*, Affinity depletion of KCTD12 from hippocampi of adult mouse brains using anti-KCTD12 antibodies leads to a codepletion of KCTD16 engaged in KCTD12/KCTD16 hetero-oligomers (depleted). Control IBs of β-tubulin III show that the neuron-specific marker protein is not depleted by anti-KCTD12 antibodies.

(in mM): 130 NaCl, 3.5 KCl, 1.5 MgCl$_2$, 1.5 CaCl$_2$, 10 glucose, 1.25 NaH$_2$PO$_4$, 24 NaHCO$_3$, pH 7.3, equilibrated with 5% CO$_2$/95% O$_2$. IPSCs were elicited by electric stimulation of stratum radiatum via bipolar electrode and isolated in the presence of DNQX (10 μM), CPP (5 μM), and SR95531 (gabazine; 15 μM, used for recording of sIPSCs). Patch pipette solution contained the following (in mM): 107.5 K-gluconate, 32.5 KCl, 10 HEPES, 0.1 EGTA, 4 Mg-ATP, 10 phosphocreatine, 0.6 Na$_2$-GTP, at pH 7.2, 290 mOsm. Pharmacological GABA$_B$ responses or IPSCs were acquired with an Axopatch 200B low-pass filtered at 1 or 5 kHz and digitized at 5 or 20 kHz using a Digidata 1440A interface (Molecular Devices) driven by pClamp 10 software (RRID:SCR_011323). Cell capacitance was calculated using membrane time-constant and cell resistance values obtained from voltage responses of cells upon applying hyperpolarizing −10 pA steps at the resting potential. The holding potential was adjusted for a measured liquid junction potential of 12 mV. Whole-cell currents and voltages were analyzed using Clampfit 10 software (Molecular Devices). All values are given as mean $\pm$ SD. Statistical significances were tested using one-way ANOVA or Student's t test (GraphPad Prism, RRID:SCR_002798). TTX was from Latoxan. DNQX, CPP, and SR95531 were from Tocris Bioscience. All other reagents were from Sigma-Aldrich.

Results
KCTD hetero-oligomers in the brain
We used immunoprecipitation (IP) experiments to address whether KCTD hetero-oligomers exist in the brain (Fig. 1A). We limited our analysis to KCTD12 and KCTD16, which in the adult brain are coexpressed in many neuronal populations, including hippocampal pyramidal neurons (Metz et al., 2011). We found that anti-KCTD12 antibodies copurified KCTD16 protein from wild-type (WT) but not from control KCTD12 knock-out (Kctd12$^{-/-}$) brain lysates (Fig. 1A). Reverse IP experiments with anti-KCTD16 antibodies confirmed the existence of KCTD12/KCTD16 hetero-oligomers in WT but not in control Kctd16$^{-/-}$ brain lysates (Fig. 1A).

We next depleted KCTD12 from hippocampal lysates to determine the fraction of KCTD16 protein participating in KCTD12/KCTD16 hetero-oligomers. Complete depletion of KCTD12 from lysates with specific anti-KCTD12 antibodies removed 64.9 $\pm$ 6.1% ($n = 3$) of the KCTD16 protein from the supernatant (Fig. 1B). In the hippocampus, approximately two-thirds of the KCTD16 protein is therefore associated with KCTD12. For unknown reasons, anti-KCTD16 antibodies inefficiently depleted KCTD16 from hippocampal lysates, which pre-
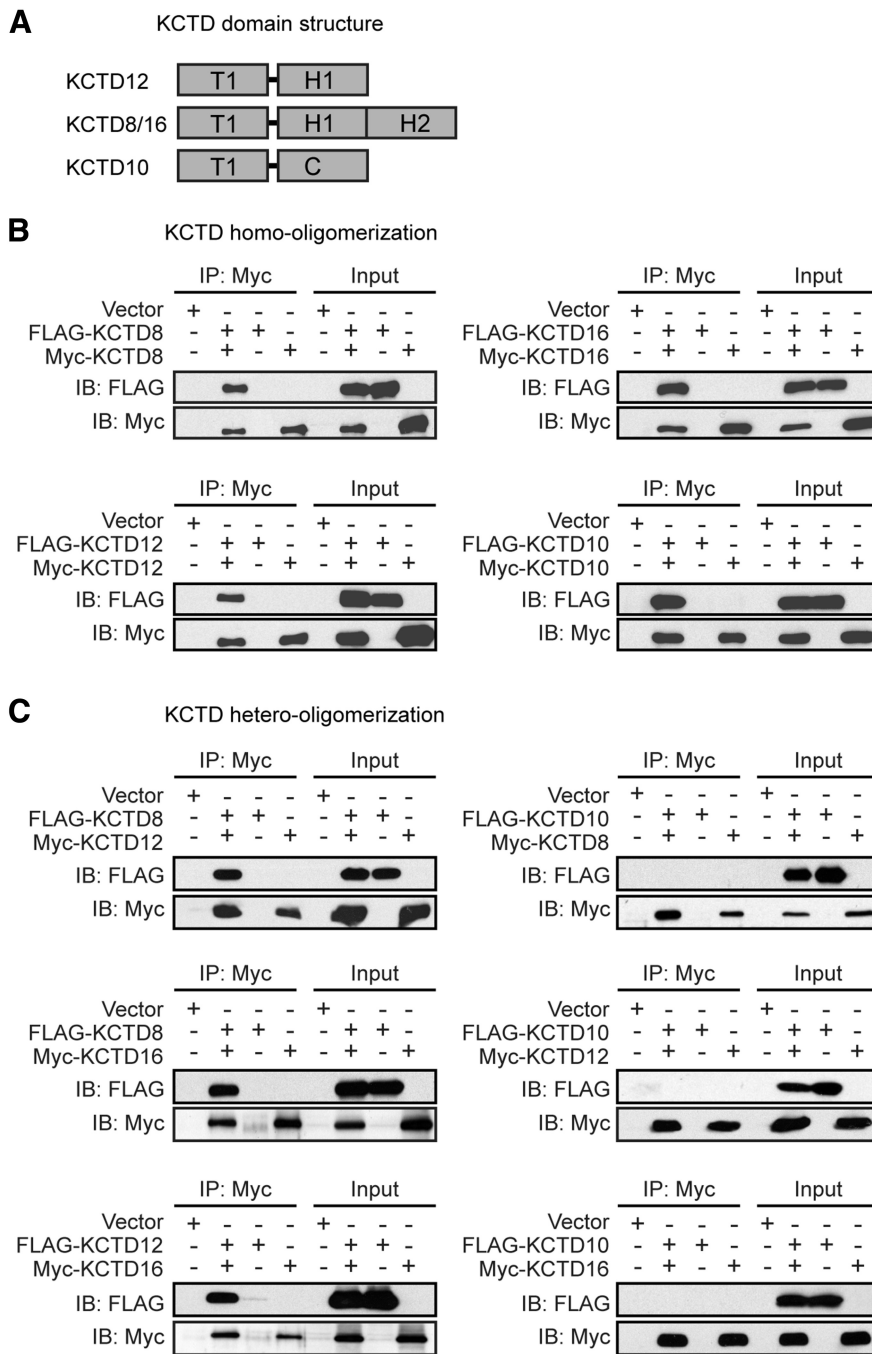
Figure 2. KCTD8, KCTD12, and KCTD16 form homo- and hetero-oligomers in transfected HEK293. **A**, KCTD domain structure. KCTDs contain T1, H1, and H2 homology domains that are not closely sequence-related with the T1 and C-terminal (C) domains of KCTD10. The H2 domains are selectively present in KCTD8 and KCTD16. **B**, KCTDs form homo-oligomeric complexes. Input lanes indicate the expression of FLAG- or Myc-tagged KCTD proteins in the cell lysates used for IP with anti-Myc antibodies. Proteins in the IPs were revealed by immunoblotting (IB) with anti-FLAG and anti-Myc antibodies. **C**, KCTD8, KCTD12, and KCTD16 form hetero-oligomers with each other, but not with KCTD10. Input lanes indicate expression of the FLAG- or Myc-tagged KCTD proteins in the cell lysates used for IPs with anti-Myc antibodies. Proteins in the IPs were revealed by IB with anti-FLAG and anti-Myc antibodies.

vented a meaningful assessment of the fraction of KCTD12 protein involved in KCTD12/KCTD16 hetero-oligomers.

T1 and H1 domains mediate homo- and hetero-oligomerization

The KCTDs are modular proteins consisting of an N-terminal T1 tetramerization domain and one or two C-terminal H1 and H2 homology domains (Fig. 2A). Earlier experiments supported that the

T1 domain of KCTD12 forms homo-oligomers (Schwenk et al., 2010; Smaldone et al., 2016). To study whether the KCTDs form hetero-oligomers in transfected HEK293 cells, we performed co-immunoprecipitation experiments with FLAG- and Myc-tagged KCTD proteins. We included KCTD10, which belongs to a different clade of the KCTD family (Seddik et al., 2012), into our analysis. KCTD10 does not associate with GABA_B receptors (Schwenk et al., 2010) and lacks H1 and H2 domains (Fig. 2A). We found that KCTD8, KCTD10, KCTD12, and KCTD16 assemble homo-oligomers in HEK293 cells (Fig. 2B); however, only KCTD8, KCTD12, and KCTD16 form hetero-oligomers in all possible dual combinations (Fig. 2C).

IP experiments with the isolated Myc-tagged T1, H1 or H2 domains of KCTD12 and KCTD16 show that both the T1 and H1 domains interact with FLAG-tagged KCTD12 (Fig. 3A) and KCTD16 (Fig. 3B) in transfected HEK293 cells. Neither the H2 domain of KCTD16 nor full-length KCTD10 interacted with KCTD12 (Fig. 3A) or KCTD16 (Fig. 3B). Collectively, these results indicate that both the T1 and H1 domains mediate KCTD homo- and hetero-oligomerization. Consistent with the H1 domains mediating oligomerization, Myc-16ΔT1, a KCTD16 mutant lacking the T1 domain, still forms homo-oligomeric FLAG-KCTD16/Myc-16ΔT1 (Fig. 3B,C) and hetero-oligomeric FLAG-KCTD12/Myc-16ΔT1 complexes (Fig. 3A,B) that interact with GABA_B2 through the T1 domain of the full-length KCTD in the complex (Fig. 3C).

Detection of KCTD homo- and hetero-oligomers in live cells

We next used a bimolecular luminescence protein-fragment complementation (BiLC) assay (Stefan et al., 2007; Armando et al., 2014) to study KCTD oligomerization in live cells. KCTD proteins were tagged at their N termini with the N- or C-terminal fragment of *Renilla* luciferase (NTRluc and CTRluc). In such a way, oligomerization of KCTD protomers can be quantified by measuring the activity (luminescence) of reconstituted Rluc. The Rluc activity measured in transfected HEK293 cells indicates that KCTD10, KCTD12, and KCTD16 all form homo-oligomers (Fig. 4A). KCTD12 and KCTD16 additionally form hetero-oligomers with each other (Fig. 4A). A 100-fold lower level Rluc activity was observed with KCTD10 in combination with KCTD12 or KCTD16 (Fig. 4A). This may represent weak nonspecific luciferase reconstitution/activity or indicate a very low level of hetero-oligomerization. KCTD homo-oligomer formation also promotes bimolecular fluorescence complementation (BiFC)

(Héroux et al., 2007) of Venus (Fig. 4A), a variant of the yellow fluorescent protein that can be used as an energy acceptor in BRET experiments. Of note, we were unable to detect a specific BiFC signal for KCTD16 homo-oligomers, suggesting that KCTD16 protomers have a lower propensity to form homo-oligomers. This is supported by two-component BRET assays using KCTD-RlucII and KCTD-GFP2 constructs, in which KCTD12 homo-oligomers showed ~9 times lower half BRET saturation values than KCTD16 homo-oligomers (KCTD12: 0.064, and KCTD16: 0.56). BiFC of Rluc and Venus allowed us to investigate whether reconstitution of Rluc and Venus from their N- and C-terminal fragments fused to KCTD monomers yields BRET due to the formation of KCTD oligomers made up from at least four protomers. Expression of increasing amounts of NTVen12 + CTVen12 with fixed amounts of NTRluc12 + CTRluc12 resulted in a hyperbolic BRET donor saturation curve (Fig. 4B), consistent with the assembly of KCTD12 homo-tetramers (or homo-pentamers) in live cells. The complementation experiments support a parallel arrangement of KCTD subunits in the oligomers. Expression of NTRluc12 + CTRluc12 or NT-Ven10 + CTVen10 with increasing amounts of NTVen10 + CTVen10 or NTRluc12 + CTRluc12, respectively, did not yield clearly saturating BRET donor curves (Fig. 4B). Inefficient complementation of Venus by NTVen16 + CTVen16 (Fig. 4A) prevented us from testing with BiFC/BRET whether KCTD16 homo- and KCTD12/KCTD16 hetero-tetramers are formed.

Figure 3. Self-interacting T1 and H1 domains mediate KCTD homo- and hetero-oligomerization in HEK293 cells. IP of FLAG-KCTD12 (**A**) or FLAG-KCTD16 (**B**) with the Myc-tagged T1 and H1 domains of KCTD12 or KCTD16. IPs were performed with anti-Myc antibodies from total cell lysates. Proteins in the IPs were revealed by immunoblotting (IB) using anti-FLAG and anti-Myc antibodies. Input lanes indicate expression of the tagged proteins in the cell lysates used for the IPs. The Myc-tagged T1 and H1 domains of KCTD12 and KCTD16, but not the Myc-tagged H2 domain of KCTD16, coprecipitate FLAG-KCTD12 and FLAG-KCTD16. KCTD16 lacking the T1 domain (Myc-16ΔT1) interacts with FLAG-KCTDs via its H1 domain. Myc-KCTD12 and Myc-KCTD16 were used as positive controls, Myc-KCTD10 as a negative control. **C**, Myc-16ΔT1 copurifies GABA_B2 (GB2-YFP) in the presence of KCTD16 or KCTD12, showing that Myc-16ΔT1 can homo- and hetero-oligomerize with KCTD16 and KCTD12 at GABA_B2. Myc-16ΔT1 does not directly interact with GABA_B2 because it lacks the T1 domain that is a prerequisite necessary for binding to GABA_B2. IPs were performed with anti-Myc antibodies from total cell lysates. Proteins in the IPs were revealed by IB using anti-GABA_B2, anti-FLAG, and anti-Myc antibodies. Input lanes (bottom) indicate expression of the tagged proteins in the cell lysates used for the IPs.

KCTD12/KCTD16 hetero-oligomers interact with the receptor and the G-protein

We used BiLC in combination with BRET to study whether KCTD hetero-oligomers interact with GABA_B receptors in intact cells. BRET-donor saturation curves were determined with fixed amounts of NTRlucKCTDs + CTRlucKCTDs and increasing amounts of Myc-GABA_B1 and the energy acceptor HA-GABA_B2-GFP (Fig. 5A). We observed specific BRET between the reconstituted Rluc and HA-GABA_B2-GFP with KCTD12 and KCTD16 homo-oligomers as well as with KCTD12/KCTD16 hetero-oligomers. We did not observe specific BRET with KCTD10 homo-oligomers and the receptor, as indicated by low BRET and a nonsaturating BRET to acceptor/donor relationship (Fig. 5A). Similarly, a nonspecific BRET signal with a linear BRET to acceptor/donor relationship ($y = 2.4x + 5.7$) was obtained in control experiments with KCTD12 homo-oligomers and a GABA_B2 acceptor in which tyrosine-902 was mutated to alanine, which prevents KCTD binding to GABA_B2 (Schwenk et al., 2010). BRET experiments therefore demonstrate that KCTD12/KCTD16 hetero-oligomers interact with GABA_B receptors in live cells.
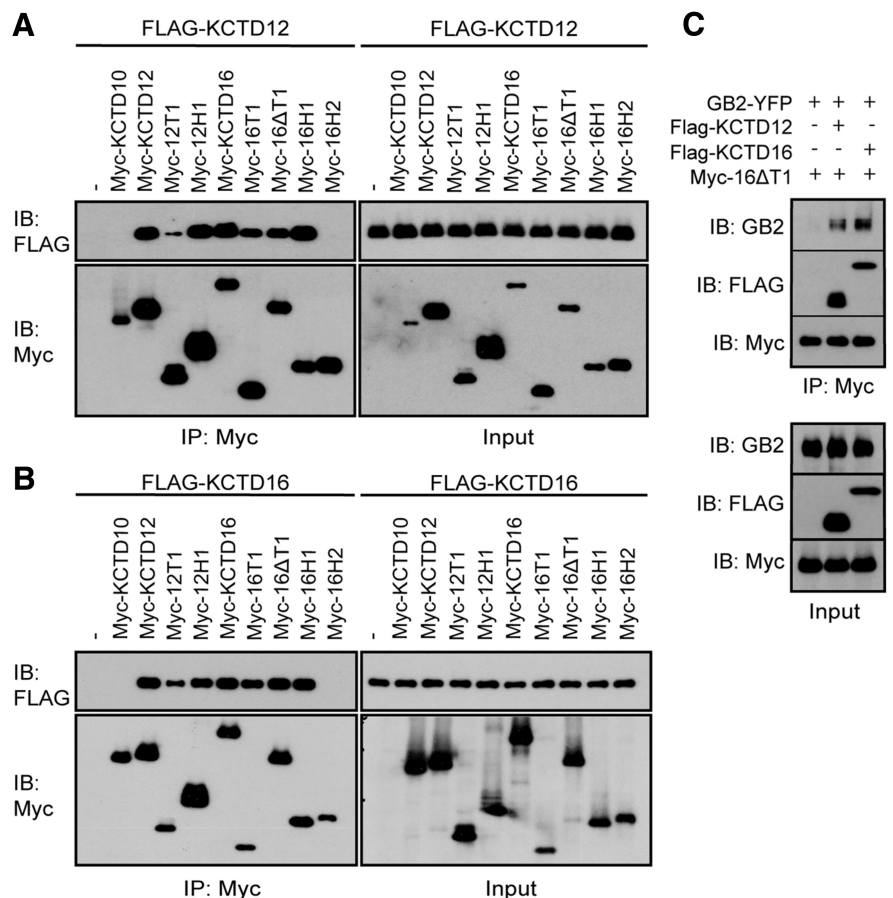
The KCTDs not only interact with the receptor but also with the G-protein (Turecek et al., 2014). It is unknown whether the KCTDs interact as monomers or oligomers with the G-protein. We therefore used BiLC in combination with BRET to study whether KCTD oligomers can interact with the G-protein. We determined BRET donor saturation curves using fixed amounts of NTRlucKCTDs + CTRlucKCTDs and increasing amounts of the G-protein subunits Gβ2 and Venus-Gγ2 (Fig. 5B). BRET between the reconstituted Rluc and Venus-Gγ2 was observed with KCTD12 and KCTD16 homo-oligomers as well as with KCTD12/KCTD16 hetero-oligomers. Because KCTD12 and KCTD16 exert distinct kinetic effects on G-protein signaling (Schwenk et al., 2010; Turecek et al., 2014), it is possible that KCTD hetero-oligomers endow receptors with novel properties.

KCTD12/KCTD16 hetero-oligomers generate unique receptor-induced K+ current responses in CHO cells

KCTD12, but not KCTD8 or KCTD16, induces strong desensitization of GABA_B receptor-activated Kir3 currents (Schwenk et al., 2010; Seddik et al., 2012; Turecek et al., 2014) (Fig. 6A–C). We
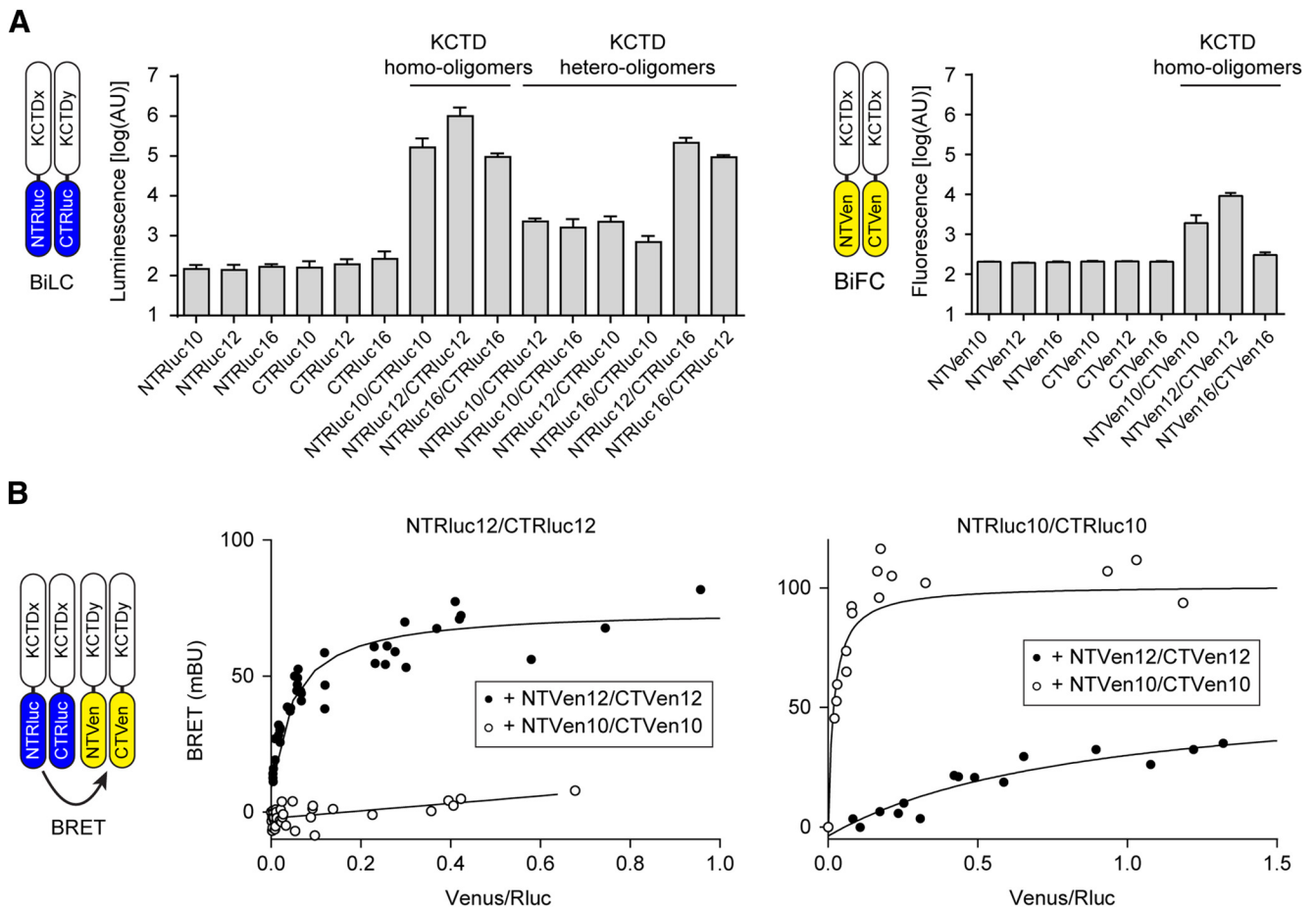
Figure 4. KCTD oligomerization in live HEK293 cells. *A*, BiLC or BiFC through oligomerization of split Rluc- or split Venus-tagged KCTDs, respectively. Cells were transfected with NTRlucKCTD and CTRlucKCTD or NTVenKCTD and CTVenKCTD constructs, and oligomerization between Rluc- or Venus-fragment-tagged KCTDs was monitored by measuring reconstituted luciferase or fluorescence activity, respectively. KCTD10, KCTD12, and KCTD16 all form homo-oligomers. KCTD12 and KCTD16 additionally form hetero-oligomers together. KCTD10 has a weak propensity to also form hetero-oligomers with KCTD12 or KCTD16. Labels in the bar graphs indicate the transfected Rluc- or Venus-fragment-tagged KCTD proteins. Data are mean ± SEM of 3 or 4 independent experiments. *B*, BRET between reconstituted Rluc and Venus in KCTD oligomers. Cells were transfected with fixed amounts of NTRlucKCTD and CTRlucKCTD constructs and increasing amounts of NTVenKCTD and CTVenKCTD constructs. BRET donor saturation curves were generated by expressing the net BRET signal detected as a function of the ratio between the total fluorescence signal and the luminescence signal (acceptor/donor ratio; expressed in milliBRET units, mBU) and demonstrate that both KCTD12 and KCTD10 can assemble into homo-tetramers or higher-order oligomers from the individually tagged monomers. KCTD12 and KCTD10 have a much weaker propensity to form hetero-tetramers. Data points represent the mean of technical duplicates combined from 4 independent experiments.

studied the influence of hetero-oligomeric KCTD12/KCTD16 complexes on K$^+$ current desensitization in transfected CHO cells expressing GABA$_B$ receptors together with Kir3 channels. We recorded K$^+$ currents in response to a prolonged application of the GABA$_B$ agonist baclofen (100 μM, 1 min). Cells coexpressing KCTD12 and KCTD16 exhibited significantly reduced and slower K$^+$ current desensitization than cells expressing KCTD12 alone (Fig. 6*A*,*C*,*E*). This may be due to the formation of hetero-oligomeric KCTD12/KCTD16 complexes and/or the simultaneous assembly of desensitizing KCTD12 and nondesensitizing KCTD16 homo-oligomers. To avoid association of KCTD16 homo-oligomers with the receptor, we substituted KCTD16 with 16ΔT1, which lacks the T1 domain that is necessary for direct binding to the receptor (Schwenk et al., 2010). However, 16ΔT1 is able to indirectly bind to the receptor through hetero-oligomerization with KCTD12 (Fig. 3*C*). Cells expressing KCTD12 and 16ΔT1 therefore form receptors associated with KCTD12/KCTD16ΔT1 hetero-oligomers or KCTD12 homo-oligomers but not with 16ΔT1 homo-oligomers. We found that cells coexpressing 16ΔT1 and KCTD12 exhibited reduced and slower K$^+$ current desensitization than cells expressing KCTD12 alone (Fig. 6*B*–*E*), which demonstrates that the kinetic properties

of KCTD12/KCTD16ΔT1 hetero-oligomers differ from those of KCTD12 homo-oligomers. As a control, expression of 16ΔT1 alone yielded nondesensitizing responses (Fig. 6*B*,*C*), similar to expression of KCTD16 alone (Fig. 6*A*,*B*). In summary, the electrophysiological data indicate that KCTD12/KCTD16 hetero-oligomers desensitize GABA$_B$-activated K$^+$ currents to a lesser extent and more slowly than KCTD12 homo-oligomers.

Analysis of the deactivation kinetics of K$^+$ currents activated by applying baclofen for 1 min revealed a novel regulatory feature of the KCTDs (Fig. 6*F*,*G*). KCTD12 and KCTD16 significantly accelerated and slowed current deactivation, respectively, compared with cells lacking KCTDs (Fig. 6*F*,*G*). A slowing of current deactivation is also observed with 16ΔT1 (Fig. 6*F*,*G*). This indicates that the deactivation does not necessarily require KCTD16 binding to the receptor and supports that the deactivation mechanism operates downstream of the receptor. Coexpression of KCTD12 with 16ΔT1 or KCTD16 yielded fast deactivating currents, showing that KCTD12 overrules the slowing effect of 16ΔT1 or KCTD16 within the hetero-oligomer (Fig. 6*F*,*G*). No accelerated current deactivation is observed in the presence of KCTD12 after a baclofen application for 2 s, which is too short to induce pronounced desensitization (Fig. 6*H*,*I*). Accelerated cur-
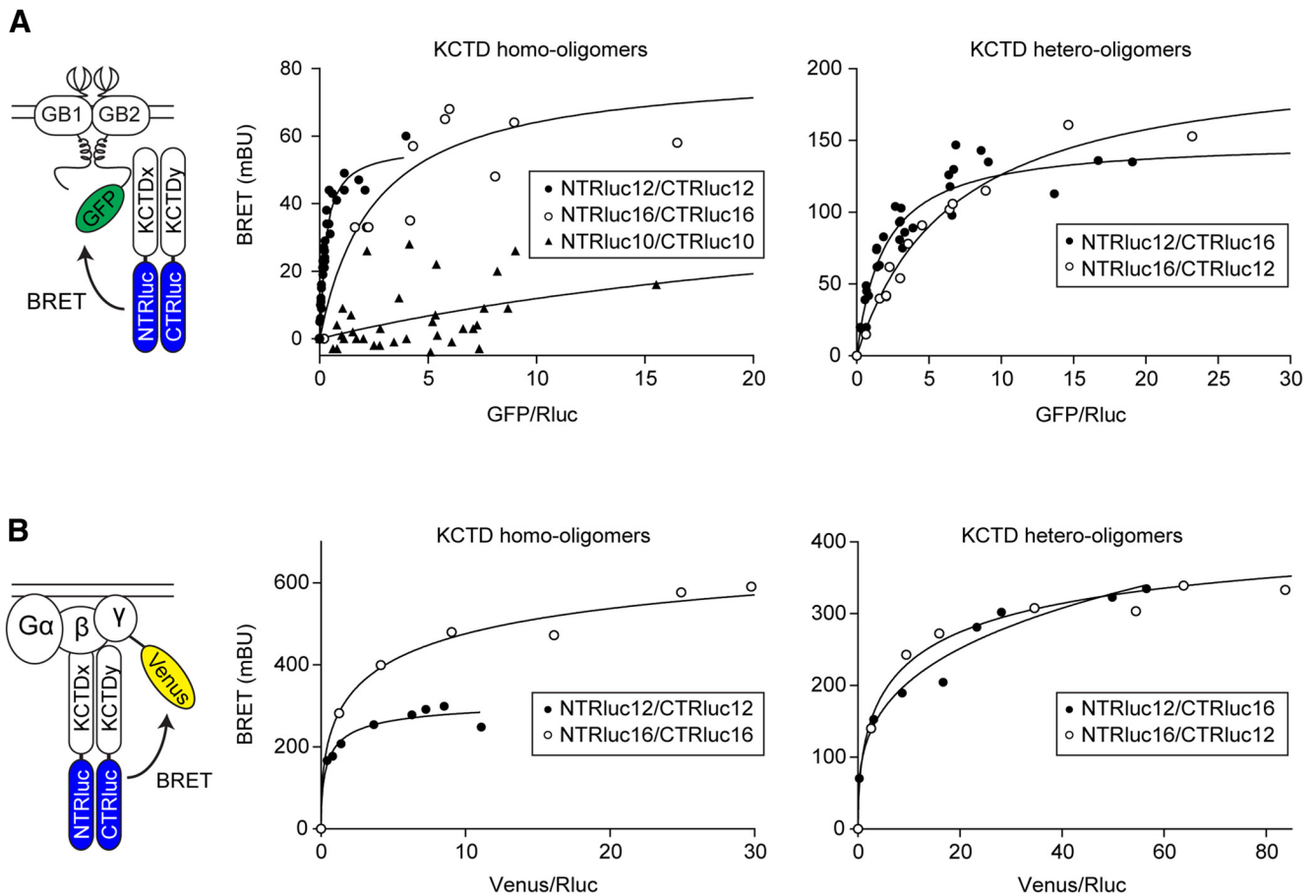
Figure 5. KCTD homo- and hetero-oligomers bind to both GABA$_B$ receptors and G-proteins in live HEK293 cells. ***A***, BRET between KCTD oligomers and GABA$_B$ receptors in living cells. Cells were transfected with fixed amounts of NTRlucKCTD and CTRlucKCTD constructs and increasing amounts of Myc-GABA$_{B1}$ and HA-GABA$_{B2}$-GFP constructs. BRET was measured between reconstituted Rluc and GABA$_{B2}$-GFP. Data points represent the mean of technical duplicates combined from 6 or 7 independent experiments. Donor/acceptor ratios needed to reach half BRET saturation (BRET$_{50}$) were as follows: KCTD12 homo-oligomer: 0.27 $\pm$ 0.03; KCTD16 homo-oligomer: 2.55 $\pm$ 0.97; KCTD12/KCTD16 hetero-oligomer: 1.91 $\pm$ 0.29; KCTD16/KCTD12 hetero-oligomer: 6.65 $\pm$ 0.71 (mean $\pm$ SEM, n = 6 or 7). ***B***, BRET between KCTD oligomers and the G-protein in live cells. Cells were transfected with fixed amounts of NTRlucKCTD and CTRlucKCTD constructs and increasing amounts of Gβ2 and Gγ2-YFP constructs. BRET was measured between reconstituted Rluc and Gγ2-YFP. Data points represent the mean of technical quadruplicates from a representative experiment (n = 3).

rent deactivation in the presence of KCTD12 thus correlates with current desensitization. This is corroborated by a similar baclofen concentration dependence of current desensitization and deactivation in the presence of KCTD12 (Fig. 7A). We did not observe a sigmoidal agonist concentration dependence of current deactivation in the absence of KCTD or in the presence of KCTD16 (Fig. 7B), which further supports that accelerated deactivation relates to KCTD12-induced desensitization. The slowing of current deactivation that is observed in the presence of KCTD16 (Fig. 6G) is use-dependent, as indicated by the linear baclofen concentration dependence of the deactivation (Fig. 7B). In summary, the data show that, after prolonged receptor activation, homo-oligomeric KCTD12 complexes yield strongly desensitizing fast deactivating K$^+$ current responses. In contrast, homo-oligomeric KCTD16 complexes yield nondesensitizing slowly deactivating current responses. Hetero-oligomeric KCTD12/KCTD16 complexes produce distinct current K$^+$ responses characterized by intermediate desensitization and fast deactivation. In contrast, during brief receptor activation, KCTD12/KCTD16 hetero-oligomers produce nondesensitizing slowly deactivating current responses.

We observed that individual and combined expression of KCTD12 and KCTD16 in transfected CHO cells significantly increases the peak K$^+$ current amplitudes (presented as current

densities) in response to a nearly saturating concentration of baclofen (Fig. 7C). No increase in current density is observed with 16ΔT1, which does not bind to the receptor (Fig. 7C). The increase in current density observed with KCTD12, KCTD16, and KCTD12/KCTD16 may therefore relate to precoupling of the G-protein at the receptor via the KCTD proteins (Turecek et al., 2014; Schwenk et al., 2016). Increased surface expression of GABA$_B$ receptors in the presence of KCTD12 (Ivankova et al., 2013) may further contribute to an increase in current amplitude. Receptors assembled with KCTD12/KCTD16ΔT1 show a trend toward increased current amplitudes, which, however, does not reach statistical significance (Fig. 7C). Possibly, precoupling of the G-protein and/or surface expression is less efficient when KCTD12 combines with 16ΔT1 than with full-length KCTD16.

We additionally determined the baclofen concentration/K$^+$ current response curves in the presence or absence of KCTD12 and KCTD16. The EC$_{50}$ values (derived from log(baclofen)/K$^+$ current response) measured in CHO cells expressing KCTD12 (9.7 $\pm$ 7.7 μM, n = 8) or KCTD16 (20.8 $\pm$ 8.7 μM, n = 7) were significantly smaller than those in cells lacking KCTD proteins (66.4 $\pm$ 26.7 μM, n = 8; p < 0.001, Dunnett's multiple-comparison test), consistent with earlier findings (Schwenk et al., 2010). The EC$_{50}$ values measured in cells expressing KCTD12 or KCTD16 do not significantly differ from each other (Bonferroni
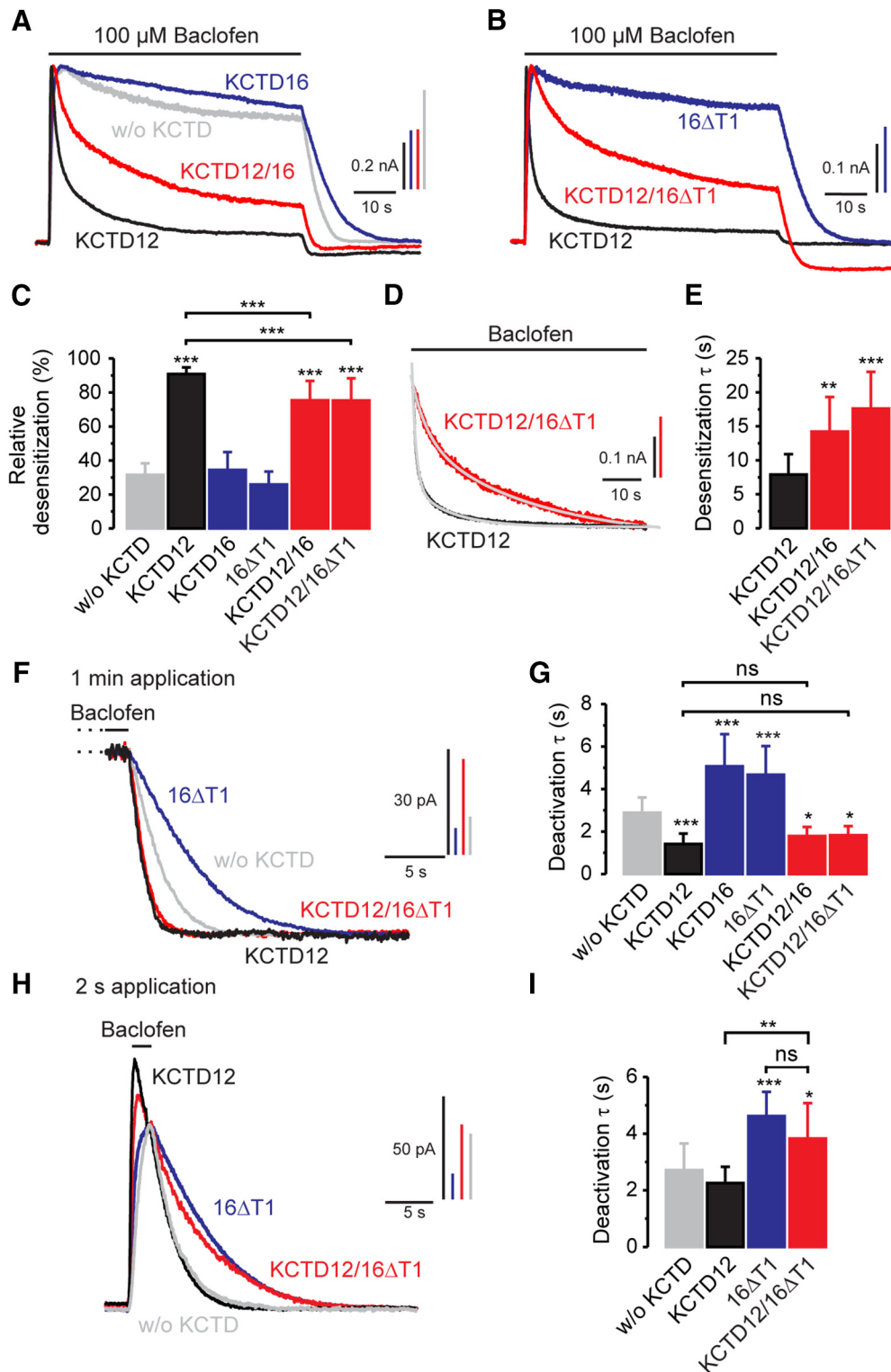
Figure 6. Bidirectional modulation of GABA_B-activated Kir3 currents by KCTD hetero-oligomers. ***A***, Representative baclofen-activated K⁺ current traces recorded at −50 mV from CHO cells expressing GABA_B receptors and Kir3.1/3.2 channels either without KCTD (without [w/o], gray trace), with KCTD12 alone (black), with KCTD16 alone (blue), or with both KCTDs (red). KCTD12, but not KCTD16, induces pronounced and rapid desensitization of K⁺ currents. Coexpression of KCTD12 and KCTD16 results in intermediate current desensitization. ***B***, Baclofen-activated K⁺ currents recorded from CHO cells either expressing KCTD12 (black), a KCTD16 mutant lacking the T1 domain (16ΔT1, blue), or both KCTD isoforms (red). Expression of KCTD12 together with 16ΔT1, which only binds to the receptor in a complex with KCTD12, reduces KCTD12-induced desensitization. ***C***, Bar graph summarizing the relative desensitization of baclofen-activated K⁺ currents. The relative desensitization was calculated as follows: $(1 - (\text{ratio of current amplitude after 60 s vs peak current})) \times 100$. Values are mean ± SD of 26 (w/o KCTD), 17 (KCTD12), 14 (KCTD16), 11 (16ΔT1), 6 (KCTD12/KCTD16), and 13 (KCTD12/KCTD16ΔT1) cells. ***D***, Normalized traces represent a slower time course of K⁺ current desensitization in CHO cells coexpressing KCTD12 and 16ΔT1 (red) compared with CHO cells expressing KCTD12 alone (black). Traces are fitted to a double exponential function (gray solid line) with time constants $\tau 1 = 1.0$ s (relative contribution to desensitization 71.7%) and $\tau 2 = 9.4$ s for KCTD12 and $\tau 1 = 3.9$ s (33.8%) and $\tau 2 = 28.4$ s for KCTD12/KCTD16ΔT1. ***E***, Bar graph showing mean amplitude-weighted time constants obtained from fits of a double exponential function to K⁺ current deactivation. ***F***, Superimposed traces of the deactivation phase of K⁺ currents activated by application of baclofen to CHO cells for 1 min as in ***A*** or ***B*** displayed with an expanded time scale. KCTD12 and KCTD16 have opposite effects on the time course of the deactivation, with KCTD12 being dominant when (*Figure legend continues.*)

pairwise comparison test). Because the KCTD proteins have marginal effects on agonist affinity at the orthosteric binding site (Rajalu et al., 2015), the decrease in EC_{50} values in the presence of KCTD12 or KCTD16 is best explained by the KCTD-mediated precoupling of the G-protein at the receptor (Turecek et al., 2014; Schwenk et al., 2016). KCTD hetero-oligomers and homo-oligomers therefore likely activate G-proteins to a similar extent.

KCTD12/KCTD16 hetero-oligomers regulate GABA_B-activated K+ currents in hippocampal neurons

We next investigated whether KCTD hetero-oligomers influence baclofen-activated K+ currents in cultured neurons. Previous experiments showed that hippocampal neurons express high levels of KCTD12 and KCTD16 (Schwenk et al., 2010; Metz et al., 2011) and that the lack of KCTDs in knock-out neurons influences desensitization of baclofen-evoked K+ currents (Turecek et al., 2014). Accordingly, we found that, during prolonged receptor activation, K+ currents desensitize significantly less in $Kctd12^{-/-}$ and $Kctd12/16^{-/-}$ neurons than in WT neurons, as expected from the lack of KCTD12 (Fig. 8A,B). When directly comparing $Kctd12^{-/-}$ and $Kctd12/16^{-/-}$ neurons, we observe significantly less desensitization in $Kctd12/16^{-/-}$ neurons than in $Kctd12^{-/-}$ neurons (Fig. 8B). Desensitization is activity-dependent and therefore influenced by the kinetic properties of the G-protein activation/deactivation cycle (i.e., the rates of GDP-GTP exchange and GTP hydrolysis at Gα) (Chuang et al., 1998; Leaney et al., 2004). Less desensitization in $Kctd12/16^{-/-}$ than in $Kctd12^{-/-}$ neurons may thus be caused by reduced precoupling of the G-protein at the receptor and a consequent slower K+ current activation. K+ currents displayed significantly increased desensitization in $Kctd16^{-/-}$ neurons versus WT neurons. Considering that two-thirds of the KCTD16 proteins in the hippocampus are associated with KCTD12 (Fig. 1B), the increased desensitization in $Kctd16^{-/-}$ neurons can be explained by the absence of KCTD12/KCTD16 complexes that normally would attenuate KCTD12-induced desensitization. In line with this proposal, expression of exogenous KCTD16 or 16ΔT1 in $Kctd16^{-/-}$ neurons significantly decreased desensitization (Fig. 8C,D), which in the case of 16ΔT1 must relate to oligomerization with endogenous KCTD12. In addition to forming hetero-oligomers with endogenous KCTD12, exogenous KCTD16 may additionally compete with endogenous KCTD12 for binding at the receptor, which further decreases desensitization. K+ current deactivation was significantly slowed in $Kctd12^{-/-}$ neurons compared with WT neurons (Fig. 8E,F), in line with a faster K+ current deactivation observed during prolonged baclofen application in the presence of KCTD12 in transfected CHO cells (Fig. 6F,G). The significantly slower current deactivation in $Kctd12^{-/-}$ compared with $Kctd12/16^{-/-}$ neurons (Fig. 8E,F) is also consistent with the observed slowing of current deactivation in CHO cells expressing KCTD16 (Fig. 6G). We also observed a

←

(*Figure legend continued.*)   coexpressed with KCTD16. **G**, Bar graph summarizing the time constants obtained from a fit of the K+ current deactivation to a single exponential function. **H**, Representative traces of K+ currents activated by baclofen (2 s) to CHO cells expressing no KCTD (w/o, gray), KCTD12 alone (black), 16ΔT1 alone (blue), or both KCTDs (red). KCTD12 neither reduces the effect of 16ΔT1 nor accelerates deactivation of brief current responses. **I**, Bar graph showing mean time constants obtained from fits of current deactivation to a one exponential function. Data are collected from 12 (w/o KCTD), 11 (KCTD12), 6 (16ΔT1), and 6 (KCTD12/KCTD16ΔT1) experiments. *p < 0.05 (Dunnett's multiple-comparison test and Bonferroni pairwise comparison test). **p < 0.01 (Dunnett's multiple-comparison test and Bonferroni pairwise comparison test). ***p < 0.001 (Dunnett's multiple-comparison test and Bonferroni pairwise comparison test).
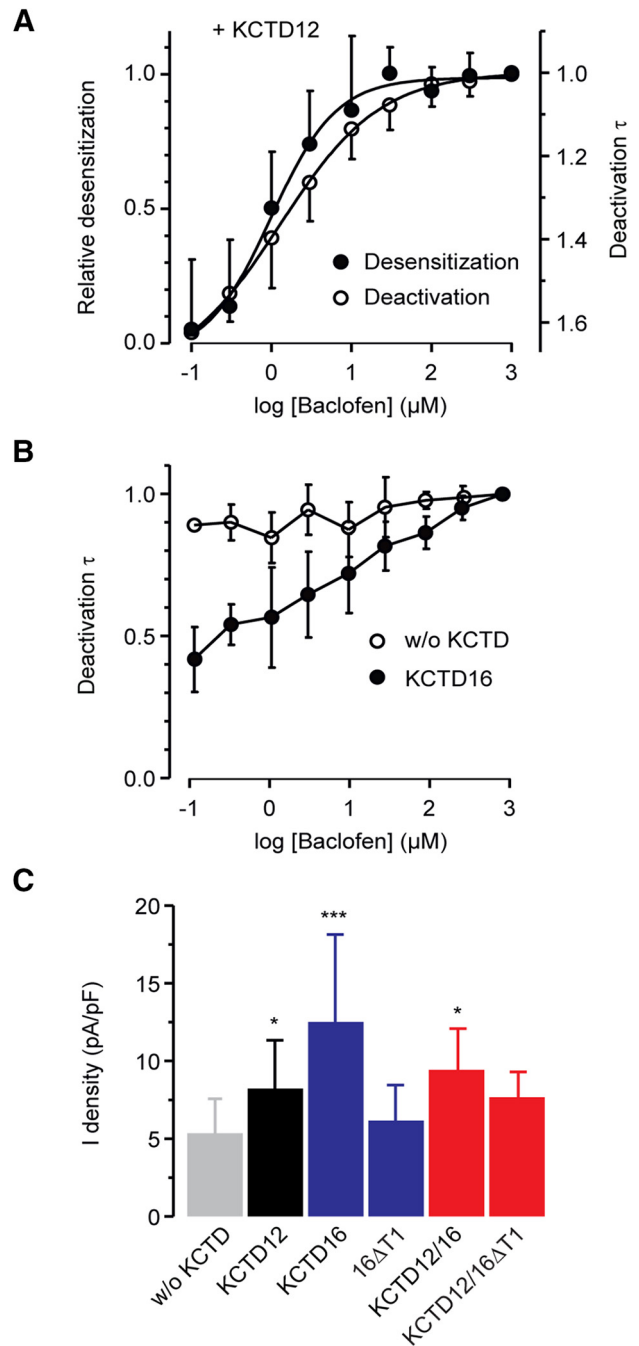
Figure 7. Influence of KCTD12 and KCTD16 on desensitization, deactivation, and amplitude of GABA_B-induced Kir3 currents in CHO cells. **A**, Agonist concentration dependence of the desensitization and deactivation of Kir3 currents in the presence of KCTD12. Each point in the curve represents the relative desensitization (mean ± SD, data from 9 cells) or deactivation time constant (8 cells) of 25-s-long baclofen responses, normalized in each cell to the value obtained at the highest baclofen concentration (1 mM). The log(baclofen)-response curves (solid black lines) were obtained by fitting the experimental data to a sigmoidal function (GraphPad Prism, RRID:SCR_002798). The half-maximal desensitization or deactivation time constant reduction was observed at 1.3 or 1.0 μM of baclofen, respectively. **B**, Agonist concentration dependence of the deactivation of Kir3 currents in the absence (without [w/o] KCTD) or presence of KCTD16. **C**, Bar graph summarizing the effects of KCTD12 and KCTD16 on K+ current densities (current normalized to cell capacitance) evoked by 100 μM baclofen. Data are the mean ± SD of 23 (w/o KCTD), 15 (KCTD12), 12 (KCTD16), 11 (16ΔT1), 5 (KCTD12/KCTD16), and 7 (KCTD12/KCTD16ΔT1) cells. KCTD12 and KCTD16 expressed alone or in combination significantly increased the amplitudes of Kir3 currents. *p < 0.05 (Dunnett's multiple-comparison test). ***p < 0.001 (Dunnett's multiple-comparison test). Data are mean ± SD of 10 (w/o KCTD) and 6 (KCTD16) cells.
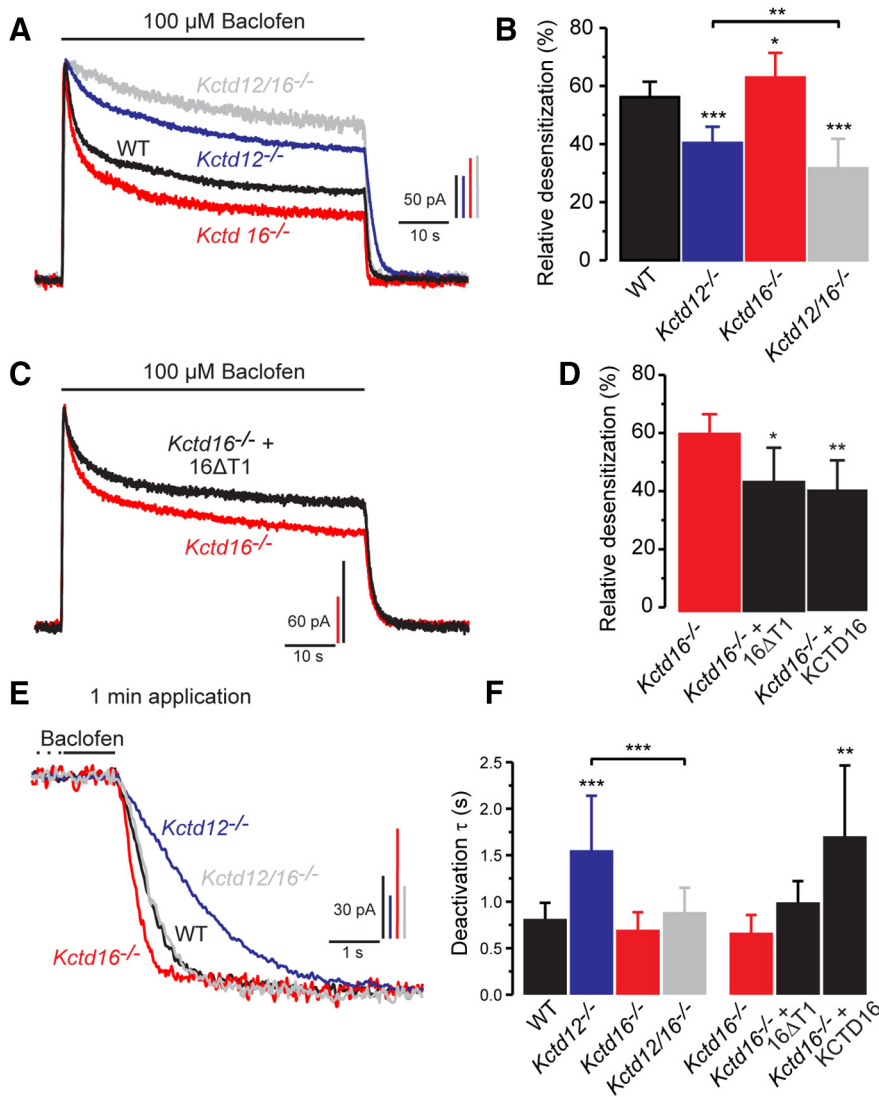
Figure 8. KCTD12/KCTD16 hetero-oligomers modulate baclofen-activated K$^+$ current responses in cultured hippocampal neurons. **A**, Representative traces of baclofen-evoked K$^+$ currents recorded neurons of WT (black), *Kctd12*$^{-/-}$ (blue), *Kctd16*$^{-/-}$ (red), or *Kctd12/16*$^{-/-}$ (gray) mice. **B**, Bar graph summarizing K$^+$ current desensitization in neurons of different genotypes. Data are mean ± SD of 18 (WT), 14 (*Kctd12*$^{-/-}$), 13 (*Kctd16*$^{-/-}$), and 12 (*Kctd12/16*$^{-/-}$) neurons. Genetic ablation of KCTD12 or KCTD16 leads to decreased or increased current desensitization, respectively. **C**, Representative traces of baclofen-evoked K$^+$ currents recorded from *Kctd16*$^{-/-}$ neurons expressing exogenous 16ΔT1. **D**, Bar graph summarizing K$^+$ current desensitization in neurons with and without 16ΔT1 or KCTD16. Data are collected of 6 (*Kctd16*$^{-/-}$), 7 (*Kctd16*$^{-/-}$ + 16ΔT1), and 6 (*Kctd16*$^{-/-}$ + KCTD16) neurons. **E**, Superimposed traces of the deactivation phase of baclofen-evoked K$^+$ currents shown in **A** displayed with an expanded time scale. **F**, Bar graph summarizing the time constants obtained from a fit of the current deactivation to a single exponential function. The current deactivation is similar in *Kctd16*$^{-/-}$ neurons and WT neurons. However, current deactivation in *Kctd12*$^{-/-}$ neurons reveals a KCTD16-mediated slowing compared with *Kctd12/16*$^{-/-}$ neurons. Expression of KCTD16, but not 16ΔT1, in *Kctd16*$^{-/-}$ neurons significantly prolonged the K$^+$ current deactivation phase, suggesting a competition of exogenous KCTD16 with endogenous KCTD12 at GABA_B receptor. Data of 18 (WT), 14 (*Kctd12*$^{-/-}$), 12 (*Kctd16*$^{-/-}$), 12 (*Kctd12/16*$^{-/-}$), 6 (*Kctd16*$^{-/-}$ + GFP), 7 (*Kctd16*$^{-/-}$ + 16ΔT1), and 4 (*Kctd16*$^{-/-}$ + KCTD16) neurons. *$p < 0.05$ (Dunnett's multiple-comparison test or Bonferroni pairwise comparison test). **$p < 0.01$ (Dunnett's multiple-comparison test or Bonferroni pairwise comparison test). ***$p < 0.001$ (Dunnett's multiple-comparison test or Bonferroni pairwise comparison test).

16ΔT1 produces similar deactivation kinetics as KCTD12 alone during prolonged baclofen application (Fig. 6 *F*, *G*). Therefore, it appears that KCTD12 dictates the deactivation kinetics in KCTD12/KCTD16ΔT1 hetero-oligomers. In summary, the analysis of hippocampal neurons supports that the KCTD composition of GABA_B receptors enables a bidirectional regulation of the desensitization and deactivation kinetics of receptor-activated K$^+$ currents.

The current densities of baclofen-evoked K$^+$ currents in *Kctd12/Kctd16*$^{-/-}$ neurons were significantly reduced compared with WT, *Kctd12*$^{-/-}$, and *Kctd16*$^{-/-}$ neurons (WT: 1.7 ± 0.6 pA/pF, $n = 18$; *Kctd12*$^{-/-}$: 1.5 ± 0.7 pA/pF, $n = 16$, *Kctd16*$^{-/-}$: 1.6 ± 0.7 pA/pF, $n = 13$, *Kctd12/Kctd16*$^{-/-}$: 1.0 ± 0.3 pA/pF, $n = 13$; $p < 0.01$; Dunnett's multiple-comparison test). This is consistent with the data from heterologous cells showing that KCTD12 and KCTD16 increase the peak amplitude of baclofen-induced K$^+$ currents (Fig. 7*C*).

Altered GABA_B-mediated sIPSCs in *Kctd16*$^{-/-}$ neurons
The data presented above suggest that the KCTD composition influences the kinetics of sIPSCs during prolonged GABA_B receptor activation (Mapelli et al., 2009; Wang et al., 2010). However, whether the KCTD composition influences sIPSCs during phasic short receptor activation (De Koninck and Mody, 1997; Lüscher et al., 1997) is unclear. We therefore analyzed the decay of neuronal GABA_B responses following a brief (1 s) pharmacological activation with baclofen (Fig. 9 *A*, *B*). The deactivation of K$^+$ currents in response to this brief baclofen stimulus is significantly faster in *Kctd16*$^{-/-}$ neurons compared with WT or *Kctd12*$^{-/-}$ neurons. This suggests that, in hippocampal neurons, KCTD16, but not KCTD12, influences the duration of GABA_B receptor-induced phasic sIPSCs. To test whether KCTD16 indeed regulates the deactivation kinetics of synaptically evoked currents, we recorded sIPSCs elicited by electric stimulation of GABAergic fibers in the stratum radiatum from CA1 pyramidal neurons clamped at −50 mV (Fig. 9*C*). Fitting of the sIPSC decay phase with a one exponential function

revealed that the decay time constant was significantly reduced in *Kctd16*$^{-/-}$ neurons compared with WT neurons (Fig. 9*C*–*E*). The maximal amplitude of sIPSCs (WT: 19.5 ± 8.0 pA, $n = 8$; *Kctd16*$^{-/-}$: 21.1 ± 8.1 pA, $n = 8$) and the decay phase of GABA_A receptor-mediated IPSCs (Fig. 9 *D*, *E*) are not altered in *Kctd16*$^{-/-}$ neurons. This makes it unlikely that the changes observed in sIPSC kinetics in *Kctd16*$^{-/-}$ neurons are due to adaptive changes in GABA uptake or degradation. In *Kctd12*$^{-/-}$ neurons, the deactivation kinetics of sIPSCs were

slowing of current deactivation when overexpressing exogenous KCTD16 in *Kctd16*$^{-/-}$ neurons (Fig. 8*F*). In this case, overexpression of exogenous KCTD16 may outcompete endogenous KCTD12 (that accelerates deactivation) at the receptor. In contrast, no slowing of K$^+$ current deactivation is observed when overexpressing exogenous 16ΔT1 in *Kctd16*$^{-/-}$ neurons, presumably because 16ΔT1 does not compete with endogenous KCTD12 for binding at the receptor. This result is consistent with results obtained in heterologous cells showing that coexpression of KCTD12 with

similar to WT neurons while their maximal amplitudes were significantly reduced (WT: 24.6 ± 9.1 pA, n = 11; $Kctd12^{-/-}$: 16.8 ± 7.4, n = 11). The reduction in amplitude may relate to a decrease in receptor surface expression in the absence of KCTD12 (Ivankova et al., 2013). In summary, we find that the kinetic properties of sIPSCs in hippocampal neurons are shaped by the KCTD16-mediated slowing of K⁺ current deactivation, an effect that is retained in hetero-oligomeric complexes with KCTD12.

Discussion

It is well established that KCTD homo-oligomers bind to GABA_B receptors and regulate G-protein signaling of the receptor (Schwenk et al., 2010; Turecek et al., 2014; Rajalu et al., 2015). Here we demonstrate that KCTDs also form hetero-oligomers in all possible dual combinations. We further show that GABA_B receptors assembled with KCTD12/KCTD16 hetero-oligomers combine regulatory properties of the individual KCTDs to generate receptors with novel signaling characteristics. In response to prolonged receptor stimulation for 1 min, KCTD12/KCTD16 hetero-oligomers produce moderately desensitizing fast deactivating currents whereas KCTD12 and KCTD16 homo-oligomers produce strongly desensitizing fast deactivating currents and nondesensitizing slowly deactivating currents, respectively. In response to brief receptor stimulation (2 s), hetero-oligomers produce nondesensitizing slowly deactivating currents. Accordingly, we show that, in hippocampal neurons, KCTD12/KCTD16 hetero-oligomers significantly slow the deactivation kinetics of phasic GABA_B receptor-induced sIPSCs.

KCTD hetero-oligomers in the brain

Hetero-oligomerization of KCTD8, KCTD12, and KCTD16 is mediated by the self-interacting T1 and H1 homology domains that also mediate homo-oligomerization (Schwenk et al., 2010; Correale et al., 2013). Hetero-oligomerization was observed within other KCTD clades (Sowa et al., 2009; De Smaele et al., 2011). Based on our BiLC experiments we conclude that KCTD oligomers arrange in parallel, similar as with KCTD5 (Dementieva et al., 2009). BiLC experiments are consistent with the proposed tetrameric or pentameric assembly of native KCTD oligomers (Schwenk et al., 2010; Correale et al., 2013; Smaldone et al., 2016). Because many neurons in the brain simultaneously express several KCTDs and some possibly all KCTDs (Metz et al., 2011), hetero-oligomers are expected to be abundant. In the hippocampus, we estimate that ap-
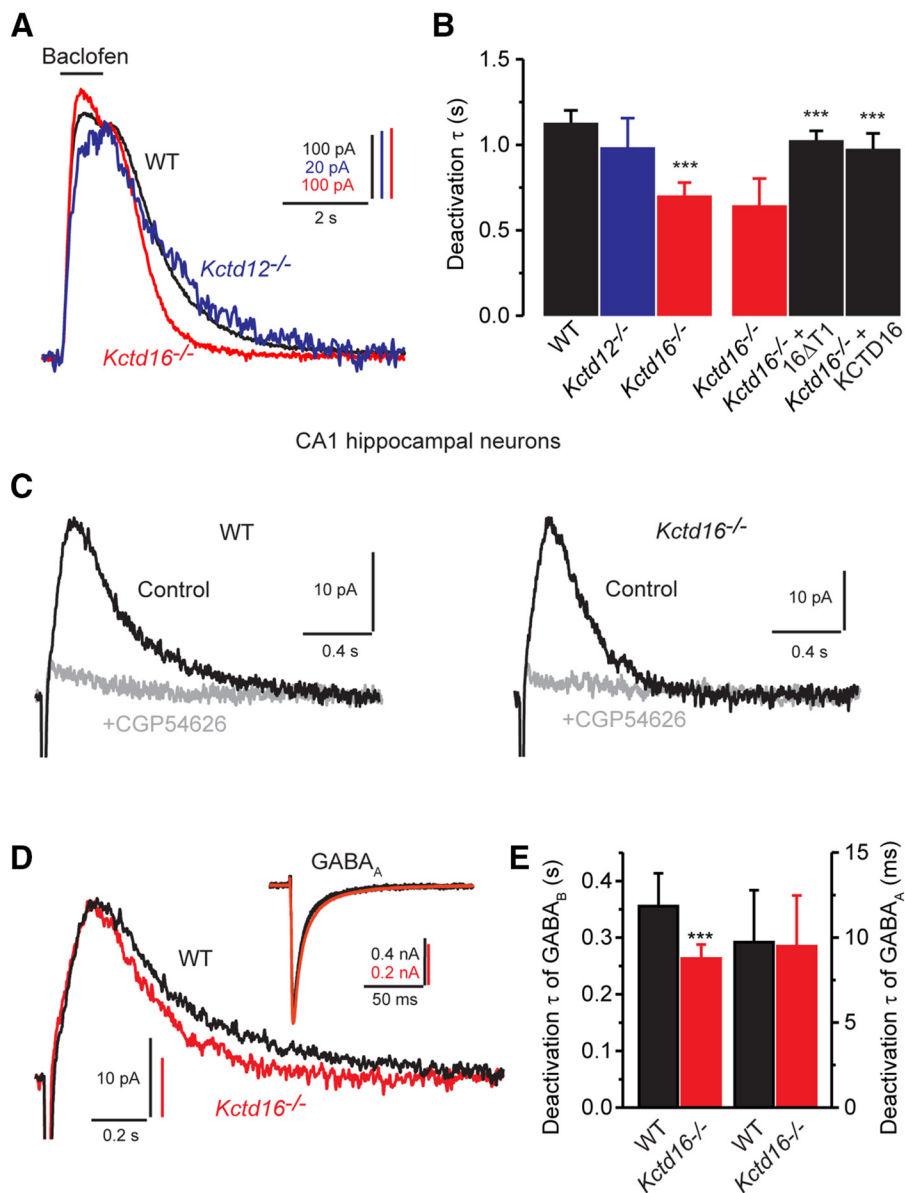
Figure 9. Rapid deactivation kinetics of sIPSCs in $Kctd16^{-/-}$ neurons. **A,** Superimposed traces showing K⁺ currents evoked by application of baclofen for 1 s to cultured hippocampal neurons of WT, $Kctd12^{-/-}$, or $Kctd16^{-/-}$ mice. **B,** Deactivation time constants obtained from fitting the deactivation phase to a single exponential function. The deactivation time constant was similar in WT and $Kctd12^{-/-}$ neurons but significantly reduced in $Kctd16^{-/-}$ neurons. The slow deactivation of the currents was restored in $Kctd16^{-/-}$ neurons transfected with 16ΔT1 or KCTD16. Data of 6 (WT), 7 ($Kctd12^{-/-}$), 8 ($Kctd16^{-/-}$), 5 ($Kctd16^{-/-}$ + 16ΔT1), and 5 ($Kctd16^{-/-}$ + KCTD16) neurons. ***$p < 0.001$ (Dunnett's multiple-comparison test). **C,** Examples of sIPSCs recorded from CA1 hippocampal neurons of WT or $Kctd16^{-/-}$ mice in the absence (Control) or presence of the specific GABA_B receptor antagonist CGP54626 (holding potential −60 mV). Traces are averages of 10 sIPSCs. **D,** Superimposed traces of control sIPSCs shown in **C** displayed with an expanded time scale. Note the faster deactivation kinetics obtained from $Kctd16^{-/-}$ neurons. Inset, GABA_A receptor-mediated IPSCs recorded from CA1 hippocampal neurons as in **C** (in the absence of gabazine), clamped at −60 mV. **E,** Bar graph summarizing the time constants obtained from a fit of the sIPSC deactivation phase to a single exponential function (left) and the amplitude-weighted mean time constants obtained from a fit of GABA_A IPSC deactivation phase to a double exponential function (right). Data are of 8 (WT) or 8 ($Kctd16^{-/-}$) experiments. ***$p < 0.001$ (unpaired Student's t test).

proximately two-thirds of the KCTD16 proteins are involved in KCTD12/KCTD16 hetero-oligomers. The KCTDs assemble with GABA_B receptors at the cytoplasmic side of the endoplasmic reticulum membrane (Ivankova et al., 2013). It is currently unknown whether KCTD hetero-oligomers assemble randomly or combine by a regulated process.

Effects on G-protein signaling

KCTD12 promotes current desensitization by uncoupling $G\beta\gamma$ subunits from effector K^+ channels via its H1 domain (Seddik et al., 2012; Turecek et al., 2014). In contrast, KCTD16 prevents desensitization via its H2 domain (Seddik et al., 2012). We now show that KCTD hetero-oligomers not only bind to the receptor but also to the G-protein. Simultaneous incorporation of distinct KCTD proteins into GABA_B receptors therefore allows combining regulatory effects on G-protein signaling into individual receptors. We found that, in KCTD12/KCTD16 hetero-oligomers, both KCTDs retain their regulatory effect on K^+ current desensitization. Reconstitution experiments in CHO cells reveal that KCTD12/KCTD16 hetero-oligomers yield K^+ currents with intermediate desensitization kinetics. We also observed that KCTD12 and KCTD16 have opposite effects on the deactivation of GABA_B receptor-activated K^+ currents; KCTD12 accelerates, whereas KCTD16 decelerates, deactivation. Interestingly, faster deactivation kinetics appear to depend on the extent of KCTD12-induced desensitization. In the presence of KCTD12, prolonged receptor activation results in desensitized K^+ currents exhibiting fast deactivation while short activation produces nondesensitized K^+ currents with slow deactivation. The underlying molecular mechanism is unknown but might relate to scavenging of $G\beta\gamma$ from the Kir3 channel by KCTD12. At steady-state desensitization, scavenging of $G\beta\gamma$ will result in lower $G\beta\gamma$ occupancy at the channel (Sadja et al., 2002; Whorton and MacKinnon, 2013; Yakubovich et al., 2015), which will accelerate dissociation of $G\beta\gamma$ and deactivation of the response. Similarly, the exact mechanism by which KCTD16 slows Kir3 current deactivation is unknown. Because the mutant 16ΔT1 slows the deactivation in the absence of binding to the receptor, the deactivation mechanism likely operates at the G-protein and/or at the effector channel. KCTD16 may, for example, slow current deactivation by facilitating binding of G-protein $\beta\gamma$ subunits at Kir3 channels. This would explain why KCTD16 slows deactivation in the absence (short receptor activation) but not in the presence of $\beta\gamma$ scavenging by KCTD12 (prolonged activation). Alternatively, it is also possible that KCTD16 slows current deactivation by interfering with the activity of endogenous regulator of G-protein signaling (RGS) proteins at the G-protein α subunit (Xie et al., 2010; Zhou et al., 2012; Ostrovskaya et al., 2014).

Physiological relevance of KCTD hetero-oligomers

Our electrophysiological experiments in hippocampal neurons support that KCTD12/KCTD16 hetero-oligomers slow the deactivation kinetics of GABA_B-induced K^+ currents during brief activation of the receptor. The deactivation kinetics of K^+ currents is known to be a limiting step for the termination of GABA_B-mediated sIPSCs (Xie et al., 2010). Accordingly, we found that, in $Kctd16^{-/-}$ hippocampal neurons, the decay of GABA_B-activated sIPSCs is significantly accelerated. Conversely, a recent study reported that the decay of GABA_B receptor-activated sIPSCs in $Kctd12^{-/-}$ cholecystokinin-containing interneurons, which normally express high amounts of KCTD12, is significantly decelerated (Booker et al., 2016). These studies highlight that the KCTDs can directly influence the kinetics of sIPSCs in select neuronal populations.

Of note, our experiments show that the kinetic changes measured in electrophysiological experiments with knock-out neurons are less pronounced than those measured in cells in which receptor assemblies are forced through overexpression of KCTD subunits. Earlier proteomic experiments revealed that ~60% of all GABA_B receptors in the adult mouse brain are devoid of

KCTD proteins (Turecek et al., 2014). In KCTD knock-out neurons, the responses of affected GABA_B receptors are partly masked by the responses of unaffected GABA_B receptors. Electrophysiological whole-cell recordings from knock-out neurons thus underestimate the kinetic changes at individual receptors. Nevertheless, we observe significant kinetic changes in knock-out neurons. These changes are likely to be of physiological relevance, given that $Kctd12^{-/-}$ and $Kctd16^{-/-}$ mice exhibit behavioral phenotypes (Cathomas et al., 2015, 2017). Of note, behavioral phenotypes in $Kctd12^{-/-}$ mice can be directly related to GABA_B receptor signaling because KCTD12 in the adult brain is exclusively associated with GABA_B receptors (Turecek et al., 2014). Modulatory effects on the kinetics of GABA_B-activated K^+ currents were also observed for RGS proteins. For example, RGS7 was shown to act in concert with $G\beta5$ to accelerate GABA_B receptor induced K^+ current deactivation (Xie et al., 2010; Zhou et al., 2012; Ostrovskaya et al., 2014), whereas RGS4 enhances K^+ current desensitization (Mutneja et al., 2005). Likewise, phosphorylation of GABA_{B2} by cAMP-dependent protein kinase (PKA) also influences the kinetics of the receptor response (Couve et al., 2002; Adelfinger et al., 2014).

Based on our findings, we propose that KCTD hetero-oligomers serve as regulatory building blocks that enable a fine-tuning of GABA_B receptor-induced K^+ currents. In this context, it will be important to determine the KCTD composition of GABA_B receptors in axonal, somatic, and dendritic compartments of identified neurons. Both the distribution of KCTD proteins (Metz et al., 2011) and the temporal dynamics of receptor activation may vary between these compartments and, as we show here, will influence the receptor response. Mounting evidence also suggests that the level of inhibition mediated by GABA_B-Kir3 signaling is tuned to changes in neuronal excitability and modified by drugs of abuse (Huang et al., 2005; Arora et al., 2011; Padgett et al., 2012; Hearing et al., 2013). It will therefore be important to address whether the composition of GABA_B/KCTD receptor complexes is regulated, as has been suggested for other GPCRs and their associated proteins (Maurice et al., 2012). For example, changes in KCTD12 expression during development (Resendes et al., 2004) or in disease (Glatt et al., 2005; Miller et al., 2008; Sibille et al., 2009; Benes, 2010; Lee et al., 2011; Cathomas et al., 2015) might alter the kinetics of receptor responses through influencing the composition of KCTD hetero-oligomers.

References

Adelfinger L, Turecek R, Ivankova K, Jensen AA, Moss SJ, Gassmann M, Bettler B (2014) GABA_B receptor phosphorylation regulates KCTD12-induced K^+ current desensitization. Biochem Pharmacol 91:369–379. CrossRef Medline

Armando S, Quoyer J, Lukashova V, Maiga A, Percherancier Y, Heveker N, Pin JP, Prezeau L, Bouvier M (2014) The chemokine CXC4 and CC2 receptors form homo- and heterooligomers that can engage their signaling G-protein effectors and βarrestin. FASEB J 10:4509–4523. CrossRef Medline

Arora D, Hearing M, Haluk DM, Mirkovic K, Fajardo-Serrano A, Wessendorf MW, Watanabe M, Luján R, Wickman K (2011) Acute cocaine exposure weakens GABA_B receptor-dependent G-protein-gated inwardly rectifying K^+ signaling in dopamine neurons of the ventral tegmental area. J Neurosci 31:12251–12257. CrossRef Medline

Bartoi T, Rigbolt KT, Du D, Köhr G, Blagoev B, Kornau HC (2010) GABA_B receptor constituents revealed by tandem affinity purification from transgenic mice. J Biol Chem 285:20625–20633. CrossRef Medline

Benes FM (2010) Amygdalocortical circuitry in schizophrenia: from circuits to molecules. Neuropsychopharmacology 35:239–257. CrossRef Medline

Biermann B, Ivankova-Susankova K, Bradaia A, Abdel Aziz S, Besseyrias V, Kapfhammer JP, Missler M, Gassmann M, Bettler B (2010) The Sushi domains of GABA_B receptors function as axonal targeting signals. J Neurosci 30:1385–1394. CrossRef Medline

Booker SA, Gross A, Althof D, Shigemoto R, Bettler B, Frotscher M, Hearing M, Wickman K, Watanabe M, Kulik Á, Vida I (2013) Differential GABA_B-receptor-mediated effects in perisomatic- and dendrite-targeting parvalbumin interneurons. J Neurosci 33:7961–7974. CrossRef Medline

Booker SA, Althof D, Gross A, Loreth D, Muller J, Unger A, Fakler B, Varro A, Watanabe M, Gassmann M, Bettler B, Shigemoto R, Vida I, Kulik A (2016) KCTD12 auxiliary proteins modulate kinetics of GABA_B receptor-mediated inhibition in cholecystokinin-containing interneurons. Cereb Cortex. Advance online publication. Retrieved Apr. 12, 2016. doi: 10.1093/cercor/bhw090. CrossRef Medline

Brewer GJ, Torricelli JR, Evege EK, Price PJ (1993) Optimized survival of hippocampal neurons in B27-supplemented Neurobasal, a new serum-free medium combination. J Neurosci Res 35:567–576. CrossRef Medline

Cathomas F, Stegen M, Sigrist H, Schmid L, Seifritz E, Gassmann M, Bettler B, Pryce CR (2015) Altered emotionality and neuronal excitability in mice lacking KCTD12, an auxiliary subunit of GABA_B receptors associated with mood disorders. Transl Psychiatry 5:e510. CrossRef Medline

Cathomas F, Sigrist H, Schmid L, Seifritz E, Gassmann M, Bettler B, Pryce CR (2017) Behavioural endophenotypes in mice lacking the auxiliary GABA_B receptor subunit KCTD16. Behav Brain Res 317:393–400. CrossRef Medline

Chalifoux JR, Carter AG (2011) GABA_B receptor modulation of synaptic function. Curr Opin Neurobiol 21:339–344. CrossRef Medline

Chuang HH, Yu M, Jan YN, Jan LY (1998) Evidence that the nucleotide exchange and hydrolysis cycle of G proteins causes acute desensitization of G-protein gated inward rectifier K+ channels. Proc Natl Acad Sci U S A 95:11727–11732. CrossRef Medline

Correale S, Esposito C, Pirone L, Vitagliano L, Di Gaetano S, Pedone E (2013) A biophysical characterization of the folded domains of KCTD12: insights into interaction with the GABA_B2 receptor. J Mol Recognit 26:488–495. CrossRef Medline

Couve A, Moss SJ, Pangalos MN (2000) GABA_B receptors: a new paradigm in G protein signaling. Mol Cell Neurosci 16:296–312. CrossRef Medline

Couve A, Thomas P, Calver AR, Hirst WD, Pangalos MN, Walsh FS, Smart TG, Moss SJ (2002) Cyclic AMP-dependent protein kinase phosphorylation facilitates GABA_B receptor-effector coupling. Nat Neurosci 5:415–424. CrossRef Medline

De Koninck Y, Mody I (1997) Endogenous GABA activates small-conductance K+ channels underlying slow IPSCs in rat hippocampal neurons. J Neurophysiol 77:2202–2208. Medline

Dementieva IS, Tereshko V, McCrossan ZA, Solomaha E, Araki D, Xu C, Grigorieff N, Goldstein SA (2009) Pentameric assembly of potassium channel tetramerization domain-containing protein 5. J Mol Biol 387:175–191. CrossRef Medline

De Smaele E, Di Marcotullio L, Moretti M, Pelloni M, Occhione MA, Infante P, Cucchi D, Greco A, Pietrosanti L, Todorovic J, Coni S, Canettieri G, Ferretti E, Bei R, Maroder M, Screpanti I, Gulino A (2011) Identification and characterization of KCASH2 and KCASH3, 2 novel Cullin3 adaptors suppressing histone deacetylase and Hedgehog activity in medulloblastoma. Neoplasia 13:374–385. CrossRef Medline

Dittert I, Benedikt J, Vyklický L, Zimmermann K, Reeh PW, Vlachová V (2006) Improved superfusion technique for rapid cooling or heating of cultured cells under patch-clamp conditions. J Neurosci Methods 151:178–185. CrossRef Medline

Gassmann M, Bettler B (2012) Regulation of neuronal GABA_B receptor functions by subunit composition. Nat Rev Neurosci 13:380–394. CrossRef Medline

Glatt SJ, Everall IP, Kremen WS, Corbeil J, Sásik R, Khanlou N, Han M, Liew CC, Tsuang MT (2005) Comparative gene expression analysis of blood and brain provides concurrent validation of SELENBP1 up-regulation in schizophrenia. Proc Natl Acad Sci U S A 102:15533–15538. CrossRef Medline

Hayasaki H, Sohma Y, Kanbara K, Otsuki Y (2012) Heterogenous GABA_B receptor-mediated pathways are involved in the local GABAergic system of the rat trigeminal ganglion: possible involvement of KCTD proteins. Neuroscience 218:344–358. CrossRef Medline

Hearing M, Kotecki L, Marron Fernandez de Velasco E, Fajardo-Serrano A, Chung HJ, Luján R, Wickman K (2013) Repeated cocaine weakens GABA_B-Girk signaling in layer 5/6 pyramidal neurons in the prelimbic cortex. Neuron 80:159–170. CrossRef Medline

Héroux M, Hogue M, Lemieux S, Bouvier M (2007) Functional calcitonin gene-related peptide receptors are formed by the asymmetric assembly of a calcitonin receptor-like receptor homo-oligomer and a monomer of receptor activity-modifying protein-1. J Biol Chem 282:31610–31620. CrossRef Medline

Huang CS, Shi SH, Ule J, Ruggiu M, Barker LA, Darnell RB, Jan YN, Jan LY (2005) Common molecular pathways mediate long-term potentiation of synaptic excitation and slow synaptic inhibition. Cell 123:105–118. CrossRef Medline

Ivankova K, Turecek R, Fritzius T, Seddik R, Prezeau L, Comps-Agrar L, Pin JP, Fakler B, Besseyrias V, Gassmann M, Bettler B (2013) Up-regulation of GABA_B receptor signaling by constitutive assembly with the K+ channel tetramerization domain-containing protein 12 (KCTD12). J Biol Chem 288:24848–24856. CrossRef Medline

Leaney JL, Benians A, Brown S, Nobles M, Kelly D, Tinker A (2004) Rapid desensitization of G protein-gated inwardly rectifying K+ currents is determined by G protein cycle. Am J Physiol Cell Physiol 287:C182–C191. CrossRef Medline

Lee MT, Chen CH, Lee CS, Chen CC, Chong MY, Ouyang WC, Chiu NY, Chuo LJ, Chen CY, Tan HK, Lane HY, Chang TJ, Lin CH, Jou SH, Hou YM, Feng J, Lai TJ, Tung CL, Chen TJ, Chang CJ, et al. (2011) Genome-wide association study of bipolar I disorder in the Han Chinese population. Mol Psychiatry 16:548–556. CrossRef Medline

Liu Z, Xiang Y, Sun G (2013) The KCTD family of proteins: structure, function, disease relevance. Cell Biosci 3:45. CrossRef Medline

Lüscher C, Slesinger PA (2010) Emerging roles for G protein-gated inwardly rectifying potassium (GIRK) channels in health and disease. Nat Rev Neurosci 11:301–315. CrossRef Medline

Lüscher C, Jan LY, Stoffel M, Malenka RC, Nicoll RA (1997) G protein-coupled inwardly rectifying K+ channels (GIRKs) mediate postsynaptic but not presynaptic transmitter actions in hippocampal neurons. Neuron 19:687–695. CrossRef Medline

Mapelli L, Rossi P, Nieus T, D'Angelo E (2009) Tonic activation of GABA_B receptors reduces release probability at inhibitory connections in the cerebellar glomerulus. J Neurophysiol 101:3089–3099. CrossRef Medline

Maurice P, Benleulmi-Chaachoua A, Jockers R (2012) Differential assembly of GPCR signaling complexes determines signaling specificity. Subcell Biochem 63:225–240. CrossRef Medline

Mercier JF, Salahpour A, Angers S, Breit A, Bouvier M (2002) Quantitative assessment of β1- and β2-adrenergic receptor homo- and heterodimerization by bioluminescence resonance energy transfer. J Biol Chem 277:44925–44931. CrossRef Medline

Metz M, Gassmann M, Fakler B, Schaeren-Wiemers N, Bettler B (2011) Distribution of the auxiliary GABA_B receptor subunits KCTD8, 12, 12b, and 16 in the mouse brain. J Comp Neurol 519:1435–1454. CrossRef Medline

Miller GE, Chen E, Sze J, Marin T, Arevalo JM, Doll R, Ma R, Cole SW (2008) A functional genomic fingerprint of chronic stress in humans: blunted glucocorticoid and increased NF-κB signaling. Biol Psychiatry 64:266–272. CrossRef Medline

Möhler H, Fritschy JM (1999) GABA_B receptors make it to the top: as dimers. Trends Pharmacol Sci 20:87–89. CrossRef Medline

Monnier C, Tu H, Bourrier E, Vol C, Lamarque L, Trinquet E, Pin JP, Rondard P (2011) Trans-activation between 7TM domains: implication in heterodimeric GABA_B receptor activation. EMBO J 30:32–42. CrossRef Medline

Mutneja M, Berton F, Suen KF, Lüscher C, Slesinger PA (2005) Endogenous RGS proteins enhance acute desensitization of GABA_B receptor-activated GIRK currents in HEK-293T cells. Pflugers Arch 450:61–73. CrossRef Medline

Ostrovskaya O, Xie K, Masuho I, Fajardo-Serrano A, Lujan R, Wickman K, Martemyanov KA (2014) RGS7/Gβ5/R7BP complex regulates synaptic plasticity and memory by modulating hippocampal GABA_BR-GIRK signaling. Elife 3:e02053. CrossRef Medline

Padgett CL, Lalive AL, Tan KR, Terunuma M, Munoz MB, Pangalos MN, Martínez-Hernández J, Watanabe M, Moss SJ, Luján R, Lüscher C, Slesinger PA (2012) Methamphetamine-evoked depression of GABA_B receptor signaling in GABA neurons of the VTA. Neuron 73:978–989. CrossRef Medline

Pin JP, Kniazeff J, Binet V, Liu J, Maurel D, Galvez T, Duthey B, Havlickova M, Blahos J, Prézeau L, Rondard P (2004) Activation mechanism of the heterodimeric GABA_B receptor. Biochem Pharmacol 68:1565–1572. CrossRef Medline

Rajalu M, Fritzius T, Adelfinger L, Jacquier V, Besseyrias V, Gassmann M, Bettler B (2015) Pharmacological characterization of GABA_B receptor

subtypes assembled with auxiliary KCTD subunits. Neuropharmacology 88:145–154. CrossRef Medline

Resendes BL, Kuo SF, Robertson NG, Giersch AB, Honrubia D, Ohara O, Adams JC, Morton CC (2004) Isolation from cochlea of a novel human intronless gene with predominant fetal expression. J Assoc Res Otolaryngol 5:185–202. CrossRef Medline

Sadja R, Alagem N, Reuveny E (2002) Graded contribution of the G$\beta\gamma$ binding domains to GIRK channel activation. Proc Natl Acad Sci U S A 99:10783–10788. CrossRef Medline

Schwenk J, Metz M, Zolles G, Turecek R, Fritzius T, Bildl W, Tarusawa E, Kulik A, Unger A, Ivankova K, Seddik R, Tiao JY, Rajalu M, Trojanova J, Rohde V, Gassmann M, Schulte U, Fakler B, Bettler B (2010) Native GABA_B receptors are heteromultimers with a family of auxiliary subunits. Nature 465:231–235. CrossRef Medline

Schwenk J, Pérez-Garci E, Schneider A, Kollewe A, Gauthier-Kemper A, Fritzius T, Raveh A, Dinamarca MC, Hanuschkin A, Bildl W, Klingauf J, Gassmann M, Schulte U, Bettler B, Fakler B (2016) Modular composition and dynamics of native GABA_B receptors identified by high-resolution proteomics. Nat Neurosci 19:233–242. CrossRef Medline

Seddik R, Jungblut SP, Silander OK, Rajalu M, Fritzius T, Besseyrias V, Jacquier V, Fakler B, Gassmann M, Bettler B (2012) Opposite effects of KCTD subunit domains on GABA_B receptor-mediated desensitization. J Biol Chem 287:39869–39877. CrossRef Medline

Sibille E, Wang Y, Joeyen-Waldorf J, Gaiteri C, Surget A, Oh S, Belzung C, Tseng GC, Lewis DA (2009) A molecular signature of depression in the amygdala. Am J Psychiatry 166:1011–1024. CrossRef Medline

Skoblov M, Marakhonov A, Marakasova E, Guskova A, Chandhoke V, Birerdinc A, Baranova A (2013) Protein partners of KCTD proteins provide insights about their functional roles in cell differentiation and vertebrate development. Bioessays 35:586–596. CrossRef Medline

Smaldone G, Pirone L, Pedone E, Marlovits T, Vitagliano L, Ciccarelli L (2016) The BTB domains of the potassium channel tetramerization domain proteins prevalently assume pentameric states. FEBS Lett 590:1663–1671. CrossRef Medline

Sowa ME, Bennett EJ, Gygi SP, Harper JW (2009) Defining the human deubiquitinating enzyme interaction landscape. Cell 138:389–403. CrossRef Medline

Stefan E, Aquin S, Berger N, Landry CR, Nyfeler B, Bouvier M, Michnick SW (2007) Quantification of dynamic protein complexes using Renilla lu-

ciferase fragment complementation applied to protein kinase A activities in vivo. Proc Natl Acad Sci U S A 104:16916–16921. CrossRef Medline

Turecek R, Vlcek K, Petrovic M, Horak M, Vlachova V, Vyklicky L Jr (2004) Intracellular spermine decreases open probability of N-methyl-D-aspartate receptor channels. Neuroscience 125:879–887. CrossRef Medline

Turecek R, Schwenk J, Fritzius T, Ivankova K, Zolles G, Adelfinger L, Jacquier V, Besseyrias V, Gassmann M, Schulte U, Fakler B, Bettler B (2014) Auxiliary GABA_B receptor subunits uncouple G protein $\beta\gamma$ subunits from effector channels to induce desensitization. Neuron 82:1032–1044. CrossRef Medline

Urwyler S, Mosbacher J, Lingenhoehl K, Heid J, Hofstetter K, Froestl W, Bettler B, Kaupmann K (2001) Positive allosteric modulation of native and recombinant γ-aminobutyric acid_B receptors by 2,6-di-tert-butyl-4-(3-hydroxy-2,2-dimethyl-propyl)-phenol (CGP7930) and its aldehyde analog CGP13501. Mol Pharmacol 60:963–971. CrossRef Medline

Villemure JF, Adam L, Bevan NJ, Gearing K, Chénier S, Bouvier M (2005) Subcellular distribution of GABA_B receptor homo- and hetero-dimers. Biochem J 388:47–55. CrossRef Medline

Wang Y, Neubauer FB, Lüscher HR, Thurley K (2010) GABA_B receptor-dependent modulation of network activity in the rat prefrontal cortex in vitro. Eur J Neurosci 31:1582–1594. CrossRef Medline

Whorton MR, MacKinnon R (2013) X-ray structure of the mammalian GIRK2-$\beta\gamma$ G-protein complex. Nature 498:190–197. CrossRef Medline

Xie K, Allen KL, Kourrich S, Colón-Saez J, Thomas MJ, Wickman K, Martemyanov KA (2010) Gβ5 recruits R7 RGS proteins to GIRK channels to regulate the timing of neuronal inhibitory signaling. Nat Neurosci 13:661–663. CrossRef Medline

Yakubovich D, Berlin S, Kahanovitch U, Rubinstein M, Farhy-Tselnicker I, Styr B, Keren-Raifman T, Dessauer CW, Dascal N (2015) A quantitative model of the GIRK1/2 channel reveals that its basal and evoked activities are controlled by unequal stoichiometry of Gα and G$\beta\gamma$. PLoS Comput Biol 11:e1004598. CrossRef Medline

Zhou H, Chisari M, Raehal KM, Kaltenbronn KM, Bohn LM, Mennerick SJ, Blumer KJ (2012) GIRK channel modulation by assembly with allosterically regulated RGS proteins. Proc Natl Acad Sci U S A 109:19977–19982. CrossRef Medline

6   Complex formation of APP with GABAB recptors links axonal trafficking to amyloidgenic processing

Margarita C. Dinamarca, Adi Raveh, Andy Schneider, Thorsten Fritzius, Simon Früh, <u>Pascal D. Rem</u>, Michal Stawarski, Txomin Lalanne, Rostislav Turecek, Myeongjeong Choo, Valérie Besseyrias, Wolfgang Bildl, Detlef Bentrop, Matthias Staufenbiel, Martin Gassmann, Bernd Fakler, Jochen Schwenk & Bernhard Bettler

Personal contribution

Proteomic analysis revealed several transmembrane proteins, including APP, that selectively co-purify with GB1a/2 receptors and potentially regulate axonal trafficking of this predominantly presynaptic receptor subtype (Schwenk et al., 2016). In this paper, my colleagues show that APP is a constituent of macromolecular GBR complexes and binds with nanomolar affinity to SD1 of GB1a. My colleagues further revealed that APP mediates axonal trafficking of GB1a/2 receptors and that the formation of APP/GB1a/2 receptor complex leads to a mutual stabilization at the cell surface. Using BRET experiments in living cells, I demonstrate that the association and dissociation between GB1a/2 and APP is not regulated by GB1a/2 receptor activity (Supplementary Fig. 2c & d). In addition, using a BRET sensor for G protein activation, I show that co-expression of APP does not modulate signaling of GB1a/2 receptors (Supplementary Fig. 4a). Further, I generated the PIANP-KO animals that were used by my colleagues for mass spectrometry (Fig.1a), Western blot analysis of brain membrane preparation (Fig. 1b), electrophysiological recordings (Fig. 3a) and immunofluorescence analysis of endogenous axonal GB1 (Supplementary Fig. 5b). A detailed description of PIANP-KO mice generation is given in section 9.

Complex formation of APP with GABA_B receptors links axonal trafficking to amyloidogenic processing

Margarita C. Dinamarca[1], Adi Raveh[1], Andy Schneider[2], Thorsten Fritzius[1], Simon Früh [1], Pascal D. Rem[1], Michal Stawarski[1], Txomin Lalanne[1], Rostislav Turecek[1,5], Myeongjeong Choo[1], Valérie Besseyrias[1], Wolfgang Bildl[2], Detlef Bentrop[2], Matthias Staufenbiel[3], Martin Gassmann [1], Bernd Fakler[2,4], Jochen Schwenk [2,4] & Bernhard Bettler[1]

GABA_B receptors (GBRs) are key regulators of synaptic release but little is known about trafficking mechanisms that control their presynaptic abundance. We now show that sequence-related epitopes in APP, AJAP-1 and PIANP bind with nanomolar affinities to the N-terminal sushi-domain of presynaptic GBRs. Of the three interacting proteins, selectively the genetic loss of APP impaired GBR-mediated presynaptic inhibition and axonal GBR expression. Proteomic and functional analyses revealed that APP associates with JIP and calsyntenin proteins that link the APP/GBR complex in cargo vesicles to the axonal trafficking motor. Complex formation with GBRs stabilizes APP at the cell surface and reduces proteolysis of APP to Aβ, a component of senile plaques in Alzheimer's disease patients. Thus, APP/GBR complex formation links presynaptic GBR trafficking to Aβ formation. Our findings support that dysfunctional axonal trafficking and reduced GBR expression in Alzheimer's disease increases Aβ formation.

[1] Department of Biomedicine, Institute of Physiology, University of Basel, Klingelbergstr. 50/70, 4056 Basel, Switzerland. [2] Faculty of Medicine, Institute of Physiology, University of Freiburg, Hermann-Herder-Str. 7, 79104 Freiburg, Germany. [3] Department of Cellular Neurology, Hertie Institute for Clinical Brain Research, University of Tübingen, Otfried-Müller-Strasse 27, 72076 Tübingen, Germany. [4] Signalling Research Centers BIOSS and CIBSS, University of Freiburg, Schänzlestr. 18, 79104 Freiburg, Germany. [5] Present address: Institute of Experimental Medicine, ASCR, Vı´denska´ 1083, 14220 Prague 4-Krc, Czech Republic. These authors contributed equally: Margarita C. Dinamarca, Adi Raveh, Andy Schneider. Correspondence and requests for materials should be addressed to J.S. (email: jochen.schwenk@physiologie.uni-freiburg.de) or to B.B. (email: bernhard.bettler@unibas.ch)

GABA$_B$ receptors (GBRs) are key regulators of synaptic transmission in the brain[1,2]. Presynaptic GBRs inhibit the release of a variety of neurotransmitters while post-synaptic GBRs generate inhibitory K$^+$ currents that hyperpolarize the membrane and inhibit neuronal activity. There is evidence for a downregulation of presynaptic GBRs in response to neuronal activity[3–5] and in disease, including Alzheimer's disease (AD)[6,7], Fragile-X syndrome[8], epilepsy[9], and Parkinson disease[10]. Despite their importance for proper brain functioning the trafficking molecules controlling presynaptic GBR abundance are still unknown. Heterodimeric GB1a/2 and GB1b/2 receptors accumulate at excitatory terminals and in the somatodendritic compartment, respectively[1,11–14]. The GBR subunit GB1a contains two N-terminal sushi domains (SDs) that, when deleted, impair axonal localization and surface stability of the receptor. GB1a knock-out (GB1a$^{-/-}$) mice therefore exhibit a lack of axonal GBRs and a deficit in GBR-mediated inhibition of glutamate release[1,12]. Native GB1a/2 receptors co-purify with kinesin-1 adapters of the c-Jun N-terminal kinase-interacting protein (JIP) and calsyntenin (CSTN) protein families[15], in agreement with kinesin-1 motors mediating long-range vesicular transport of GB1a/2 receptors in axons[16]. As the SDs of GB1a face the luminal side of cargo vesicles, an as-yet unidentified transmembrane protein must link the SDs to cytoplasmic kinesin-1 motors. Proteomic analysis revealed several transmembrane proteins that selectively co-purify with GB1a/2 receptors and potentially link SDs to kinesin-1 motors, including the β-amyloid precursor protein (APP), the adherence-junction associated protein 1 (AJAP-1) and the PILRα-associated neural protein (PIANP)[15]. APP is the source of β-amyloid (Aβ) peptides, a hallmark of Alzheimer's disease (AD)[17–19]. AJAP-1 interacts with the E-cadherin-catenin complex at adherens junctions, which mediate adhesion between pre-and postsynaptic membranes[20]. PIANP shares sequence-similarity with AJAP-1, undergoes polarized sorting in epithelial cells and attenuates E-cadherin cleavage by γ-secretase[21].

In the present study, we analyzed the interaction of APP, AJAP-1, and PIANP with GB1a and addressed the role of these proteins in presynaptic GBR transport and expression. Proteomic approaches indicate that APP, AJAP-1, and PIANP participate in distinct GBR complexes. NMR studies identify sequence-related epitopes in APP, AJAP-1, and PIANP that bind to the N-terminal SD (SD1) of GB1a, with a rank order of affinities AJAP-1 > PIANP >> APP. Selectively APP links GB1a/2 receptors to vesicular trafficking and, when deleted, induces a significant deficit in GBR-mediated inhibition of glutamate release. Intriguingly, APP/GB1a complex formation not only mediates presynaptic GB1a/2 receptor trafficking but also limits the availability of APP for endosomal processing to Aβ. The association of presynaptic GBR expression with APP processing can explain pathological features observed in AD and suggests APP/GB1a complex stabilization as a promising therapeutic strategy.

Results

APP, AJAP-1, and PIANP assemble into distinct GBR complexes. To investigate the interdependence of protein constituents in GBR complexes we analyzed the composition of affinity-purified GBRs from GB1a$^{-/-}$, APP$^{-/-}$, AJAP-1$^{-/-}$, PIANP$^{-/-}$, and APP/AJAP-1$^{-/-}$ double knock-out brains using quantitative mass spectrometry[15] (Fig. 1a, Source Data). Lack of GB1a largely prevented assembly of APP, APLP-2, AJAP-1, PIANP, ITM2B/C, CSTN-3, and Synaptotagmin-11 (Syt-11) into GBR complexes, indicating that these proteins directly or indirectly interact with presynaptic GBRs (Fig. 1a). Analysis of protein levels in APP$^{-/-}$, AJAP-1$^{-/-}$, PIANP$^{-/-}$, and APP/AJAP-1$^{-/-}$ mice showed that

APP, AJAP-1, and PIANP form independent GBR complexes (Fig. 1a). GBRs of APP$^{-/-}$ brains lacked APP, APLP-2, ITM2B/C, CSTN-3, and Syt-11. In contrast, GBRs of AJAP-1$^{-/-}$ and PIANP$^{-/-}$ brains selectively lacked the deleted protein. Interestingly, deletion of APP or AJAP-1 increased the amount of PIANP in GBR complexes, likely because of the increased availability of SDs for binding (Fig. 1a). GBRs in APP/AJAP-1$^{-/-}$ mice exhibited roughly additive changes in protein constituents when compared to individual knock-out mice, corroborating that APP and AJAP-1 assemble into distinct GBR complexes (Fig. 1a). Whole brain membranes of APP$^{-/-}$ mice showed an increased abundance of PIANP after genetic ablation of APP (Fig. 1b), suggesting that lack of APP frees SDs that bind and stabilize PIANP. Together, these results indicate that APP, AJAP-1, and PIANP form separate complexes with GB1a. Only the APP/GB1 complex binds CSTN-3, a protein implicated in vesicular trafficking[22] and synapse formation[23] that provides a potential link to axonal kinesin-1 motors.

APP interacts with CSTN kinesin-1 adapters. We isolated native APP, AJAP-1 and PIANP complexes in a series of multi-epitope affinity-purifications[15] to address whether these proteins interact with trafficking factors (Fig. 1c, Source Data). Quantitative analysis of affinity purifications by mass spectrometry confirmed that all three proteins co-assemble with GB1, GB2 and KCTDs into multiprotein complexes. However, selectively APP associated with several additional constituents of the GBR proteome, including APLP-2, ITM2B/C, Syt-11, NSG1/2, and the kinesin-1 adapters CSTN-1/-2/-3. JIP-1, a linker between kinesin-1 and APP[22], and JIP-3, a protein indirectly associated with GB1a[15], did not co-purify with APP in significant amounts, possibly because of dynamic interaction(s) or sterical hindrance by the antibodies used for affinity purification. Together, these proteomic experiments confirm that selectively APP links GBRs to the trafficking machinery.

APP, AJAP-1 and PIANP bind with nanomolar affinities to SD1. Deletion mapping revealed that the extracellular acidic domain (AcD) of APP encompassing amino acids 191–294 interacts with the N-terminal SD1 of GB1a (Fig. 2a, b). Detailed structural analysis of the complex by two-dimensional ^{1}H-^{15}N heteronuclear single quantum coherence (HSQC) spectra delineated amino acids 202–219 in the purified AcD as the SD1 binding-site (Fig. 2c). The intrinsically disordered AcD exhibits low signal dispersion of the backbone amide protons (8.0–8.6 ppm) in the presence or absence of recombinant SD1/2 protein (Fig. 2c). The extracellular domains of AJAP-1 and PIANP exhibit sequence similarity with APP residues 202–219 in a stretch of six amino acids featuring a conserved WG motif preceded by hydrophobic residues (Fig. 2c). These six amino acids represent a crucial element of the binding interface, as shown by ^{1}H–^{15}N HSQC spectra of AJAP-1 and PIANP with and without SD1/2 (Supplementary Fig. 1a). Subsequent mutagenesis confirmed that deletion of APP residues 202–219 or replacement of AJAP-1 residues 181–186 with alanine abolishes binding to GB1a (Fig. 2d). Surface binding assays indicated a rank order of SD binding affinities AJAP-1 (K_D 6.4 ± 2.4 nM, mean ± s.e.m.) > PIANP (29.1 ± 5.5 nM) >> APP (187.6 ± 27.9 nM) (Supplementary Fig. 1b). APLP-2 completely lacks sequence similarity with the SD-binding site of APP (Fig. 2c), consistent with APLP-2 interacting with GB1a via APP (Fig. 1a, c). GBR activity did not significantly influence the amount of APP, AJAP-1, PIANP, and other GB1-interacting proteins co-immunoprecipitating with GB1a (Supplementary Fig. 2a, b). Likewise, GBR activity did not modify the bioluminescence resonance energy transfer (BRET)
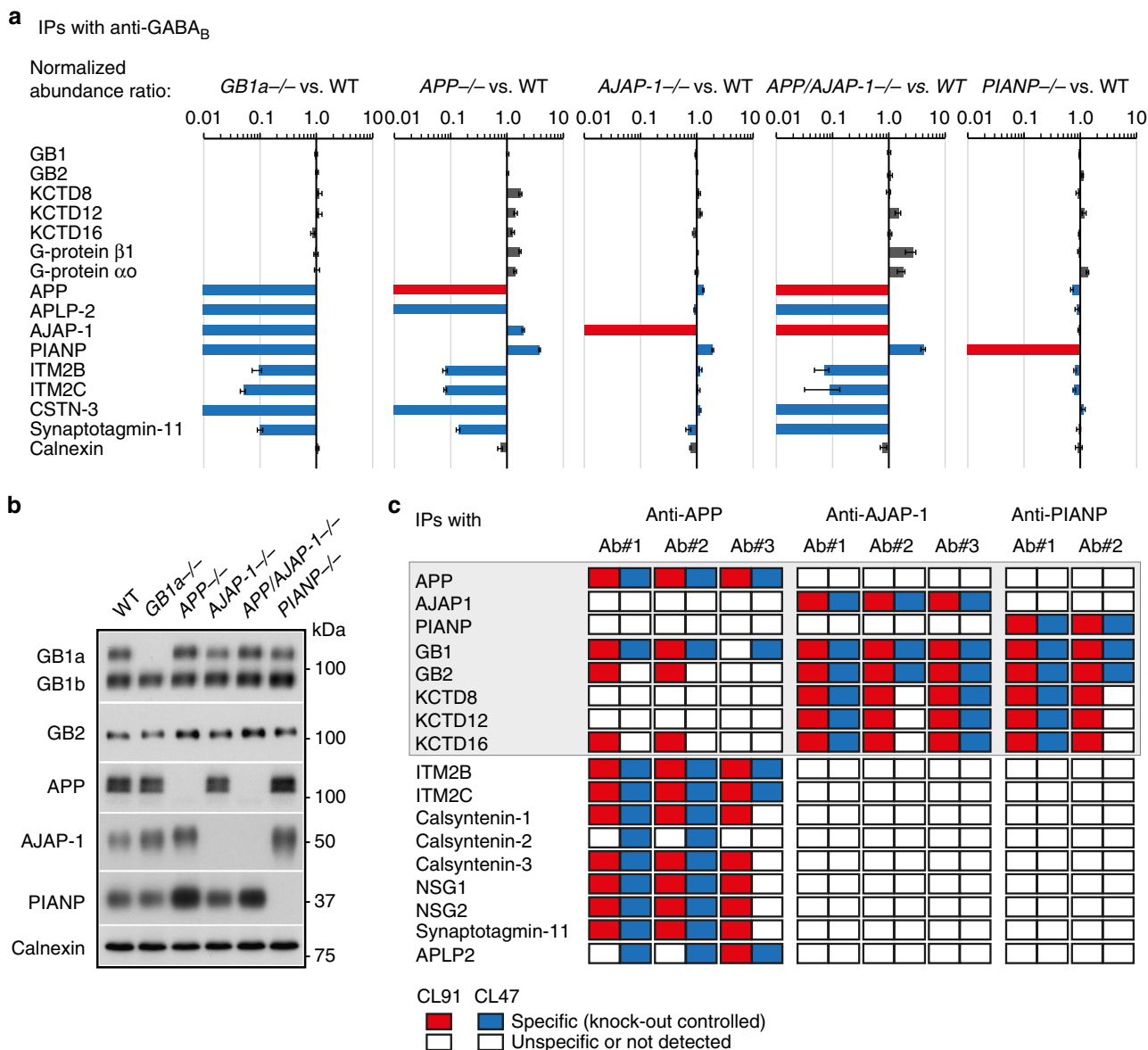
Fig. 1 Proteomic analysis of native GBR complexes. **a** Protein abundance ratios for GBR proteome constituents ($n = 3$ measurements, data are presented as mean ± s.e.m.) in GBR IPs from membrane fractions of WT, $GB1a^{-/-}$, $APP^{-/-}$, $AJAP^{-/-}$, $APP/AJAP^{-/-}$, and $PIANP^{-/-}$ brains solubilized with the intermediate stringency detergent CL91 (normalized to GB1/2). APP, AJAP-1, and PIANP directly bind to GB1a while APLP2 binds to GB1a via APP. Common changes in the GBR proteomes of $GB1a^{-/-}$ and $APP^{-/-}$ mice identify APP as a putative linker between GB1a and the trafficking machinery. **b** Immunoblot analysis of GBR constituents in brain membrane preparations from knock-out mice. Calnexin serves as a loading control. Lack of APP upregulates PIANP. **c** APP, AJAP-1, and PIANP assemble into independent GBR complexes. The table summarizes results of co-immunoprecipitations with anti-APP, anti-AJAP-1, and anti-PIANP antibodies from mouse brain membranes solubilized with mild (CL47) and intermediate stringency (CL91) detergents. Knock-out brains were used in control immunoprecipitations. Source data are provided as a Source Data file

between APP-Venus and GB1a-Rluc in transfected HEK293 cells (Supplementary Fig. 2c, d).

Lack of APP impairs presynaptic GBR-mediated inhibition. We next addressed whether the lack of APP, AJAP-1, or PIANP impairs GBR-mediated inhibition of excitatory postsynaptic currents (EPSCs) at CA3/CA1 synapses. The prototypical GBR agonist baclofen was less efficient in reducing the amplitude of evoked EPSCs in $APP^{-/-}$ than in WT hippocampal slices (WT: 53.2 ± 2.7%, $APP^{-/-}$: 38.7 ± 2.8%; $P < 0.01$; Fig. 3a). There was also a trend towards reduced presynaptic inhibition of EPSC amplitudes in $AJAP-1^{-/-}$ and $PIANP^{-/-}$ slices, which however did not reach

significance ($P > 0.05$, Fig. 3a). Consistent with impaired baclofen-mediated inhibition of evoked EPSCs in $APP^{-/-}$ slices we also observed impaired baclofen-mediated inhibition of the miniature EPSC (mEPSC) frequency (WT: 64.4 ± 2.6%; $APP^{-/-}$: 43.9 ± 3.2%; $P < 0.001$; Fig. 3b). Baseline mEPSC frequency and amplitude were unaltered in $APP^{-/-}$ slices (Fig. 3b). Similarly, baclofen-mediated inhibition of the mEPSC frequency in cultured hippocampal neurons was impaired in $APP^{-/-}$ mice (WT: 74.07 ± 0.98%, $APP^{-/-}$: 57.01 ± 4.37%; $P < 0.001$), without a change of mEPSC amplitude ($P > 0.05$, Supplementary Fig. 3). Of note, the deficit in presynaptic inhibition in cultured $APP^{-/-}$ neurons was less pronounced than in $GB1a^{-/-}$ neurons (WT: 73.4 ± 1.7%,
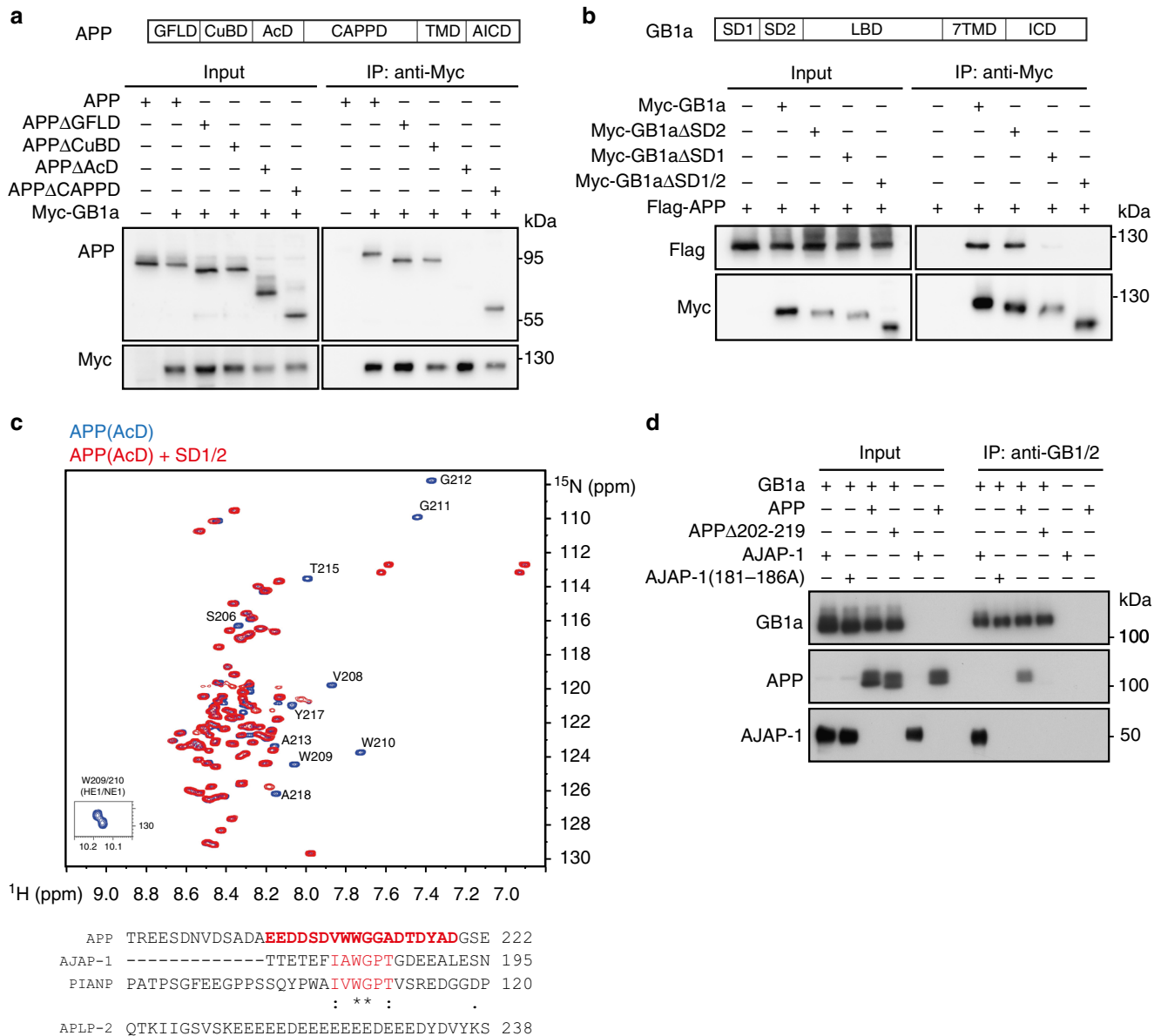
Fig. 2 Interacting epitopes of APP, AJAP-1 and PIANP with GB1a. **a** The acidic domain (AcD) of APP comprising amino acids 191–294 is necessary for GB1a binding. Immunoprecipitations using anti-Myc-antibodies from HEK293 cells expressing Myc-GB1a together with APP or APP deletion mutants. Abbreviations: GFLD, growth factor-like domain; CuBD, copper-binding domain; CAPPD, central APP domain; TMD, transmembrane domain; AICD, APP intracellular domain. **b** The N-terminal SD1 is necessary for binding of APP. Immunoprecipitations from HEK293 cells expressing Flag-APP together with GB1a deletion mutants lacking SD1, SD2 or both SD1/2. **c** The AcD of APP interacts with recombinant SD1/2 protein via amino acid residues 202–219 containing a WG sequence motif. Top: Two-dimensional ^{1}H–^{15}N heteronuclear single quantum coherence (HSQC) spectra of ^{13}C/^{15}N labeled APP (AcD residues 191–294), alone (blue) or in complex (red) with unlabeled recombinant SD1/2. In complex with SD1/2 several APP residues exhibit chemical shift changes or disappear. These residues participate in protein-protein interaction (red in the sequence alignment). Amino acid assignment of APP was performed from a standard set of 3D experiments using ^{13}C–^{15}N labeled AcD[65]. Bottom: Alignment of the APP epitope with related sequences in AJAP-1 and PIANP (red). APLP-2 exhibits no sequence similarity with the binding epitope of APP. **d** Deletion or mutation to alanine of the binding epitopes in APP and AJAP-1 prevents binding to GB1a, as shown in co-immunoprecipitation experiments. Source data are provided as a Source Data file

$GB1a^{-/-}$: 29.8 ± 2.5%; $P < 0.0001$; Supplementary Fig. 3), suggesting that a fraction of GBRs traffics to axon terminals in the absence of APP.

APP does not influence GBR dependent G protein signaling. It is conceivable that lack of APP impairs presynaptic GBR-mediated inhibition because APP normally exerts a positive allosteric effect on receptor-induced G protein signaling. We carried out BRET experiments[24] in transfected HEK293 cells to analyze whether APP influences conformational changes of the G protein during GB1a/2 receptor activation. APP influenced neither the baseline BRET nor the magnitude or kinetics of the BRET change during G protein activation (Supplementary Fig. 4a). Because soluble extracellular APP fragments (sAPPα) are reported to signal through G proteins[17,25,26] we additionally incubated GB1a/2 receptors expressed in HEK293 cells with conditioned medium containing recombinant sAPPα
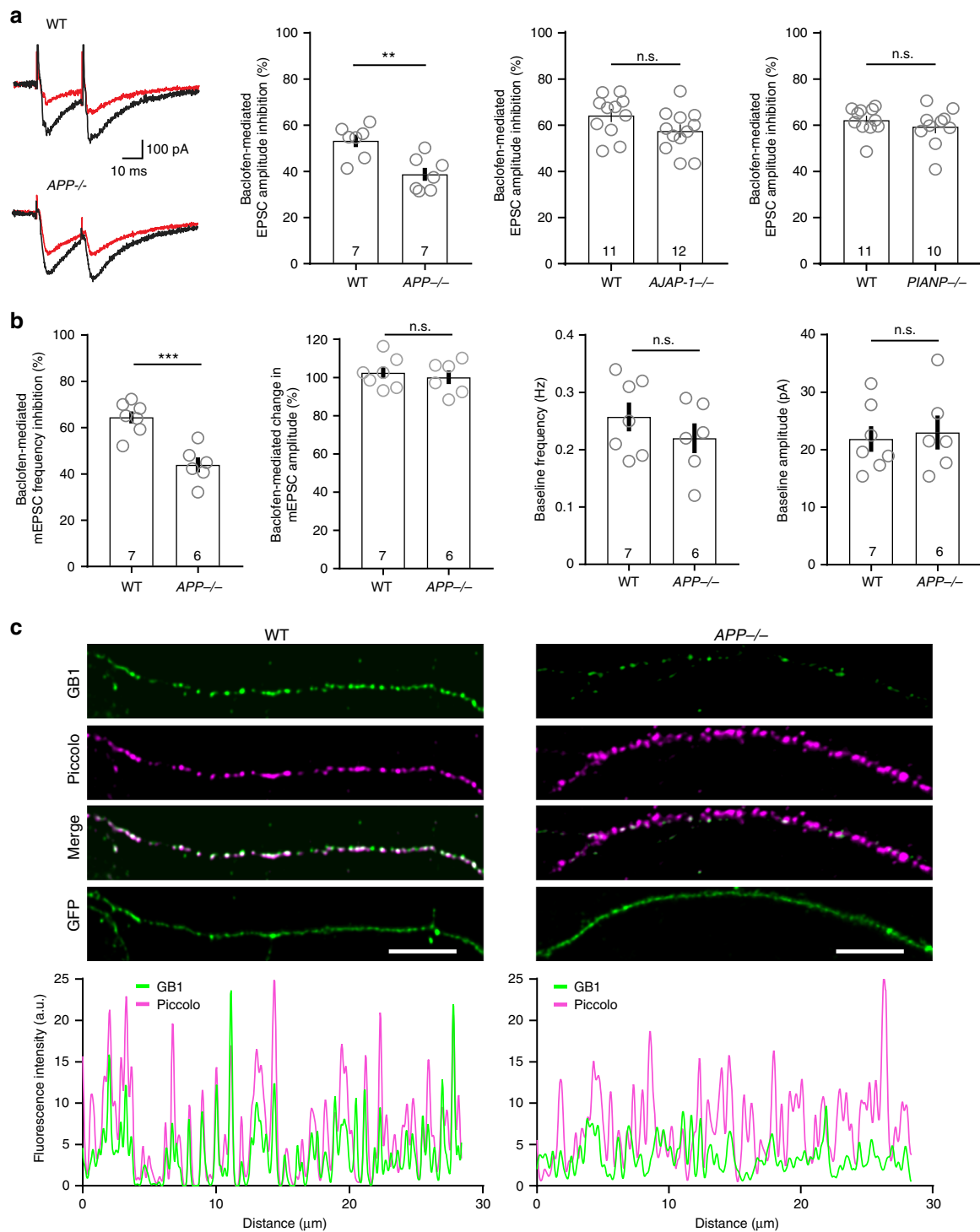
Fig. 3 Reduced axonal GBR expression and presynaptic inhibition in $APP^{-/-}$ mice. **a** Representative traces of evoked EPSC recordings in CA1 neurons of acute hippocampal slices of $APP^{-/-}$ mice under baseline conditions (control, black) and during 50 μM baclofen application (red). Bar graphs show reduced baclofen-mediated EPSC amplitude inhibition in $APP^{-/-}$ mice (**$P < 0.01$, unpaired Student's t-test) while EPSC amplitude inhibition in $AJAP-1^{-/-}$, PIANP$^{-/-}$ mice and WT littermate mice did not differ ($P > 0.05$). The n number of neurons is indicated. **b** Bar graphs showing reduced baclofen-mediated inhibition of the mEPSC frequency in CA1 pyramidal neurons of $APP^{-/-}$ mice (***$P < 0.001$, unpaired Student's t-test). Baclofen had no effect on the mEPSC amplitude in $APP^{-/-}$ and WT littermate mice. Baseline mEPSC frequency and amplitude were similar in $APP^{-/-}$ and WT littermate mice ($P > 0.05$, unpaired t-test). **c** Top: Immunofluorescence of endogenous GB1 protein in axons of hippocampal WT (left) and $APP^{-/-}$ (right) neurons. Neurons expressing GFP were fixed at DIV10, permeabilized, and immunostained for endogenous GB1 (green) and the presynaptic marker piccolo (magenta). GFP served as a volume marker. Merged images show GB1 and piccolo co-localization. Scale bar 5 μm. Bottom: Intensity gray value profile graphs of GB1 (green) and piccolo (magenta). Source data are provided as a Source Data file. Data are presented as mean ± s.e.m
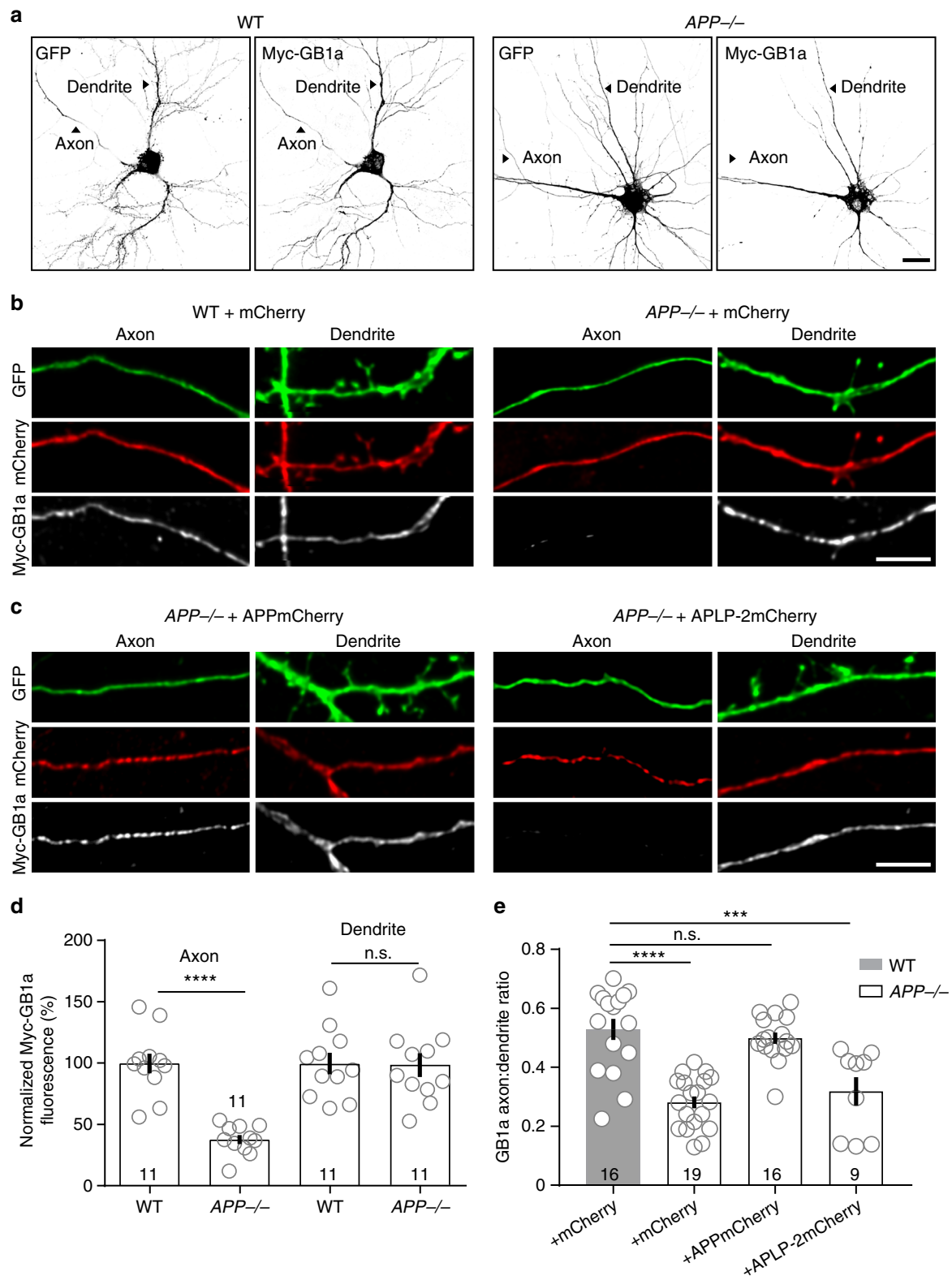
(Supplementary Fig. 4b). BRET analysis revealed no G protein activation upon sAPPα application. Brain membranes of $APP^{-/-}$ and WT littermate mice exhibited no difference in GABA-stimulated GTPγ[^{35}S] binding, corroborating that APP does not influence receptor-induced G protein signaling (Supplementary Fig. 4c). BRET and GTPγ[^{35}S] binding experiments therefore support that APP and sAPP do not modulate GBR activity.

Reduced endogenous GB1 protein in axons of $APP^{-/-}$ neurons. Lack of APP influence on GBR-induced G protein signaling suggests that reduced receptor numbers underlie impaired pre-synaptic inhibition in $APP^{-/-}$ neurons. We therefore determined endogenous GB1 expression in the axons of cultured hippo-campal $APP^{-/-}$ neurons using immunofluorescence staining (Fig. 3c). Normalization of GB1 immunofluorescence to that of

Fig. 4 APP localizes exogenous GB1a protein to axons in cultured hippocampal neurons. **a** Representative images of hippocampal neurons co-expressing Myc-GB1a and GFP in $APP^{-/-}$ and control littermate (WT) mice. Neurons were transfected at DIV5, fixed at DIV10, permeabilized and then stained with anti-Myc antibodies. Note that $APP^{-/-}$ neurons exhibit significantly reduced axonal Myc-GB1a expression. Dendrites were distinguished from axons using morphological criteria[66]. Scale bar 10 μm. **b** Higher magnification images of distal axons and dendrites from $APP^{-/-}$ and WT neurons expressing exogenous Myc-GB1a, GFP and mCherry. Scale bar 10 μm. **c** Images of distal axons and dendrites from $APP^{-/-}$ neurons expressing exogenous Myc-GB1a, GFP and APPmCherry or APLP-2mCherry. Note that APPmCherry but not APLP-2mCherry rescues axonal localization of Myc-GB1a. Scale bar 10 μm. **d** Exogenous Myc-GB1a levels in axons and dendrites of transfected $APP^{-/-}$ or WT neurons. Normalized fluorescence refers to the Myc-GB1a immunofluorescence intensity normalized to the GFP fluorescence intensity. ****$P < 0.0001$, unpaired Student's t-test. **e** Axon:dendrite (A:D) ratio of Myc-GB1a in $APP^{-/-}$ and WT neurons transfected with Myc-GB1a in the presence of mCherry, APPmCherry or APLP-2mCherry (DIV10). The n number of neurons analyzed is indicated. ***$P < 0.001$, ****$P < 0.0001$, one-way ANOVA. Data are presented as mean ± s.e.m. Source data are provided as a Source Data file

---

the volume marker GFP revealed a 74% reduction in GB1 expression in $APP^{-/-}$ axons (WT: 100 ± 10.1%, $APP^{-/-}$: 26.0 ± 3.7%; $n = 10$ neurons, 6 independent transfections per group, $P < 0.0001$, unpaired t-test). In WT and $APP^{-/-}$ axons 48 and 25%, respectively, of the GB1 clusters co-localized with piccolo, a protein associated with the presynaptic cytoskeleton (Fig. 3c). As a control, normalization of piccolo staining to GFP fluorescence revealed no significant difference between genotypes (WT: 22.7 ± 3.5 a.u.; $APP^{-/-}$: 16.6 ± 2.1 a.u.; $n = 10$ neurons, 6 independent transfections per group, $P > 0.05$, unpaired t-test). $APP^{-/-}$ neurons therefore exhibit reduced GB1 expression in axons and putative presynaptic structures. However, GB1 protein is still detectable in $APP^{-/-}$ axons, in agreement with electrophysiological data indicating residual GBR-mediated presynaptic inhibition in $APP^{-/-}$ neurons (Fig. 3a, b). $AJAP-1^{-/-}$ and $PIANP^{-/-}$ mice exhibit normal levels of endogenous GB1 protein in the axons of cultured hippocampal neurons (Supplementary Fig. 5), explaining why presynaptic GBR-mediated inhibition in these mice is normal (Fig. 3a).

Rescue of axonal GBR localization in $APP^{-/-}$ neurons. We next studied the localization of N-terminally tagged Myc-GB1a in cultured hippocampal $APP^{-/-}$ neurons. We transfected Myc-GB1a or control Myc-GB1b together with the volume-markers GFP and mCherry and determined the subunit distribution by immunostaining[13]. In WT neurons Myc-GB1a was present in axons, somata and dendrites (Fig. 4a, b) while Myc-GB1b was mostly excluded from axons (Supplementary Fig. 6a, b), as reported earlier[13]. To quantify axonal and dendritic Myc-GB1a and Myc-GB1b expression, we normalized the anti-Myc fluorescence to GFP fluorescence. Axonal Myc-GB1a expression was reduced by 64% in $APP^{-/-}$ neurons (WT: 100 ± 7.3%, $APP^{-/-}$: 36.4 ± 3.6%, $n = 12$ neurons; $P < 0.0001$) while dendritic Myc-GB1a expression remained normal (WT: 100 ± 8.8%, $APP^{-/-}$: 98.7 ± 9.7%: $n = 11$ neurons, $P > 0.05$; unpaired Student's t-test; Fig. 4d). Accordingly, the axon-to-dendrite (A:D) ratio of Myc-GB1a was significantly reduced in $APP^{-/-}$ neurons (WT: 0.53 ± 0.04, $APP^{-/-}$ 0.28 ± 0.02; $P < 0.0001$; Fig. 4e). In contrast, axonal Myc-GB1b expression and the A:D ratio (WT: 0.34 ± 0.03, $APP^{-/-}$ 0.30 ± 0.03; $P > 0.05$) were similar in $APP^{-/-}$ and WT neurons and markedly lower than for Myc-GB1a (Supplementary Fig. 6c, d). We examined whether exogenous APP expression in $APP^{-/-}$ neurons rescues axonal localization of Myc-GB1a. We co-transfected cultured hippocampal neurons from $APP^{-/-}$ mice with mCherry-tagged APP (APPmCherry) and Myc-GB1a or Myc-GB1b, together with GFP as a volume marker (Fig. 4c, Supplementary Fig. 6d). APPmCherry significantly increased the A:D ratio of Myc-GB1a compared to control transfections with mCherry alone (+mCherry: 0.28 ± 0.02, +APPmCherry: 0.50 ± 0.02; $P < 0.0001$; Fig. 4c, e). In contrast, transgenic expression of

APPmCherry in $APP^{-/-}$ neurons had no effect on the A:D ratio of Myc-GB1b (+mCherry: 0.30 ± 0.03, +APPmCherry: 0.31 ± 0.02; $P > 0.05$; Supplementary Fig. 6d). Similarly, APLP-2mCherry did not rescue axonal localization of Myc-GB1a (Fig. 4c) and had no significant effect on the A:D ratio of GB1a in $APP^{-/-}$ neurons (+mCherry: 0.28 ± 0.02, +APLP-2mCherry: 0.32 ± 0.05; $P > 0.05$; Fig. 4e). These experiments identify APP as a key factor mediating axonal localization of GBRs.

Visualization of APP/GB1a complexes in axons and dendrites. We used bimolecular fluorescence complementation[27] (BiFC) to investigate APP/GB1a complex localization in axons, after tagging the two proteins at their C-termini with the N-terminal and C-terminal fragments of fluorescent Venus protein (VN, VC; Fig. 5a). BiFC in transfected HEK293 cells was successful between APP-VN and GB1a-VC but not between APP-VN and GB1b-VC (Supplementary Fig. 7a). BiFC imaging in HEK293 cells using total internal reflection fluorescence (TIRF) microscopy showed that the APP-VN/GB1a-VC complex is assembled early in the biosynthetic pathway in the perinuclear region and requires GB2 for surface expression[1] (Supplementary Fig. 7b). Transfected cultured hippocampal neurons exhibited APP-VN/GB1a-VC BiFC in axons, soma and dendrites (Fig. 5a). Co-expression of APP-VN with GB1b-VC generated no BiFC (Fig. 5a) even though the fusion proteins expressed normally (Supplementary Fig. 7c). In axons, the APP-VN/GB1a-VC complex partly co-localized with piccolo (Fig. 5b, correlation coefficients for BiFC/piccolo: Pearson 0.69 ± 0.02, Mander's 0.55 ± 0.03, $n = 11$ neurons, 4 independent transfections per group). The APP-VN/GB1a-VC complex also co-localized with the co-expressed presynaptic marker Synaptophysin-mCherry at boutons opposing PSD-95-positive spines (Supplementary Fig. 8). In dendrites, the APP-VN/GB1a-VC complex was present in the shafts but excluded from the spines (Fig. 5b), as shown by lack of co-localization with PSD-95 (overlap coefficient BiFC with PSD-95: Pearson 0.05 ± 0.01, Mander's 0.04 ± 0.02, $n = 11$ neurons, 4 independent transfections per group). This agrees with earlier findings showing that GB1a is not entering dendritic spines[3,12].

APP/GB1a complexes traffic in axons. Our proteomic data suggest that members of the CSTN and JIP family of proteins, which are kinesin-1 adapters[22,28], associate with GB1a/2 receptors through APP[15] (Fig. 1). We studied whether APP-VN/GB1a-VC complexes (identified by BiFC) co-localize with CSTN-1/-3 and JIP-1/-3 in the axons of transfected hippocampal neurons (Fig. 5c, Supplementary Fig. 9). Mander's overlap coefficient analysis indicated that a fraction of APP-VN/GB1a-VC complexes co-localizes with CSTN-1/-3 and JIP-1/-3 (Fig. 5d). Moreover, the APP-VN/GB1a-VC complex partly co-localized with endogenous kinesin light-chain 1 (KLC1) protein (Fig. 5c, Supplementary Fig. 9), consistent with reports on CSTN and JIP family members
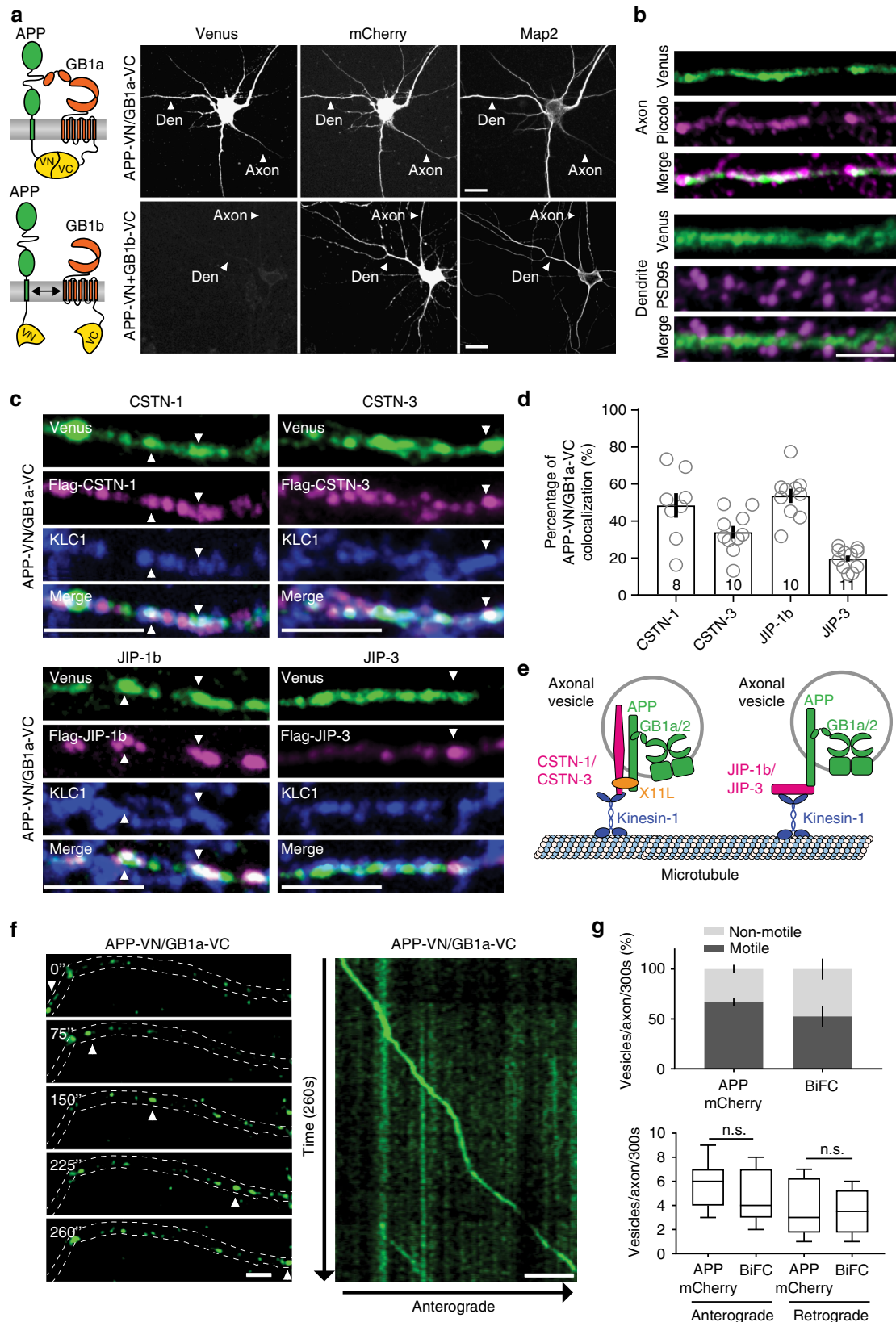
linking APP to kinesin motors[22,28] (Fig. 5e). We used live-cell confocal imaging to visualize axonal trafficking of the APP-VN/GB1a-VC complex and APPmCherry in cultured hippocampal neurons (Fig. 5f, Supplementary movie 1). Kymographs revealed

anterograde and retrograde axonal transport of APPmCherry and APP-VN/GB1a-VC BiFC complexes (Fig. 5g, Supplementary Fig. 10a), similarly as previously observed for APP[29]. The majority of APP vesicles colocalized with NPY, a marker for

Fig. 5 The APP/GB1a complex co-localizes with CSTN and JIP proteins in axons. **a** Scheme depicting the BiFC principle[27]. Complex formation of APP-VN with GB1a-VC reconstitutes Venus fluorescence and leads to BiFC. GB1b-VC serves as a negative control. Representative confocal images show hippocampal neurons (DIV10) expressing APP-VN together with GB1a-VC or GB1b-VC. BiFC is observed in axons and dendrites for GB1a-VC. Microtubule-associated protein Map2 identifies dendrites; mCherry served as a volume marker. Neurons were imaged 7 h post-transfection[27]. Scale bar 10 μm. **b** Higher magnification of axons and dendrites of hippocampal neurons transfected with APP-VN and GB1a-VC. The BiFC complex (Venus) partly co-localizes with piccolo (magenta) in axons. The BiFC complex is also present along dendritic shafts but excluded from spines (PSD-95, magenta). Scale bar 5 μm. **c** Partial co-localization (white, arrowheads) of the BiFC complex (green) with FLAG-CSTN-1, FLAG-CSTN-3, FLAG-JIP-1b, and FLAG-JIP-3 (magenta) and endogenous kinesin light-chain 1 (KLC1) (blue) in the axons of neurons. Scale bar 5 μm. **d** Quantification of the co-localization of the BiFC complex with FLAG-CSTN-1, FLAG-CSTN-3, FLAG-JIP-1b, and FLAG-JIP-3. The *n* numbers of neurons analyzed are indicated. **e** Scheme illustrating that APP together with interacting JIP and CSTN proteins link the GB1a/APP complex in cargo vesicles to axonal kinesin-1 motors. The neural adaptor protein X11-like (X11L) connects APP to CSTN-1[22]. **f** Time-lapse images of a well-separated APP-VN/GB1a-VC complex trafficking anterogradely in axons (acquisition times in seconds). White arrowheads mark a fluorescent APP-VN/GB1a-VC complex. A kymograph shows the entire time-lapse recording (right). Scale bars 25 μm. Data are presented as mean ± s.e.m. **g** Top: Analysis showing the percentage of mobile and non-mobile vesicles per axon within 5 min in hippocampal neurons expressing APPmCherry or the BiFC complex. Bottom: Number of vesicles moving antero-gradely and retrogradely per axons within 5 min. Data are presented in a min to max-box and whisker plot, with whiskers representing the smallest and largest values, the boxes representing the 25–75% percentile and the middle line representing the median. *P* > 0.05, one-way ANOVA. Source data are provided as a Source Data file


Golgi-derived vesicles[29]. 51% GB1a-GFP and 54% APP-VN/GB1a-VC axonal vesicles also contained NPY-mCherry (Supplementary Fig. 11). The percentage of mobile APPmCherry vesicles in axons was similar to that reported for APP vesicles in cultured hippocampal/cortical neurons[30] and similar to that of APP-VN/GB1a-VC (Fig. 5g) or APPmCherry/GB1a-GFP vesicles (Supplementary Fig. 10b). However, significantly less GB1a-GFP (23%) than APPmCherry (73%) or APPmCherry/GB1a-GFP (66%) vesicles were mobile (Supplementary Fig. 10b), suggesting that endogenous APP is limiting for axonal transport of over-expressed GB1a-GFP. The fraction of vesicles trafficking anterogradely or retrogradely in axons was similar for APP-VN/GB1a-VC and APPmCherry (Fig. 5g, Supplementary Fig. 10b). The mean anterograde (2.2 ± 0.4 μm/s, *n* = 29 vesicles) and retrograde (2.0 ± 0.2 μm/s, *n* = 29) trafficking velocities of APPmCherry in axons were similar as reported for dendrites[29]. APPmCherry/GB1a-GFP (antero: 1.6 ± 0.2 μm/s, *n* = 16: retro: 1.3 ± 0.2 μm/s, *n* = 26) and APP-VN/GB1a-VC vesicles (antero: 1.6 ± 0.1, *n* = 19; retro: 1.5 ± 0.1 μm/s, *n* = 8) had lower mean transport velocities than APPmCherry alone. GB1a-GFP vesicles (anterograde: 1.0 ± 0.1, *n* = 15; retrograde: 1.2 ± 0.1 μm/s, *n* = 25) had even lower transport velocities, similarly as observed before[16].

Interaction of APP with GB1a inhibits Aβ generation. Similar to other APP interacting proteins[22], GB1a/2 receptors may influence continuous proteolytic processing of APP. We investigated whether GB1a protects APP from cleavage by the β-site APP cleaving enzyme (BACE1) that, together with γ-secretase, generates Aβ[18] (Fig. 6a). Immunoblot analysis of transfected HEK293 cells indeed showed that co-expression of GB1a/2 receptors with APP markedly reduced the BACE1-cleavage products sAPPβ and β-carboxy-terminal fragment (APP-βCTF). Densitometric analysis revealed a reduction in the APP-βCTF/APP-FL and sAPPβ/APP-FL ratio by 60% (*P* < 0.0001 vs. exogenous APP together with BACE1) and 57% (*P* < 0.01), respectively, in the presence of GB1a/2 receptors (Fig. 6b). GB1b/2 receptors had no significant effect on BACE1 cleavage (Fig. 6b). GB1a/2 receptors had no effect on APP processing by ADAM10, an enzyme involved in non-amyloidogenic processing of APP (Supplementary Fig. 12a). We also studied amyloid-β40 (Aβ40) production in HEK293 cells expressing APP with GB1a/2 or GB1b/2, together with BACE1 or ADAM10 (Fig. 6c). The amount of Aβ40 secreted into the conditioned medium was determined 32 h post-transfection using a commercial ELISA. Expression of BACE1 but not ADAM10 increased Aβ40 secretion by one order

of magnitude. The presence of GB1a/2 receptors reduced this BACE1-mediated Aβ40 secretion by 77% (*P* < 0.01 vs. exogenous APP with BACE1). A smaller non-significant decrease in Aβ40 secretion was also observed in the presence of GB1b/2 receptors (*P* > 0.05 vs. exogenous APP with BACE1).

GB1a/2 receptors stabilize APP at the cell surface. GBRs activity did not influence Aβ40 secretion in cultured hippocampal neurons (Fig. 6d), consistent with GBR activity not influencing the APP/GB1a interaction (Supplementary Fig. 2). However, cultured hippocampal neurons of *GB1a*^{−/−} mice exhibited a significant increase in secreted Aβ40 protein (*P* < 0.0001 vs. WT, Fig. 6e) indicating that loss of GB1a promotes amyloidogenic processing of APP. Control neurons of *GB1b*^{−/−} mice exhibited no increase in Aβ40 secretion (*P* > 0.05 vs. WT, Fig. 6e). Infection of cultured hippocampal neurons of *GB1a*^{−/−} or WT mice with lentiviral particles expressing GFP-GB1a significantly reduced Aβ40 secretion (*P* < 0.05 vs. GFP or GFP-GB1b, Fig. 6f). We investigated how GB1a/2 receptors inhibit amyloidogenesis. Immunoprecipitation experiments with transfected HEK293 cells showed that GB1a does not compete with BACE1 for APP (Supplementary Fig. 12b). Surface biotinylation experiments with cultured hippocampal neurons indicated that loss of GB1a but not GB1b significantly (*P* < 0.01) reduces APP levels (Fig. 7a), suggesting that GB1a stabilizes APP at the plasma membrane. Consistent with this hypothesis, surface biotinylation experiments in transfected HEK293 cells confirmed that GB1a/2 receptors significantly (*P* < 0.05) increased APP at the cell surface while GB1b/2 receptors failed to exert such an effect (*P* > 0.05, Fig. 7b).

We next investigated whether increased APP surface expression in the presence of GB1a reflects reduced endocytosis. We fused a 13 amino-acid α-bungarotoxin (BTX) binding site (BBS) to the N-terminus of APPmCherry[27] (Fig. 7c). TIRF microscopy was used to analyze time-dependent changes in surface fluorescence of BTX-488 (Alexa488-labeled BTX) and mCherry in HEK293 cells expressing BBS-APPmCherry in the absence or presence of GB1a/2 or GB1b/2 receptors (Fig. 7c). Endocytosis decreased BTX-488 cell surface fluorescence during a 15 min period, both in the absence of GBRs (residual TIRF intensity 58.9 ± 3.1%) and in the presence of GB1b/2 receptors (59.5 ± 5.5%). GB1a/2 receptors significantly reduced the decrease in BTX-488 cell surface fluorescence (81.0 ± 2.8%, *P* < 0.001), indicating that association with GB1a/2 receptors reduces APP endocytosis (Fig. 7c). Of note, the cell surface mCherry fluorescence remained unaltered during the internalization period (control 103.7 ± 7.0%, GB1a/2 101.0 ± 5.1%, GB1b/2 112.6 ± 8.0%, normalized to the
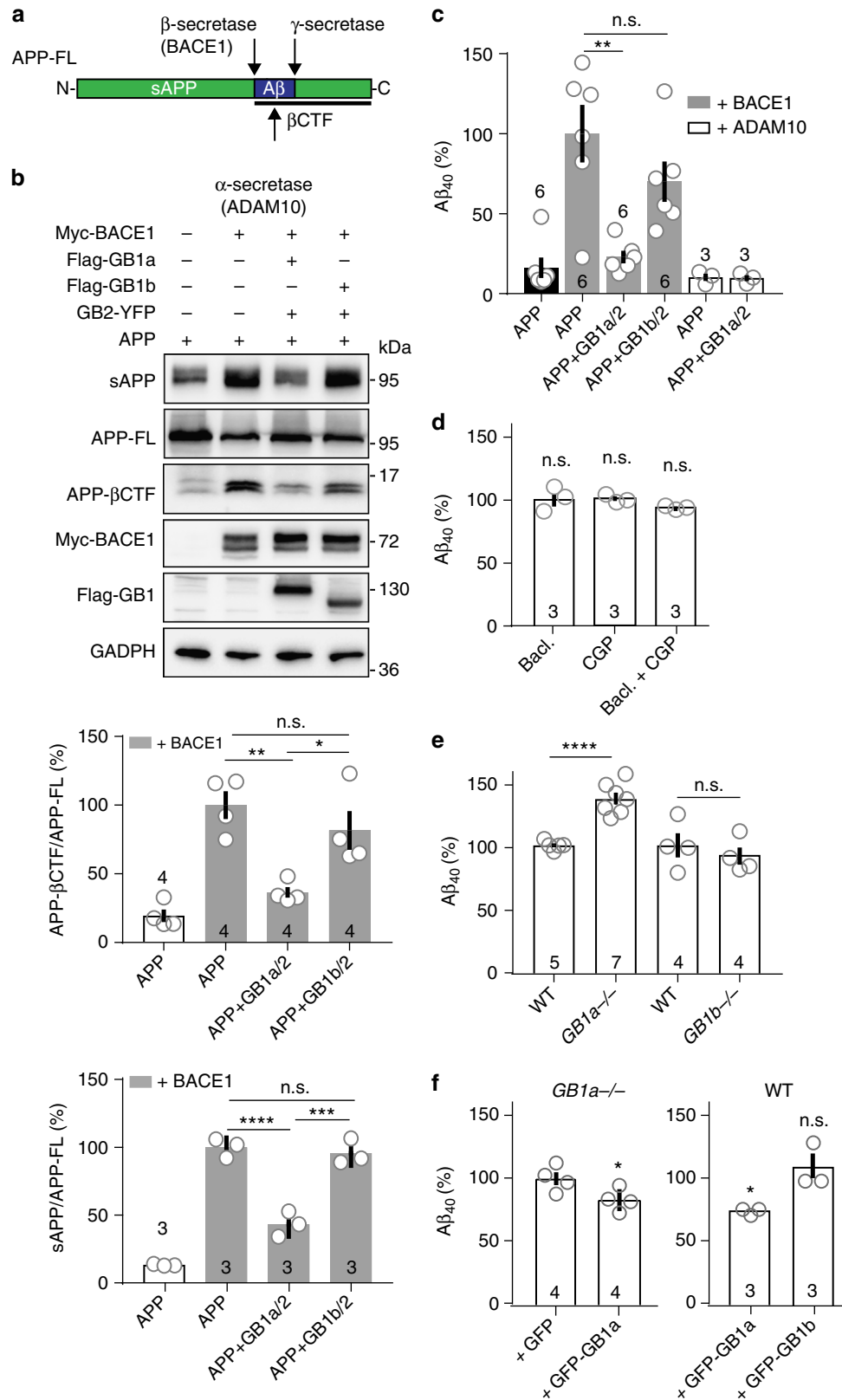
fluorescence at t_0; Fig.7c), suggesting that transfected BBS-APPmCherry reached a steady-state level at the plasma membrane.

We additionally studied APP endocytosis in live HEK293 cells using time-lapse confocal microscopy, which allowed monitoring

surface BTX-488/APPmCherry internalization (Fig. 7d). In the absence of GBRs or in the presence of GB1b/2 receptors, we observed internalized BTX-488-labeled vesicles after 10 min (Fig. 7d). However, in the presence of GB1a/2 receptors we did not detect internalized BTX-488-labeled vesicles before 30 min.

Fig. 6 GB1a inhibits BACE1-mediated APP proteolysis and Aβ40 generation. **a** Scheme indicating proteolytic cleavage sites in APP for α-secretase, β-secretase (BACE1) and γ-secretase. APP-FL, APP full-length; sAPP, soluble APP; APP-βCTF, β carboxy-terminal fragment of APP. **b** Immunoblot of APP cleavage products in HEK293 cells expressing Myc-BACE1, APP and GB2-YFP together with Flag-GB1a or Flag-GB1b. For sAPP analysis, the cell culture medium was filtered and concentrated 32 h post-transfection. Glyceraldehyde 3-phosphate dehydrogenase (GADPH) served as loading control. A significant reduction in the APP-βCTF/APP-FL and the sAPP/APP-FL ratio is observed in the presence of GB1a vs. GB1b. One-way ANOVA, $n = 3$–4 independent experiments. **c** Bar graphs of Aβ40 secretion into the culture medium of HEK293 cells expressing APP with or without Myc-BACE1 or Myc-ADAM10 in the presence of GB1a/2 or GB1b/2 (32 h post-transfection). Note that selectively GB1a/2 significantly prevents Aβ40 secretion. One-way ANOVA, $n = 6$ independent experiments. **d** GBR activity does not influence Aβ40 production. Bar graphs of the amount of Aβ40 secreted into the culture medium of WT hippocampal neurons after treatment for 7 days with baclofen (10 μM) or CGP54626 (CGP, 10 nM) or both. Values normalized to untreated (100%). One-way ANOVA, $n = 3$ independent neuronal cultures. **e** Bar graphs of the amount of Aβ40 secreted within 10 days into the culture medium of hippocampal neurons of $GB1a^{-/-}$, $GB1b^{-/-}$ and control WT littermate mice. Neurons from $GB1a^{-/-}$ but not $GB1b^{-/-}$ mice exhibit increased Aβ40 secretion. Unpaired Student's t-test, $n = 4$–7 independent neuron preparations. **f** Lentiviral expression of GB1a but not GB1b decreases Aβ40 secretion in neuronal cultures from $GB1a^{-/-}$ and WT mice. Bar graphs of Aβ40 secreted within 10 days into the culture medium of hippocampal neurons infected with purified lentiviral particles expressing GFP, GFP-GB1a or GFP-GB1b. $GB1a^{-/-}$ cultures; unpaired Student's t-test, $n = 4$ independent neuronal cultures. WT cultures normalized to uninfected (100%); one-way ANOVA, $n = 3$ independent neuronal cultures. *$P < 0.05$, **$P < 0.01$, ***$P < 0.001$, ****$P < 0.0001$. Data are presented as mean ± s.e.m. Source data are provided as a Source Data file

Simultaneous monitoring of the decay in BTX-488 surface fluorescence showed that GB1a/2 receptors led to a more than 3-fold increase in the respective time constant (no GBRs: $\tau = 5.6$ min, GB1b/2: 5.4 min, GB1a/2: 16.5 min; Fig. 7e). These results indicate that GB1a/2 receptors increase APP surface expression by reducing APP internalization, which prevents amyloidogenic processing in recycling endosomes. GB1a/2 receptors exhibit slower internalization and longer surface stability than GB1b/2 receptors in neurons[11]. It is therefore possible that APP reciprocally stabilizes GB1a/2 receptors at the cell surface, although we did not directly test this.

We addressed whether the presence of GB1a prevents sorting of APP into endosomes in cultured hippocampal neurons (DIV14) transfected with GB1a-GFP, APPmCherry or both. To identify recycling endosomes we incubated neurons with Alexa-AF647 conjugated transferrin. Co-expression of GB1a-GFP indeed significantly decreased the presence of APP-mCherry in transferrin-AF657 positive endosomes (Supplementary Fig. 13). We further analyzed whether neuronal activity influences APP-mCherry and GB1a-GFP sorting into endosomes. To induce neuronal activity we used an established glycine/bicuculline stimulation protocol[29]. This protocol did not significantly alter endosomal localization of APP-mCherry in the presence and absence of GB1a-GFP (Supplementary Fig. 13).

Discussion

Presynaptic GBRs regulate neurotransmitter release at most synapses in the brain[1]. Presynaptic GBR expression is itself subject to regulation by neuronal activity[3–5] and frequently impaired in disease[6–10]. The SDs of GB1a are essential for presynaptic localization and membrane stabilization of GBRs[11–14]. Proteomic analysis identified several proteins that selectively and directly interact with presynaptic GB1a/2 receptors, including APP, AJAP-1, and PIANP[15,31,32]. We now found that sequence-related epitopes in these proteins interact with the N-terminal SD1 of GB1a. Electrophysiological analysis of $AJAP-1^{-/-}$, $PIANP^{-/-}$, and $APP^{-/-}$ mice revealed that selectively the absence of APP generates a deficit in GBR-mediated presynaptic inhibition. Proteomic, electrophysiological and trafficking data show that binding of APP to the SD1 serves to sort GB1a/2 receptors into axonally destined vesicles. At the same time, binding to surface GB1a/2 receptors interferes with APP processing to Aβ peptides in recycling endosomes. Our results therefore support that APP/GB1a/2 complex formation simultaneously regulates bioavailability and localization of the partner proteins.

APP is reported to link cargo vesicles via adaptor proteins to axonal kinesin-1 motors[22,28,33]. Our proteomic data support that APP/GB1a complexes bind to adaptor proteins of the JIP and CSTN families. BiFC directly showed that APP/GB1a complexes traffic anterogradely in axons. We additionally observed retrograde trafficking of complexes, presumably mediated by dynein motors[28]. $APP^{-/-}$ mice exhibit a 74% reduction but not a complete absence of GBRs in axons. Likewise, $APP^{-/-}$ mice show an impairment but not a complete loss of GBR-mediated inhibition of glutamate release. Differences in the transport velocities of GB1a-GFP and APPmCherry/GB1a-GFP vesicles further suggest the existence of an APP-independent GB1a transport. Possibly, some GB1a/2 receptors also diffuse laterally in the membrane and accumulate at terminals by binding to SD-interacting proteins[14]. It is unclear whether APP, AJAP-1 and/or PIANP retain GB1a/2 receptors at terminals after delivery. The interacting epitopes of SD1 and APP represent intrinsically disordered regions with dynamically interconverting structures, suggestive of a transient regulatory interaction[34,35]. After anterograde trafficking APP may therefore transfer GB1a/2 receptors to the higher affinity binding-sites of PIANP and AJAP-1. In support of such a scenario, $AJAP-1^{-/-}$ and $PIANP^{-/-}$ mice show a trend towards reduced presynaptic GBR-mediated inhibition in electrophysiological experiments. Moreover, both proteins are expected to localize to synaptic adherens junctions[20] and should therefore be well positioned to anchor GB1a/2 receptors at presynaptic terminals. APP/GB1a complexes are also present in dendritic shafts. This is consistent with axonal proteins not being restricted to axons because endoplasmic reticulum and Golgi apparatus extend into dendrites. However, it is also possible that some APP/GB1a complexes internalize in axons and transcytose to the dendrites, as proposed for APP[36,37].

$GB1a^{-/-}$ and $APP^{-/-}$ mice share several phenotypes, including a deficit in GBR-mediated presynaptic inhibition[12] (this study), increased seizure susceptibility[1,17], deficits in long-term potentiation[12,17,38], cognitive impairments[1,12,38], altered network oscillations[39,40], and circadian locomotor activity[1,38]. This is consistent with the proposal that genetic ablation of genes whose protein products belong to the same functional complex produce similar phenotypes[41]. Some phenotypes of $APP^{-/-}$ mice may also relate to a down-regulation of the K$^+$–Cl$^-$ transporter KCC2 and a resulting decrease in GABA$_A$ receptor inhibition[42]. Interestingly, GBRs and KCC2 are reported to associate with one another and GBR activity reduces KCC2 levels at the cell surface[43]. Loss of GBRs may therefore counteract downregulation of KCC2 in $APP^{-/-}$ mice.
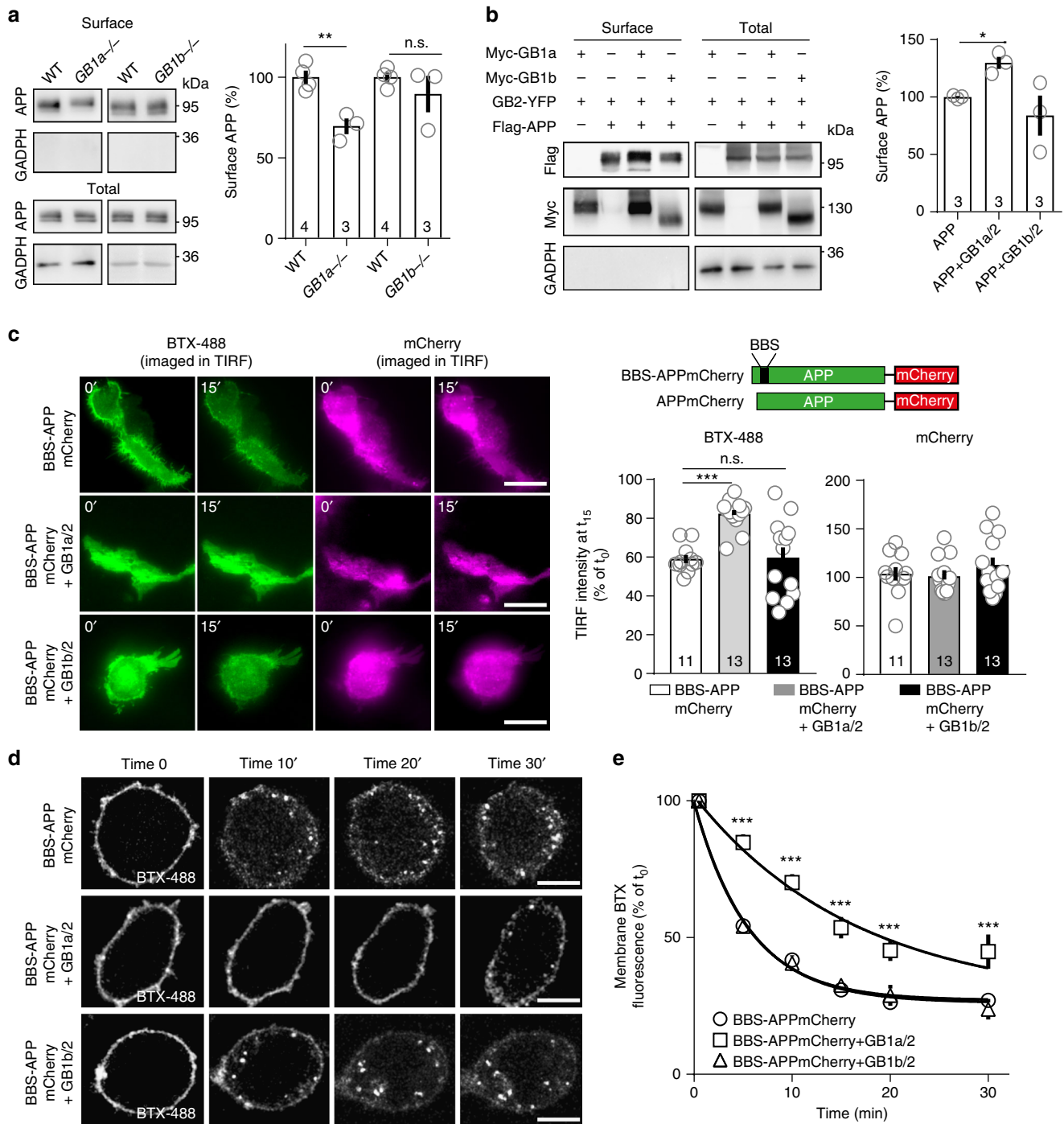
Fig. 7 GB1a stabilizes APP at the cell surface. **a** Cell surface biotinylation of APP in cultured hippocampal neurons of $GB1a^{-/-}$, $GB1b^{-/-}$, and control WT littermate mice. Bar graph summarizes the densitometric quantification of APP surface levels: WT $100.0 \pm 4.1\%$, $GB1a^{-/-}$ $69.6 \pm 4.9\%$, **$P < 0.01$, unpaired Student's t-test; WT $100.0 \pm 2.9\%$, $GB1b^{-/-}$, $89.6 \pm 11.2\%$, $P > 0.05$, Mann-Whitney. **b** Cell surface biotinylation of APP in HEK293 cells in the presence or absence of GB1a or GB1b. Bar graphs summarizes the densitometric quantification of APP surface levels. APP: $100 \pm 0.9\%$; APP + GB1a/2: $129.7 \pm 5.3\%$; APP + GB1b/2: $83.9 \pm 17.5\%$; *$P < 0.05$, one-way ANOVA; $n = 3$ independent experiments. **c** To study APP internalization the α-BTX binding site (BBS) was fused to the extracellular N-terminus of APPmCherry (BBS-APPmCherry). BTX-488 and mCherry cell surface fluorescence of HEK293 expressing BBS-APPmCherry with or without GB1a/2 or GB1b/2 before (time 0′) and after BBS-APPmCherry internalization for 15 min at 37 °C (15′). Bar graphs show the mean surface BTX-488 and mCherry fluorescence intensity after 15 min of BBS-APPmCherry internalization. ***$P < 0.001$, one-way ANOVA, BBS-APPmCherry $n = 11$, BBS-APPmCherry + GB1a/2 $n = 13$, BBS-APPmCherry + GB1b/2 $n = 13$ independent experiments. Scale bar 20 μm. **d** Representative confocal images of the BTX-488 fluorescence in HEK293 cells expressing BBS-APPmCherry with or without GB1a/2 or GB1b/2 before (0′) and after BBS-APPmCherry internalization for 10, 20, and 30 min. Scale bar 10 μm. **e** Decrease of BTX-488 surface fluorescence in **c** over time. $n = 14$ cells per group, 3 independent transfections per group. ***$P < 0.001$, one-way ANOVA. Data are presented as mean ± s.e.m. Source data are provided as a Source Data file

In amyloidogenic processing, Aβ is liberated from APP by the concerted action of BACE1 and γ-secretase[17,18]. BACE1 is present in axons and dendrites but highly polarized to axonal domains[44], which are the main source of Aβ[45]. Nevertheless, dendritic compartments also release Aβ[46]. BACE1 activity typically occurs in the acidified environment of recycling endosomes[27,47]. While GBR activity influences neither the APP/GB1a interaction nor Aβ40 production, we found that GB1a protects APP from BACE1-dependent endosomal processing by stabilizing APP at the cell surface. Adding to its protective role, GB1a also keeps APP out of dendritic spines that are particularly rich in recycling endosomes[48]. Most neurons in the brain express GB1a, which therefore should markedly influence APP processing. Accordingly, cultured hippocampal neurons of $GB1a^{-/-}$ mice exhibited a ~40% increase in secreted Aβ levels compared to WT littermate mice.

While several genome-wide association studies link GBRs to mental health disorders[1,49], no such study directly links GBRs to AD. However, several reports describe a downregulation of GBRs in AD[6,7,49]. GBR downregulation is likely a consequence of the disease, for example caused by increased GBR activity due to excess GABA release by reactive astrocytes[50,51]. Likewise, dysregulated axonal transport, an early pathological feature in AD associated with increased Aβ production[45,52], will reduce the number of GB1a/2 receptors on glutamatergic terminals and promote NMDA receptor-dependent GBR degradation[3,4]. GBR downregulation in AD[6,7] may not only increase Aβ production but also contribute to excitotoxicity and the high incidence in seizures and memory deficits in patients[53], which is supported by the pathology of $GB1a^{-/-}$ and $APP^{-/-}$ mice. Increased GABA release by reactive astrocytes in AD[50,51] may help to counteract excess glutamate release and therefore play opposing roles in excitotoxic processes.

According to the amyloid hypothesis, accumulation of Aβ in the brain drives AD pathogenesis. Reducing Aβ production is therefore expected to ameliorate AD symptoms[18,19]. Our study shows that stabilizing APP with GB1a at the cell surface prevents Aβ formation. NMDA receptor blockade prevents GBR degradation[3,4] and provides a means to stabilize APP/GB1a complexes. Although controversial, Memantine®, a noncompetitive NMDA receptor antagonist used to treat AD patients, is reported to stabilize APP at the cell surface and to reduce Aβ levels[54]. Thus it is possible that Memantine® stabilizes APP at the cell surface by preventing NMDA receptor-induced GBR internalization[3,4]. GBR antagonists provide another means to stabilize GBRs at the cells surface by preventing GBR degradation[51,55]. GBR antagonists are already undergoing evaluation as possible AD therapeutics because they promote excitatory neurotransmitter release and enhance cognition[55]. Moreover, signaling pathways that increase cAMP levels, such as activation of β-adrenergic receptors, increase GBR availability at the cell surface[56]. Thus, pharmacological stabilization of APP/GB1a complexes at the cell surface may have potential for symptomatic amelioration in AD patients.

Methods

Molecular biology. Plasmids were gifts from D. Selkoe and T. Young-Pearse (pCAX-APP695, pCAX-FLAG-APP695, pCAX-APPs-α; Addgene #30137, #30154, #30147), R. Davis (pcDNA3-Flag-JIP-1b, Addgene #52123), R. Derynck (pRK5M-ADAM10, Addgene #31717), W. Almers (NPY-mCherry, Addgene #67156), P. Scheiffele (Synaptophysin-mCherry), M. Di Luca (Myc-BACE1), J.P. Pin (pRK6-Flag-GB1a), and K. Kaupmann (pCI-HA-GB2-YFP). AJAP-1 (Source BioScience) was subcloned into pcDNA3, PIANP cDNA (OriGene) placed into pCMV6 with an HA-tag insertion after amino acid 27. Myc-GB1a, Myc-GB1b, GB1a-GFP and GB1b-GFP, Myc-GB1aΔSD1, Myc-GB1aΔSD2 and Myc-GB1aΔSD1/2 were as described[57]. pRK6-Flag-GB1b was constructed by replacing the GB1a MluI-BamH1 fragment in pRK6-Flag-GB1a with GB1b. GB1a-Rluc, GB1b-Rluc, APP-Venus and APPmCherry were constructed using overlap extension polymerase

chain reaction and cloned into the pCI vector (Promega). For transfection experiments we used the predominant neuronal APP isoform, APP695[17] (hereafter named APP). The APP deletion mutants APPΔGFLD(Δ28–123), APPΔCuBD (Δ124–189), APPΔAcD(Δ191–294) and APPΔCAPPD (Δ295–504) were generated by overlap extension in the pCAX vector. Numbers indicate the residues deleted in APP. To construct APP-VN, the Venus in APP-Venus was replaced with the N-terminal Venus residues 1–172. To construct GB1a-VC or GB1b-VC, the GFP in Myc-GB1a-GFP or Myc-GB1b-GFP was replaced with the C-terminal Venus residues 155–238. Split Venus constructs include the PRARDPPVAT linker 5' of the Venus fragments. BBS-APPmCherry was created by adding the α-bungarotoxin (BTX) binding site (BBS) WRYYESSLEPYPD at the N-term of APPCherry between amino acids A30 and E31 (Trenzyme, Germany)[27].

Mouse strains. $GB1a^{-/-}$, $GB1b^{-/-}$, and $GB2^{-/-}$ mice were kept in the BALB/c background[12,58], $APP^{-/-}$ mice in the C57BL/6 background[59]. $AJAP-1^{-/-}$ mice were generated by blastocyst injection of embryonic stem cell clone HEPD0583_2_B09 harboring a knockout-first promotor-driven tm1a allele (AJAP-1tm1a(EUCOMM)Hmgu)[60] and subsequent crossing of founders with the Cre-deleter strain B6.C-Tg(CMV-cre)1Cgn/J. In the converted tm1b allele exon 2 of the AJAP-1 gene was deleted leaving a LacZ reporter behind, which contains an en-2 splice acceptor and an internal ribosomal entry site. $PIANP^{-/-}$ mice (B6-Pian-p^em1Bet) in the C57BL/6 background were generated using the Alt-R CRISPR/Cas9 targeting system (IDT, Leuven, Belgium). The Cas9 target sequence 5'-GACCCCA CACTATAGCCCAAGGG-3' in the Pianp gene (MGI:2441908) was selected using the CRISPOR search algorithm http://crispor.tefor.net. Enzymatic mutation altered the targeting sequence to 5'-GACCCCACACTATAGGTGTGAGATGGG-3' resulting in a frame shift after P97 and premature termination of translation. All mouse experiments were conducted in accordance with Swiss guidelines and received ethical approval from the veterinary office of Basel-Stadt.

Affinity purifications from brain membranes. Plasma-membrane enriched protein fractions were prepared from whole brain isolated from a pool of 10 WT and 2–4 knock-out mice[61]. Concentrations of protein fractions were determined by Bradford assays (Biorad). Membrane proteins were solubilised with CL-47 and CL-91 buffers at 1 mg protein per ml (Logopharm GmbH, Germany). After 30 min incubation on ice and clearing by ultracentrifugation (10 min, 150,000 × g) solubilisates were incubated with the immobilized antibodies and incubated for 2 h on ice. 10–15 µg of the following antibodies were used for an immunoprecipitation out of 1 mg of solubilised membrane proteins: anti-APP, Ab#1, rabbit anti-APP (A8717, Sigma), Ab#2, rabbit anti-APP (ABIN1741750, Antikörper-online), Ab#3, goat anti-APP (sc-7498, Santa Cruz); anti-AJAP-1, Ab#1, sheep anti-AJAP-1 (AF7970, R&D Systems), Ab#2, rabbit anti-AJAP-1 (HPA012157, Sigma), Ab#3, goat anti-AJAP-1 (sc-163371, Santa Cruz); anti-PIANP, Ab#1, rabbit anti-PIANP (PAB21925, Abnova), Ab#2, rabbit anti-PIANP (raised against epitope: mouse PIANP aa 221–237, generated by Young in Frontier, South Korea) (Fig. 1c). For a quantitative comparison of GBRs in two samples (Fig. 1a), a mixture of anti-GB antibodies including rabbit anti-GB1 (322102, Synaptic Systems), rabbit anti-GB2 (322203, Synaptic Systems), guinea pig anti-GB2 (322204/5, Synaptic Systems)) was applied to isolate the complete pool of receptor protein complexes, which was controlled by immunoblot analysis of the respective supernatant after antibody incubation. After two washes, proteins were eluted and the majority processed for MS-analysis. Proteins were separated on SDS-PAGE gels and silver-stained. Lanes were cut into two sections (high and low MW) and digested with sequencing-grade modified trypsin (Promega, Mannheim, Germany). Peptides were extracted and prepared for MS analysis as described[15]. Influence of GBR activity on complex formation was analyzed by incubating unsolubilized membranes with 1 mM GABA or 4 µM CGP54626 in PBS buffer for 1 h at room temperature. Subsequently membrane proteins were solubilised and processed for immunoprecipitations as described above (Supplementary Fig. 2a).

Mass-spectrometry and protein identification. Mass spectrometric analysis was carried out as described[61]. Peptide samples dissolved in 0.5% trifluoroacetic acid were loaded onto a trap column (C18 PepMap100, 5 µm particles; Thermo Scientific), separated by reversed phase chromatography via a 10 cm C18 column (PicoTip™ Emitter, 75 µm, tip: 8 µm, New Objective, self-packed with ReproSil-Pur 120 ODS-3, 3 µm, Dr. Maisch HPLC; flow rate 300 nl/min) using an UltiMate 3000 RSLCnano HPLC system (Thermo Scientific), and eluted by an aqueous organic gradient (eluent "A": 0.5% acetic acid; eluent "B" 0.5% acetic acid in 80% acetonitrile; "A"/"B" gradient: 5 min 3% B, 60 min from 3% B to 30% B, 15 min from 30% B to 100% B, 5 min 100% B, 5 min from 100% B to 3% B, 15 min 3% B). Sensitive and high-resolution MS-analyses were executed on an Orbitrap Elite mass spectrometer with a Nanospray Flex Ion Source (both Thermo Scientific). Precursor signals (LC-MS) were acquired with a target value of 1,000,000 and a nominal resolution of 240,000 (FWHM) at m/z 400; scan range 370 to 1700 m/z). LC-MS/MS data were extracted using "msconvert.exe" (part of ProteoWizard; http://proteowizard.sourceforge.net/, version 3.0.6906). Peak lists were searched against a UniProtKB/Swiss-Prot database (containing all rat, mouse and human entries) using Mascot 2.6.0 (Matrix Science, UK). One missed trypsin cleavage and

common variable modifications including S/T/Y phosphorylation were accepted for peptide identification. Significance threshold was set to $p < 0.05$.

Mass-spectrometry based protein quantification. Label-free quantification of proteins was based on peak volumes (PVs = peptide m/z signal intensities integrated over time) of peptide features[61]. Peptide feature extraction was done with MaxQuant[62] (http://www.maxquant.org/, version 1.4) with integrated effective mass calibration. Features were then aligned between different LC-MS/MS runs and assigned to peptides with retention time tolerance ±1 min and mass tolerance: ±1.5 ppm using an in-house developed software. The resulting peptide PV tables formed the basis for protein quantification (Fig. 1). For relative quantification of proteins in two samples (Fig. 1a, Supplementary Fig. 2a), protein ratios (rPVs) were determined from protein profiles[61]. Briefly, for each peptide, the PVs were then normalized to their maximum over all AP data sets yielding relative peptide profiles, ranked for each protein by pairwise Pearson correlation. These values were normalized to the molecular abundance of GBRs (Source Data File) to obtain the degree of association with the target. The median from all peptides, assigned as unique for each individual protein, was used to calculate the abundance difference of GBR constituents in knock-outs vs. WT (Fig. 1a). Interactome analysis were performed by comparing relative protein abundance in a sample vs. control (rPV, Fig. 1c, Source Data File), determined by the TopCorr method as the median of at least 2–6 individual peptide PV ratios of the best correlating protein-specific peptides (as determined by Pearson correlation of their abundance values)[63]. Specificity thresholds of APs were determined from rPV histograms of all proteins detected in the respective AP vs. control. Constituents of the GBR proteome were considered specifically co-purified when rPVs (wild-type mouse vs. IgG and KO) were above the threshold.

Transferrin treatment and neuronal activity induction. Lipofectamine 2000 (Life Technologies) was used to transfect HEK293 cells. The amount of DNA in the transfections was kept constant by supplementing with pCI plasmid DNA (Promega). For preparation of cultured neurons embryonic day 16.5 mouse hippocampi were dissected, digested with 0.25% trypsin (Invitrogen) in HBSS (Gibco, 14170–088) medium for 13 min at 37 °C, dissociated by trituration and plated on glass coverslips coated with 1 mg/ml poly-L-lysine hydrobromide (PLL, Sigma) in 0.1 m borate buffer (boric acid/sodium tetraborate)[13]. Neurons were seeded at a density of ~550 cells/mm^2 in neurobasal medium (Invitrogen) supplemented with B27 (Invitrogen) and 0.5 mM L-glutamine and cultured in a humidified atmosphere (5% CO$_2$) at 37 °C. Cultured hippocampal neurons were transfected using Lipofectamine 3000 (Life Technologies) or Effectene (Qiagene). Transferrin-AF647 (Invitrogen) and bicuculline/glycine treatment[29] was performed at DIV14, 30 min before transferrin-AF647 treatment, neurons were incubated with fresh Neurobasal medium. Incubation of Transferrin-AF647 was added at a final concentration of 50 μg/μl for 1 h, For activity induction neurons were treated with 20 μM bicuculline/200 μM glycine for 5 min in Neurobasal medium. The medium was then replaced with fresh medium supplemented with 20 μM bicuculline for 15 min. Control cultures were kept in pure Neurobasal medium. Cultures were washed with 1× PBS, fixed for 10 min at room temperature in 4% PFA/4% sucrose and mounted on microscope slides with Dako Fluorescence Mounting Medium (Agilent). Samples were imaged on Zeiss LSM880 confocal microscope equipped with Plan-Apochromat ×63/1.4 Oil objective. Collected Z-stacks were quantified using Fiji and Adobe Photoshop CC 2018.

IP and immunoblot experiments. Hippocampal neurons or HEK293 cells were harvested 24 h after transfection, washed twice with ice-cold PBS, and subsequently lysed in NETN buffer supplemented with complete EDTA-free protease inhibitor mixture (Roche). After rotation for 10 min at 4 °C, lysates were cleared by centrifugation at 10,000×g for 10 min at 4 °C. Lysates were directly used for immunoblot analysis or immunoprecipitated with antibodies coupled to Protein-G/A Agarose beads (Roche). Membrane protein fractions from brains (prepared as described above), lysates from cultured cells and immunoprecipitates were resolved using standard SDS-PAGE gels and decorated with the indicated antibodies. SuperSignal Femto chemiluminescence detection kit (Thermo Scientific) or ECL Prime (Amersham Biosciences) were used for visualization using a Fusion FX Chemiluminescence System (Vilber Lourmat, Witec AG). Band intensities were quantified by ImageJ software (NIH). Uncropped and unprocessed scans of immunoblots are shown in the Source Data file.

To determine whether GBR activity regulates binding of APP, AJAP-1, and PIANP to GB1a, we prepared brain membrane fragments as for [^{35}S]GTPγS binding assays and resuspended them in NET buffer (100 mM NaCl, 1 mM EDTA, 20 mM Tris/HCl, pH 7.4) supplemented with EDTA-free protease inhibitor mixture (Roche) for 90 min at 4 °C. Membranes were treated with 1 mM GABA or 4 μM CGP54626 or left untreated for 1 h at room temperature. Nonidet P-40 detergent was added to a final concentration of 0.5%. Incubation with antibodies (α-APP, (Y188, Abcam), α-AJAP1 (AF7970, R&D Systems), α-PIANP (PAB21925, Abnova)) was for 16 h at 4 °C, followed by IP. For densitometric analysis of immunoblots, the GB1a signal was divided by the signal of the immunoprecipitated protein (APP, AJAP-1, PIANP) and normalized as 1.0 for untreated control samples.

The antibodies used for immunoprecipitation were: rabbit anti-c-myc (C3956, Sigma), mouse anti-c-myc 9E10 (sc-40, Santa Cruz), mouse anti-flag M2 (F1804, Sigma), rabbit anti-flag (F7425, Sigma), rabbit anti-GB1 (rat aa 857–960), rabbit anti-GB2 (322203, Synaptic Systems), rabbit anti-APP Y188 (ab32136, Abcam) and rabbit anti-APP Y188 (ab32136, Abcam). The primary antibodies used for immunoblot analysis were: mouse anti-GB1 (ab55051, Abcam), rabbit anti-GB1 (rat aa 857–960), mouse anti-GB2 (75–124, NeuroMab), mouse anti-c-myc 9E10 (sc-40, Santa Cruz), rabbit anti-c-myc (C3956, Sigma), rabbit anti-flag (F7425, Sigma), mouse anti-APP A4 22C11 (mab348, Millipore), rabbit anti-APP Y188 (ab32136, Abcam), sheep anti-AJAP-1 (AF7970, R&D Systems), rabbit anti-PIANP (PAB21925, Abnova), rabbit anti-Calnexin (ab75801, Abcam), rabbit anti-β-Actin 13E5 (#4970, Cell Signaling) and mouse anti-GADPH (sc-32233, Santa Cruz). The secondary antibodies were: HRP-conjugated anti-rabbit (NA9340V, GE Healthcare, UK), anti-mouse (NA9310V, GE Healthcare, UK), anti-sheep (ab7111, Abcam), anti-mouse (sc-2005, Santa Cruz), anti-rabbit (sc-2004, Santa Cruz).

Purification of proteins for structural analysis. SD1/2 was produced as secreted protein in *Sf21* insect cells and subsequently purified by Ni-chelate affinity-matrix and size exclusion chromatography, as described[15]. APP(191–294), AJAP-1 (175–279), and PIANP(27–174) were subcloned into pET30 (Novagen) with a N-terminal His-tag followed by the B1 domain of streptococcal protein G as a solubility enhancement tag (SET) and a TEV cleavage site. Protein expression was induced in *E.coli* BL21 (DE3) by 1 mM IPTG. Cells were either grown on LB-medium (MP Biomedicals) or for isotopic protein labeling on M9 minimal medium made with ^{15}NH$_4$Cl and ^{13}C-Glucose (both Cambridge Isotope Laboratories). After cultivation (LB medium: 4 h, 37 °C, M9 medium: 16 h, 30 °C) cells were lysed in 20 mM Tris/HCl pH 8, 300 mM NaCl, 10 mM imidazole, 0.5 mM EDTA/EGTA by sonication. Lysates were cleared by centrifugation (20,000 x g, 4 °C, 20 min), loaded on a HisTrap HP sepharose column (GE Healthcare) and His-tagged proteins subsequently eluted with 500 mM imidazole. Respective fractions of the APP construct were pooled and dialyzed against 50 mM Tris/HCl pH 8, 150 mM NaCl, 0.5 mM EDTA, 1 mM DTT before adding the TEV-protease. After 14 h incubation, the digest was loaded on a HisTrap HP sepharose column to remove all His-tag-containing species. The cleavage step was omitted for the AJAP-1 and PIANP constructs. Final purification was done by size exclusion separations (Superdex 200 10/300 GL column, GE Healthcare). The purity of the samples was determined by separating proteins on SDS-PAGE and visualized by conventional Coomassie stain solutions. Proteins were concentrated by Vivaspin® 6 centrifugal concentrators (Vivascience) and directly used for biophysical characterizations.

Protein NMR spectroscopy. The NMR spectra were recorded at 293 K on a Bruker Avance 600 equipped with a cryogenically cooled pulsed-field gradient triple-resonance probe (TXI) operating at 600.13 MHz. The sequence-specific assignment of backbone atoms of APP191–294 both in the absence and the presence of SD1/2 protein was obtained from the following experiments: ^{1}H-^{15}N HSQC, HNCA, HN(CO)CA, HNCO, HN(CA)CO, CBCA(CO)NH, HBHA(CO)NH, CBCANH, NOESY-^{1}H-^{15}N-HSQC (250 ms mixing time), and HN(CA)NNH. The interaction site of APP with SD1/2 was determined by observation of chemical-shift changes and cross-peak intensity changes in ^{1}H–^{15}N HSQC spectra of ^{15}N-labeled or ^{13}C/^{15}N-labeled APP during titrations with unlabeled SD1/2 protein up to a stoichiometric ratio of 1:1.1. The NMR samples contained 0.1–0.65 mM APP in 50 mM sodium phosphate buffer (pH 6.8) with 50 mM NaCl, 0.5 mM EDTA, 0.5 mM EGTA, and 10% D$_2$O (v/v). Similarly, complex formation of ^{15}N-labeled AJAP-1(175–279) or PIANP(27–174), each with a solubility enhancement tag (SET[64], see Protein Expression), was monitored by ^{1}H–^{15}N HSQC spectra during titrations with unlabeled SD1/2. 4,4-Dimethyl-4-silapentane-1-sulfonate (DSS) was used as internal standard for ^{1}H chemical shift referencing.

Cell surface binding. To estimate binding of purified Myc-SDI/II to APP, AJAP-1 and PIANP, cDNAs were transfected into tsA201 cells. After 2 days of cultivation, cells were incubated for 30 min at room temperature with SD1/2 in reduced serum OptiMEM® medium. Myc-SD1/2 was added to the medium to give a final concentration of 0.2 to 2000 nM. Cells were subsequently fixed in 4% PFA, blocked in 1% BSA and then incubated with mouse anti-c-Myc 9E10 (11667149001, Roche) to determine bound SD1/2 and goat anti-APP (sc-7498, Santa Cruz), sheep anti-AJAP-1 (AF7970, R&D Systems) or rat anti-HA (HA-PIANP) (clone 3F10, 11867423001, Roche), respectively, and detected with Alexa-conjugated secondary antibodies (Alexa Fluor® 488 donkey anti-goat IgG, Alexa Fluor® 488 donkey anti-rat IgG, Alexa Fluor® 555 donkey anti-mouse IgG all from Life Technologies). Average intensity values of bound and expressed proteins in individual cells using drawn region of interests around the perimeter of each cell were determined after background subtraction and put into ratio. For each measurement, $n = 3$–20 cells were used. Apparent dissociation constants (K_D values) were determined using a Hill equation with a coefficient of 1.

Electrophysiology. Three hundred μm-thick hippocampal slices were prepared with a Leica VT1200S vibratome from P12-P21 *APP$^{-/-}$*, *AJAP-1$^{-/-}$*, *PIANP$^{-/-}$* or WT littermate mice and incubated for 15 min at 32 °C in aCSF containing 126 mM NaCl, 26 mM NaHCO$_3$, 2.5 mM KCl, 1.25 mM NaH$_2$PO$_4$, 2 mM CaCl$_2$, 1 mM

MgCl₂, and 10 mM glucose. Slices were kept at room temperature until recording at 32 °C submerged in a recording chamber perfused with ACSF. CA1 pyramidal cells were visually identified using a ×60 objective under video infrared Nomarski optics with a BX51WI microscope (Olympus). Cell cultures were prepared from WT, *APP*⁻/⁻, or *GB1a*⁻/⁻ mice as described above. After 10–13 days in vitro, coverslips were transferred into a submerged chamber and perfused with aCSF at 32 °C. Whole-cell voltage-clamp recordings were obtained with 4–6 MΩ borosilicate glass pipettes via an intracellular solution containing 135 mM CsCH₃O₃S, 8 mM NaCl, 4 mM Mg-ATP, 0.3 mM Na₃-GTP, 0.1 mM TEA-Cl, 5 mM QX-314 and 10 mM HEPES. A liquid junctional potential of −10 mV was left uncorrected. Cells were voltage-clamped at −60 mV with a Multiclamp700B amplifier (Molecular Devices). Spontaneous mEPSCs were recorded in the presence of 0.2 μM TTX and 100 μM picrotoxin. EPSCs were evoked with extracellular monopolar current pulses generated by a custom-made isolated current stimulator and applied via a patch-pipette filled with aCSF and positioned to activate the Schaeffer Collateral pathway. All recordings were filtered at 4–10 kHz and digitized at 10–20 kHz with a Digidata 1550B digitizer (Molecular Devices).

BRET and [³⁵S]GTPγS binding assays. BRET experiments monitoring G protein activation were conducted and analyzed as described[24]. Mouse brain membranes for [³⁵S]GTPγS binding assays were prepared and analyzed as described[12].

Biotinylation assay. HEK293 cells were biotinylated using the Pierce Cell Surface Protein Isolation Kit (Pierce, 89881). Transfected HEK293 cells on 6-well plates were incubated with 1 mg/ml sulfo-NHS-SS-biotin (Pierce) in PBS for 30 min at 4 °C. After quenching the biotinylation reaction with 50 mM glycine and rinsing of the cells with ice-cold TBS (Tris-buffered saline) and PBS, cells were scrapped from the plates and lysed in NETN buffer (100 mM NaCl, 1 mM EDTA, 0.5% Nonidet P-40, 20 mM Tris/HCl, pH 7.4) supplemented with an EDTA-free protease inhibitor mixture (Roche). The lysate was incubated at 4 °C for 15 min then centrifuged 10,000 × *g* for 10 min at 4 °C and proteins in the supernatant quantified. Biotinylated surface proteins were purified using NeutrAvidin-agarose (Pierce), washed, and resuspended in protein loading buffer. Proteins were identified on immunoblots.

Immunofluorescence. Neurons on glass coverslips were fixed for 5 min in 4% PFA/4% sucrose at RT, permeabilized with PBS⁺/⁺ (D8662, Sigma, supplemented with 1 mM MgCl2 and 0.1 mM CaCl₂))/Triton-0.1%, blocked with PBS⁺/⁺/5% BSA and labeled with primary antibodies in PBS⁺/⁺ (D8662, Sigma) and 5% BSA for 2 h and secondary antibodies for 45 min. PBS⁺/⁺ washes were performed after each antibody incubation. Coverslips were mounted on glass slides in Fluoromount™ (F4680, Sigma). Images were captured using Zeiss LSM-700 system with a Plan-Apochromat 63 × /NA 1.40 oil DIC, using Zen 2010 software.

Primary antibodies used: mouse anti-GB1 (ab55051, Abcam), chicken anti-map2 (ab5392, Abcam), mouse anti-c-myc 9E10 (11667149001, Roche), mouse anti-piccolo (142111, Synaptic System), rabbit anti-KLC1 (ab187179, Abcam), rabbit anti-GFP (ab290, Abcam), mouse anti-flag M2 (F1804, Sigma), mouse anti-PSD-95 (ab2723, Abcam). Secondary antibodies used: Alexa Fluor® 647 donkey anti-chicken IgY (Millipore), Alexa Fluor® 555 donkey anti-mouse IgG (Life Technologies), Alexa Fluor® 488 donkey anti-rabbit IgG (Life Technologies), Alexa Fluor® 647 donkey anti-mouse IgG (Invitrogen), and Alexa Fluor® 568 donkey anti-rabbit IgG (Invitrogen).

TIRF microscopy and live confocal imaging. Transfected HEK293 cells were incubated for 15 min at 16 °C in the dark in PBS⁺/⁺ containing 3 μg/ml BTX conjugated to Alexa-488 (Thermo Scientific). Cells were washed three times with PBS⁺/⁺ at 16 °C and mounted on 37 °C incubator stages of a TIRF Olympus IX81 inverted Microscope equipped with a motorized TIRF system and an Apo N 60 × / NA 1.49 TIRF objective (Olympus, Japan). Excitation of GFP/Venus and mCherry was at 488 nm and 561 nm, respectively. Images were acquired with a Hamamatsu imagEM c9100–13 EMDCCD camera using Xcellence software (Olympus). TIRF measurements with transfected HEK293 cells was on 35 mm μ-Dishes, high Glass Bottom (Ibidi, Germany), in serum free DMEM/F-12 medium (Gibco 11320–074) (Fig. 7c and Supplementary Fig. 6b and 7b). Live confocal imaging was with a Zeiss point scanning confocal LSM-800 inverted microscope, using a heated stage and a 63 × /NA 1.4 Plan-Apochromat objective. Excitation was at 488 nm and 555 nm; images were collected at a rate of 1 frame/s (Fig. 7d, Supplementary Fig. 10a, Supplementary Movie 1).

Image analysis and quantification. Images were taken under identical acquisition parameters for all conditions within the experiment. Saturation was avoided by using image acquisition software to monitor intensity values. Images were analyzed by Fiji analysis software. For quantification, values were averaged over multiple neurons from at least three independent culture preparation. Pearson and Mander correlation coefficient statistics were used to analyze the colocalization between fluorophores using the JACoP plugin of Fiji.

Axon-to-dendrite (A:D) ratio of exogenous Myc-GB1a or Myc-GB1b protein were performed as described[13], using GFP as a volume marker and Fiji analysis

software. For rescue experiments, the neurons were co-transfected with either mCherry, APPmCherry or APLP-2mCherry (Fig. 4e). Kymographs for analysis of vesicle transport were created by drawing one-pixel-wide lines traced from the soma to the axon tip using the KimographBuilder plugin of Fiji. The trafficking velocities were obtained using the Velocity measurement tool. Episodes of directed vesicle movement are represented in kymographs as displacements in the anterograde or retrograde direction. Non-mobile episodes produce straight vertical lines with short horizontal displacements resulting from the "wiggling" of vesicles.

Aβ40 quantification. Transfected HEK293 cells were incubated with serum free DMEM/F-12 medium (Gibco 11320–074) for 24 h. After determining the total amount of protein in the supernatant the Wako II Aβ40 ELISA kit was used for Aβ40 quantification. For Aβ40 quantification in neurons, 1 × 10⁵ neurons from *GB1a*⁻/⁻, *GB1b*⁻/⁻ or WT littermate mice were incubated for 10 days in conditioned medium. In some experiments purified lentiviral particles (GeneCopoeia: 217LPP-Rn10234-Lv122 GFP-GB1a, 217LPP-Rn10298-Lv122 GFP-GB1b, 217LPP-EGFP-Lv242 GFP) were added at a concentration of 1 transforming unit per neuron after 3 days for 24 h in 200 μl conditioned medium, before adding 800 μl pre-warmed conditioned medium. After 10 days, the conditioned medium was cleared at 1000×*g* for 15 min at 4 °C and processed for Aβ40 quantification.

Statistical analysis. Data analysis was with GraphPad Prism version 7.0 (GraphPad Software, La Jolla, CA). Individual data sets were tested for normality with the Shapiro-Wilk or the D'Agostino-Pearson test (for *n* ≥ 8). Statistical significance of differences between two groups was assessed by unpaired two-tailed Student's *t*-test or ANOVA as indicated. For non-normal distribution the non-parametric Mann–Whitney test was used. *P*-values < 0.05 were considered significant. Data are presented as mean ± standard error of the mean (s.e.m.).

Reporting summary. Further information on experimental design is available in the Nature Research Reporting Summary linked to this article.

Data availability

Data supporting the findings of this study are available within the paper and in the Supplementary Information and Source Data files. The mass spectrometry proteomics data have been deposited to the ProteomeXchange Consortium via the PRIDE partner repository with the dataset identifier PXD012487.

References

1. Gassmann, M. & Bettler, B. Regulation of neuronal GABA_B receptor functions by subunit composition. *Nat. Rev. Neurosci.* **13**, 380–394 (2012).
2. Frangaj, A. & Fan, Q. R. Structural biology of GABA_B receptor. *Neuropharmacology* **136**, 68–79 (2018).
3. Guetg, N. et al. NMDA receptor-dependent GABA_B receptor internalization via CaMKII phosphorylation of serine 867 in GABA_{B1}. *Proc. Natl Acad. Sci. USA* **107**, 13924–13929 (2010).
4. Terunuma, M. et al. Prolonged activation of NMDA receptors promotes dephosphorylation and alters postendocytic sorting of GABA_B receptors. *Proc. Natl Acad. Sci. USA* **107**, 13918–13923 (2010).
5. Orts-Del'Immagine, A. & Pugh, J. R. Activity-dependent plasticity of presynaptic GABA_B receptors at parallel fiber synapses. *Synapse* **72**, e22027 (2018).
6. Chu, D. C., Penney, J. B. Jr. & Young, A. B. Cortical GABA_B and GABA_A receptors in Alzheimer's disease: a quantitative autoradiographic study. *Neurology* **37**, 1454–1459 (1987).
7. Iwakiri, M. et al. Changes in hippocampal GABA_BR1 subunit expression in Alzheimer's patients: association with Braak staging. *Acta Neuropathol.* **109**, 467–474 (2005).
8. Kang, J. Y. et al. Deficits in the activity of presynaptic γ-aminobutyric acid type B receptors contribute to altered neuronal excitability in fragile X syndrome. *J. Biol. Chem.* **292**, 6621–6632 (2017).
9. Thompson, S. E., Ayman, G., Woodhall, G. L. & Jones, R. S. Depression of glutamate and GABA release by presynaptic GABA_B receptors in the entorhinal cortex in normal and chronically epileptic rats. *Neurosignals* **15**, 202–215 (2006).
10. Borgkvist, A. et al. Loss of striatonigral GABAergic presynaptic inhibition enables motor sensitization in parkinsonian mice. *Neuron* **87**, 976–988 (2015).
11. Hannan, S., Wilkins, M. E. & Smart, T. G. Sushi domains confer distinct trafficking profiles on GABA_B receptors. *Proc. Natl Acad. Sci. USA* **109**, 12171–12176 (2012).

12. Vigot, R. et al. Differential compartmentalization and distinct functions of GABA$_B$ receptor variants. *Neuron* **50**, 589–601 (2006).
13. Biermann, B. et al. The sushi domains of GABA$_B$ receptors function as axonal targeting signals. *J. Neurosci.* **30**, 1385–1394 (2010).
14. Hannan, S., Gerrow, K., Triller, A. & Smart, T. G. Phospho-dependent accumulation of GABA$_B$Rs at presynaptic terminals after NMDAR activation. *Cell Rep.* **16**, 1962–1973 (2016).
15. Schwenk, J. et al. Modular composition and dynamics of native GABA$_B$ receptors identified by high-resolution proteomics. *Nat. Neurosci.* **19**, 233–242 (2016).
16. Valdes, V. et al. Endoplasmic reticulum sorting and kinesin-1 command the targeting of axonal GABA$_B$ receptors. *PLoS ONE* **7**, e44168 (2012).
17. Muller, U. C., Deller, T. & Korte, M. Not just amyloid: physiological functions of the amyloid precursor protein family. *Nat. Rev. Neurosci.* **18**, 281–298 (2017).
18. Selkoe, D. J. & Hardy, J. The amyloid hypothesis of Alzheimer's disease at 25 years. *EMBO Mol. Med.* **8**, 595–608 (2016).
19. Huang, Y. & Mucke, L. Alzheimer mechanisms and therapeutic strategies. *Cell* **148**, 1204–1222 (2012).
20. Yamada, S. & Nelson, W. J. Synapses: sites of cell recognition, adhesion, and functional specification. *Annu. Rev. Biochem.* **76**, 267–294 (2007).
21. Evdokimov, K. et al. Leda-1/Pianp is targeted to the basolateral plasma membrane by a distinct intracellular juxtamembrane region and modulates barrier properties and E-Cadherin processing. *Biochem. Biophys. Res. Commun.* **475**, 342–349 (2016).
22. Eggert, S., Thomas, C., Kins, S. & Hermey, G. Trafficking in Alzheimer's Disease: Modulation of APP Transport and Processing by the Transmembrane Proteins LRP1, SorLA, SorCS1c, Sortilin, and Calsyntenin. *Mol. Neurobiol.* **55**, 5809–5829 (2018).
23. Pettem, K. L. et al. The specific α-neurexin interactor calsyntenin-3 promotes excitatory and inhibitory synapse development. *Neuron* **80**, 113–128 (2013).
24. Turecek, R. et al. Auxiliary GABA$_B$ receptor subunits uncouple G protein βγ subunits from effector channels to induce desensitization. *Neuron* **82**, 1032–1044 (2014).
25. Pasciuto, E. et al. Dysregulated ADAM10-mediated processing of APP during a critical time window leads to synaptic deficits in Fragile X syndrome. *Neuron* **87**, 382–398 (2015).
26. Fogel, H. et al. APP homodimers transduce an amyloid-β-mediated increase in release probability at excitatory synapses. *Cell Rep.* **7**, 1560–1576 (2014).
27. Das, U. et al. Visualizing APP and BACE-1 approximation in neurons yields insight into the amyloidogenic pathway. *Nat. Neurosci.* **19**, 55–64 (2016).
28. Fu, M. M. & Holzbaur, E. L. JIP1 regulates the directionality of APP axonal transport by coordinating kinesin and dynein motors. *J. Cell Biol.* **202**, 495–508 (2013).
29. Das, U. et al. Activity-induced convergence of APP and BACE-1 in acidic microdomains via an endocytosis-dependent pathway. *Neuron* **79**, 447–460 (2013).
30. Chiba, K. et al. Quantitative analysis of APP axonal transport in neurons: role of JIP1 in enhanced APP anterograde transport. *Mol. Biol. Cell* **25**, 3569–3580 (2014).
31. Norstrom, E. M., Zhang, C., Tanzi, R. & Sisodia, S. S. Identification of NEEP21 as a β-amyloid precursor protein-interacting protein in vivo that modulates amyloidogenic processing in vitro. *J. Neurosci.* **30**, 15677–15685 (2010).
32. Bai, Y. et al. The in vivo brain interactome of the amyloid precursor protein. *Mol. Cell Proteom.* **7**, 15–34 (2008).
33. Muller, U. & Kins, S. APP on the move. *Trends Mol. Med.* **8**, 152–155 (2002).
34. Blein, S. et al. Structural analysis of the complement control protein (CCP) modules of GABA$_B$ receptor 1a: only one of the two CCP modules is compactly folded. *J. Biol. Chem.* **279**, 48292–48306 (2004).
35. Coburger, I. et al. Analysis of the overall structure of the multi-domain amyloid precursor protein (APP). *PLoS One* **8**, e81926 (2013).
36. Yamazaki, T., Selkoe, D. J. & Koo, E. H. Trafficking of cell surface β-amyloid precursor protein: retrograde and transcytotic transport in cultured neurons. *J. Cell Biol.* **129**, 431–442 (1995).
37. Simons, M. et al. Intracellular routing of human amyloid protein precursor: axonal delivery followed by transport to the dendrites. *J. Neurosci. Res.* **41**, 121–128 (1995).
38. Ring, S. et al. The secreted β-amyloid precursor protein ectodomain APPs α is sufficient to rescue the anatomical, behavioral, and electrophysiological abnormalities of APP-deficient mice. *J. Neurosci.* **27**, 7817–7826 (2007).
39. Craig, M. T., Mayne, E. W., Bettler, B., Paulsen, O. & McBain, C. J. Distinct roles of GABA$_{B1a}$- and GABA$_{B1b}$-containing GABA$_B$ receptors in spontaneous and evoked termination of persistent cortical activity. *J. Physiol.* **591**, 835–843 (2013).
40. Huo, Q. et al. Prefrontal cortical GABAergic dysfunction contributes to aberrant UP-state duration in APP knockout mice. *Cereb. Cortex* **27**, 4060–4072 (2017).
41. Lage, K. et al. A human phenome-interactome network of protein complexes implicated in genetic disorders. *Nat. Biotechnol.* **25**, 309–316 (2007).
42. Chen, M. et al. APP modulates KCC2 expression and function in hippocampal GABAergic inhibition. *eLife* **6**, e20142 (2017).
43. Wright, R. et al. Neuronal chloride regulation via KCC2 is modulated through a GABA$_B$ receptor protein complex. *J. Neurosci.* **37**, 5447–5462 (2017).
44. Buggia-Prevot, V. et al. A function for EHD family proteins in unidirectional retrograde dendritic transport of BACE1 and Alzheimer's disease Aβ production. *Cell Rep.* **5**, 1552–1563 (2013).
45. Kins, S., Lauther, N., Szodorai, A. & Beyreuther, K. Subcellular trafficking of the amyloid precursor protein gene family and its pathogenic role in Alzheimer's disease. *Neurodegener. Dis.* **3**, 218–226 (2006).
46. DeBoer, S. R., Dolios, G., Wang, R. & Sisodia, S. S. Differential release of β-amyloid from dendrite- versus axon-targeted APP. *J. Neurosci.* **34**, 12313–12327 (2014).
47. Vassar, R. et al. β-secretase cleavage of Alzheimer's amyloid precursor protein by the transmembrane aspartic protease BACE. *Science* **286**, 735–741 (1999).
48. Park, M. et al. Plasticity-induced growth of dendritic spines by exocytic trafficking from recycling endosomes. *Neuron* **52**, 817–830 (2006).
49. Puthiyedth, N., Riveros, C., Berretta, R. & Moscato, P. Identification of differentially expressed genes through integrated study of Alzheimer's disease affected brain regions. *PLoS ONE* **11**, e0152342 (2016).
50. Jo, S. et al. GABA from reactive astrocytes impairs memory in mouse models of Alzheimer's disease. *Nat. Med.* **20**, 886–896 (2014).
51. Benke, D. Mechanisms of GABA$_B$ receptor exocytosis, endocytosis, and degradation. *Adv. Pharmacol.* **58**, 93–111 (2010).
52. Thinakaran, G. & Koo, E. H. Amyloid precursor protein trafficking, processing, and function. *J. Biol. Chem.* **283**, 29615–29619 (2008).
53. Amatniek, J. C. et al. Incidence and predictors of seizures in patients with Alzheimer's disease. *Epilepsia* **47**, 867–872 (2006).
54. Ito, K. et al. Memantine reduces the production of amyloid-β peptides through modulation of amyloid precursor protein trafficking. *Eur. J. Pharmacol.* **798**, 16–25 (2017).
55. Froestl, W. et al. SGS742: the first GABA$_B$ receptor antagonist in clinical trials. *Biochem. Pharmacol.* **68**, 1479–1487 (2004).
56. Fairfax, B. P. et al. Phosphorylation and chronic agonist treatment atypically modulate GABA$_B$ receptor cell surface stability. *J. Biol. Chem.* **279**, 12565–12573 (2004).
57. Pagano, A. et al. C-terminal interaction is essential for surface trafficking but not for heteromeric assembly of GABA$_B$ receptors. *J. Neurosci.* **21**, 1189–1202 (2001).
58. Gassmann, M. et al. Redistribution of GABA$_{B1}$ protein and atypical GABA$_B$ responses in GABA$_{B2}$-deficient mice. *J. Neurosci.* **24**, 6086–6097 (2004).
59. Lorenzo, A. et al. Amyloid β interacts with the amyloid precursor protein: a potential toxic mechanism in Alzheimer's disease. *Nat. Neurosci.* **3**, 460–464 (2000).
60. Skarnes, W. C. et al. A conditional knockout resource for the genome-wide study of mouse gene function. *Nature* **474**, 337–342 (2011).
61. Brechet, A. et al. AMPA-receptor specific biogenesis complexes control synaptic transmission and intellectual ability. *Nat. Commun.* **8**, 15910 (2017).
62. Cox, J. & Mann, M. MaxQuant enables high peptide identification rates, individualized p.p.b.-range mass accuracies and proteome-wide protein quantification. *Nat. Biotechnol.* **26**, 1367–1372 (2008).
63. Bildl, W. et al. Extending the dynamic range of label-free mass spectrometric quantification of affinity purifications. *Mol. Cell Proteom.* **11**, M111–007955 (2012).
64. Gronenborn, A. M. et al. A novel, highly stable fold of the immunoglobulin binding domain of streptococcal protein G. *Science* **253**, 657–661 (1991).
65. Rule, G. S. & Hitchens, T. K. *Fundamentals of protein NMR spectroscopy.* (Springer, Dordrecht, The Netherlands 2006).
66. Kaech, S. & Banker, G. Culturing hippocampal neurons. *Nat. Protoc.* **1**, 2406–2415 (2006).

Acknowledgements

Author contributions

M.C.D., A.R., M.G., B.F., J.S., and B.B. designed research; M.C.D., A.R., A.S., P.D.R., M.S., S.F., T.F., T.L., R.T., M.C., V.B., W.B., D.B., and M.G. performed experiments; M.S. contributed important reagents and M.C.D., A.R., J.S., and B.B. wrote the paper with input from the other authors.

Additional information

SUPPLEMENTARY INFORMATION

Complex formation of APP with GABA$_B$ receptors links axonal trafficking to amyloidogenic processing

Margarita C. Dinamarca et al.,

a

b
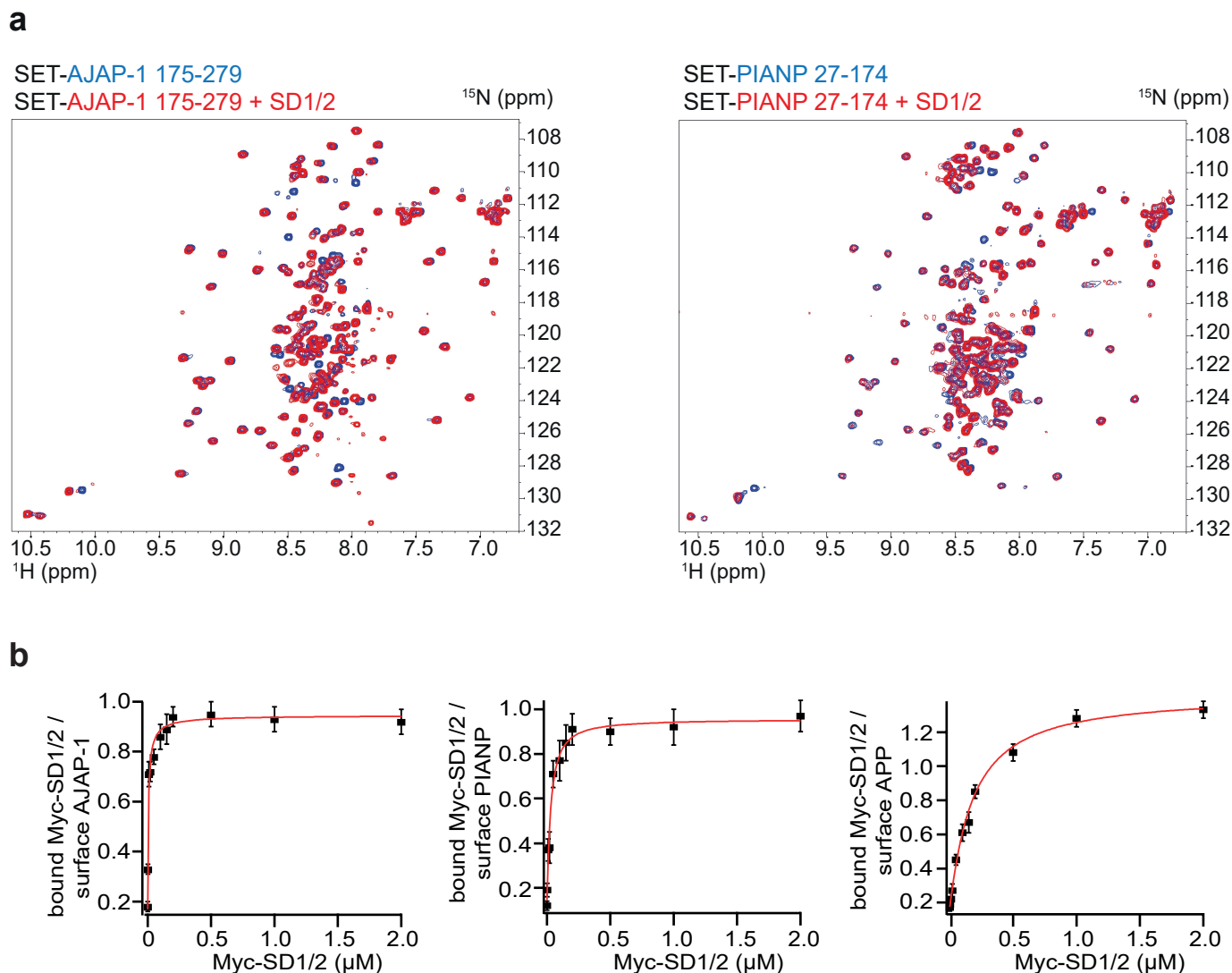
Supplementary Figure 1 AJAP-1, PIANP and APP interact with GB1a via a common WG motif. (**a**) ^{1}H-^{15}N heteronuclear single quantum coherence (HSQC) spectra show complex formation of ^{15}N labeled SET-AJAP-1 175-279 and SET-PIANP 27-174 with unlabeled SD1/2, which identifies a tryptophan-glycine (WG) motif as the central element of the binding interface. The cross peak of the sidechain NH of the respective W disappeared after complex formation with SD1/2. The cross peaks of the solubility enhancement tag (SET = 56-residue B1 domain of streptococcal protein G) were virtually unaffected by the interaction with SD1/2. (**b**) Binding of Myc-SD1/2 to cells expressing APP, AJAP-1 or PIANP was saturable. The estimated apparent dissociation constants (Kd) are 6.4 ± 2.4 nM for AJAP-1, 29.1 ± 5.5 nM for PIANP and 187.6 ± 27.9 nM for APP. Ratio calculated from 3-20 cells for each concentration and fitted by Hill equation with a coefficient of 1. Data are presented as mean ± s.e.m. Source data are provided as a Source Data file.
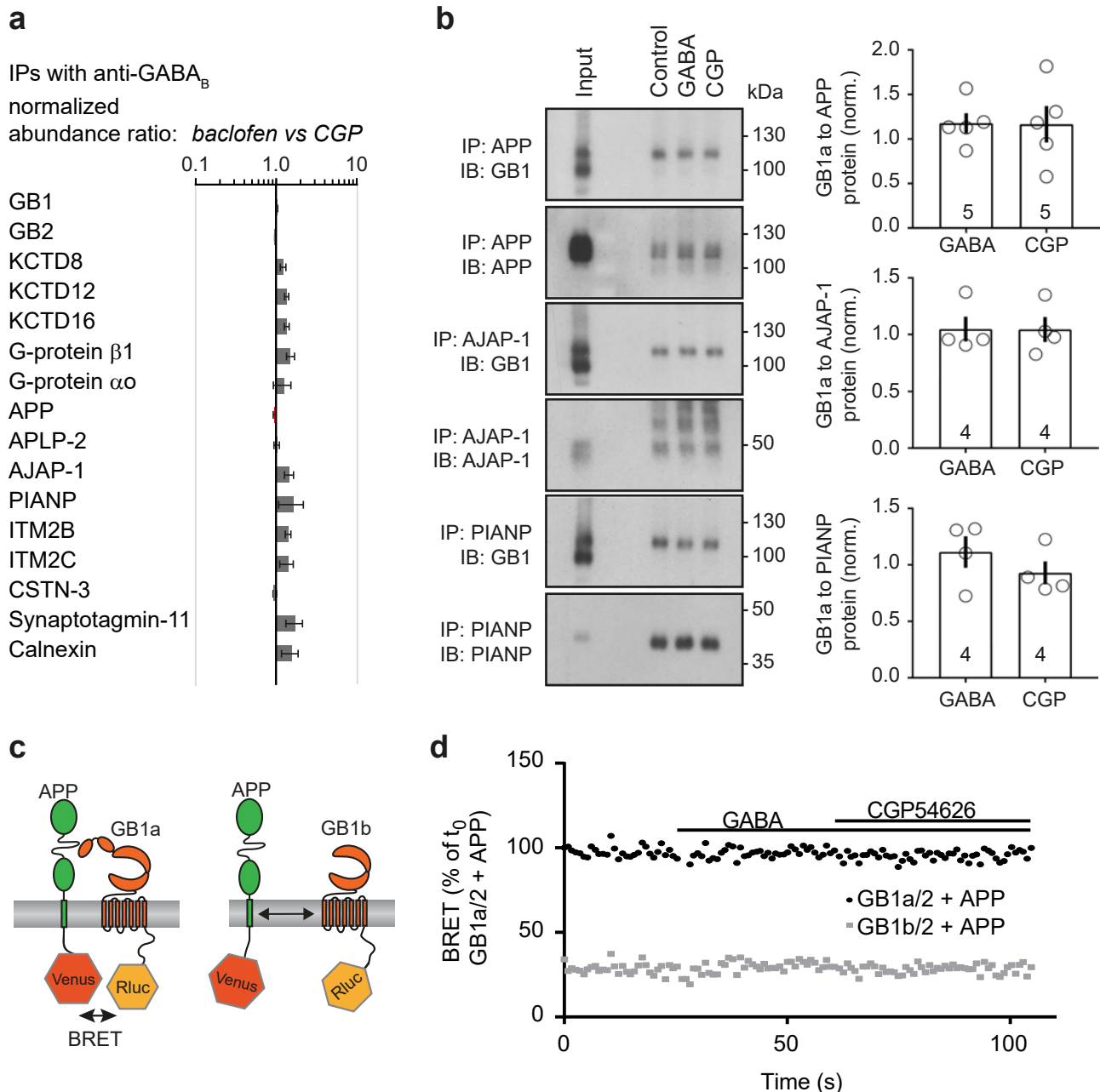
Supplementary Figure 2 GBR activity does not influence the interaction of AJAP-1, PIANP or APP with GB1a. (**a**) Proteomic analysis of native GBR complexes after receptor activation and blockade. Protein abundance ratios for GBR proteome constituents (n = 4 measurements, data are presented as mean ± s.e.m.) in GBR IPs from membrane fractions pre-incubated with baclofen or CGP54626 (normalized to GB1/2). Proteins were solubilized before IP with the intermediate stringency detergent CL91. GBR activity did not influence binding of GB1a-specific interactors (marked in gray). (**b**) Left: Activation or blockade of GBRs with GABA (1 mM) or CGP54626 (CGP, 4 μM), respectively, for 1 hour at room temperature in non-solubilized brain membrane fragments did not significantly alter the amount of GB1a protein co-immunoprecipitating with APP, AJAP-1 or PIANP. IPs from untreated membrane fragments served as controls. Right: Bar graphs summarizing the densitometric quantification of co-immunoprecipitated GB1a protein relative to the immun-precipitated protein. GB1a/APP: control 1.0, GABA 1.18 ± 0.25, CGP 1.17 ± 0.46; GB1a/AJAP-1: control 1.0, GABA 1.05 ± 0.22, CGP 1.04 ± 0.22; GB1a/PIANP: control 1.0, GABA 1.11 ± 0.28, CGP 0.93 ± 0.20 ($P > 0.05$, Tukey's multiple comparison test). Values normalized to control (100%). n = 4-5 mice. Data are presented as mean ± s.e.m. (**c**) Scheme depicting that complex formation between APP-Venus and GB1a-Rluc leads to BRET. GB1b-Rluc serves as a negative control. (**d**) GABA (1 mM) and CGP54626 (25 μM) did not alter BRET between APP-Venus and GB1a-Rluc in HEK293 cells co-transfected with GB2. Representative traces from 3 independent experiments in quadruplicates are shown. Source data are provided as a Source Data file.
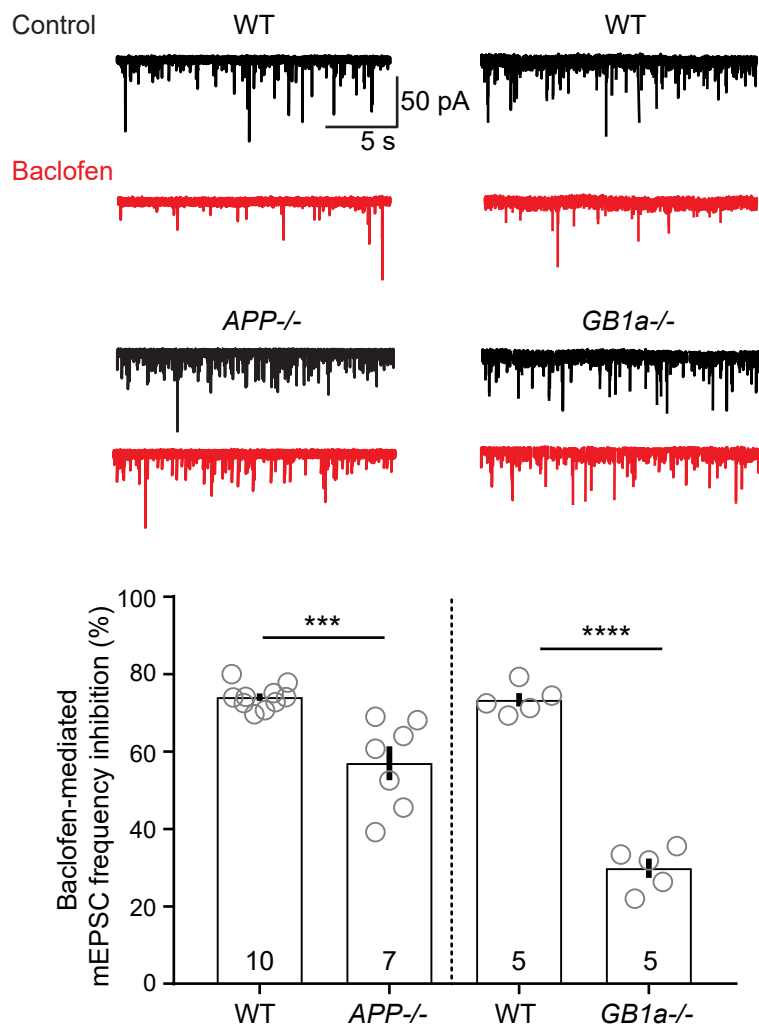
Supplementary Figure 3 Top: Representative mEPSC recordings under baseline conditions (control, black) and during 50 μM baclofen application (red) in cultured days-in-vitro 10 (DIV10) hippocampal neurons of $APP^{-/-}$, $GB1a^{-/-}$ and WT littermate mice. Bottom: Bar graphs showing that the baclofen-mediated decrease in mEPSC frequency is blunted in $APP^{-/-}$ (WT: 74.07 ± 0.98%, $APP^{-/-}$: 57.01 ± 4.37%; *** $P < 0.001$, unpaired Student's t-test) and $GB1a^{-/-}$ neurons (WT: 73.4 ± 1.7%, $GB1a^{-/-}$: 29.8 ± 2.5%; **** $P < 0.0001$, unpaired Student's t-test) compared to WT neurons. Data are presented as mean ± s.e.m. Source data are provided as a Source Data file.
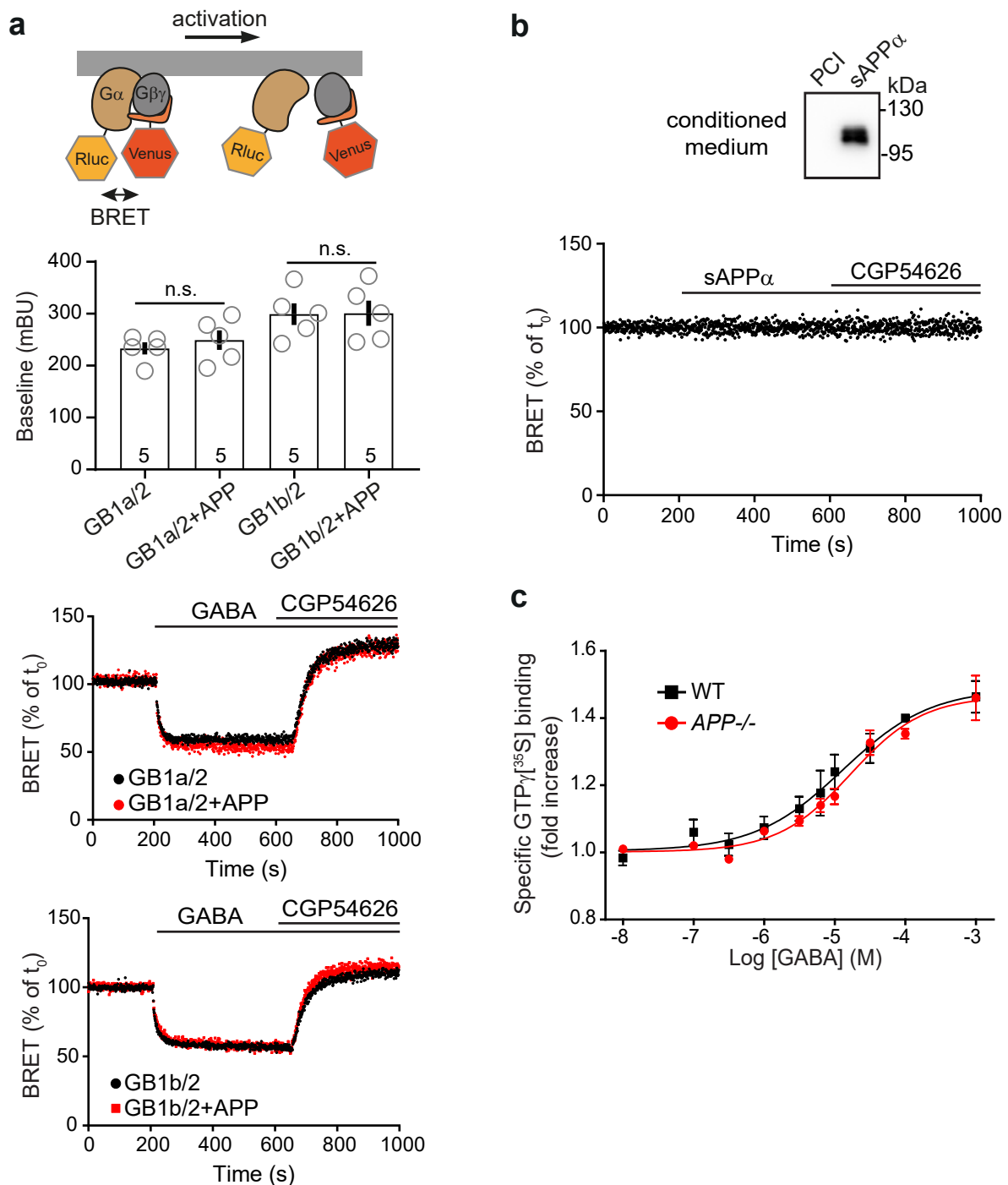
Supplementary Figure 4 APP does not influence receptor-induced G-protein activation. (**a**) Top: Scheme showing that conformational changes during G-protein activation reduce BRET between Gαo-Rluc and Venus-Gγ2. Bottom: Bar graphs indicate that APP does not influence baseline BRET in the presence of GB1a/2 or GB1b/2 receptors ($P > 0.05$, one-way ANOVA). GABA (1 mM) induced changes in BRET in HEK293 cells expressing GB1a/2 or GB1b/2 together with Gαo-Rluc, Venus-Gγ2 and Gβ2, in the presence or absence of APP. After receptor blockade with the antagonist CGP54626 (25 µM) the heterotrimeric G protein re-associates and BRET increases. Receptor activation in the presence and absence of APP induced similar BRET changes. Single experiments carried out in parallel are shown (n = 3 independent experiments). (**b**) Immunoblot analysis of conditioned medium of HEK293 cells expressing sAPPα (APP amino acid residues 1–612). Conditioned medium of HEK293 cells transfected with the PCI vector served as a control. Conditioned medium was collected 48h post-transfection and secreted sAPPα detected using the αAPP antibody 22c11. BRET measurements with transfected HEK293 cells expressing GB1a/2 receptors together with Gαo-Rluc, Venus-Gγ2 and Gβ2 reveal no changes in BRET in response to sAPPα-conditioned medium and the receptor antagonist CGP54626 (25 µM). (**c**) [^{35}S]-GTPγS binding to brain membrane preparations of *APP*$^{-/-}$ (red circles) or control WT littermate mice (black squares) upon stimulation with increasing concentrations of GABA. Data are presented as mean ± s.e.m. Source data are provided as a Source Data file.
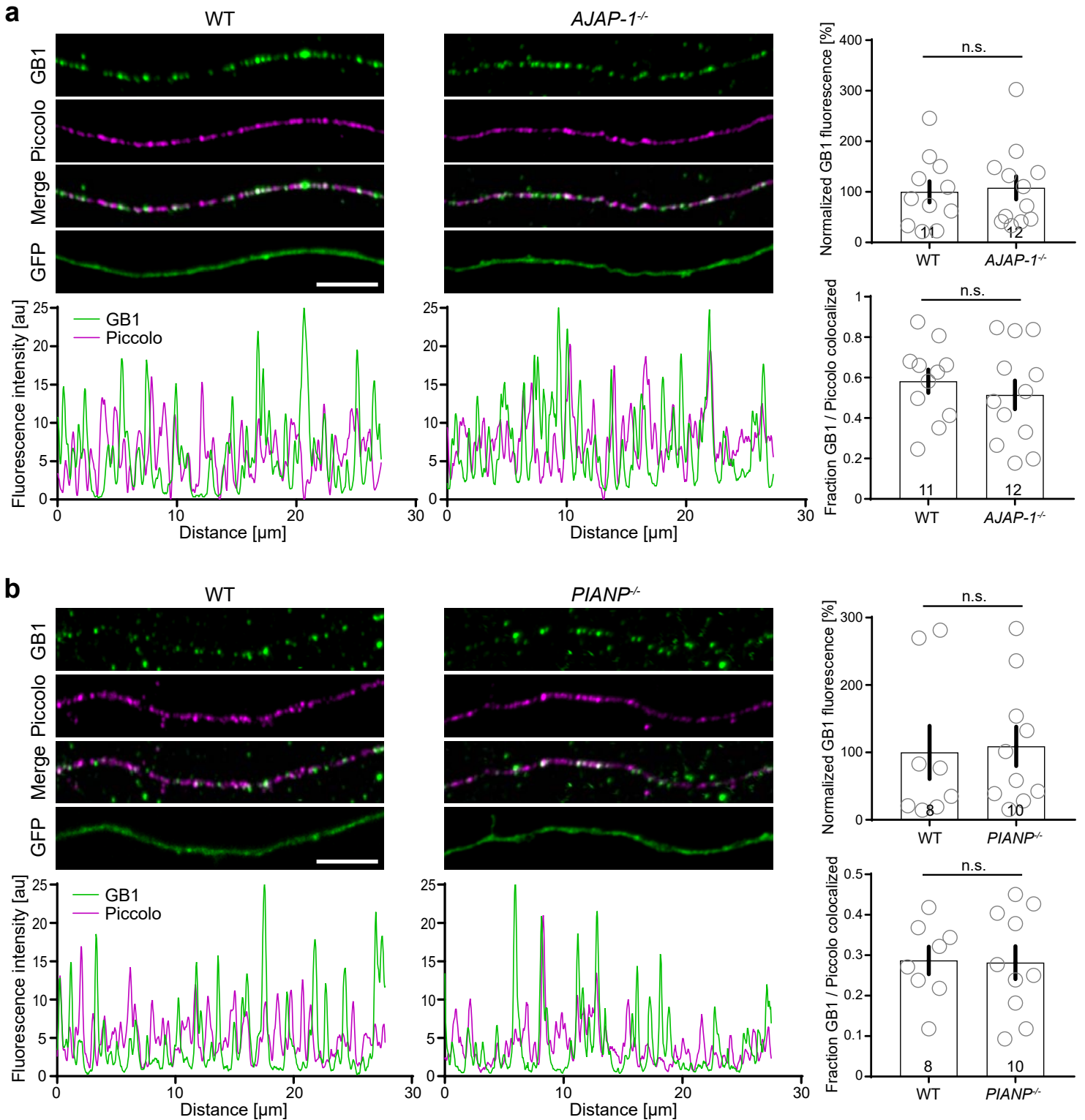
Supplementary Figure 5 Normal axonal GBR expression in *AJAP-1*^{-/-} and *PIANP*^{-/-} mice. (**a**) Top: Immunofluorescence of endogenous GB1 protein in axons of hippocampal *AJAP-1*^{-/-} and WT littermate neurons. Neurons expressing GFP were fixed at DIV10, permeabilized, and immunostained for endogenous GB1 protein (green) and the presynaptic marker piccolo (magenta). GFP served as a volume marker. Merged images show GB1 and piccolo co-localization. Bottom: Intensity grey value profile graphs of GB1 (green) and piccolo (magenta). Normalized GB1 fluorescence refers to the GB1 immunofluorescence intensity normalized to the GFP fluorescence intensity. $P > 0.05$, unpaired t-test. Scale bar 5 μm. (**b**) Immunofluorescence of endogenous GB1 protein in axons of hippocampal *PIANP*^{-/-} and WT littermate neurons. Analysis as in (**a**). Data are presented as mean ± s.e.m. Source data are provided as a Source Data file.
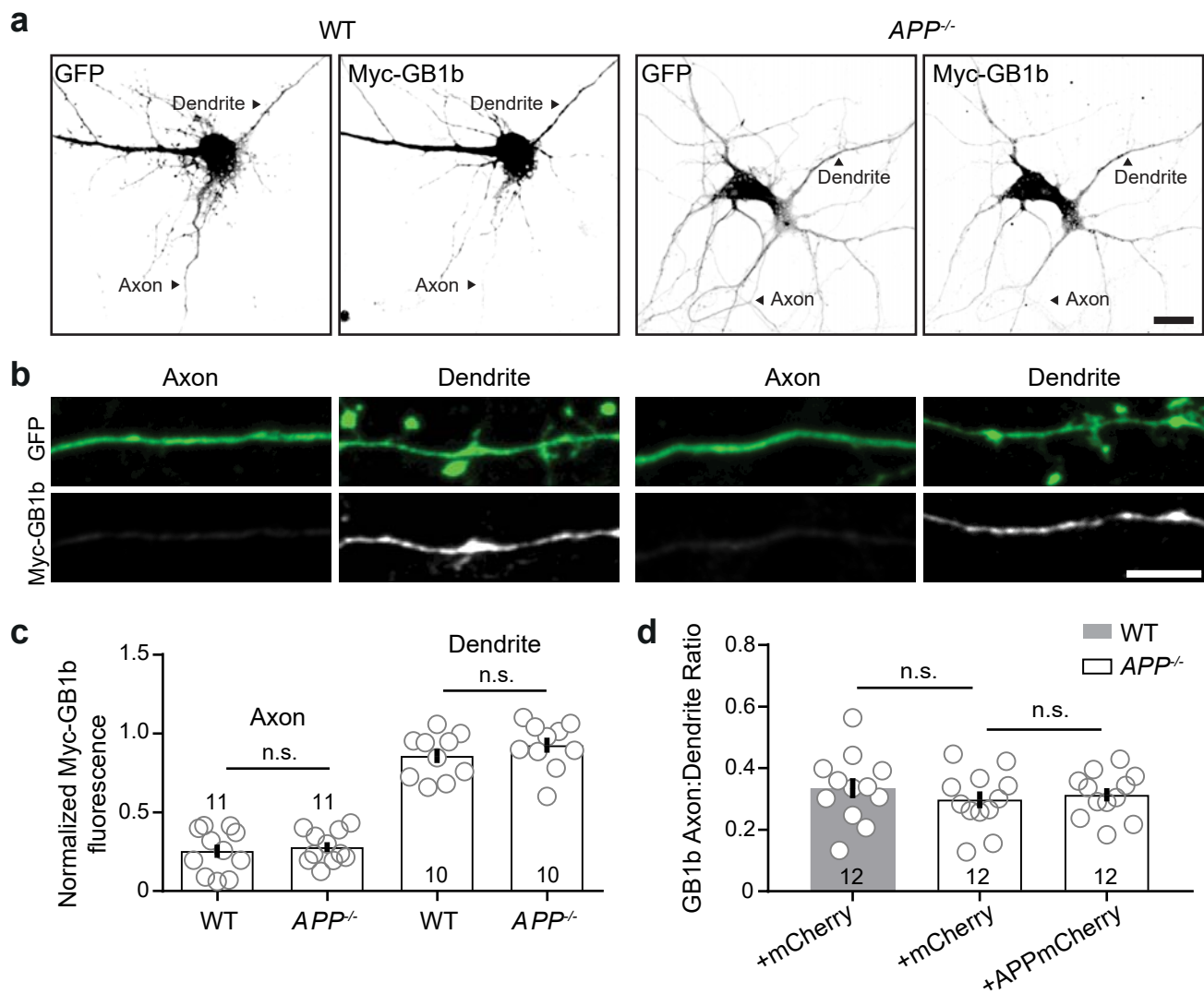
Supplementary Figure 6 APP does not influence Myc-GB1b distribution in cultured hippocampal neurons. (**a**) Representative images of neurons co-expressing Myc-GB1b and GFP in $APP^{-/-}$ and control WT littermate mice. Transfected neurons were fixed at DIV10, permeabilized, and stained with anti-Myc antibodies. Scale bar 10 μm. (**b**) Higher magnification images of the Myc-GB1b and GFP distribution in distal axons and dendrites of $APP^{-/-}$ and WT neurons. Note that Myc-GB1b is present in dendrites but not axons. Scale bar 5 μm. (**c**) Bar graphs showing the normalized Myc-GB1b fluorescence in axons and dendrites of transfected WT or $APP^{-/-}$ neurons. Normalized fluorescence refers to the Myc-Gb1b immunofluorescence intensity normalized to the GFP fluorescence intensity (Axon: WT, 0.25 ± 0.04, $n = 11$, $APP^{-/-}$, 0.28 ± 0.03, $n = 11$, $P > 0.05$, unpaired t-test; Dendrite: WT, 0.86 ± 0.04, $n = 10$, $APP^{-/-}$, 0.93 ± 0.04, $n = 10$, $P > 0.05$, unpaired t-test). (**d**) A:D ratio of Myc-GB1b in $APP^{-/-}$ and WT neurons transfected with Myc-GB1b in the presence of mCherry and APPmCherry (DIV10). Note that APPmCherry does not promote axonal localization of Myc-GB1b. $P > 0.05$, one-way ANOVA. Data are presented as mean ± s.e.m. Source data are provided as a Source Data file.
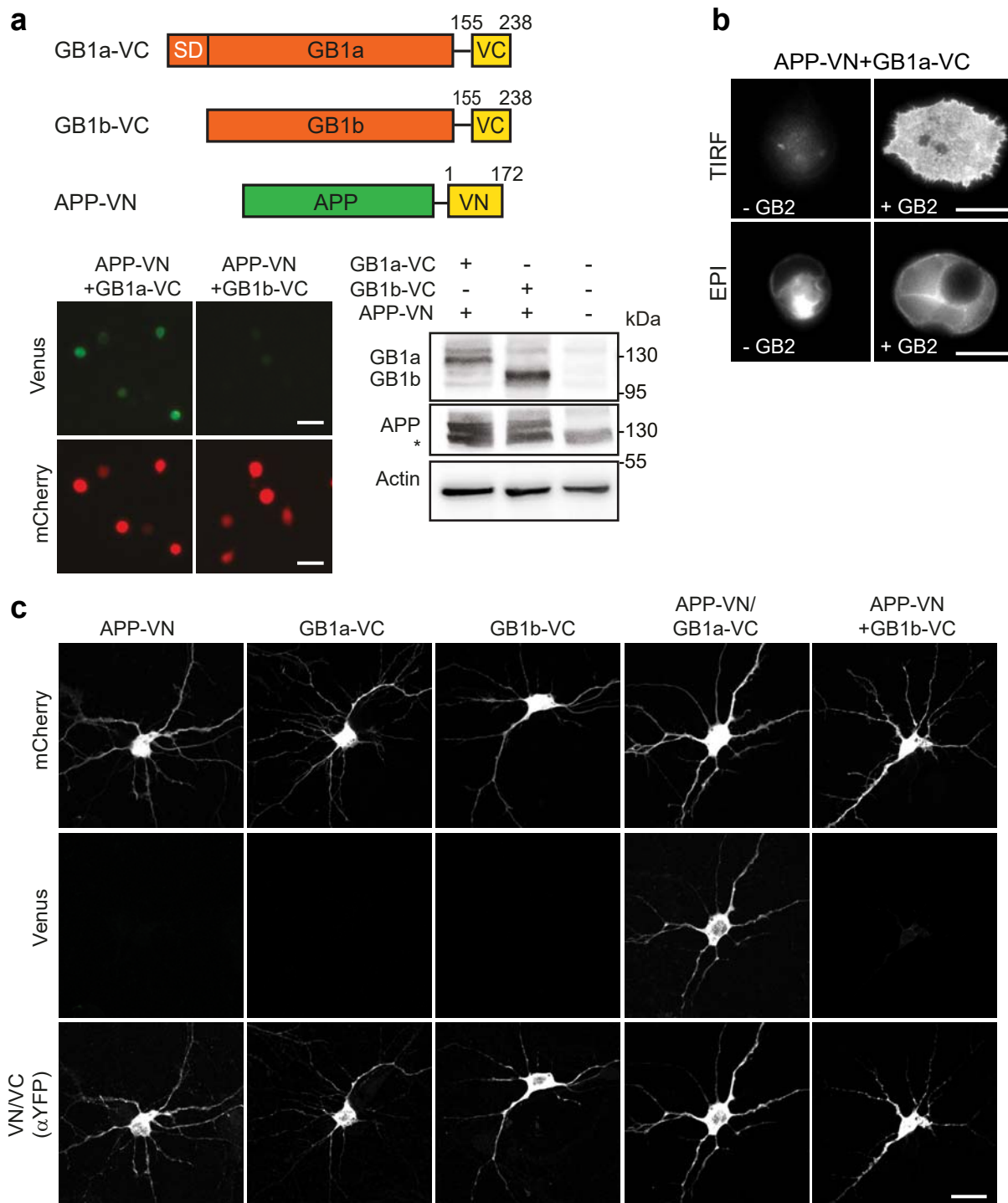
Supplementary Figure 7 The APP-VN/GB1a-VC complex leads to BiFC in transfected HEK293 cells and cultured hippocampal neurons. (**a**) A scheme describing the BiFC constructs is shown on the left. Numbers denote amino-acid residues in Venus. SD, sushi domains; VC, Venus C-terminal domain; VN, Venus N-terminal domain. Images show HEK293 cells expressing GB1a-VC or GB1b-VC together with APP-VN and mCherry as a transfection marker. Cells were analyzed for BiFC of Venus (green) 7-8 hours post-transfection. BiFC with APP-VN is observed for GB1a-VC but not for GB1b-VC. Immunoblotting confirms that cells express similar amounts of GB1a-VC and GB1b-VC. The asterisk indicates endogenous APP. Scale bar 40 µm. (**b**) Representative TIRF and epifluorescence (EPI) images of HEK293 cells expressing GB1a-VC and APP-VN with or without GB2 show that APP/GB1a complexes require GB2 for surface expression. Scale bar 10 µm. (**c**) Expression of GB1a-VC, GB1b-VC and APP-VN alone or in combination in cultured hippocampal neurons. Soluble mCherry served as a volume marker. Neurons were fixed 7-8 hours post-transfection and immunostained with a polyclonal anti-GFP antibody that detects both VC and VN. Note that VC and VN by themselves exhibit no fluores-cence. Scale bar 20 µm. Source data are provided as a Source Data file.
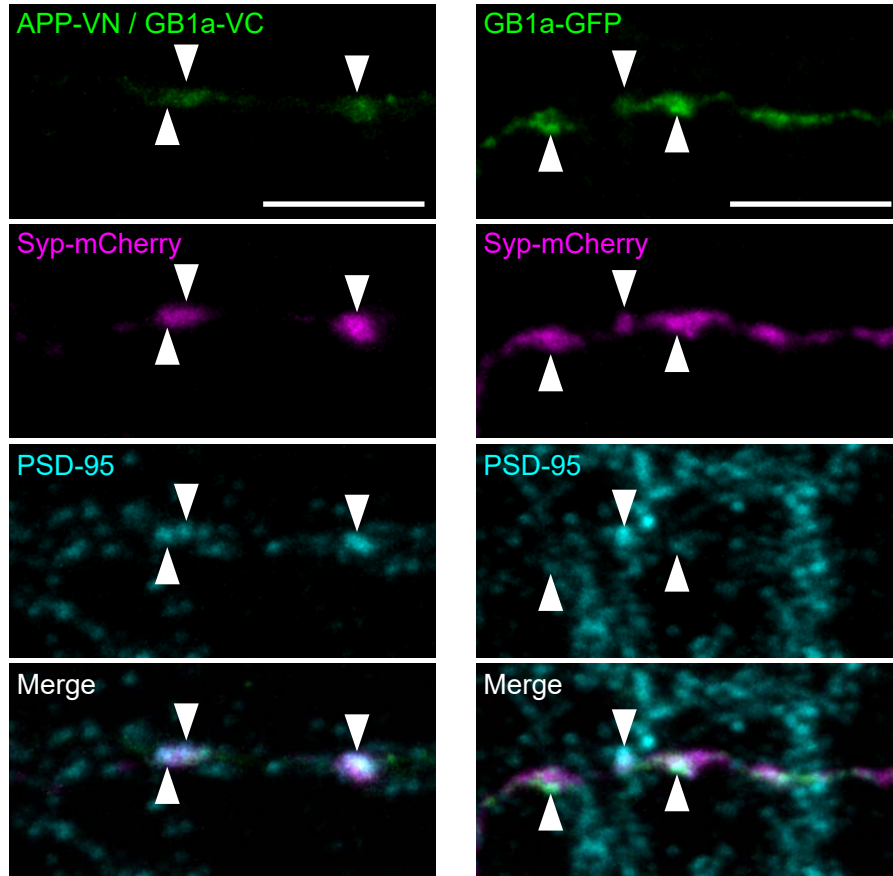
Supplementary Figure 8 The APP-VN/GB1a-VC complex and GB1a-GFP localize to synaptic boutons. Cultured hippocampal neurons were transfected with either APP-VN/GB1a-VC (BiFC) or GB1a-GFP together with Synaptophysin-mCherry. Neurons were fixed at DIV14 and immunolabeled for PSD-95. Synaptic boutons were identified by Synaptophysin-mCherry fluorescence apposed to PSD-95 puncta. Fluorescence for both the APP-VN/GB1a-VC complex and GB1a-GFP were detected at synaptic boutons (arrowheads). Scale bars 5 μm.
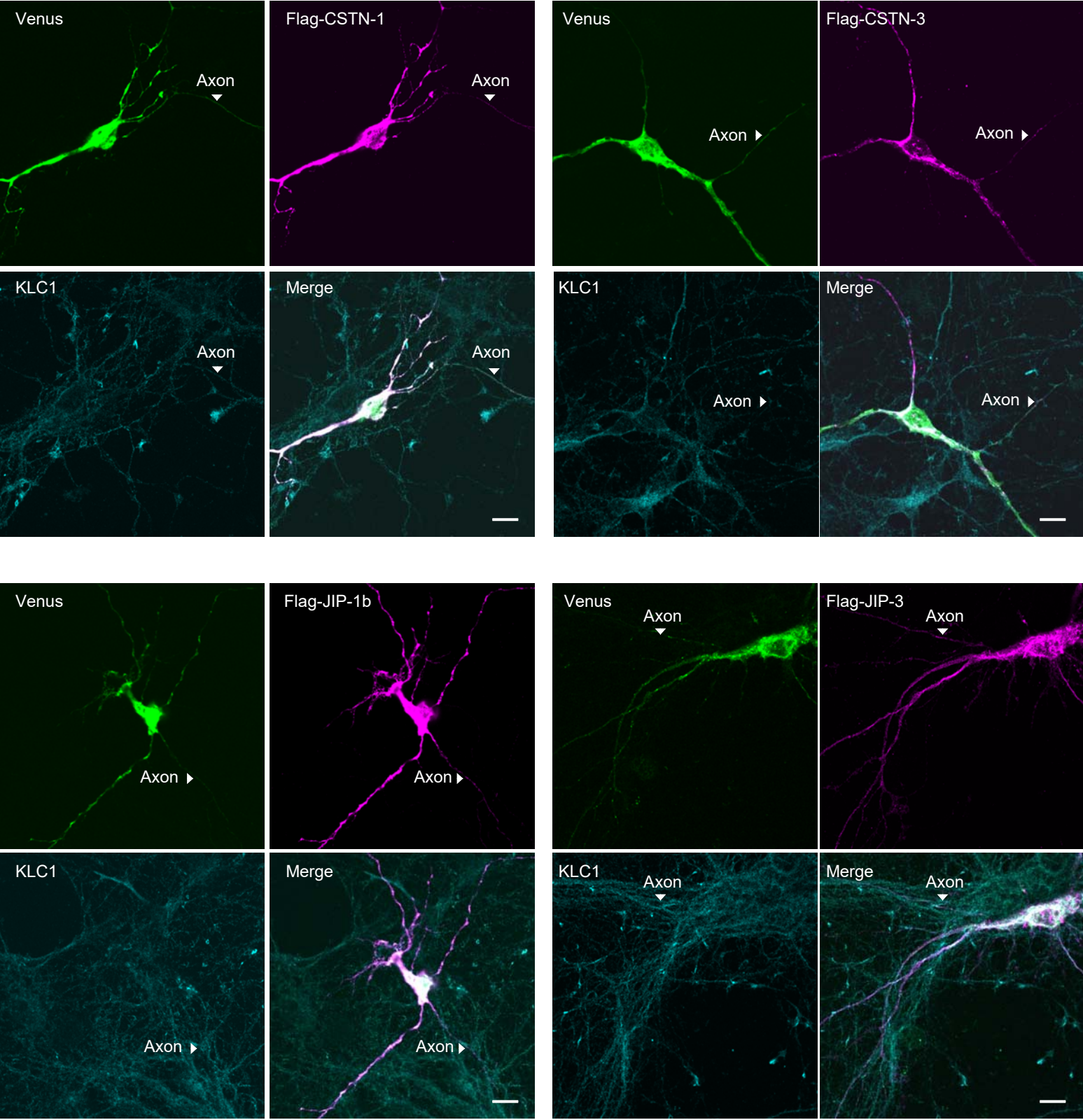
Supplementary Figure 9 The APP-VN/GB1a-VC BiFC complex (green) partly colocalizes with CSTN and JIP in neurons. Co-localization (white, arrowheads) of the APP-VN/GB1a-VC BiFC complex (green) with FLAG-CSTN-1, FLAG-CSTN-3, FLAG-JIP-1b and FLAG-JIP-3 (cyan) and the endogenous kinesin light-chain 1 (KLC1) (blue) in transfected neurons. Note that KLC1 is expressed in axons and dendrites. Scale bar 10 μm. Higher magnification images of axons are shown in **Fig 5c**.
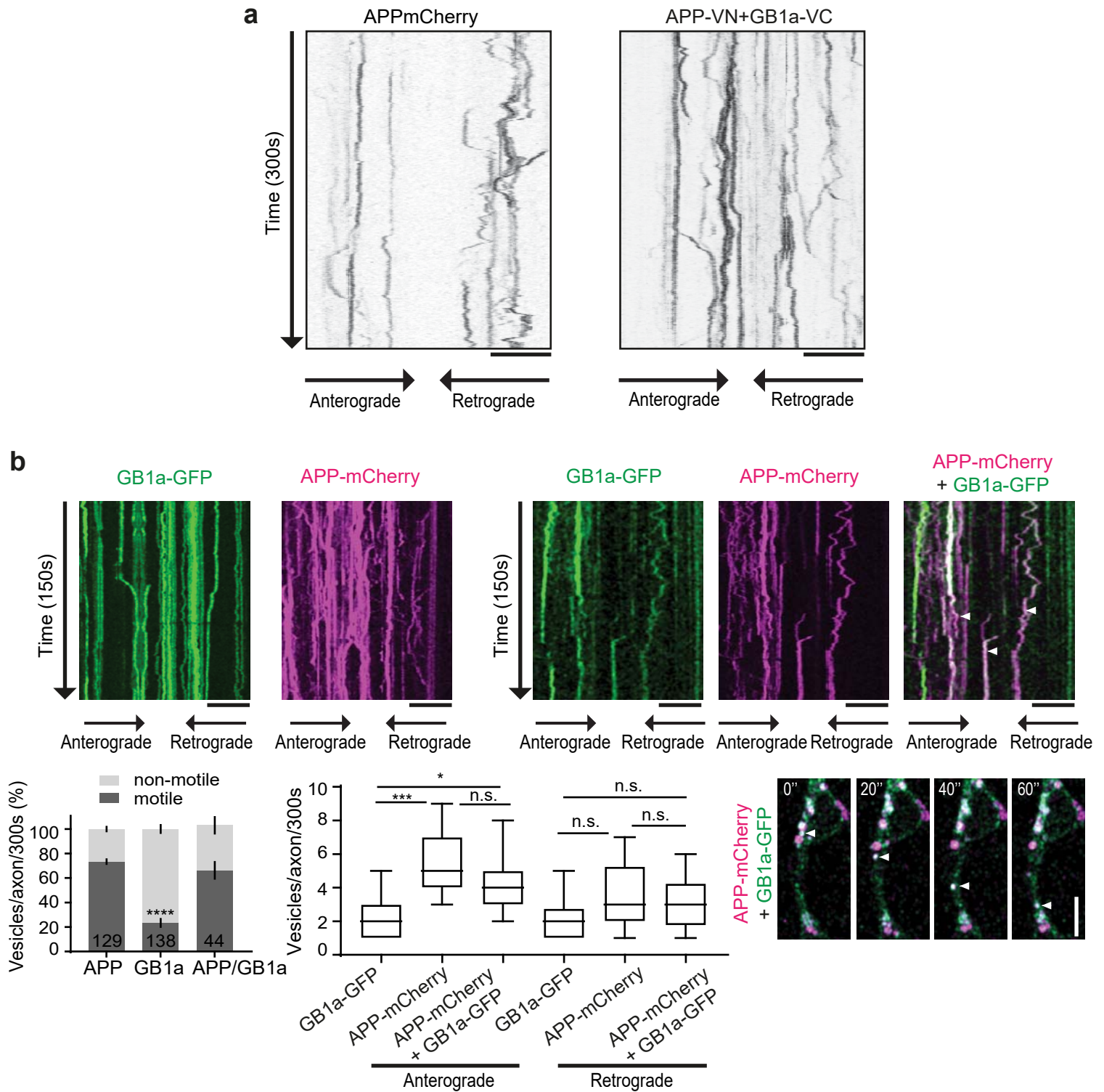
Supplementary Figure 10 Axonal trafficking of APP, GB1a and APP/GB1a complexes in cultured hippocampal neurons. (**a**) Representative kymographs of fluorescent vesicles in axons expressing APPmCherry or APP-VN/GB1a-VC BiFC complexes. Confocal imaging was 12 hours posttransfection at DIV 7 (1 frame/sec). (**b**) Kymographs of vesicles in axons of cultured hippocampal neurons expressing GB1a-GFP, APPmCherry or both. Overlay of kymographs from axons coexpressing GB1a-GFP and APPmCherry identifies APPmCherry/GB1a-GFP complexes (arrowheads). Likewise, time-lapse imaging of axons co-expressing GB1a-GFP and APPmCherry identifies mobile APPmCherry/GB1a-GFP vesicles (arrowheads, acquisition times in seconds). TIRF imaging was 24 hours post-transfection at DIV8. Bar graphs show that fewer GB1a-GFP than APPmCherry or APPmCherry/GB1a-GFP vesicles are mobile. Data are presented as mean ± s.e.m. The number of vesicles moving antero- and retrogradely per axons within 5 min are shown in a min to max - box and whisker plot, with whiskers representing the smallest and largest values, the boxes representing the 25% - 75% percentile and the middle line representing the median. Statistical analysis one-way ANOVA. Scale bars 25 μm. Source data are provided as a Source Data file.
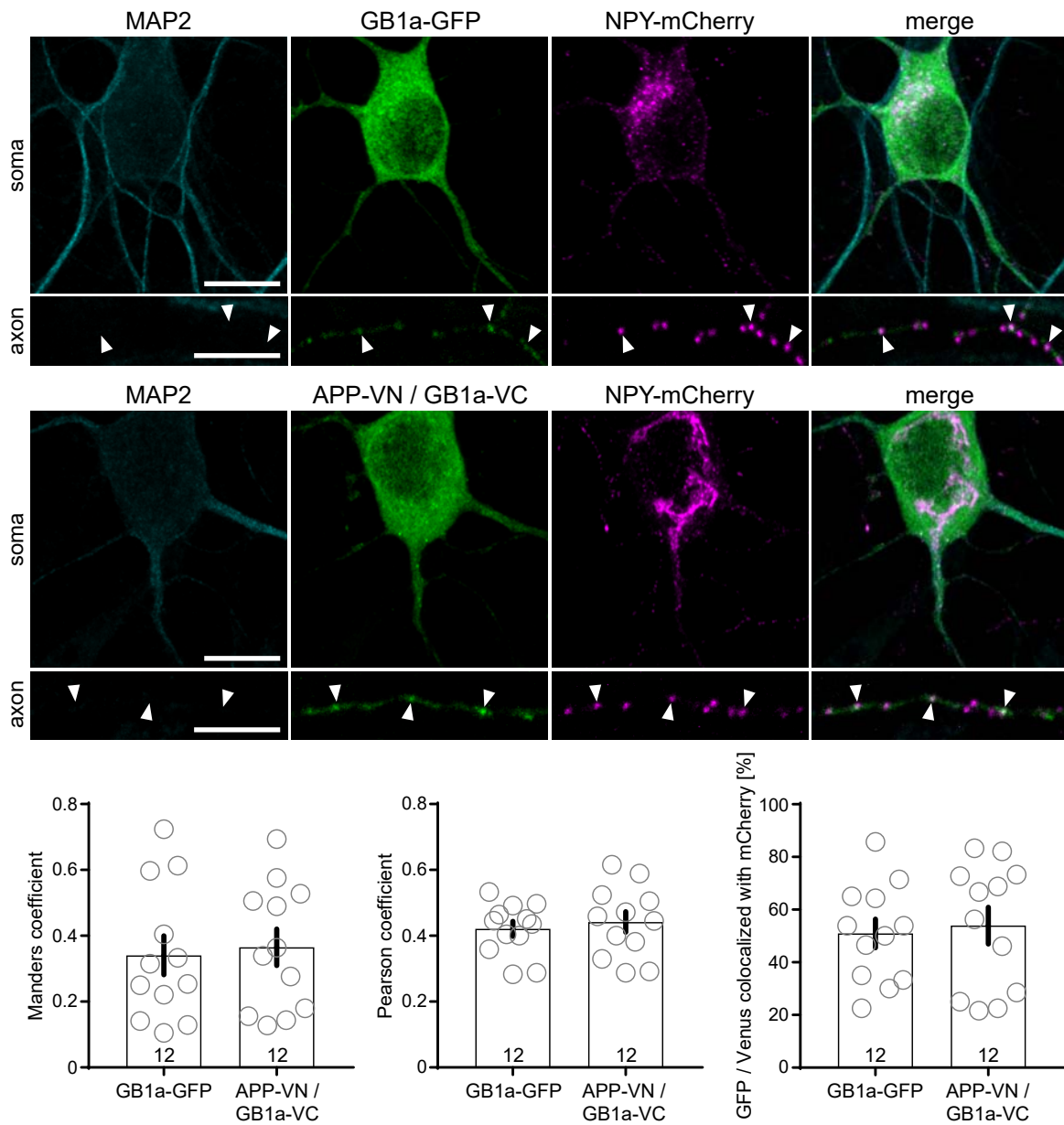
Supplementary Figure 11 NPY-mCherry positive vesicles convey GB1a-GFP and APP-VN/ GB1a-VC protein in axons. Hippocampal neurons were transfected at DIV5 and imaged at DIV6. Arrowheads indicate co-localization of NPY-mCherry with GB1a-GFP or APP-VN/GB1a-VC (BiFC). Scale bars 10 μm (top), 5 μm (bottom). Bar graphs indicate the percentage of GB1a-GFP and APP-VN/GB1a-VC positive vesicles that contain NPY-mCherry, as well as the Mander's and Pearson coefficients for co-localization with NPY-mCherry. Data are presented as mean ± s.e.m. Source data are provided as a Source Data file.

a

Myc-ADAM10	-	+	+	-	-	
Myc-BACE1	-	-	-	+	+	
Flag-GB1a	-	-	+	-	+	
GB2-YFP	-	-	+	-	+	
APP	+	+	+	+	+	kDa

APP-FL — -130

APP-βCTF / APP-αCTF — -17

Myc — -95 / -72

GADPH — -36

b

	Input				IP: anti-APP				
APP	-	+	+	+	-	+	+	+	
Flag-GB1a	+	+	-	+	+	+	-	+	
Myc-BACE1	+	+	+	-	+	+	+	-	kDa

APP — -95

Flag — -130

Myc — -72 / -55
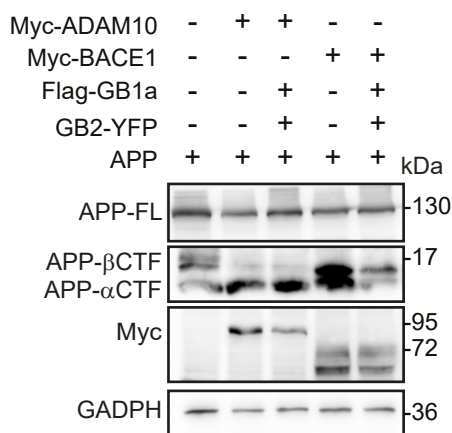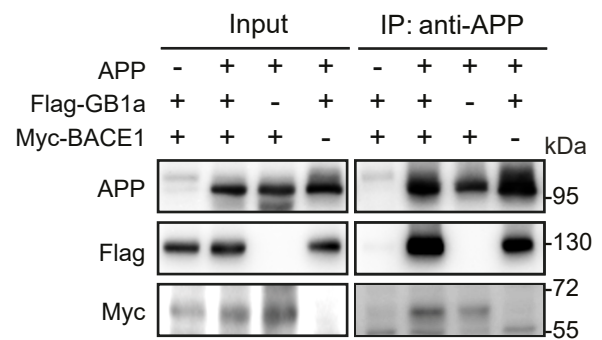
Supplementary Figure 12 GB1a/2 receptors neither prevent interaction of APP with BACE1 nor influence ADAM10 activity. (**a**) Immunoblots of HEK293 expressing APP with or without GB1a/2 receptors together with Myc-BACE1 or Myc-ADAM10. GB1a/2 reduces BACE1 but not ADAM10 proteolysis. APP full length, APP-FL; β-carboxy-terminal fragment of APP, APP-βCTF; α-carboxy-terminal fragment of APP, APP-αCTF. Glyceraldehyde 3-phosphate dehydrogenase (GADPH) served as a loading control. (**b**) Immunoblot of the co-IP of Myc-BACE1 with APP in the presence or absence of Flag-GB1a from transfected HEK293 cells. Note that GB1a does not prevent binding of BACE1 to APP. Source Data are provided as a Source Data file.
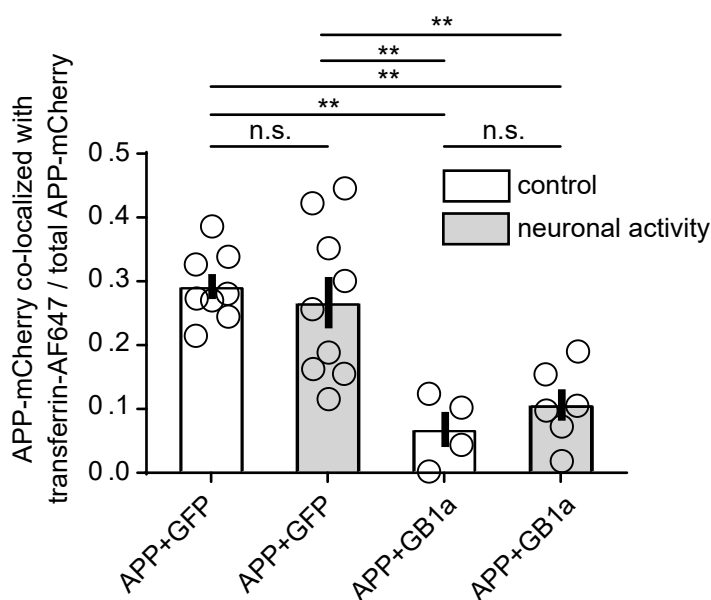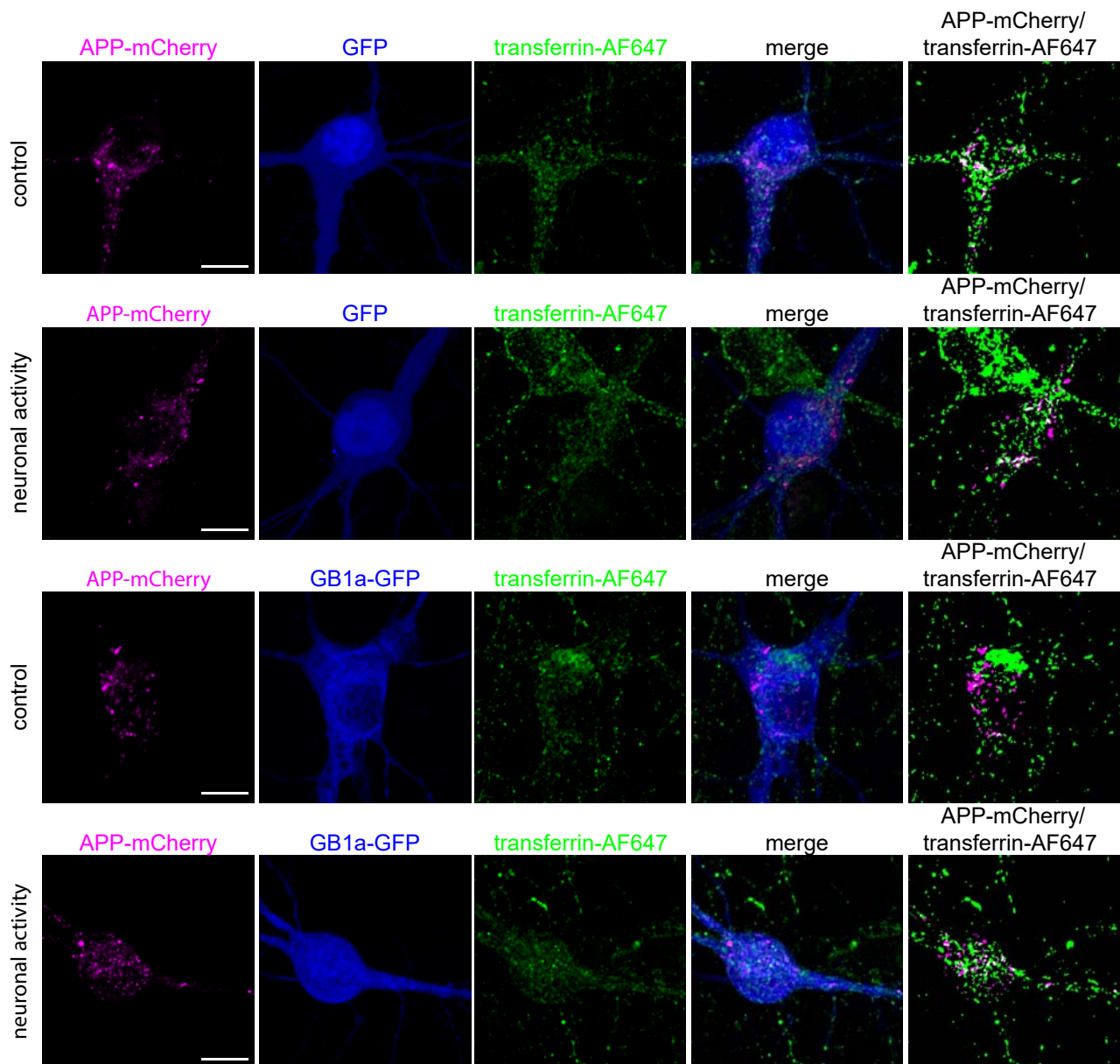
Supplementary Figure 13 Expression of GB1a-GFP in cultured hippocampal neurons decreases localization of APP-mCherry in early endosomes. Transfected hippocampal neurons were incubated with transferrin-AF647 at DIV14 to determine co-localization of APP-mCherry with transferrin-AF647 positive endosomes. Neuronal activity was elicited in parallel cultures using 20 μM bicuculline and 200 μM glycine. GB1a-GFP significantly decreased the presence of APP-mCherry in transferrin-AF647 positive endosomes. Neuronal activity did not significantly alter endosomal localization of APP-mCherry, both in the presence and absence of GB1a-GFP. Binary images indicate the fraction of APP-mCherry (magenta) present in early endosomes (green) as white regions. Scale bars 10 μm. Bar graphs indicate the ratio of APP-mCherry to total APP-mCherry in early endosomes. Statistical analysis was performed with one-way ANOVA and Tukey's multiple comparison test. **$P < 0.01$, $n = 4 - 9$ neurons. Data are presented as mean ± s.e.m. Source data are provided as a Source Data file.

7   Secreted amyloid-β precursor protein peptide does not regulate GABA_B receptor activity

<u>Pascal Dominic Rem</u>, Vita Sereikaite, Txomin Lalanne, Diego Fernandez-Fernandez, Thorsten Fritzius, Yang, Jochen Schwenk, Bernd Fakler, Martin Gassmann, Philippe Rondard, Jean-Philippe Pin, Kristian Strømgaard, Bernhard Bettler

Personal contribution

The experiments of this work were designed, performed and analyzed predominantly by myself. I further designed and created all figures and I contributed to writing the figure legend, material and methods, and the manuscript in its present form. This work was realized in collaboration with Vita Sereikaite, who generated tetramethylrhodamine (TMR)-labeled APP17 and scrambled-APP17 (sc-APP17) and performed isothermal calorimetric titration experiments, Txomin Lalanne & Diego Fernandez-Fernandez, who contributed electrophysiological recordings of mEPSCs and Kir3 currents, respectively, Daniel Ulrich, who analyzed neuronal activity in acute brain slices by measuring Calcium spikes, and Thorsten Fritzius, who performed [^{35}S]GTPγS assays.

7.1 Abstract

A 17 amino-acid peptide (APP17) derived from the secreted amyloid-β precursor protein (sAPP) was reported to influence neuronal processes by binding to the sushi domain 1 (SD1) of GABA$_B$ receptors (GBRs), however whether APP17 influences GBR receptor signaling was not analyzed. Previous work showed that APP exerts synaptic effects through the release of sAPP acting at unknown cell-surface receptor(s). The neuronal effects observed with sAPP and APP17 were similar to those of the GBR agonist baclofen and blocked by a GBR antagonist, which led to the proposal that sAPP exerts its effects through GBRs. Here, we used biochemical and electrophysiological assays to show that APP17 binding to SD1 has no agonistic, inverse agonistic or allosteric properties at GBRs in heterologous cells and neurons. Likewise, we found no evidence that APP17 regulates synaptic release or neuronal activity in cultured neurons and acute brain slices. We therefore conclude that APP17 binding to GBRs does not influence GBR-mediated signaling in heterologous cells and neurons.

7.2   Introduction

Sequential proteolytic processing of the amyloid precursor protein (APP) generates neurotoxic amyloid-β peptides (Aβ), key etiological agents of Alzheimer's disease (AD). Cleavage by secretases within the APP ectodomain additionally releases the secreted APP (sAPP) variants α, β and η (Haass and Willem, 2019; Muller et al., 2017; Tang, 2019). sAPPα modulates spine density, synaptic transmission and plasticity and rescues synaptic deficits in $APP^{-/-}$ mice, indicating that sAPPα acts at neuronal cell-surface receptors (Haass and Willem, 2019; Richter et al., 2018; Tang, 2019). Recent data showed that sAPPα and full-length APP (flAPP) bind to the N-terminal extracellular sushi domain 1 (SD1) of the GBR subunit GB1a (Dinamarca et al., 2019; Rice et al., 2019; Schwenk et al., 2016). GBRs are G protein coupled receptors that block presynaptic neurotransmitter release and hyperpolarize postsynaptic membranes by gating voltage-gated Ca^{2+} channels and Kir3-type K^+ channels (Pin and Bettler, 2016). Structurally, GBRs are obligate heterodimers made of GB1 and GB2 subunits. Two GB1 isoforms, GB1a and GB1b, differ by the presence of two N-terminal sushi domains, SD1 and SD2, in GB1a. Binding of flAPP to SD1 in the lumen of cargo vesicles is required for efficient anterograde axonal trafficking and presynaptic localization of GBRs (Dinamarca et al., 2019). The binding site for SD1 in the ectodomain of flAPP is evolutionary conserved and present in the sAPP variants α, β and η (Dinamarca et al., 2019; Rice et al., 2019). A synthetic APP peptide of 17 amino acid residues, referred to as APP17, is sufficient to bind to SD1 (Rice et al., 2019). APP, sAPPα and APP17 bind to SD1 with a K_D of 183, 431 and 810 nM, respectively (Dinamarca et al., 2019; Rice et al., 2019). APP17 or sAPP binding converts the normally unfolded SD1 into a stable structure, which raises the possibility that sAPP influences synaptic transmission by allosterically regulating GBRs. Similar to the orthosteric GBR agonist baclofen, sAPPα, at a concentration of 250 nM, inhibited miniature excitatory and inhibitory postsynaptic currents (mEPSCs and mIPSCs, respectively)(Rice et al., 2019). APP17 mimicked the effects of sAPPα on release at concentrations of 25 nM - 1 μM. Corroborating that sAPPα and APP17 activate presynaptic GBRs, the orthosteric GBR antagonist CGP55845 reduced the inhibitory effect of sAPPα/APP17 on release (Rice et al., 2019). Similar to baclofen, 5 μM APP17 also inhibited Ca^{2+} transients of CA1 hippocampal neurons in anesthetized mice expressing the Ca^{2+} indicator GCaMP6s (Rice et al., 2019), compatible with GBR-mediated activation of inhibitory Kir3 channels. Based on these functional effects, Rice and colleagues (2019) concluded that GBRs are the receptors that mediate the synaptic and neuronal effects of sAPP (reviewed by (Haass and Willem, 2019; Korte, 2019; Tang, 2019; Yates, 2019)). However, Rice and colleagues (2019) did not analyze whether binding of sAPP and APP17 to SD1 indeed influences GBR-mediated G protein activation and Gα and/or Gβγ signaling to effectors.

The effects of APP17 on synaptic release and neuronal activity support that APP17 is either an agonist or positive allosteric modulator of GBRs. This finding is intriguing because SD1 is not part of the binding sites for orthosteric or allosteric GBR ligands, does not influence pharmacological properties (Kaupmann et al., 1998) and has not been linked to receptor activation. Binding of intracellular KCTD8 proteins to GBRs has been shown to reduce constitutive activity (Rajalu et al., 2015), presumably by restricting conformational changes involved in receptor activation. It is therefore conceivable that binding of flAPP to GBRs (Dinamarca et al., 2019) reduces constitutive receptor activity and that displacement of flAPP by APP17 brings back constitutive activity to normal levels. Such scenarios could also explain the increased pre- and postsynaptic inhibition observed by Rice and colleagues (2019).

To clarify the mechanism of action of APP17, we studied whether APP17 regulates GBR activity in transfected HEK293T cells and neurons. We confirm that APP17 binds with nanomolar affinity to recombinant SD1 protein and GB1a/2 receptors expressed in HEK293T cells. However, we did not observe functional effects of APP17 in assay systems reporting conformational changes of the receptor, G protein activation, Gα or Gβγ signaling. APP17 also did not modulate constitutive GBR activity in the absence or presence of flAPP. Moreover, APP17 did not influence pre- and postsynaptic GBR functions in cultured neurons or modulate neuronal activity in acute brain slices. We conclude that binding of APP17 to GBRs does not influence receptor signalling.

7.3 Material and Methods

7.3.1 Plasmids and reagents

The following plasmids were used: Flag-GB1a (Adelfinger et al., 2014); Flag-GB2, APP965 (Dinamarca et al., 2019); Gαo-RLuc, Venus-Gγ2 (Ayoub et al., 2009); Flag-Gβ2 (Rajalu et al., 2015); Myc-GB1a, HA-GB2 (Pagano et al., 2001); Kir3.1/Kir3.2 concatamer (Wischmeyer et al., 1997); PKA-Reg-RLuc-NT, PKA-Cat-RLuc-CT (Stefan et al., 2007) and SRE-FLuc (Cheng et al., 2010). GABA, CGP54626, forskolin, picrotoxin, and tetrodotoxin (TTX) were from Tocris Bioscience, Bristol, England.

7.3.2 Peptide characterization

APP17 (acetyl-DDSDVWWGGADTDYADG-amide (Rice et al., 2019)) and sc-APP17 (acetyl-DWGADTVSGDGYDAWDD-amide) peptides were from Insight Biotechnology, London, England (>98% purity). ESI-LC-MS (Poroshell, 300SB-C18, 2.1 × 75 mm, Agilent Technologies, Santa Clara, United States of America) and RP-UPLC (Acquity, Waters Corporation, Milford, United States of America) was used to confirm peptide mass and purity. ITC experiments were carried out in a microcalorimeter (Microcal ITC200, GE healthcare, Chicago, United States of America) at 25 °C with a stirring speed of 600 rpm in a buffer containing 20 mM NaPi (pH 6.8), 50 mM NaCl and 0.5 mM EDTA. For titration, APP17 or sc-APP17 (each 300 µM) were injected (1st injection 0.5 µl, followed by 25 injections of 1.5 µl) into the sample cell containing purified SD1/2 protein (30 µM) (Schwenk et al., 2016). Control measurements of peptide versus buffer were subtracted from the peptide versus SD1/2 measurements. Data were analyzed with Microcal ITC200 Origin software, using a one-site binding model.

7.3.3 Cell culture and transfection

HEK293T cells were maintained in DMEM-GlutaMAX™ (Life Technologies, Thermo Fisher Scientific, Waltham, United States of America) supplemented with 10% FBS (GE Healthcare) and 2% penicillin/streptomycin (Sigma-Aldrich, St. Louis, United States of America) at 37°C with 5% CO_2. HEK293T cells were transiently transfected in Opti-MEM™ (Gibco, Thermo Fisher Scientific) using Lipofectamine™ 2000 (Thermo Fisher Scientific). The total amount of transfected DNA was kept equal by supplementing with pCI plasmid DNA (Promega, Madison, United States of America). For electrophysiological recordings, transfected cells were seeded on poly-L-lysine (Sigma-Aldrich) coated coverslips. Transfected cells were identified by their EGFP fluorescence. To establish primary cultures of hippocampal neurons, pregnant C57BL/6 mice were sacrificed under anesthesia by decapitation. Dissected hippocampi of E17/18 embryos were collected in HBSS (Gibco, Thermo Fisher Scientific) and dissociated with 0.25% trypsin (Invitrogen, Thermo Fisher Scientific) at 37°C for 10 min. Cells were suspended in dissection medium [MEM Eagle (Sigma-Aldrich); 0.5% D(+)glucose; 10% horse serum (Gibco, Thermo Fisher Scientific); 0.1% Pen-Strep (Sigma-Aldrich)] to block trypsin activity. Cells were plated on 13 mm cell culture coverslips coated with 0.01 mg/ml poly-L-lysine hydrobromide (Sigma-Aldrich) at a density of 50,000 cells/cm^2. Two hours after dissection, the medium was replaced with Neurobasal™ Medium (Gibco, Thermo Fisher Scientific) supplemented with B-27™ (Gibco, Thermo Fisher Scientific) and GlutaMAX™ (Thermo Fisher Scientific) and the primary hippocampal neurons were maintained in a humidified incubator with 5% CO_2 at 37 °C.

7.3.4 APP17-TMR binding experiments

Transfected HEK293T cells expressing Flag-GB1a and Flag-GB2 were seeded into 96-well microplates (Greiner Bio-One, Kremsmünster, Austria) at 50,000 cells/well. After 18 h, peptides were mixed with conditioned medium at the following final concentrations: APP17-TMR (1 µM) with either APP17 (10 µM), sc-APP17 (10 µM) or PBS (vehicle); sc-APP17-TMR (1 µM) in PBS was used as a negative control. After removal of medium, peptide mixes were added to the wells and cells incubated in the dark for 1h at RT. After removal of the peptides, PBS with $MgCl_2$ and $CaCl_2$ (Sigma-Aldrich) was added to the wells. TMR fluorescence was monitored with a Spark® microplate reader (Tecan Group, Männerdorf, Schwitzerland) using

a monochromator (Excitation 544 nM, 20 nM bandwidth; detection 594 nM, 25 nm bandwidth). TMR fluorescence was determined after subtraction of the sc-APP17-TMR fluorescence measured at HEK293T cells transfected with pCI plasmid.

7.3.5 BRET

BRET measurements were performed as described (Dinamarca et al., 2019; Ivankova et al., 2013; Turecek et al., 2014). HEK293T cells were transiently transfected with Flag-GB1a, Flag-GB2, Gαo-RLuc, Gβ2 and Venus-Gγ2 plasmids with or without APP965. Transfected cells were seeded into 96-well microplates (Greiner Bio-One) at 100,000 cells/well. After 18 h, cells were washed and coelenterazine h (5 µM, NanoLight Technologies, Prolume Ltd., Pinetop-Lakeside, United States of America) added for 5 min. Luminescence and fluorescence signals were alternatively recorded for a total of 845 s using a Spark® microplate reader. Peptide, GABA or CGP54626 were injected with the Spark® microplate reader injection system at either 146s or 457s. The BRET ratio was calculated as the ratio of the light emitted by Venus-Gγ2 (530 – 570 nm) over the light emitted by Gαo-RLuc (370 – 470 nm). BRET ratios were adjusted by subtracting the ratios obtained when RLuc fusion proteins were expressed alone. Each data point represents a technical quadruplicate.

7.3.6 PKA assay

PKA measurements were performed as described in (Stefan et al., 2007). HEK293T cells were transiently transfected with Flag-GB1a, Flag-GB2, PKA-Reg-RLuc-NT, PKA-Cat-RLuc-CT with or without APP965. Transfected cells were distributed into 96-well microplates (Greiner Bio-One) at a density of 80,000 cells/well. After 42 h, cells were washed and coelenterazine h (5µM, NanoLight Technologies) added for 5 min. Luminescence signals were detected for a total of 1276 s using a Spark® microplate reader. To induce PKA dissociation, 1 mM forskolin was added manually at 108 s. Peptide, GABA or CGP54626 were injected at either 529s or 905s. Luminescence signals were adjusted to luminescence signals obtained by injecting PBS at 529s and 905s. The luminescence was normalized to baseline luminescence. Curves were plotted after forskolin addition and the time point 71 s prior the first injection was set to 0. Each data point represents a technical quadruplicate.

7.3.7 SRE-luciferase accumulation assay

HEK293 cells stably expressing Gαqi were transiently transfected with Flag-GB1a, Flag-GB2 and SRE-FLuc with or without APP965. Transfected cells were distributed into 96-well microplates (Greiner Bio-One) at a density of 80,000 cells/well. After 24 h, the culture medium was replaced with Opti-MEM™-GlutaMAX™. Peptides were incubated in Opti-MEM™-GlutaMAX™ for 1 h. In presence of peptide, GB1a/2 receptors were activated with various concentrations of GABA for 15 h. FLuc activity in lysed cells was measured using the Dual-Luciferase® Assay Kit (Promega) using a Spark® microplate reader. Luminescence signals were adjusted by subtracting the luminescence obtained when expressing SRE-FLuc fusion proteins alone.

7.3.8 [^{35}S]GTPγS binding

Preparation of mouse brain membranes was performed as described in detail earlier (Olpe et al., 1990; Rajalu et al., 2015). On the day of the experiment, frozen membranes were thawed, homogenized in 10 ml ice-cold assay buffer I containing 50 mM Tris-HCl buffer (pH 7.7); 10 mM MgCl$_2$, 1.8 mM CaCl$_2$, 100 mM NaCl, and centrifuged at 20,000 g for 15 min. The pellet was re-suspended in the same volume of cold buffer. Thereafter the re-suspension was centrifuged twice as above with 30 min of incubation on ice in between the centrifugation steps. The resulting pellet was re-suspended in 150 µl of assay buffer II (per point) containing 50 mM Tris-HCl buffer (pH 7.7); 10 mM MgCl$_2$, 1.8 mM CaCl$_2$, 100 mM NaCl, 30 µM guanosine 5'-diphosphate (GDP; Sigma-Aldrich) and 20 µg of total membrane protein. To this, 8 µM of the APP17 peptide was added in 25 µl of phosphate buffer (50 mM sodium phosphate, pH 6.8, 50 mM NaCl, for + APP17) or 25 µl of phosphate buffer alone (for – APP17) and incubated for 30 min. The reaction was started by adding various concentrations of GABA and 0.2 nM of [^{35}S]GTPγS (PerkinElmer, Waltham, United States of America) in a final volume of 200 µl per

point and assayed as described earlier (Rajalu et al., 2015). Unlabeled GTPγS (10 µM; Sigma-Aldrich) was used to detect non-specific binding. The incubation of the reagents, the filtering, and the detection were performed as described earlier (Rajalu 2015) but with the following differences: The reagents were incubated for 1h at room temperature and the Whatman filter fibers were dried for 2h at 50°C.

7.3.9 Primary cultures of hippocampal neurons

Brains of wild-type C57BL/6 mouse embryos were collected at 17/18 days (E17/18). Pregnant mice were sacrificed through anesthesia and decapitation, then embryos were recovered and hippocampi were rapidly isolated. Hippocampi were collected in HBSS (Gibco, Thermo Fisher Scientific) and dissociated by 10 min incubation at 37°C with 0.25% trypsin (Invitrogen). Cells were suspended in dissection medium [Miminum Essential Medium Eagle (Sigma-Aldrich); 0.5% D(+)glucose; 10% horse serum (Gibco, Thermo Fisher Scientific); 0.1% Pen-Strep (Sigma-Aldrich)] to block the action of trypsin. Cells were plated on 13mm cell culture coverslips coated with 0.01 mg/ml poly-L-lysine hydrobromide (Sigma-Aldrich) at the density of 50,000 cells/cm^2 in dissecting medium. Two hours after dissection, medium was replaced with growth medium [Neurobasal™ Medium (Gibco, Thermo Fisher Scientific) supplemented with B-27 ™ (Gibco, Thermo Fisher Scientific) and GlutaMAX™ (Gibco, Thermo Fisher Scientific)] and the primary hippocampal neurons were maintained in a humidified incubator with 5% of CO_2 at 37 °C.

7.3.10 Electrophysiology

HEK293T cells were transiently transfected with Myc-GB1a, HA-GB2, Kir3.1/3.2 concatamers. and EGFP. Coverslips with transfected HEK293T cells (day 1 after transfection) or hippocampal neurons (DIV 12-15) were transferred to a chamber containing a low-K$^+$ bath solution (in mM): 145 NaCl, 4 KCl, 5 HEPES, 5.5 D-glucose, 1 $MgCl_2$ and 1.8 $CaCl_2$ (pH 7.4 adjusted with NaOH). Cells were visualized using an Olympus BX61WI microscope. Recordings were performed at room temperature using borosilicate pipettes of 3-5 MΩ resistance tips, filled with K-gluconate-based pipette solution (in mM): 150 K-gluconate, 1.1 EGTA, 10 HEPES, 10 Tris-phosphocreatine, 0.3 NaGTP and 4 MgATP (pH 7.2 adjusted with KOH). Cells were held in voltage-clamp mode at −70 mV (with no correction for liquid junction potential). Kir3 currents were induced in a high-K$^+$ bath solution (in mM): 120 NaCl, 25 KCl, 5 HEPES, 5.5 D-glucose, 1 $MgCl_2$ and 1.8 $CaCl_2$ (pH 7.4 adjusted with NaOH). Experiment in neurons were performed in the presence of 100 µM picrotoxin and 200 nM TTX. All tested compounds were dissolved in the high-K$^+$ bath solution, which was applied directly to the cell under study using a ValveLink 8.2 fast perfusion system (AutoMate Scientific, Berkeley, United States of America). A Multiclamp 700B (Axon Instruments, Molecular Devices, San José, United States of America) amplifier was used to perform the experiments. The signal was sampled at 5 kHz and lowpass filtered at 1 kHz. Data were digitized using a Digidata 1440A and analyzed offline using the software pClamp10 (Molecular Devices). Peak and steady-state currents were measured for each experiment but only those experiments with stable, low (<18 MΩ) access resistances were included in the analysis.

Cell cultures for mEPSC recordings were prepared from WT mice and performed as described in (Dinamarca et al., 2019) with following differences: The coverslips were used after 14-18 days *in vitro* and the cells were voltage-clamped at -70 mV.

7.3.11 Calcium Imaging

We crossed Ai95(RCL-GCaMP6f)-D mice with Nex-Cre mice to obtain GCaMP6f expression in pyramidal cells of hippocampus. Horizontal slices (0.3-0.4 mm thick) of the ventral hippocampus were cut on a vibratome (Leica VT1200S, Leica Biosystems, Wetzlar, Germany) and kept under submerged conditions at 35°C for 1h and subsequently at room temperature in standard aCSF containing (in mM) 125 NaCl, 1.25 NaH_2PO_4, 2.5 KCl, 1 $MgCl_2$, 2 $CaCl_2$, 10 Glucose, 25 $NaHCO_3$, pH 7.2 adjusted with 5%CO_2/95%O_2. The CA1 region was imaged under an upright microscope (BX51 WI, Olympus, Tokyo, Japan) using a blue LED (optoLED, Cairn Research, Faversham, England) and an EMCCD camera (Evolve 512 Delta, Teledyne Photometrics, Tucson, United States of America). Schaffer collaterals were

stimulated via bipolar Pt/Ir wire electrodes with an insulated stimulator (500-700 µA, 0.5 ms). Carbachol (50 µM; Sigma-Aldrich) was added to enhance excitability. All other drugs were bath applied individually for > 5 min. at the concentrations indicated. The bath temperature was 32 °C. The flow rate was 2 ml/min. Data acquisition and analysis was performed with micromanager and Image J, respectively. ROIs of 10-20 active cells were selected and the mean fluorescence intensity measured over a time period of 20 s. A baseline was fitted to the recordings and subtracted. Ca^{2+} transients were detected by setting an intensity threshold. Selected cells had to be active at the beginning of the experiment under control conditions and at the end of the experiments in the presence of 1 µM CGP52432.

7.3.12 Statistical analysis

Data was analyzed with GraphPad Prism version 8 (GraphPad, San Diego, United States of America). The normality of individual data sets was tested with the Shapiro-Wilk or D'Agostino-Pearson test (for $n \geq 8$). Statistical significance of data sets against 0 or 100 was assessed by one sample t test. For non-normal distribution, the non-parametric one sample Wilcoxon test was used. Statistical significance between two groups containing one variable was assessed by student's t-test. Statistical significance between three or more groups containing one variable was assessed by ordinary or paired one-way ANOVA with Holm-Sidak's multiple comparisons test. For non-normal distribution, the non-parametric Friedman test with Dunn's multiple comparisons test was used. Statistical significance between groups containing two variable was assessed by ordinary two-way ANOVA with Sidak's multiple comparisons test. Statistical significance between dose-response curves was assessed by extra sum-of-squares F test of non-linear regression curve fits. P-values < 0.05 were considered significant. Data are presented as mean ± standard error of mean (SEM) or mean ± standard deviation (SD) as indicated in the figure legends.

7.4 Results

7.4.1 APP17 binds to recombinant SD1/2 protein and GB1a/2 receptors expressed in heterologous cells

In order to minimize potential variations in peptide quality, we ordered APP17 and scrambled control sc-APP17 peptide from the same commercial source as Rice and colleagues (2019) (Fig. 1a). For displacement experiments we also synthesized fluorescent APP17 and sc-APP17 peptides labelled with TAMRA (Carboxytetramethylrhodamine; APP17-TMR, sc-APP17-TMR; Fig. 1a). ESI-LC-MS (Agilent, Poroshell, 300SB-C18, 2.1 × 75 mm) and RP-UPLC (Waters Acquity) revealed that the peptides had the expected mass and purity (Fig. 1a). Isothermal titration calorimetry (ITC) was used to determine stoichiometry and binding affinity of the binding reaction of APP17 to purified SD1/2 protein (Schwenk et al., 2016) in solution. ITC showed that APP17 interacts with purified recombinant SD1/2 protein with a 1:1 stoichiometry and a KD of 543 nM, whereas sc-APP17 peptide exhibited no measurable binding (Fig. 1b). This agrees well with earlier binding data that determined a KD of 431 nM for APP17 binding to SD1 (Rice et al., 2019). APP17-TMR showed significantly more binding to transfected HEK293T cells expressing GB1a/2 receptors than sc-APP17-TMR (Fig. 1c). Accordingly, APP17 but not sc-APP17 displaced APP17-TMR from transfected HEK293T cells (Fig. 1c). In all subsequent experiments, we used the commercial APP17 validated for binding to recombinant SD1/2 protein and GB1a/2 receptors.

7.4.2 APP17 does not influence GB1a/2 receptor-mediated G protein activation

We addressed whether APP17 influences GBR signaling using a bioluminescent resonance energy transfer (BRET) assay monitoring G protein activation (Turecek et al., 2014). Application of GABA to HEK293T cells expressing GB1a/2 together with the G protein subunits Gαo-RLuc, Venus-Gγ2 and Gβ2 lead to the expected decrease in BRET between Gαo-RLuc and Venus-Gγ2 (Fig. 2a, b). Subsequent blockade of activated GB1a/2 receptors by the inverse agonist CGP54626 (Grunewald et al., 2002) increased BRET again due to re-association of the G protein subunits (Fig. 2b). CGP54626 increased BRET above baseline (Fig. 2b, c), consistent with constitutive GBR activity (Grunewald et al., 2002; Rajalu et al., 2015). At 1 or 10 µM, APP17 and sc-APP17 had no significant effect on GBR activity while subsequent GABA applications at the same concentrations induced robust decreases in BRET (Fig. 2d, e). This supports that APP17 is neither an agonist nor inverse agonist at GB1a/2 receptors. GABA-induced BRET decreases were similar in the presence of APP17 or sc-APP17, thus providing no evidence for allosteric effects by the peptides (Fig. 2d, e, Suppl. Fig. 1b). GB1a/2 receptors associate with flAPP (Dinamarca et al., 2019) and APP17 might therefore influence basal GBR activity by displacing flAPP from the receptor. However, application of APP17 to HEK293T cells expressing GB1a/2 receptors in the presence of flAPP revealed no changes in BRET and subsequent application of GABA was equally effective in inducing BRET decreases in the presence and absence of APP17 (Fig. 2f, g). This shows that APP17 does not influence constitutive GBR activity in the presence of flAPP.

7.4.3 APP17 does not influence GB1a/2 receptor-mediated Gα signaling

We next analyzed whether APP17 influences GB1a/2-mediated Gαi signaling using an assay monitoring cAMP-dependent Protein Kinase A (PKA) activity in transfected HEK293T cells (Fig. 3a). The assay is based on regulatory and catalytic PKA subunits tagged with the N- and C-terminal fragments of RLuc (R-RLuc-N and C-RLuc-C, respectively)(Stefan et al., 2007). Activation of GB1a/2 receptors inactivates PKA, which is monitored by an increase in luminescence due to association of R-RLuc-N with C-RLuc-C (Fig. 3a, b). Blockade of activated GB1a/2 receptors with CGP54626 decreased luminescence below baseline, again revealing constitutive GB1a/2 receptor activity (Fig. 3b). APP17 or sc-APP17 exhibited no agonistic or inverse agonistic properties at GB1a/2 receptors in the PKA assay (Fig. 3c). GB1a/2 receptor-mediated PKA inactivation was comparable in the presence of APP17 or sc-APP17, supporting that APP17 exerts no allosteric effects (Fig. 3c). Moreover, APP17 did not alter constitutive GB1/2 receptor activity in the presence of flAPP (Fig. 3d).

The BRET and PKA assays used might miss subtle functional effects of APP17 at GB1a/2 receptors. We therefore additionally tested APP17 in a more sensitive accumulation assay based on artificially coupling GB1a/2 receptors to phospholipase C (PLC) via chimeric Gαqi (Conklin et al., 1993)(Fig. 4a). PLC activity is monitored using a serum responsive element-luciferase (SRE-Luciferase) reporter amplifying the receptor response. This assay is well suited to determine dose-response curves. Increasing concentrations of GABA but not APP17 or sc-APP17 generated a typical sigmoidal dose-response curve, showing the absence of agonistic properties for the peptides at concentrations up to 100 µM (Fig 4b). CGP54626 blocked constitutive and GABA-induced receptor activity (Fig. 4c). In contrast, the peptides did not block basal GB1a/2 receptor activity at concentrations of 1 or 10 µM (Fig. 4d). The presence of 1µM or 10µM of APP17 or sc-APP17 peptide did not significantly influence the GABA dose-response curve in the absence (Fig. 4e) or presence of flAPP (Fig. 4f), corroborating that the peptides lack allosteric properties.

7.4.4 APP17 peptide has no agonistic, antagonistic or allosteric properties at native GB1a/2 receptors in [^{35}S]GTPγS binding experiments

Native GBRs form multi-protein complexes with a range of auxiliary proteins (Pin and Bettler, 2016; Schwenk et al., 2016). It is therefore conceivable that the functional APP17 effects observed by Rice and colleagues (2019) depend on the presence of GBR-associated proteins that are absent in our heterologous expression systems. Therefore, we analysed the binding of radioactive ligand [^{35}S]guanosine-5'-O-(3-thio)triphosphate ([^{35}S]GTPγS) to the Gα subunit after activating GBRs in brain membranes with various concentrations of GABA in the presence of APP17 (Fig. 5). The presence of APP17 influenced neither basal [^{35}S]GTPγS binding, EC50 nor EMax values, corroborating that APP17 peptide exerts no agonistic, antagonistic or allosteric effects at native GBRs in [^{35}S]GTPγS binding experiments.

7.4.5 APP17 peptide does influence GBR-activated Kir3 currents in neurons and transfected HEK293T cells

We further tested whether APP17 influences GB1a/2 receptor-mediated Gβγ signaling in cultured hippocampal neurons. Application of 5 µm APP17 or sc-APP17 did not elicit any currents in neurons (Fig. 6a, b). In contrast, baclofen induced robust K$^+$ currents that, however, were not modulated in amplitude by the presence of APP17 or sc-APP17. Consistent with the findings in neurons, APP17 or sc-APP17 also did not activate or inhibit K$^+$ currents in transfected HEK293T cells expressing Kir3 channels (Suppl. Fig. 3a, b). Moreover, co-application of GABA and APP17 or sc-APP17 elicited Kir3 currents in HEK293T cells of similar amplitudes as GABA alone. APP17 therefore has no agonistic, antagonistic of allosteric effect GB1a/2 receptor activated Kir3 currents.

7.4.6 APP17 does not regulate GBR-mediated inhibition of neurotransmitter release

Rice and colleagues (2019) found that APP17 at concentration of 250 nM or 1 µm reduces the probability of neurotransmitter release in cultured mouse hippocampal neurons (Rice et al., 2019). We therefore similarly studied whether APP17 and sc-APP17 influence mEPSC frequency recorded in mouse hippocampal neurons. We found that baclofen but not APP17 or sc-APP17 at 1 µm (Fig. 7a, b) and 250 nM (Fig. 7c, d) significantly reduced mEPSC frequency, without altering mEPSC amplitude. This again supports that APP17 does not regulate presynaptic GBRs.

7.4.7 APP17 does not influence neuronal activity in hippocampal slices

Rice and colleagues (2019) found that APP17 at 5 µM suppresses neuronal activity of CA1 pyramidal neurons *in vivo* (Rice et al., 2019). To similarly analyze whether APP17 inhibits neuronal activity, we crossed Ai95(RCL-GCaMP6f)-D mice (Madisen et al., 2015) with Nex-Cre mice (Goebbels et al., 2006) to express GCaMP6f in pyramidal cells of the hippocampus. We then recorded neuronal activity of pyramidal cells in acute hippocampal slices of mice expressing GCaMP6f. To enhance neuronal activity we stimulated Schaffer collaterals via bipolar Pt/Ir wire electrodes and added carbachol (Cole and Nicoll, 1984). We monitored the Ca^{2+} fluorescence intensity in neurons at baseline and in the successive presence of 5 µM

APP17, 5 µM baclofen, and 1 µM CGP54626 (Fig. 8a, b). The time plots of Ca^{2+} fluorescence intensity showed that baclofen but not APP17 reduced neuronal activity (Fig. 8b, c). As expected, CGP54626 counteracted the decrease in neuronal activity seen after baclofen application (Fig. 8b, c).

7.5 Discussion

Proteolytic APP processing through the non-amyloidogenic pathway liberates sAPPα that was shown to modulate spine density (Muller et al., 2017), LTP (Hick et al., 2015), synaptic transmission (Bour et al., 2004; Ishida et al., 1997; Richter et al., 2018), and plasticity (Aydin et al., 2011; Claasen et al., 2009; Taylor et al., 2008). However, the neuronal receptors for sAPPα remained elusive until recently when SD1 of GB1a was identified to interact with sAPPα and APP (Dinamarca et al., 2019; Rice et al., 2019). The functional effects of sAPPα and APP17 through GB1a/2 receptors, however, remained controversial. We therefore analyzed whether APP17 modulates recombinant and native GB1a/2 receptor signaling in carefully controlled experiments. We could confirm that APP17 binds with nanomolar affinity to recombinant SD1 and GB1a/2 receptors. However, we did not observe any functional effects of APP17 on GB1a/2 receptor signaling *in vitro* or *in vivo*. APP17 also did not change constitutive GB1a/2 receptor activity in the presence or the absence of flAPP. Hence, our results support the findings of Dinamarca and colleagues (2019) and clearly show that APP17 does not modulate the signaling of recombinant or native GB1a/2 receptors.

Rice and colleagues (2019) did not explain the mechanism of the modulatory properties of APP17 that they observed. A reasonable explanation is difficult because the SD1 is neither part of the orthosteric nor allosteric binding sites (Evenseth et al., 2020). Agonist-mediated GBR activation induces conformational changes within the extracellular venus-flytrap domains (VFTDs) that are propagated to the heptahelical transmembrane domains (7TMD), which activate the G protein (Geng et al., 2013; Kim et al., 2020; Park et al., 2020; Shaye et al., 2020). The VFTDs face opposite directions and are composed of two opposing lobes (LB1 and LB2) (Geng et al., 2013). Upon GBR activation, the conformational change of the VFTDs results in the contact of the distinct LB2s (Geng et al., 2013). Locking the LB2 interface is sufficient to activate GBRs, defining the contact of the distinct LB2s as a hallmark of GBR activation (Geng et al., 2013). Therefore, a ligand binding to SD1 would need to result in the contact of the LB2s to elicit GB1a/2 receptor activation. However, in our experiments monitoring GB1a/2 receptor-mediated G protein and effector activation, binding to SD1 did not activate GB1a/2 receptors. Since APP17 did not affect the conformation of VFTDs, it seems unlikely that binding to SD1 affects the conformation within the 7TMDs and thus allosterically modulates GB1a/2 receptors. Not surprising therefore, we did not observe allosteric properties of APP17 at GB1a/2 receptors in our experiments. Nevertheless, it is conceivable that binding of flAPP to SD1 could constrain the conformation of VFTDs, affecting constitutive GB1a/2 receptor activity. Hence, displacing flAPP with the competitive APP17 at SD1 could restore constitutive activity of GB1a/2 receptors to normal levels. However, flAPP did not modulate recombinant GB1a/2 receptors, and accordingly, APP17 did not exert allosteric properties at recombinant GBRs in the presence of flAPP in our experiments. We conclude that the absence of modulatory properties rely on the incapability of the APP17 to induce conformational changes within the VFTDs that result in either the contact between the LB2s or in conformational changes within the 7TMDs. Thus, our results agree with findings by Dinamarca and colleagues (2019), which observed no GB1a/2 receptor-mediated G protein activation by sAPPα.

Rice and colleagues (2019) exclusively analyzed the effect of APP17 in neurons. It is therefore possible that functional properties of APP17 depend on additional proteins that are missing in the heterologous system. Therefore, we analyzed whether APP17 exerts functional effects at native GBRs. However, APP17 neither influenced G protein activation in membrane preparations nor changed GBR-mediated mEPSCs in organotypic slices. Rice and colleagues (2019) further showed that 5 µM of APP17 suppresses neuronal activity through presynaptic GB1a/2 receptors. We used the same concentration of APP17 and did not observe a suppression of neuronal activity, whereas 5 µM of baclofen almost completely shut down presynaptic activity. Subsequent application of GBR antagonists restored the presynaptic activity, showing that the elimination is not due to cell death during the experiment. Hence, our results demonstrate that APP17 does not modulate GBR signaling *in vivo*.

In general, we put extensive efforts into the analysis of APP17 and its influence on GBR-mediated signaling. We confirmed that APP17 binds to recombinant SD1 and GB1a/2

receptors. Thus, we can exclude that the absence of modulatory properties is due to the absence of APP17 binding to GB1a/2 receptors that we used in our experiments. We further elucidated the effect of APP17 on GBR-mediated G protein activation, Gα signaling, and Gβγ signaling in the heterologous system. In order to detect possible subtle influences of APP17 on GBR-mediated signaling, we used highly sensitive assays. To exclude the involvement of additional, yet unidentified proteins that are only present under native conditions, we further elucidated the effect of APP17 on GBR-mediated signaling *in vivo*. In all our experiments, we used elaborated controls to omit wrong conclusions. Considering all this, we confidently conclude that APP17 does not exert modulatory properties at GBRs.

7.6 Figures & Supplementary Figures

7.6.1 Figures

a

Name	Sequence	MW	Purity
APP17	Acetyl-DDSD**VWWGGA**DTDYADG-NH$_2$	1886	> 98 %
sc-APP17	Acetyl-DWGADTVSGDGYDAWDD-NH$_2$	1886	> 98 %
APP17-TMR	TMR-PEG2-DDSD**VWWGGA**DTDYADG-NH$_2$	2401	> 95 %
sc-APP17-TMR	TMR-PEG2-DWGADTVSGDGYDAWDD-NH$_2$	2401	> 95 %

b

c
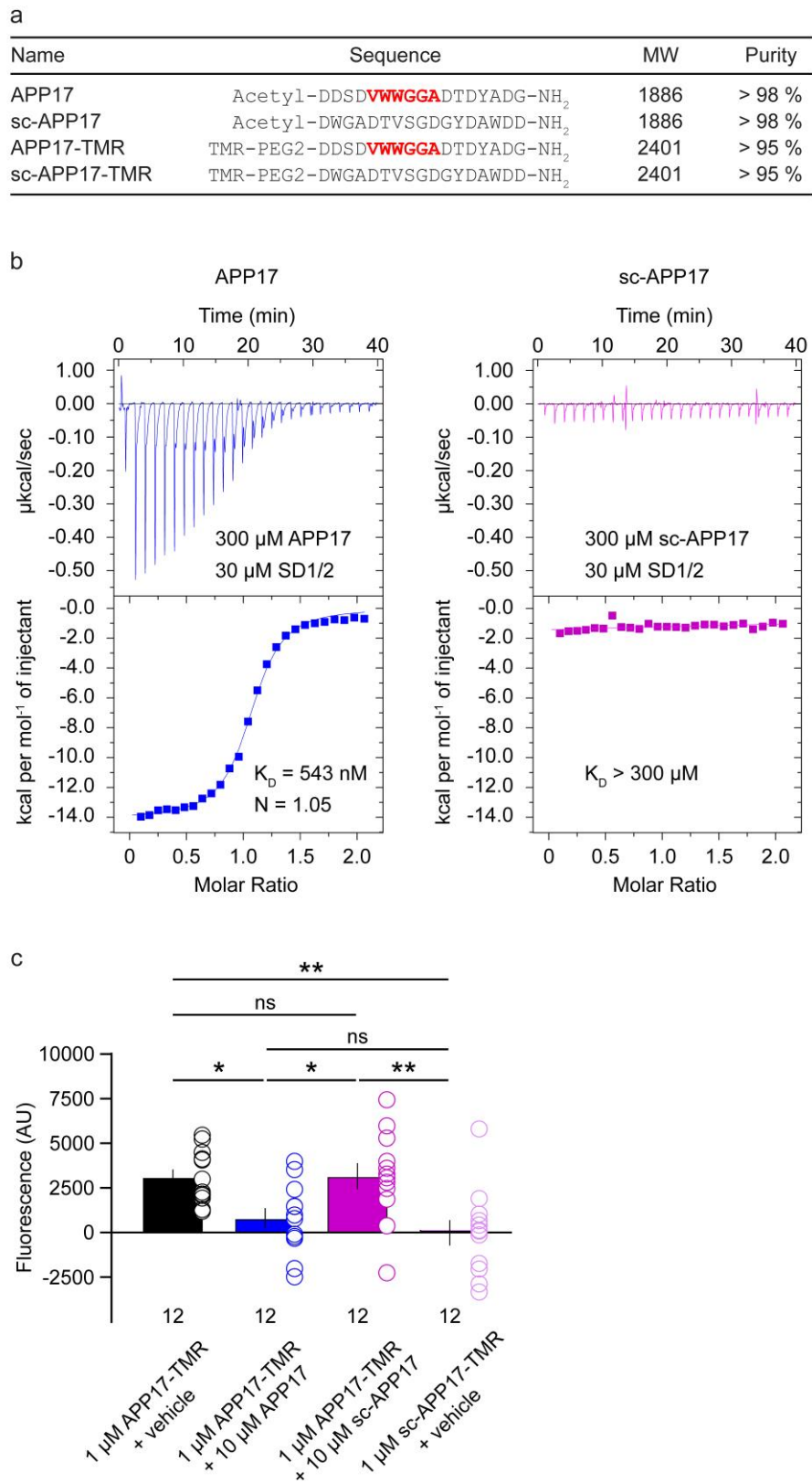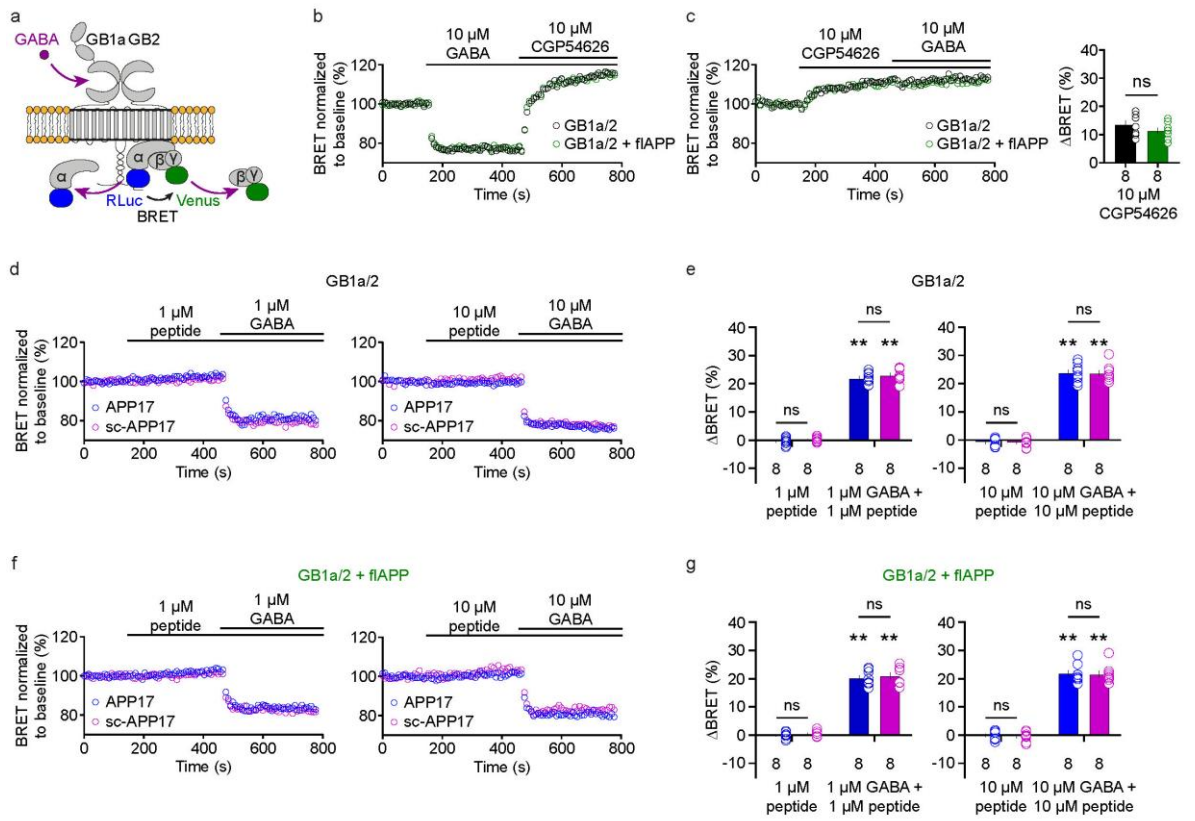
Rem et al. Figure 1

Rem et al. Figure 2
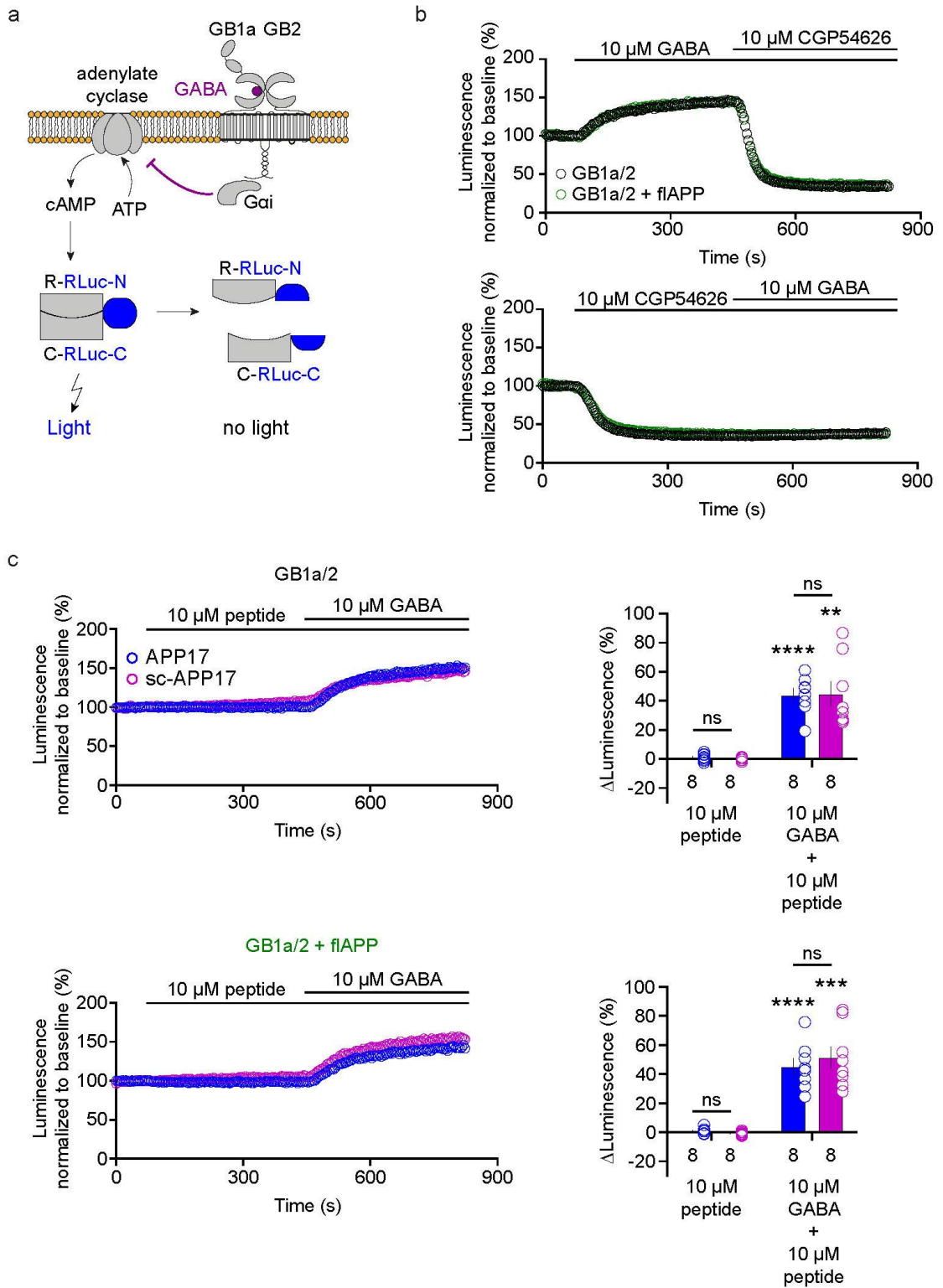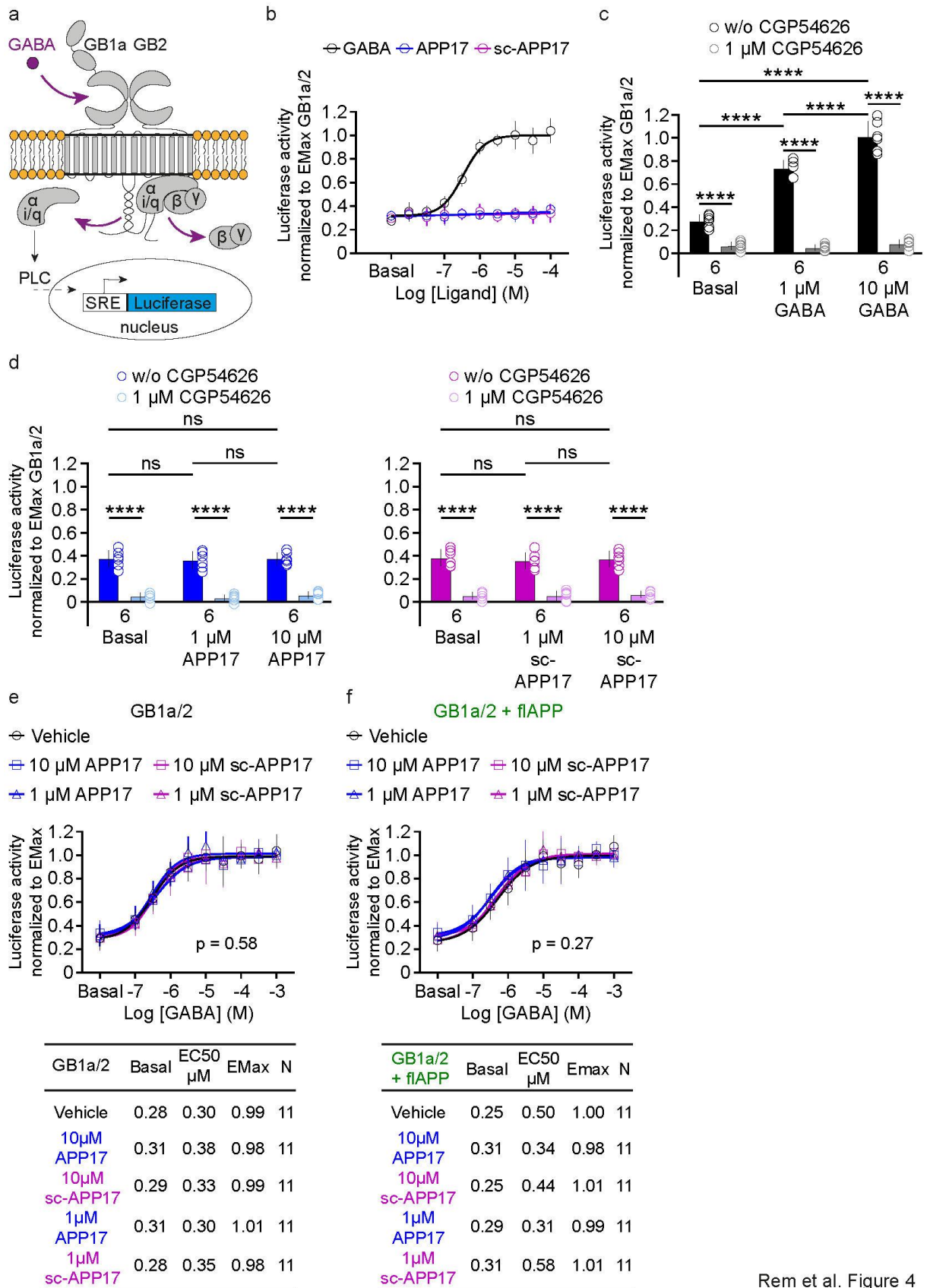
Rem et al. Figure 3
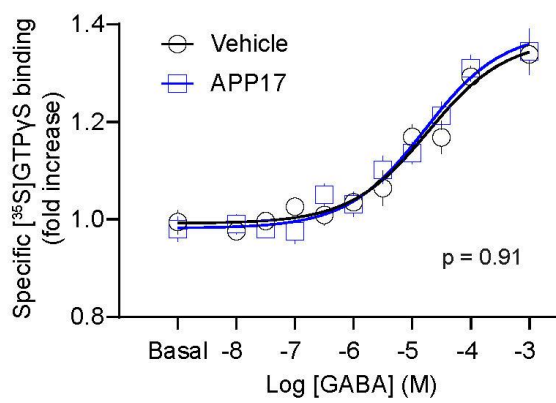
	Basal	EC50 µM	EMax	N
Vehicle	0.99	18.82	1.37	9
APP17	0.98	16.37	1.39	8

Rem et al. Figure 5

a

b

Rem et al. Figure 6

a

Baseline

APP17

Baclofen

40 pA

2 s

b

Baseline

sc-APP17

Baclofen

40 pA

2 s

c

Baseline

APP17

Baclofen

40 pA

2 s

d

Baseline

sc-APP17

Baclofen

40 pA

2 s

Rem et al. Figure 7

a

ROI	Baseline	5 µM APP17	5 µM baclofen	1 µM CGP54626

b

Baseline   5 µM APP17   5 µM baclofen   1 µM CGP54626

Cells

Time (s)

Ca²⁺ fluorescence intensity (AU)

c

Number Ca²⁺ transients per 10 s

Baseline	5 µM APP17	5 µM baclofen	1 µM CGP54626
64	64	64	64

ns
ns
****
ns   ****   ****

7.6.2 Supplementary figures

a

b

Rem et al. Supplementary Figure 1

Legend (plot):
- GB1a/2
- GB1a/2 + flAPP

Plot axes:
- Y-axis: Luciferase activity normalized to EMax (0 to 1.2)
- X-axis: Log [GABA] (M), from Basal, -7, -6, -5, -4, -3
- p = 0.20

	Basal	EC50 μM	EMax	N
GB1a/2	0.27	0.46	0.99	11
GB1a/2 + flAPP	0.24	0.54	1.00	11

a

b

7.7 Figure and supplementary figure legends

7.7.1 Figure legends

Fig. 1 Characterization of synthetic APP17 and sc-APP17 peptides. **a** Sequence alignment of APP17, sc-APP17, APP17-TMR and sc-APP17-TMR peptides. Residues critical for SD1 binding are shown in red. **b** Representative ITC diagrams of the titrations of SD1/2 protein in solution (30 µm) with APP17 or sc-APP17 (300 µm in the syringe); raw heat signature (top) and integrated molar heat release (bottom). The calculated stoichiometry of APP17:SD1/2 protein is 1.05. **c** Bar graph showing APP17-TMR (1 µM) binding to HEK293T cells expressing GB1a/2 receptors in the presence of vehicle (black), 10 µM APP17 (blue), and 10 µM sc-APP17 (magenta). sc-APP17-TMR (1 µM) binding in presence of vehicle (light magenta) to HEK293T cells expressing GB1a/2 receptors served as a negative control. The background fluorescence of sc-APP17-TMR (1 µM) at HEK293T cells transfected with empty vector was subtracted. Data are means ± SEM. The number of independent experiments is indicated in the bar graph. ns = not significant, *p < 0.05, **p < 0.01, one-way ANOVA with Holm-Sidak's multiple comparisons test.

Fig. 2 APP17 is not an agonist or antagonist at GB1a/2 receptors expressed in HEK293T cells when monitoring G protein activation using BRET. **a** Assay measuring BRET between Gαo-RLuc and Venus-Gγ2. GB1a/2 receptor activation leads to dissociation of the heterotrimeric G protein and a consequent decrease in BRET. **b** Individual experiments showing GABA induced BRET changes at GB1a/2 receptors in the absence (black) and presence (green) of flAPP. The inverse agonist CGP54626 reverses GABA induced BRET changes above baseline, indicative of constitutive GB1a/2 receptor activity. **c** CGP54626 similarly increased BRET in the absence (black) and presence (green) of flAPP. Subsequent application of GABA did not overcome receptor blockade. Bar graph showing similar BRET changes induced by CGP54626 determined in experiments as shown to the left. **d** Neither APP17 (blue) nor sc-APP17 (magenta) at 1 µM (left) and 10 µM (right) altered BRET in cells expressing GB1a/2 receptors. In the same cells, GABA at 1 µM (left) and 10 µM (right) induced the expected decrease in BRET. **e** Bar graphs of BRET changes determined in experiments as in **d**. **f, g** Experiments as in **d, e** in the presence of flAPP. Data are means ± SEM. The number of independent experiments is indicated in the bar graphs. ns = not significant, Two-way ANOVA with Sidak's multiple comparisons test. **p < 0.01, One sample Wilcoxon test (non-parametric) against 0.

Fig. 3 APP17 is not an agonist or antagonist at GB1a/2 receptors expressed in HEK293T cells when monitoring PKA activity. **a** Assay monitoring dissociation of the regulatory (R) and the catalytic (C) subunits of the tetrameric PKA holoenzyme upon cAMP binding. PKA subunits were tagged with the N- and C-terminal fragments of RLuc (R-RLuc-N, C-RLuc-C). **b** Individual experiments showing GB1a/2 receptor-mediated luminescence changes in the absence (black) or presence (green) of flAPP. *Top* GB1a/2 receptor activation by GABA reduces cAMP levels, promotes reconstitution of RLuc activity and an increase in luminescence. Block of GB1a/2 receptor activity with CGP54626 decreased luminescence below baseline, indicating constitutive GB1a/2 receptor activity. *Bottom* CGP54626 application to GB1a/2 receptors leads to a luminescence decrease due to inhibition of constitutive receptor activity. Subsequent application of GABA did not overcome receptor blockade. **c** Neither APP17 (blue) nor sc-APP17 (magenta) altered luminescence in the absence (top) or presence (bottom) of flAPP. In the same cells, GABA induced the expected luminescence increases. Bar graphs show luminescence changes determined in experiments as shown to the left. Data are means ± SEM. The number of independent experiments is indicated. ns = not significant, Two-way ANOVA with Sidak's multiple comparison test. **p < 0.01, ***p < 0.001; ****p < 0.0001, One sample t test against 0.

Fig. 4 APP17 is not an agonist, allosteric modulator or antagonist at recombinant GB1a/2 receptors in an accumulation assay monitoring PLC activity. **a** Scheme depicting the assay monitoring PLC dependent RLuc expression under control of the serum response element (SRE). GB1a/2 receptors were artificially coupled to PLC by stably expressing the chimeric G protein subunit Gαqi. GB1a/2 receptors and SRE-RLuc reporter are co-expressed transiently in HEK293-Gαqi cells. **b** Dose-response curve showing that only GABA (black), but

not APP17 (blue) or sc-APP17 (magenta) induces RLuc activity in cells expressing GB1a/2 receptors together with SRE-RLuc. **c** CGP54626 blocks constitutive and GABA (1 or 10 µM) induced GB1a/2 receptor-mediated RLuc activity. **d** Constitutive GB1a/2 receptor activity is unchanged in the presence of APP17 (left) or sc-APP17 (right) at 1 or 10 µM, suggesting that the peptide exert no inverse agonistic properties at GB1a/2 receptors. **e, f** APP17 (blue) or sc-APP17 (magenta) at 1 µM (squares) or 10 µM (triangles) did not significantly alter GABA dose-response curves in the absence (**e**) or presence (**f**) of flAPP, indicating that the peptides have no allosteric properties at recombinant GB1a/2 receptors. Tables show basal, EC50 and Emax values derived from the curve fits. All data are mean ± SD. The number of independent experiments is indicated in the bar graphs. Linear regression curve fit of 6 (**b**, APP17 & sc-APP17) independent experiments per condition. Non-linear regression curve fits of 6 (**b**, GABA) or 11 (**e**, **f**) independent experiments per condition. $p = 0.58$, $p = 0.27$, extra sum-of-squares F test.

Fig. 5 APP17 is not an agonist, antagonist or allosteric modulator at native GB1a/2 receptors in [^{35}S]GTPγS binding experiments. **a** [^{35}S]GTPγS binding in membrane preparations of WT mice induced by various concentrations of GABA is not altered in the presence of APP17 (blue). The table shows the basal, EC50 and Emax values derived from non-linear regression curve fits. Experiments with vehicle and APP17 were performed with membrane preparations from the same mouse. Data are mean ± SEM. Non-linear regression curve fit of 9 (vehicle) and 8 (APP17) independent experiments with 9 different mice. $p = 0.91$, extra sum-of-squares F test.

Fig. 6 APP17 does not evoke or influence GB1a/2 receptor-mediated Kir3 currents in cultured hippocampal neurons. **a, b** Representative traces showing that neither APP17 (**a**) nor sc-APP17 (**b**) evoke GB1a/2 receptor-induced K$^+$ currents in cultured hippocampal neurons. Application of baclofen alone or in the presence of APP17 (**a**) or sc-APP17 (**b**) yielded similar current amplitudes, showing that APP17 does not allosterically modulate baclofen-induced currents. Bar graphs showing K$^+$ current densities determined in experiments as shown to the left. Data are means ± SEM. The number of independent experiments is indicated in the bar graphs. ns = not significant, **$p < 0.01$, ***$p < 0.001$ Paired one-way ANOVA with Holm-Sidak's multiple comparisons test (to compare different means) and One sample t-test against 0.

Fig. 7 APP17 does not influence presynaptic inhibition in cultured hippocampal neurons. **a, b** Representative traces of mEPSC recordings in cultured hippocampal neurons under baseline conditions (gray) and during 1 µM application of either APP17 (**a**, blue), sc-APP17 (**b**, magenta), and baclofen (black). Bar graphs are showing that Baclofen but not APP17 (**a**) or sc-APP17 (**b**) at 1 µM reduces the mEPSC frequency, while mEPSC amplitudes are unaffected. **c**, **d** Representative traces of mEPSC recordings in cultured hippocampal neurons under baseline conditions (gray) and during 250 nM application of either APP17 (**c**, blue), sc-APP17 (**d**, magenta), and baclofen (black). Bar graphs are showing that Baclofen but not APP17 (**c**) or sc-APP17 (**d**) at 250 nM reduces the mEPSC frequency, while mEPSC amplitudes are unaffected. Data are means ± SEM. The number of recorded neurons is indicated in the bar graphs. ns = not significant, *$p < 0.05$, **$p < 0.01$, ***$p < 0.001$, One sample t test against 100, unpaired student's t-test (to compare two means), and paired one-way ANOVA with Holm-Sidak's multiple comparisons test (to compare three means).

Fig. 8 APP17 does not influence neuronal activity in acute brain slices. **a** *Left*, wide-field fluorescence image of the hippocampal CA1 region with the analyzed neurons indicated (scale bar, 20 µm). *Right*, Time plots of Ca^{2+} fluorescence intensity in the corresponding neurons at baseline and in the presence of APP17 (5 µM), baclofen (5 µM), and CGP54626 (1 µM). The numeration corresponds to the neuron number in the heat map. **b** Heat map of all neurons analyzed. The heat map is sorted in descending order of basal activity in the analyzed neurons across all experiments. **c** Box plots of the number of Ca^{2+} transients/10s in all neurons under the indicated recording conditions. Box plot indicate the median, quartiles, minimum, and maximum. ns = not significant, ****$p < 0.0001$, paired Friedman test (non-parametric) with Dunn's multiple comparisons test.

7.7.2 Supplementary figure legends

Suppl. Fig. 1 flAPP and APP17 do not allosterically modulate recombinant GB1a/2 receptors in a BRET assay monitoring G protein activation. **a** *Left* Individual experiments showing similar BRET changes induced by GABA at GB1a/2 receptors in the absence (black) and presence (green) of flAPP. *Right* Bar graphs showing that BRET changes induced by 1 μM GABA in the absence (black) or presence (green) of flAPP are similar, indicating that flAPP does not allosterically influence recombinant GB1a/2 receptor responses. **b** Bar graphs showing GABA-induced BRET changes of experiments shown in **a**, **Fig. 2d**, and **Fig. 2f**. The presence of 1 μM APP17 or sc-APP17 did not influence BRET changes induced by 1 μM GABA, both in the absence (black) or presence (green) of flAPP. Competition of APP17 and flAPP for SD1 binding therefore does not allosterically influence the receptor response. Data are mean ± SEM. The number of independent experiments is indicated in the bar graphs. ns = not significant, two-way ANOVA with Sidak's multiple comparisons test. **p < 0.01, One sample Wilcoxon test (non-parametric) against 0.

Suppl. Fig. 2 flAPP does not allosterically modulate recombinant GB1a/2 receptors in an assay monitoring PLC activity. **a** GABA dose-response curves in HEK293T cells expressing GB1a/2 receptors in the absence (black) or presence (green) of flAPP are similar, indicating that flAPP does not exert allosteric properties at recombinant GB1a/2 receptors. Table shows basal, EC50, and Emax values derived from the curve fits. Non-linear regression curve fits of 11 independent experiments per condition. p = 0.20, extra sum-of-squares F test.

Suppl. Fig. 3 APP17 does not evoke or influence GB1a/2 receptor-mediated Kir3 currents in transfected HEK293T cells. **a, b** Representative traces showing that neither APP17 (**a**) nor sc-APP17 (**b**) evoke GB1a/2 receptor-induced K$^+$ currents in transfected HEK293T cells. Application of GABA alone or in the presence of APP17 (**a**) or sc-APP17 (**b**) yielded similar current amplitudes, showing that the peptides do not allosterically modulate GABA-induced currents. Bar graphs showing K$^+$ current densities determined in experiments as shown to the left. Data are means ± SEM. The number of independent experiments is indicated in the bar graphs. ns = not significant, *p < 0.05, **p < 0.01, ***p < 0.001 Paired one-way ANOVA with Holm-Sidak's multiple comparisons test (to compare different means) and One sample t-test against 0.

8 AJAP1 and PIANP mediate precise localization and induce negative allosteric modulation of GB1a/2 receptors *in trans*

Pascal D. Rem

The following data complete the work of my colleagues and will be included into a future publication of the lab with me as co-author.

Personal contribution

      I designed, performed and analyzed all experiments. Further I designed and created all figures, wrote the figure legends, material and methods, and the manuscript in its present form.

8.1 Introduction

GABA$_B$ receptors (GBRs) are essential regulators of synaptic transmission in the brain (Gassmann and Bettler, 2012). At the presynapse, GBRs prevent vesicle release of various neurotransmitters and at the postsynapse they block neuronal activity by inducing hyperpolarization of the cell. There is evidence that altered GBR activity and levels are associated with diverse diseases including but not limited to anxiety, depression, epilepsy, schizophrenia, autism spectrum disorder (ASD), or Alzheimer's disease (AD) (Gassmann and Bettler, 2012; Heaney and Kinney, 2016; Kasten and Boehm, 2015; Kumar et al., 2013). Therefore, GBRs represent a promising target for drug development. In search of new treatments, a plethora of agonists, antagonists, and positive allosteric modulators of GBRs have been identified, whereas negative allosteric modulators are relatively scarce (Evenseth et al., 2020; Sun et al., 2016). So far, only the GBR specific agonist Baclofen has received approval for the market and is used to treat patients suffering from spasticity. The effectiveness of Baclofen as a treatment for alcohol abuse is still controversial (Agabio and Leggio, 2018). Hence, there is still an unmet need to discover and develop specific drugs targeting GBRs.

GBRs are obligate heterodimers composed of GB1 and GB2 subunits that are structurally related. Both subunits contain an extracellular N-terminal venus fly-trap domain (VFTD), a seven-transmembrane domain (7TMD), and an intracellular C-terminal domain (Evenseth et al., 2020). The C-terminal domain of GB1 contains an endoplasmic reticulum (ER) retention signal, which is shielded by the interaction with the C-terminus of GB2, enabling GB1/2 receptor trafficking to cell surfaces (Margeta-Mitrovic et al., 2000; Pagano et al., 2001). Despite the structural homologies, GB1 and GB2 subunits exert different functions. Extracellular GBR agonists and antagonists bind within the orthosteric site of the VFTD of GB1, whereas the intracellular trimeric G proteins of the Gi/o-type bind to the 7TMD of GB2 (Evenseth et al., 2020). GB1/2 receptor activation causes the rearrangement of both VFTDs resulting in a conformational change of both 7TMDs thereby activating G proteins (Geng et al., 2013; Matsushita et al., 2010; Monnier et al., 2011; Shaye et al., 2020). In contrast to agonists and antagonists, positive and negative allosteric modulators bind within the 7TMD of GB2 subunits stabilizing the active or inactive conformation, respectively (Evenseth et al., 2020).

The GB1 subunit further exists in two isoforms, GB1a and GB1b (Kaupmann et al., 1997). Heterodimeric GB1a/2 receptors are located at pre-and postsynaptic sites, whereas heterodimeric GB1b/2 receptors accumulate exclusively in somatodendritic compartments (Vigot et al., 2006). The sole difference between the two isoforms is two sushi domains (SDs) at the N-terminus of GB1a (Hawrot et al., 1998; Kaupmann et al., 1997). SDs are decisive for axonal localization and stabilization of GB1a/2 receptors at the cell surface (Biermann et al., 2010; Hannan et al., 2012). GB1a knock-out mice lack axonal GBRs, show impaired GBR-mediated inhibition of glutamate release, and exert spontaneous epileptiform activity (Gassmann and Bettler, 2012; Vienne et al., 2010). SD1 of GB1a interacts mutually exclusive with either the β-amyloid precursor protein (APP), adherens junction-associated protein 1 (AJAP1), or PILRα-associated neural protein (PIANP), leading to the formation of distinct complexes (Dinamarca et al., 2019). APP, AJAP1, and PIANP share a six amino acid stretch featuring a conserved WG motif within their extracellular domains that mediate the interaction with SD1 (Dinamarca et al., 2019). However, they all have distinct affinities for SD1 binding with the rank order AJAP1 > PIANP >> APP (Dinamarca et al., 2019). The interaction of APP with SD1 links GB1a/2 receptors to the kinesin motor and mediates presynaptic GB1a/2 receptor trafficking (Dinamarca et al., 2019). At the cell surface, GB1a/2 receptors stabilize APP and inhibit Aβ generation, a hallmark of AD (Dinamarca et al., 2019; Huang and Mucke, 2012; Muller et al., 2017; Selkoe and Hardy, 2016). Aβ peptide production results from APP processing in the amyloidogenic pathway whereas in the non-amyloidogenic pathway, APP is the source for soluble extracellular APP fragments (sAPPα) (Muller et al., 2017). sAPPα is reported to signal through GBRs and binds SD1 of GB1a (Fogel et al., 2014; Muller et al., 2017; Pasciuto et al., 2015; Rice et al., 2019). Conversely, a recent publication has shown that sAPPα does not induce GB1a/2 receptor-mediated G protein activation (Dinamarca et al., 2019). Hence, it needs to be elucidated whether binding to SD1 of GB1a can influence GB1a/2 receptor activity.

Compared to APP, AJAP1 and PIANP are not required for axonal transport of GB1a/2 receptors (Dinamarca et al., 2019). AJAP1 interacts with the E-cadherin/β-catenin complex at adherens junctions that are crucial in establishing the adhesion between pre-and postsynaptic membranes (Bharti et al., 2004; Han et al., 2017; Yamada and Nelson, 2007). A postdoc in our lab showed that AJAP1 is located exclusively in dendrites of cultured hippocampal neurons and is expressed in mossy cells in the hilus of the dentate gyrus. In AJAP1-KO mice, presynaptic localization of GB1a/2 receptors at synapses onto mossy cells is abrogated (S. Früh personal communication). At CA3/CA1 and granule cells/mossy cell synapses, AJAP1-KO mice exhibited a deficit in presynaptic GBR-mediated inhibition of miniature excitatory postsynaptic current (mEPSC) frequency (T. Lalanne personal communication). AJAP1 and GB1 were downregulated in patients suffering from temporal lobe epilepsy (TLE) and in a mouse model of epilepsy (Zhang et al., 2020). The downregulated GB1 levels in the epileptic mouse model were rescued by lentiviral induced expression of AJAP1, resulting in a reduction of spontaneous recurrent seizures (SRSs) (Zhang et al., 2020). Frequent downregulation of AJAP1 is further observed in oligodendroglioma and neuroblastoma, which resulted in increased tumor cell migration and invasion, suggesting that AJAP1 acts as a tumor suppressor (Zeng et al., 2014a). PIANP shares a homologous C-terminus with AJAP1 and localizes at E-cadherin positive adherens junctions (Geraud et al., 2010). PIANP attenuates E-cadherin cleavage by γ-secretase and is itself processed by various proteases, like the γ-secretase (Biswas et al., 2016; Evdokimov et al., 2013; Evdokimov et al., 2016). In the brain, PIANP is expressed in neurons throughout all brain regions and is located in axons and somatodendritic compartments of neurons (Winkler et al., 2019). PIANP-KO mice show impaired GBR-mediated inhibition of glutamate release and exert an autism-like behavior (Winkler et al., 2019).

A large family of synaptic adhesion molecules necessary for synaptic transmission comprises the proteins extracellular leucine-rich repeat and fibronectin type-III domain-containing 1 (ELFN1) and ELFN2. Comparable to AJAP1 and PIANP, ELFN1 and ELFN2 belong to group I of single-spanning membrane proteins and are localized predominantly to the postsynaptic site of glutamatergic neurons (Dunn et al., 2019; Sylwestrak and Ghosh, 2012). Postsynaptic ELFN1 and ELFN2 recruit and alter pharmacological properties of transcellular presynaptic group III metabotropic glutamate receptors (mGluRs) (Dunn et al., 2018; Dunn et al., 2019; Tomioka et al., 2014). Group III mGluRs are coupled to Gi/o-type G proteins, localize predominantly to presynaptic sites, and regulate glutamate neurotransmitter release (Niciu et al., 2012; Nicoletti et al., 2011; Niswender and Conn, 2010). Mice lacking ELFN1 or ELFN2 exert multiple neuropsychiatric phenotypes such as epilepsy, which is in line with dysregulation of presynaptic group III mGluRs (Dunn et al., 2019; Tomioka et al., 2014).

In the present study, I show that AJAP1 and PIANP do not influence GB1a/2 receptor signaling *in cis*. However, the interaction between GB1a/2 receptors and AJAP1 or PIANP *in trans* leads to the recruitment and clustering of GB1a/2 receptors. Moreover, AJAP1 and PIANP stabilize and negatively regulate recombinant transcellular GB1a/2 receptors. To unfold the negative allosteric effects, AJAP1 needs to be anchored in the opposite cell membrane. These findings suggest that GB1a/2 receptors are trafficked to cell surfaces by APP, where they are transferred to AJAP1 or PIANP that precisely localize GB1a/2 receptors at presynapses and influence their activity.

8.2 Material and Methods

8.2.1 Molecular biology

The plasmids encoding Flag-GB1a (Adelfinger et al., 2014), Flag-GB2, AJAP1 and PIANP (Dinamarca et al., 2019), Gαo-RLuc and Venus-Gγ2 (Ayoub et al., 2009), and Flag-Gβ2 (Rajalu et al., 2015) have been described earlier. The plasmid encoding AJAP1-SDBM was a gift from J. Schwenk. AJAP1-mCherry, AJAP1-SDBM-mCherry, PIANP-mCherry and PIANP-SDBM-mCherry were constructed using overlap extension polymerase chain reaction and cloned into pCI vector (Cat.No. E1731, Promega, WI, US). PIANP-SDBM was generated by removing the mCherry tag using Q5 site directed mutagenesis (Cat.No. E0554S, New England Biolabs, MA, US). The plasmid encoding SRE-FLuc was a gift from J.S. Cho and is described in (Cheng et al., 2010). For transient transfection Lipofectamine™ 2000 (Cat.No. 11668027, Thermo Fisher Scientific, MA, US) was used. To keep the total amount of transfected DNA equal, pCI plasmid DNA was supplemented.

8.2.2 Cell lines and culturing

HEK293T cells and HEK293 cells stably expressing Gαqi chimera were maintained in DMEM-GlutaMAX™ (Cat.No. 61965026, Life Technologies, Ca, USA) supplemented with 10% FBS (Cat.No. 10270106, GE Healthcare, Buckinghamshire, UK) and 2% penicillin and streptomycin (Cat.No. P4333, Sigma-Aldrich, MS, USA) at 37°C with 5% CO_2.

8.2.3 Mouse strains

The generation of GB1-eGFP Bacterial Artificial Chromosome (BAC) transgenic mice were kept in BALB/c background and are described in (Casanova et al., 2009). All experiments involving mice were performed according to the Swiss guidelines and received ethical approval from the veterinary office of Basel-Stadt.

8.2.4 Drugs

GBRs were activated by GABA (Cat.No. 0344, Tocris Bioscience, UK) at final concentrations as indicated. GBR inverse agonist CGP54626 hydrochloride (Cat.No. 1088, Tocris Bioscience, UK) was used at final concentrations as indicated.

8.2.5 Co-immunoprecipitation and western blot

Co-immunoprecipitation and western blot analysis was performed as described in (Dinamarca et al., 2019). Briefly, transfected HEK293T cells were washed once with ice-cold PBS, lysed in NETN buffer (100 mM NaCl, 1 mM EDTA, 0.5% Nonidet P-40, 20 mM Tris/HCl, pH 7.4) supplemented with cOmplete™ EDTA-free protease inhibitor cocktail (Cat.No. 11873580001, Hoffmann-La Roche, Basel, CH) and harvested using a cell scraper. After rotation for 10 min at 4°C, lysates were cleared by centrifugation at full speed for 10 min at 4°C and the lysates were used directly for western blotting (input) or immunoprecipitation. Immunoprecipitation was performed according to the manufacturer's manual of Dynabeads® Protein G (Cat.No. 1004D, Thermo Fisher Scientific, MA, US). 1 µg mouse anti-Myc clone 9E10 antibody (Cat.No. sc-40, Santa Cruz Biotechnologies, TX, US) diluted in 200 µL PBS supplemented with 0.1% Tween®-20 (Cat.No. 93773, Sigma-Aldrich, MO, US) was bound to 1 mg Dynabeads® by rotation for 15 min at RT. After washing Dynabeads®-antibody complexes once with PBS + 0.1% Tween®-20, the lysate was added and incubated with rotation for 15 min at RT to allow the antigen to bind the Dynabead®-antibody complex. After washing the Dynabeads®-antibody-antigen complex four times with PBS + 0.1% Tween®-20, proteins were uncoupled and denatured by 1x Lämmli Buffer. Lysate and immunoprecipitations were resolved using standard SDS-PAGE and probed with the primary antibodies rabbit anti-Myc (1:1'000, Cat.No. C3956, Sigma-Aldrich, MO, US) and rabbit anti-RFP (1:1'000, Cat.No. ab62341, Abcam, Cambridge, United Kingdom) and incubated in PBS containing 5% nonfat dry milk and 0.1% Tween®-20 over night at 4°C on a rotary shaker. After washing the membrane thrice with PBS + 0.1% Tween®-20, peroxidase-coupled secondary donkey anti-rabbit IgG antibodies (1:10'000, Cat.No. NA9340V, Amersham Biosciences, Little Chalfont, United Kingdom) were probed and incubated in PBS containing 5% nonfat dry milk and 0.1% Tween®-20 for 45 min at RT on a

rotary shaker. SuperSignal™ Femto chemiluminescence detection kit (Cat.No. 34096, Thermo Fisher Scientific, MA, US) was used for visualization using a Fusion FX Chemiluminescence System (Vilber Lourmat, Witec AG, Sursee, CH).

8.2.6 BRET assay

BRET measurements were performed as described in (Dinamarca et al., 2019; Ivankova et al., 2013; Turecek et al., 2014). HEK293T cells were transiently transfected with GBRs (Flag-GB1a and Flag-GB2 plasmids) and the G protein heterotrimer (Gαo-RLuc, Gβ2 and Venus-Gγ2 plasmids) with or without AJAP1, AJAP1-SDBM, PIANP, or PIANP-SDBM plasmid in Opti-MEM™ (Cat.No. 31985070, Gibco, Thermo Fisher Scientific, MA, US). To elucidate the effect of AJAP1 or PIANP on transcellular GB1a/2 receptors the cells were separated into two pools: 1) HEK293T cells transiently transfected with GBR (Flag-GB1a and Flag-GB2 plasmids) and the G protein heterotrimer (Gαo-RLuc, Gβ2 and Venus-Gγ2 plasmids), and 2) HEK293T cells transiently transfected with either empty pCI plasmid, AJAP1, AJAP1-SDBM, PIANP, or PIANP-SDBM. Six hours later, transfected HEK293T cells were dislodged with 0.25% Trypsin-EDTA (Cat.No. 25200056, Gibco, Thermo Fisher Scientific, MA, US), collected with pre-warmed DMEM-GlutaMAX™ supplemented with 10% FBS and 2% penicillin and streptomycin, centrifuged at RT with 230 x g, and resuspended in 1 mL pre-warmed DMEM-GlutaMAX™ supplemented with 10% FBS and 2% penicillin and streptomycin. Equal amount of cells from pool 1) and 2) were combined and mixed by gently pipetting up and down. Transfected HEK293T cells were distributed into 96-well microplates (7.655 083, Greiner Bio-One, Kremsmünster, AUT) at a density of 100,000 cells/well. Eighteen hours later cells were washed and coelenterazine h (Cat.No. 301, NanoLight Technologies, AZ, USA) at a final concentration of 5 µM was added for 5min. Luminescence and fluorescence signals were detected alternatively for a total of 708s using a Spark® microplate reader (Tecan, Männerdorf, CH). Indicated concentrations of GABA or CGP54626 hydrochloride were injected with the Spark® microplate reader injection system at 134s or 417s, respectively. The BRET ratio was calculated as the ratio of the light emitted by Venus-Gγ2 (530 - 570nm) over the light emitted by Gαo-RLuc (370 – 470nm) and were adjusted by subtracting the ratios obtained when RLuc fusion proteins were expressed alone. Each data point represents a technical triplicate.

8.2.7 Neuron / HEK293T co-culture, immunocytochemistry and image analysis

Embryonic day 16.5 GB1-GFP mouse hippocampi were dissected in ice-cold HBSS medium (Cat.No. 14170–088, Gibco, Thermo Fisher Scientific, MA, US), digested with 0.25% trypsin (Cat.No. 17504-044, Gibco, Thermo Fisher Scientific, MA, US) in HBSS medium for 12 min at 37 °C, dissociated by trituration and plated on Ø13 mm glass coverslips (Cat.No. 631-0150, VWR International, PA, US) coated with 1 mg / mL poly-L-lysine hydrobromide (Cat.No. P9155, Sigma-Aldrich, MO, US) in 0.1 M borate buffer (boric acid / sodium tetraborate, Cat.No. 0500 & 6308, respectively, Merck KGaA, Darmstadt, DE). Neurons were seeded at a density of ~210 cells / mm^2 in MEM medium (Cat.No. M4655, Sigma-Aldrich, MO, US) containing 10% horse serum (Cat.No. 26050-070, Gibco, Thermo Fisher Scientific, MA, US) and 0.6 % glucose (Cat.No. G8769, Sigma-Aldrich, MO, US) and cultured at 37 °C in a humidified incubator (5% CO_2). After 2h, medium was replaced with Neurobasal medium (Cat.No. 21103-049, Gibco, Thermo Fisher Scientific, MA, US) supplemented with B-27™ (Cat.No. 17504-044, Gibco, Thermo Fisher Scientific, MA, US) and 1% GlutaMAX™ Supplement (Cat.No. 35050-061, Gibco, Thermo Fisher Scientific, MA, US). HEK293T cells were transiently transfected with either AJAP1-mCherry, AJAP1-SDBM-mCherry, PIANP-mCherry or PIANP-SDBM-mCherry. Transfected cells were distributed at a density of 158 cells/mm^2 on coverslips containing DIV7 cultured hippocampal neurons of GB1-GFP mice. HEK293T / hippocampal neuron co-cultures were fixed at DIV9 by immersion in phosphate buffered saline (PBS) containing 4% paraformaldehyde (Cat.No. P6148, Sigma-Aldrich, MO, US) for 10 min at RT. After rinsing in PBS, cells were permeabilized with 0.1% Triton™ X-100 (Cat.No. X100, Sigma-Aldrich, MO, US) in PBS containing 5% goat serum (Cat.No. 16210, Gibco , Thermo Fisher Scientific, MA, US) for 10 min at RT. Cell cultures were incubated with the following primary antibodies diluted in PBS containing 5% goat serum for 2h at RT: Chicken anti-MAP2 (Cat.No. ab5392, Abcam,

Cambridge, United Kingdom), rabbit anti-GFP (Cat.No. ab209, Abcam, Cambridge, United Kingdom). After washing with PBS, cells were incubated with the following secondary antibodies for 45 min at RT: Donkey anti-chicken IgY Alexa Fluor® 647 (Cat.No. AP194SA6, Merck KGaA, Darmstadt, DE), goat anti-rabbit IgG Alexa Fluor® 488 (Cat.No. A-11008, Thermo Fisher Scientific, MA, US). Coverslips were mounted with Fluoromount™ mounting medium (Cat.No. F4680, Merck KGaA, Darmstadt, DE). Images were captured by point scanning confocal airyscan Zeiss microscope (LSM 880, Carl Zeiss Microscopy, Jena, Germany) equipped with Plan-Apochromat x63/1.4 Oil objective. For the quantification of GB1 GFP fluorescence images were analyzed with ImageJ 1.53C. GFP fluorescence intensities were measured in dendrites at a minimal distance of 5 μm from the cell soma. GFP intensities were normalized to the measured area. GB1 GFP fluorescence intensity ratios were calculated by dividing the measured GFP fluorescence of dendrite / HEK293T contact sites normalized to the area by the GFP fluorescence of dendrites in the absence of HEK293T contact sites normalized to the area using Excel (Microsoft, NM, US).

8.2.8 SRE-Luciferase accumulation assay

HEK293 cells stably expressing Gαqi were transiently transfected with GBRs (Flag-GB1a and Flag-GB2 plasmids) and SRE-FLuc plasmid with or without AJAP1, AJAP1-SDBM, PIANP, or PIANP-SDBM plasmid in Opti-MEM™ (Cat.No. 31985070, Gibco, Thermo Fisher Scientific, MA, US). To elucidate the effect of AJAP1 or PIANP on transcellular GB1a/2 receptors the cells were separated into two pools: 1) HEK293-Gαqi cells transiently transfected with GBR (Flag-GB1a and Flag-GB2 plasmids) and the SRE-FLuc plasmid, and 2) HEK293-Gαqi cells transiently transfected with either AJAP1, AJAP1-SDBM, PIANP, or PIANP-SDBM. Six hours later, transfected HEK293-Gαqi cells were dislodged with 0.25% Trypsin-EDTA (Cat.No. 25200056, Gibco, Thermo Fisher Scientific, MA, US), collected with pre-warmed DMEM-GlutaMAX™ supplemented with 10% FBS and 2% penicillin and streptomycin, centrifuged at RT with 230 x g, and resuspended in 1 ml pre-warmed DMEM-GlutaMAX™ supplemented with 10% FBS and 2% penicillin and streptomycin. Equal amount of cells from pool 1) and 2) were combined and mixed by gently pipetting up and down. Transfected cells were distributed into 96-well microplates (7.655 083, Greiner Bio-One, Kremsmünster, AUT) at a density of 100,000 cells/well. Twenty-four hours later, the culture medium was replaced with Opti-MEM™ supplemented with GlutaMAX™ (Cat.No. 51985042, Thermo Fisher Scientific, MA, US) and 2% penicillin and streptomycin. GB1a/2 receptors were activated with the indicated concentrations of GABA in Opti-MEM™ supplemented with GlutaMAX™ and 2% penicillin and streptomycin. Fifteen hours later, cells were lysed and FLuc activity was measured according to the standard Dual-Luciferase® Assay Kit (E1910, Promega, WI, USA) using a Spark® microplate reader (Tecan, Männerdorf, CH). Luminescence signals were adjusted by subtracting the luminescence obtained when SRE-FLuc fusion proteins were expressed alone.

8.2.9 Statistical analysis

Data was analyzed with GraphPad Prism version 8 (GraphPad Software, CA, USA). The normality of individual data sets were tested with the Shapiro-Wilk (for n < 8) or D'Agostino-Pearson test (for n ≥ 8). Statistical significance between two groups was assessed by unpaired two-tailed student's t-test (parametric) and between three groups by ordinary ANOVA with Dunnett's multiple comparisons test. The non-parametric Mann-Whitney test was used for non-normal distribution. Statistical significance between dose-response curves was assessed by extra sum-of-squares F test of non-linear regression curve fits. P-values < 0.05 were considered significant. Data are presented as mean ± standard error of mean (SEM).

8.3 Results

8.3.1 Amino acids 106 – 111 of PIANP mediate the interaction with SD1 of GB1a.

Sequence alignment of APP, AJAP1, and PIANP shows a conserved WG motif within amino acids 208 – 213, 181 – 186, and 106 – 111, respectively (Fig. 8.1a). Two-dimensional 1H-15N heteronuclear single quantum coherence (HSQC) spectra analysis of APP, AJAP1, and PIANP in complex with the SD1/2 identified these amino acids as crucial for SD1 binding. Deletion of amino acids 202 – 219 of APP and the mutation to alanine of amino acids 181 – 186 of AJAP1 (AJAP1-SDBM) abolished the interaction with SD1 of GB1a (Dinamarca et al., 2019). Because PIANP shares the six amino acid stretch containing the conserved WG motif, it is conceivable that they also mediate the interaction with GB1a. Subsequent replacement of amino acids 106 – 111 of PIANP with alanine (PIANP-SDBM) abrogated SD1 binding in co-immunpprecipitation experiments (Fig 8.1b). The existence of a conserved sequence within APP, AJAP1, and PIANP that binds to SD1 of GB1a is in line with the formation of distinct complexes (Dinamarca et al., 2019). On the one hand, AJAP1 and PIANP are found at adherens junctions that connect pre- and postsynaptic membranes, and on the other hand, APP mediates trafficking of GB1a/2 receptors to the cell surface. Hence, it is thinkable that GB1a/2 receptors are trafficked to cell surfaces by APP and then transferred to AJAP1 or PIANP that precisely localize GB1a/2 receptors and/or influence GB1a/2 receptor activity.
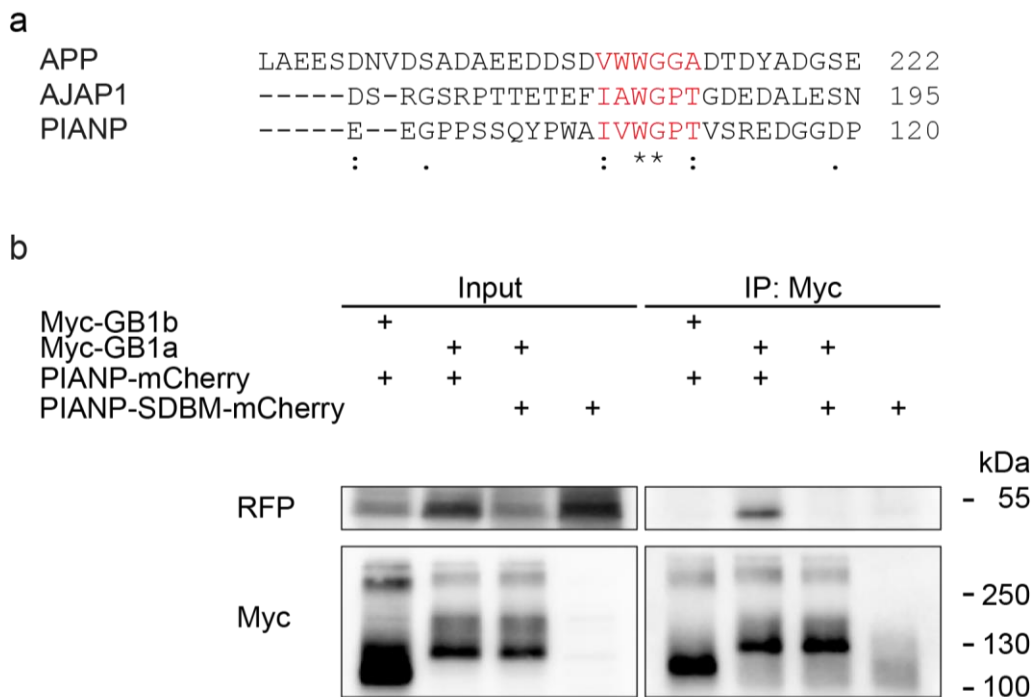
Figure 8.1 Amino acids 106 – 111 of PIANP mediate the interaction with SD1 of GB1a. **a** Sequence alignment of APP, AJAP1, and PIANP. Residues critical for binding SD1 are shown in red. **b** Mutations to alanine of the binding epitopes in PIANP prevent binding to GB1a. Immunoprecipitations using anti-Myc antibodies from HEK293T cells expressing Myc-GB1b, Flag-GB2 together with PIANP-mCherry (negative control) or HEK293T cells expressing Myc-GB1a, Flag-GB2 together with either PIANP-mCherry or PIANP-SDBM-mCherry. HEK293T cells expressing only PIANP-SDBM-mCherry represent the IP control.

8.3.2 AJAP1 and PIANP do not influence GB1a/2 receptor-mediated G protein signaling *in cis*.

GBR activation by an agonist induces conformational changes of the receptor resulting in G protein activation (Shaye et al., 2020). It has been reported that sAPPα binds SD1 and leads to GBR activation (Muller et al., 2017; Rice et al., 2019), suggesting that binding outside of the orthosteric binding site is able to promote the active conformation of GBRs. To elucidate whether the interaction of AJAP1 or PIANP with SD1 modulates GB1a/2 receptor activity, I performed bioluminescence resonance energy transfer (BRET) experiments measuring GB1a/2 receptor-mediated G protein activation using Gαo-renilla Luciferase (RLuc) and Gγ2-Venus (Fig. 8.2a). The presence of AJAP1 or PIANP did not influence the baseline BRET (Fig. 8.2b, c). Similar basal BRET levels indicate that AJAP1 or PIANP do not stabilize GB1a/2 receptors at cell surfaces because increased surface levels of GB1a/2 receptors would result in elevated levels of trimeric G proteins. GBRs are known to exhibit constitutive activity that is blocked by inverse agonists (Grunewald et al., 2002). Blockade of constitutive GBR activity promotes the trimeric state of G proteins. Therefore, unchanged basal BRET levels additionally suggest that AJAP1 and PIANP do not influence constitutive GB1a/2 receptor activity. Positive allosteric modulators stabilize the active conformation of GBRs, thereby increasing the GBR response in the presence of agonist (Evenseth et al., 2020). In contrast, negative allosteric modulators stabilize the inactive conformation of GBRs, thereby attenuating the GBR response (Sun et al., 2016). It is conceivable that the interaction of AJAP1 or PIANP with SD1 induces conformational changes favoring either the active or the inactive conformation of GB1a/2 receptors. In the presence of AJAP1 or PIANP, the magnitude of G protein activation upon GB1a/2 receptor stimulation with 10 µM GABA was unchanged, suggesting the absence of allosteric modulation of GB1a/2 receptors (Fig. 8.2b, d). In case of increased GB1a/2 receptor surface levels or blocked constitutive activity of GB1a/2 receptors, the magnitude of G protein activation would be increased. Hence, the unchanged GB1a/2 receptor activation in the presence of AJAP1 or PIANP further supports that neither AJAP1 nor PIANP influences GB1a/2 receptor stabilization at cell surfaces or constitutive GB1a/2 receptor activity. Elevated levels of GB1a/2 receptors at cell surfaces lead to an increased amount of trimeric G proteins upon GB1/2 receptor blockade. Blockade of activated GB1a/2 receptors with the inverse agonist CGP54626 in the presence of AJAP1 or PIANP showed a similar magnitude of BRET changes, supporting that AJAP1 and PIANP do not affect surface levels of GB1a/2 receptors (Fig. 8.2b & e). Of note, after GB1a/2 receptor blockade, BRET levels rose above baseline, indicating constitutive activity of GB1a/2 receptors in the presence and absence of AJAP1 or PIANP. Taken together, these data indicate that the interaction of AJAP1 or PIANP with SD1 does not change the surface level or the conformation of GB1a/2 receptors *in cis*.

Figure 8.2 AJAP1 and PIANP do not influence GB1a/2 receptor-induced G protein signaling. **a** Scheme depicting the assay monitoring G protein activation using BRET between Gαo-RLuc and Venus-Gγ2. **b** *Left* Individual experiments showing BRET changes in HEK293T cells expressing GB1a/2 in the absence (black) or the presence of either AJAP1 (blue) or AJAP1-SDBM (light blue). *Right* Individual experiments are showing BRET changes in HEK293T cells expressing GB1a/2 in the absence (black) or the presence of either PIANP (magenta) or PIANP-SDBM (light magenta). In all cases, GB1a/2 receptor activation by 10 µM GABA leads to the dissociation of heterotrimeric G proteins and a consequent decrease in BRET. Block of activated GB1a/2 receptors by 25 µM of the inverse agonist CGP54626 increased BRET above baseline, indicating constitutive GB1a/2 receptor activity. **c** Bar graphs of basal BRET levels determined in experiments as in **b**. **d** Bar graphs of BRET changes induced by 10 µM GABA determined in experiments as in **b**. **e** Bar graphs of BRET changes induced by 25 µM CGP54626 determined in experiments as in **b**. Data are means ± SEM. The number of independent experiments is indicated in the bar graphs. ns, not significant, one-way ANOVA with Dunnett's multiple comparison test against GB1a/2.
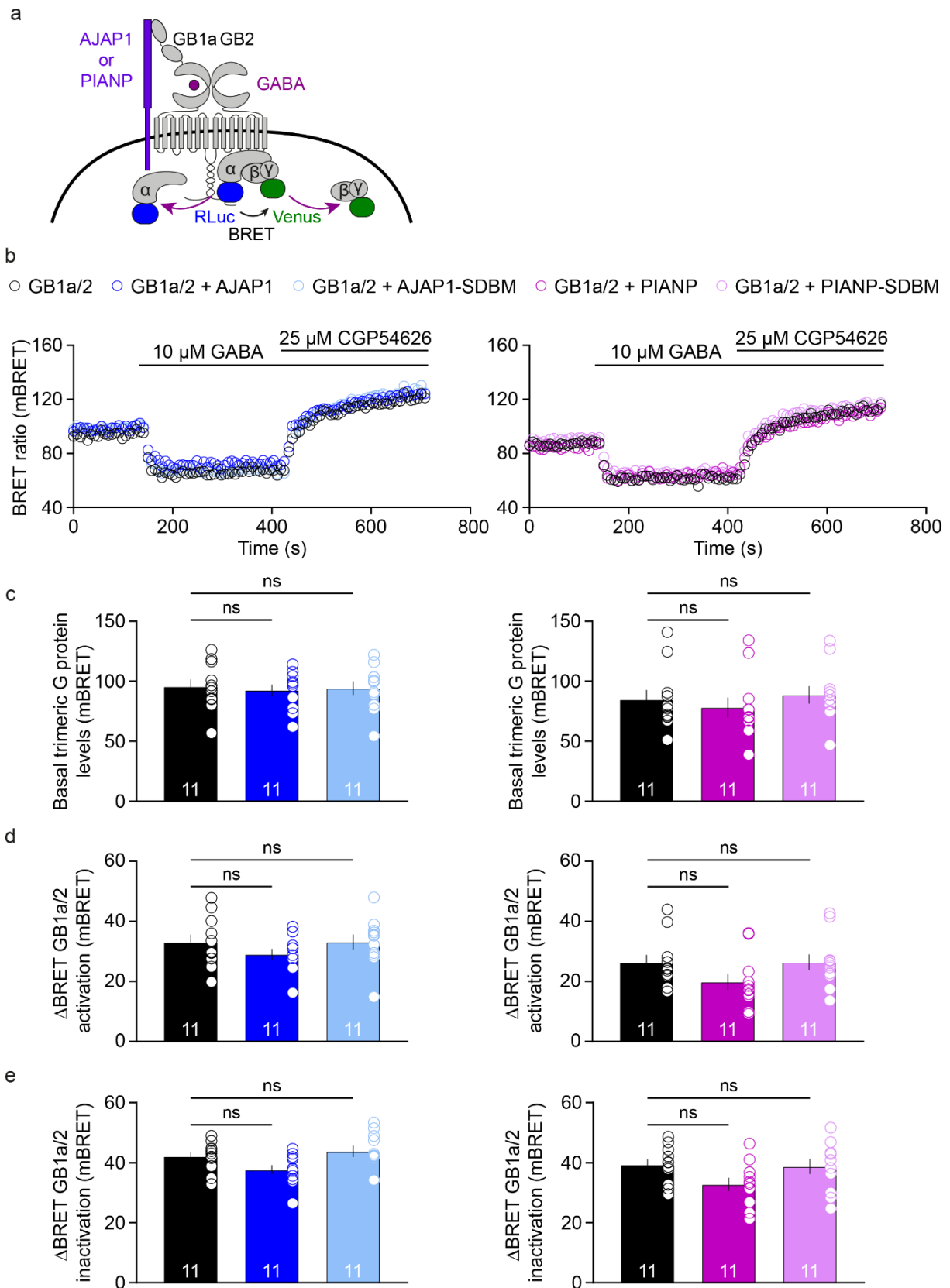
a

AJAP1 or PIANP   GB1a GB2

GABA

RLuc   Venus

BRET

b

○ GB1a/2   ○ GB1a/2 + AJAP1   ○ GB1a/2 + AJAP1-SDBM   ○ GB1a/2 + PIANP   ○ GB1a/2 + PIANP-SDBM

c

d

e

Figure 8.2 legend on previous page

8.3.3 AJAP1 and PIANP decrease the efficacy of GB1a/2 receptor mediated PLC activity independent of GB1a binding.

Examination of potential subtle allosteric properties of AJAP1 or PIANP at GB1a/2 receptors requires a robust and sensitive assay that generates dose-response curves. Therefore, GB1a/2 receptors were artificially coupled to Phospholipase C (PLC) by expressing chimeric G protein subunit Gαqi stably integrated into the genome of HEK293 (HEK293-Gαqi) cells. GB1a/2 receptor activation is monitored by the expression and accumulation of Firefly-Luciferase (FLuc) under the serum response element (SRE). Hence, activation of GB1a/2 receptors by various GABA concentrations over a long period leads to the accumulation of FLuc that will potentiate small allosteric effects (Fig. 8.3a). Positive allosteric modulators increase the basal activity of GBRs, shift the half-maximal effective concentration (EC50) towards lower agonist concentrations, and elevate the maximum efficacy (EMax) (Pin and Prezeau, 2007). In contrast, negative allosteric modulators reduce the basal activity of GBRs, shift the EC50 towards higher concentrations, and reduce the EMax (Chen et al., 2014; Sun et al., 2016). In the absence of agonists, the presence of AJAP1 or PIANP did not change the basal FLuc activity, supporting that constitutive activity of GB1a/2 receptors is not altered by AJAP1 or PIANP (Fig. 8.3b). The EC50 values did also not shift when AJAP1 or PIANP were co-expressed with GB1a/2 receptors, indicating that AJAP1 and PIANP do not influence GABA potency at GB1a/2 receptors (Fig. 8.3b). Unexpectedly, the EMax of GB1a/2 receptors was significantly reduced in the presence of AJAP1 or PIANP, as well as in the presence of AJAP1-SDBM and PIANP-SDBM, suggesting that the reduction in the EMax is independent of GB1a binding (Fig. 8.3b). There is evidence that AJAP1 represses gene transcription and attenuates β-catenin reporter activity (Han et al., 2017; Zeng et al., 2014b). Therefore, it is conceivable that AJAP1 interferes with the PLC pathway artificially coupled to GB1a/2 receptor activity, resulting in an EMax reduction. Despite the lack of evidence that PIANP is involved in the regulation of gene transcription, the homology with AJAP1 suggests the ability of PIANP to interfere with the PLC pathway as well. All together, the interaction of AJAP1 or PIANP with SD1 does not exert allosteric properties at GB1a/2 receptors *in cis*.

Figure 8.3 AJAP1 and PIANP decrease the efficacy of GB1a/2 receptor-mediated PLC activity independent of GB1a binding. **a** Scheme is depicting the assay monitoring PLC dependent FLuc expression under control of the serum response element (SRE). GB1a/2 receptors were artificially coupled to PLC by expressing the chimeric G protein subunit Gαqi stably integrated into the genome of HEK293 cells. **b** *Left* Dose-response curves of GABA-induced FLuc activity in cells expressing SRE-FLuc sensor together with GB1a/2 in the absence (black) or in the presence of either AJAP1 (blue) or AJAP1-SDBM (light blue). A single curve does not fit all data sets (p < 0.0001). The presence of both AJAP1 and AJAP1-SDBM decreased the efficacy of GB1a/2 receptor-mediated FLuc expression (p < 0.0001), indicating that this effect is independent of GB1a binding. The basal GB1a/2 receptor-mediated FLuc expression or EC50 values are unchanged. *Bottom* Table showing the basal, EC50, and maximum efficacy (Emax) values derived from the curve fit. *Right* Dose-response curves of GABA-induced FLuc activity in cells expressing SRE-FLuc sensor together with GB1a/2 in the absence (black) or the presence of either PIANP (magenta) or PIANP-SDBM (light magenta). A single curve does not fit all data sets (p < 0.0001). The presence of both PIANP and PIANP-SDBM decreased the efficacy of GB1a/2 receptor-mediated FLuc expression (p = 0.0052 and p < 0.0001, respectively), indicating that this effect is independent of GB1a binding. The basal GB1a/2 receptor-mediated FLuc expression and EC50 values do not differ significantly from one another. *Bottom* Table showing the basal, EC50, and Emax values derived from the curve fit. Data are presented as mean ± SEM with a non-linear regression curve fit of 8 independent experiments. Statistical differences were analyzed by the extra sum-of-squares F test.

a

b
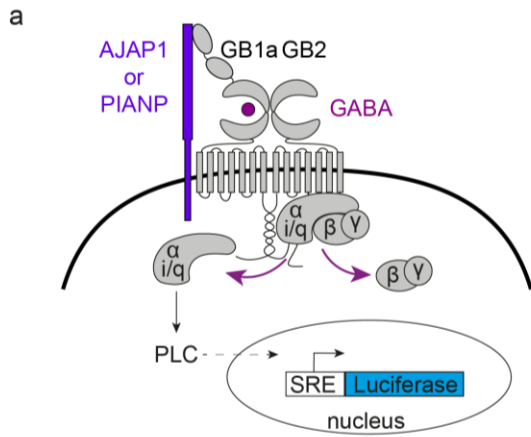
⊖ GB1a/2   ⊖ GB1a/2 + AJAP1   ⊖ GB1a/2 + AJAP1-SDBM   ⊖ GB1a/2 + PIANP   ⊖ GB1a/2 + PIANP-SDBM
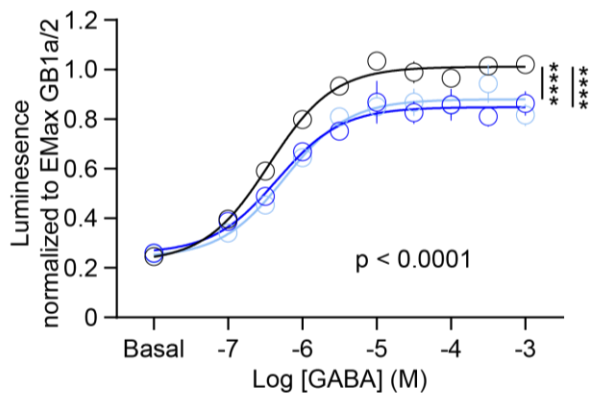
	Basal	EC50 µM	EMax	N
GB1a/2	0.22	0.36	1.01	8
GB1a/2 + AJAP1	0.26	0.45	0.85	8
GB1a/2 + AJAP1-SDBM	0.24	0.57	0.88	8
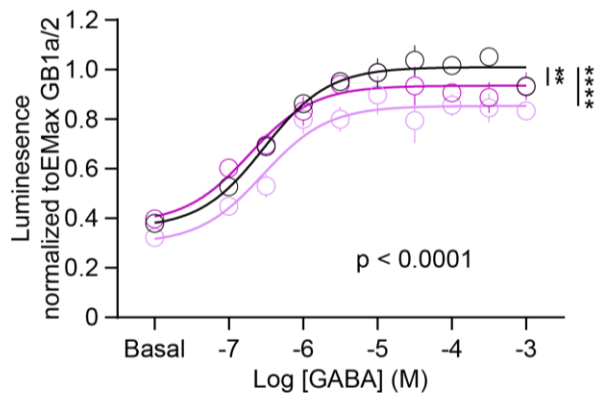
	Basal	EC50 µM	EMax	N
GB1a/2	0.36	0.30	1.01	8
GB1a/2 + PIANP	0.38	0.19	0.94	8
GB1a/2 + PIANP-SDBM	0.30	0.29	0.85	8

Figure 8.3 legend on previous page

121

8.3.4 AJAP1 and PIANP recruit and cluster transcellular GB1a in a neuron/HEK293T co-culture assay.

The postsynaptic localization of AJAP1 (S. Früh personal communication), together with an impaired presynaptic GBR activity in AJAP1-KO mice (T. Lalanne personal communication), suggests that the interaction between AJAP1 and SD1 of GB1a occurs *in trans*. To address this hypothesis, I co-cultured hippocampal neurons expressing endogenous GB1 tagged with a GFP (Casanova et al., 2009) together with HEK293T cells expressing AJAP1-mCherry (Fig. 8.4a) or AJAP1-SDBM-mCherry (Fig. 8.4b). At contact sites between dendrites and HEK293T cells expressing AJAP1-mCherry, the GB1-GFP signal was increased compared to the GB1a-GFP signal in dendrites in the absence of HEK293 cells, indicating that AJAP1 recruits and clusters transcellular GB1 (Fig. 8.4c & e). GB1-GFP signals in dendrites showed no difference whether HEK293T cells expressing AJAP1-SDBM-mCherry were in contact or not, supporting that GB1-GFP clustering by transcellular AJAP1 is specific to SD1 binding (Fig. 8.4d & f). The GB1-GFP intensity ratio (Fig. 8.4g) in presence of AJAP1-mCherry was significantly different from one, supporting the specific recruitment and clustering of transcellular GB1-GFP (Fig. 8.4h). In contrast, the GB1-GFP intensity ratio in presence of AJAP1-SDBM was not different from one, indicating equal amounts of GB1 in dendrites in the presence or the absence of HEK293T cells expressing AJAP1-SDBM (Fig. 8.4h). The GB1-GFP intensity ratios from the conditions of AJAP1-mCherry and AJAP1-SDBM-mCherry significantly differ from one another, showing that SD1 binding induces the recruitment and clustering of GB1 (Fig. 8.4h). Similar to AJAP1, PIANP binds SD1 of GB1a. PIANP-KO mice show altered presynaptic localization of GBRs, and exhibit impaired presynaptic GBRs activity (Winkler et al., 2019), suggesting that PIANP binds GB1a/2 receptors *in trans* as well. I used the same co-culture assay as above, co-culturing neurons expressing endogenous GB1-GFP with HEK293T cells expressing either PIANP-mCherry (Fig. 8.5a) or PIANP-SDBM-mCherry (Fig. 8.5b). Indeed, at contact sites between dendrites and HEK293T cells expressing PIANP-mCherry elevated GB1-GFP signals were observable compared to the GB1-GFP signal in dendrites in the absence of HEK293 cell contact, showing that PIANP recruits and clusters transcellular GB1 (Fig. 8.5c & e). Of note, clustered GB1-GFP signal at contact sites with HEK293T cells expressing PIANP-mCherry that lack MAP2 staining represents axonal GB1. GB1-GFP signal in the presence or absence of transcellular PIANP-SDBM-mCherry were similar, indicating that the recruitment and the clustering of GB1-GFP are specifically due to the interaction of PIANP with SD1 (Fig. 8.5d & f). The GB1-GFP intensity ratio (Fig. 8.5g) in presence of PIANP-mCherry was significantly different from one, supporting the specific recruitment and clustering of GB1-GFP (Fig. 8.5h). In comparison, the GB1-GFP intensity ratio in presence of PIANP-SDBM-mCherry was similar to one, indicating equal amounts of GB1 in dendrites in the presence or the absence of HEK293T cells expressing PIANP-SDBM-mCherry (Fig. 8.5h). The GB1-GFP intensity ratios from the conditions of PIANP-mCherry and PIANP-SDBM-mCherry significantly differ from one another, showing that SD1 binding induces the recruitment and clustering of GB1 (Fig. 8.5h). Collectively, these data show that AJAP1 and PIANP recruit and cluster GB1a *in trans*.

a AJAP1-mCherry

b AJAP1-SDBM-mCherry

c dendrite / HEK293T contact site

AJAP1-mCherry   GB1-GFP

Map2   Merge

d dendrite / HEK293T contact site

AJAP1-SDBM-mCherry   GB1-GFP

Map2   Merge

e No dendrite / HEK293T contact site

AJAP1-mCherry   GB1-GFP

Map2   Merge

f No dendrite / HEK293T contact site

AJAP1-SDBM-mCherry   GB1-GFP

Map2   Merge

g

$$\text{GB1-GFP fluorescence intensity ratio} = \frac{\text{GB1-GFP fluorescence intensity at dendrite / HEK293T contact sites normalized to area}}{\text{GB1-GFP fluorescence intensity in dendrites without HEK293T contact sites normalized to area}}$$
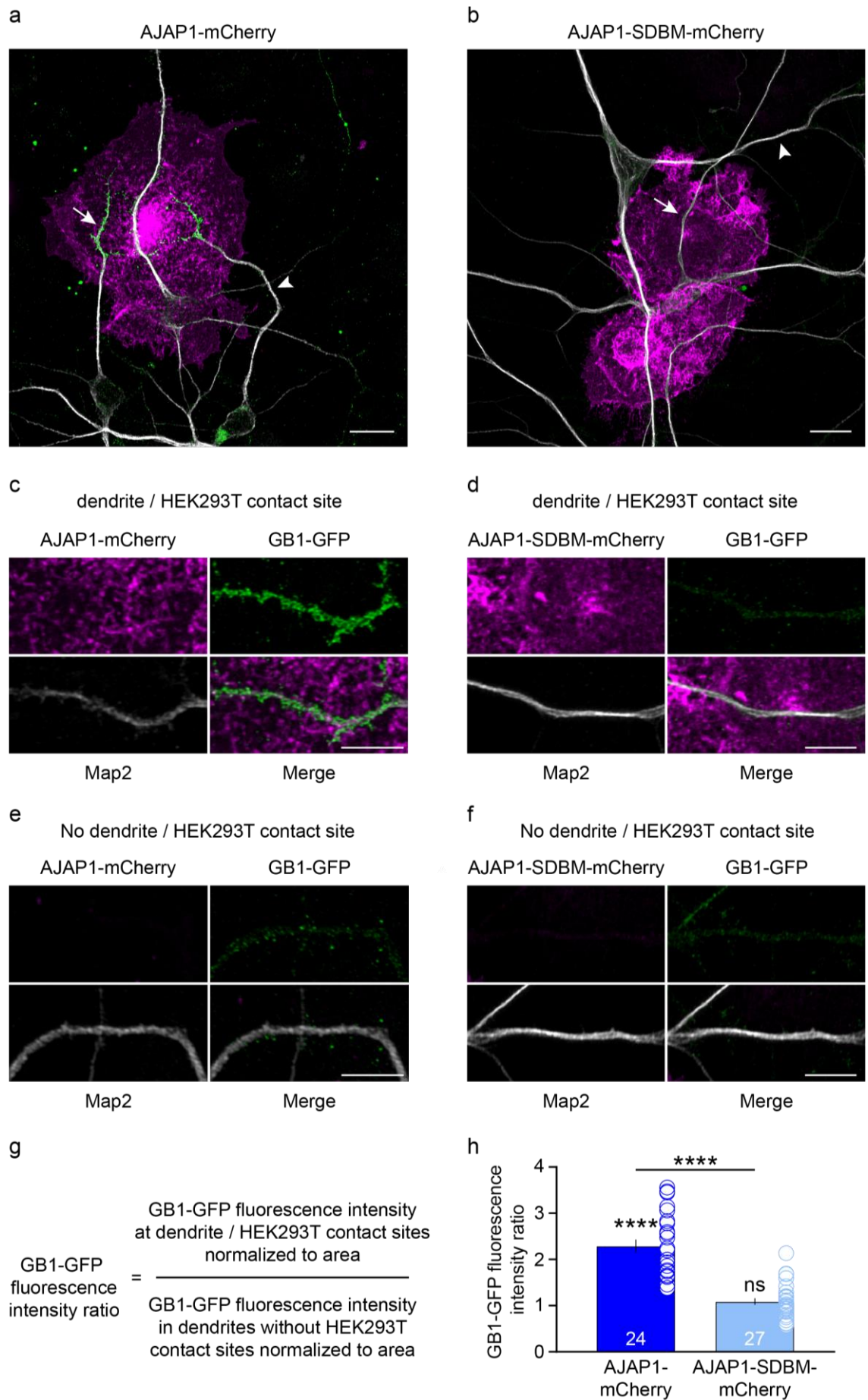
h

Figure 8.4 legend on next page

Figure 8.4 AJAP1 recruits and clusters transcellular GB1 in a neuron/HEK293T co-culture assay. Representative confocal images of hippocampal neurons expressing endogenous GB1 tagged with GFP co-cultured at DIV7 with HEK293T cells expressing either AJAP1-mCherry (**a**) or AJAP1-SDBM-mCherry (**b**). Neuron/HEK293T co-cultures were fixed at DIV9, permeabilized, and stained with anti-GFP antibody (green) to amplify GB1 detection and anti-MAP2 antibody (gray) to mark dendrites. Arrows indicate contact sites between dendrites and HEK293T cells, whereas the arrowheads point to sites where dendrites and HEK293T cells are not in contact with one another. Note that GB1 clusters at contact sites between dendrites and HEK293T cells expressing AJAP1-mCherry. Scale bar 10 µm. **c** Higher magnification of the contact site between dendrites and HEK293T cells expressing AJAP1-mCherry (magenta) from **a**. Scale bar 5 µm. **d** Higher magnification of the contact site between dendrites and HEK293T cells expressing AJAP1-SDBM-mCherry (magenta) from **b**. Scale bar 5 µm. **e** Higher magnification of dendrites in the absence of HEK293T cell contacts from the same neuron/HEK293T cell co-culture as in **a**. Scale bare 5 µm. **f** Higher magnification of dendrites in the absence of HEK293T cell contacts from the same neuron/HEK293T cell co-culture as in **b**. Scale bare 5 µm. **g** Definition of GB1-GFP fluorescence intensity ration used to determine clustering of transcellular GB1. **h** Bar graphs of GB1-GFP fluorescence intensity ratios determined in experiments as in **a** and **b**. The GB1-GFP fluorescence intensity ratio significantly differs from one only in the condition with AJAP1-mCherry ($p < 0.0001$), showing GB1 recruitment and clustering at contact sites between dendrites and HEK293T cells expressing AJAP1-mCherry. The GB1-GFP intensity ratios from the conditions of AJAP1-mCherry and AJAP1-SDBM-mCherry significantly differ from one another ($p < 0.0001$), showing that SD1 binding induces the recruitment and clustering of GB1. Data are means ± SEM. The number of neurons analyzed of 4 independent experiments is indicated in the bar graph. ****$p < 0.0001$, One sample t-test against 1; ****$p < 0.0001$; Mann-Whitney test (non-parametric).

Figure 8.5 PIANP recruits and clusters transcellular GB1 in a neuron/HEK293T co-culture assay. Representative confocal images of hippocampal neurons expressing endogenous GB1 tagged with GFP co-cultured at DIV7 with HEK293T cells expressing either PIANP-mCherry (**a**) or PIANP-SDBM-mCherry (**b**). Neuron/HEK293T co-cultures were fixed at DIV9, permeabilized, and stained with anti-GFP antibody (green) to amplify GB1 detection and anti-MAP2 antibody (gray) to mark dendrites. Arrows indicate the contact sites between dendrites and HEK293T cells, whereas the arrowheads point to sites where dendrites and HEK293T cells are not in contact with one another. Note that GB1 clusters at contact sites between dendrites and HEK293T cells expressing PIANP-mCherry. Scale bar 10 µm. **c** Higher magnification of the contact site between dendrites and HEK293T cells expressing PIANP-mCherry (magenta) from **a**. Note that the GFP signal in the absence of MAP2 staining represents axonal GB1a. Scale bar 5 µm. **d** Higher magnification of the contact site between dendrites and HEK293T cells expressing PIANP-SDBM-mCherry (magenta) from **b**. Scale bar 5 µm. **e** Higher magnification of dendrites in the absence of HEK293T cell contacts from the same neuron/HEK293T co-culture as in **a**. Scale bare 5 µm. **f** Higher magnification of dendrites in the absence of HEK293T cell contacts from the same neuron/HEK293T co-culture as in **b**. Scale bare 5 µm. **g** Definition of GB1-GFP fluorescence intensity ration used to determine clustering of transcellular GB1. **h** Bar graphs of GB1-GFP fluorescence intensity ratios determined in experiments as in **a** and **b**. The GB1-GFP intensity ratio significantly differs from one only in the condition with PIANP-mCherry ($p = 0.0009$), showing GB1 recruitment and clustering at contact sites between dendrites and HEK293T cells expressing PIANP-mCherry. The GB1-GFP intensity ratios from the conditions of PIANP-mCherry and PIANP-SDBM-mCherry significantly differ from one another ($p = 0.0026$), showing that SD1 binding induces the recruitment and clustering of GB1. Data are means ± SEM. The number of neurons analyzed of 4 independent experiments is indicated in the bar graph. ***$p = 0.0009$, One sample t-test against 1; **$p = 0.0026$, Unpaired two-tailed student's t-test.

a   PIANP-mCherry

b   PIANP-SDBM-mCherry

c   dendrite / HEK293T contact site

PIANP-mCherry   GB1-GFP

Map2   Merge

d   dendrite / HEK293T contact site

PIANP-SDBM-mCherry   GB1-GFP

Map2   Merge

e   No dendrite / HEK293T contact site

PIANP-mCherry   GB1-GFP

Map2   Merge

f   No dendrite / HEK293T contact site

PIANP-SDBM-mCherry   GB1-GFP

Map2   Merge

g

$$\text{GB1-GFP fluorescence intensity ratio} = \frac{\text{GB1-GFP fluorescence intensity at dendrite / HEK293T contact sites normalized to area}}{\text{GB1-GFP fluorescence intensity in dendrites without HEK293T contact sites normalized to area}}$$
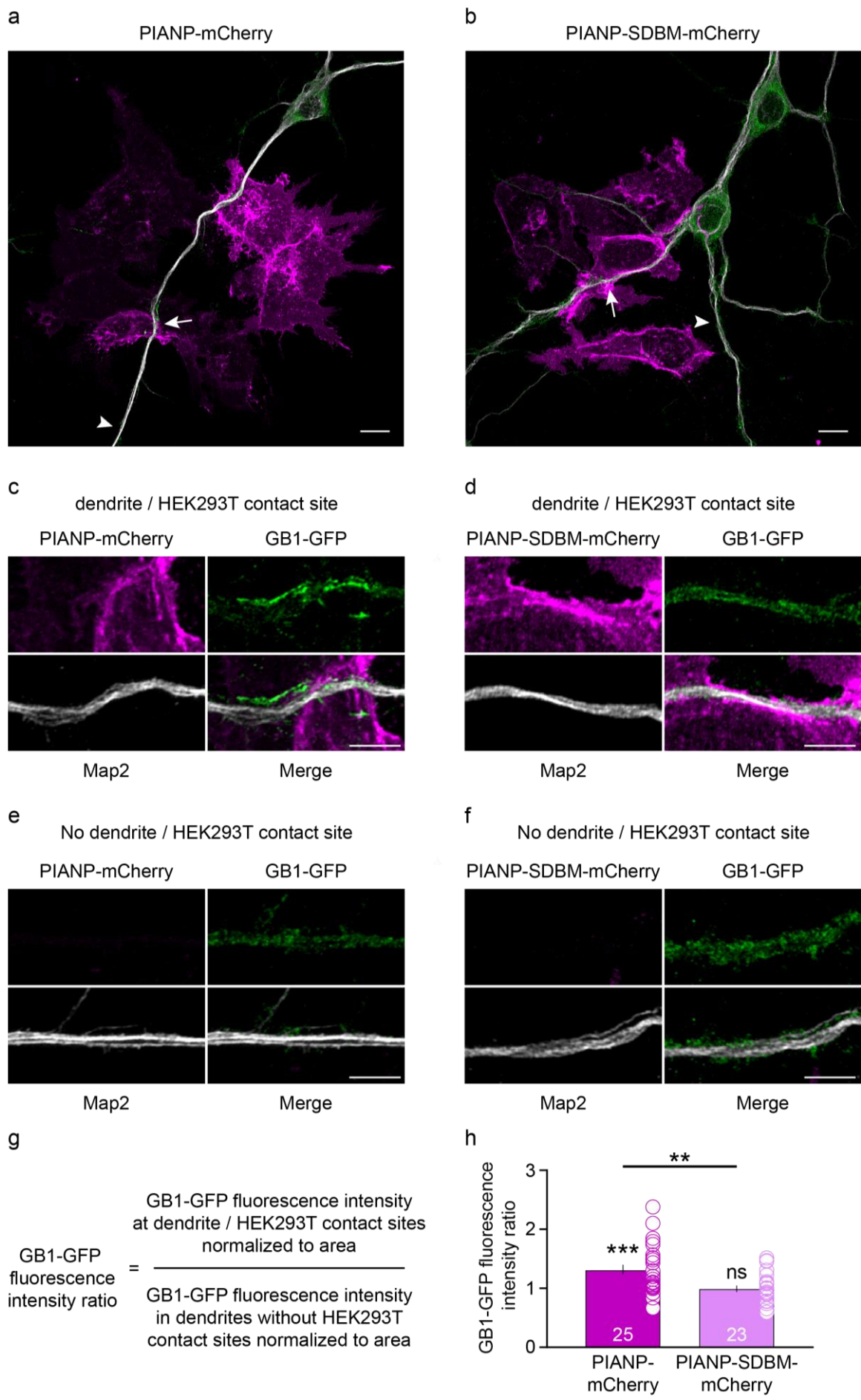
h

Figure 8.5 legend on previous page

8.3.5 AJAP1 and PIANP stabilize transcellular GB1a/2 receptors.

By interacting *in trans*, ELFN1 or ELFN2 exert allosteric properties at transcellular group III mGluRs (Dunn et al., 2018; Dunn et al., 2019). Hence, it is conceivable that binding of AJAP1 or PIANP to SD1 *in trans* influences transcellular GB1a/2 receptor activity. To elucidate this question, I took advantage of the BRET system mentioned above but used two different pools of transfected HEK293T cells to ensure GB1a/2 receptor binding exclusively *in trans*. The first pool of HEK293T cells expressed Gαo-RLuc and Gγ2-Venus together with GB1a/2 receptors and was exposed to the second pool of HEK293T cells expressing either AJAP1, AJAP1-SDBM, PIANP, or PIANP-SDBM. In the presence of AJAP1 or PIANP, basal trimeric G protein levels were significantly elevated, indicating increased levels of GB1a/2 receptors at cell surfaces and/or reduced constitutive GB1a/2 receptor activity (Fig. 8.6a, b & e, f). In both cases, GB1a/2 receptor activation would generate increased BRET decreases. Indeed, in the presence of AJAP1 or PIANP, GB1a/2 receptor activation with 10µM GABA lead to an increased change in BRET compared to control and SD1 binding deficient conditions (Fig. 8.6a, c & e, g). In the case that AJAP1 or PIANP stabilizes and elevates the levels of transcellular GB1a/2 receptor at cell surfaces, blockade of activated GB1a/2 receptors should lead to increased BRET changes. Enlarged changes in BRET upon blockade of activated GB1a/2 receptors with 25µM CGP54626 were observed in the presence of AJAP1 and PIANP, supporting that AJAP1 and PIANP stabilize and elevate surface levels of transcellular GB1a/2 receptors (Fig. 8.6a, d & e, h). Note that upon blockade of activated GB1a/2 receptors, BRET levels rose above baseline, indicating the presence of constitutive activity in all conditions. To further analyze whether AJAP1 or PIANP influences constitutive activity of GB1a/2 receptors *in trans*, GB1a/2 receptors were blocked by the inverse agonist CGP54626. In all conditions, BRET levels rose above baseline, indicating the presence of constitutive GB1a/2 receptor activity (Fig. 8.6i & j). Due to the elevated levels of GB1a/2 receptors at cell surfaces, the constitutive activity of G1a/2 receptors should be increased in the presence of AJAP1 or PIANP. However, BRET changes induced by CGP54626 were similar, and for this, an effect on the constitutive activity of GB1a/2 receptors cannot be excluded entirely (Fig. 8.6i & j). In general, the BRET changes induced by CGP54626 were minimal (about 10% increased to baseline), showing that this system is not suitable to elucidate the influence of AJAP1 and PIANP on constitutive activity of GB1a/2 receptors. Taken together, these data indicate that by interacting *in trans*, AJAP1 and PIANP stabilize and elevate the level of GB1a/2 receptors at cell surfaces.
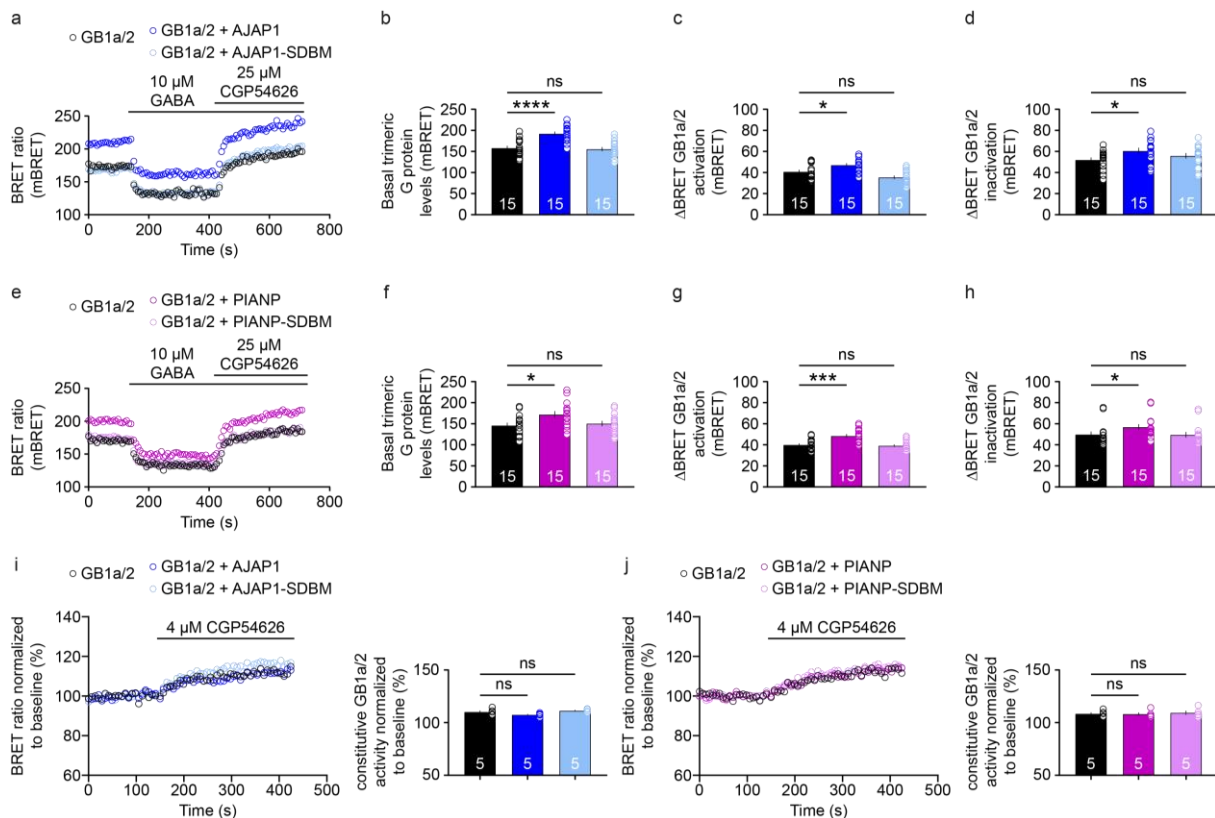
Figure 8.6 AJAP1 and PIANP stabilize transcellular GB1a/2 receptors in transfected HEK293T cells. **a** Individual experiments are showing BRET changes between Gαo-RLuc and Gγ2-Venus in HEK293T cells expressing GB1a/2 exposed to naïve HEK293T cells (black) or HEK293T cells expressing AJAP1 (blue) or AJAP1-SDBM (light blue). GB1a/2 receptor activation by 10 µM GABA leads to the dissociation of heterotrimeric G proteins and a consequent decrease in BRET, whereas the block of activated GB1a/2 receptors by 25 µM of the inverse agonist CGP54626 induces re-association of trimeric G proteins and an increase in BRET. Note that in the presence of transcellular AJAP1 basal BRET levels increased, indicating elevated levels or reduced constitutive activity of transcellular GB1a/2 receptors. **b, c, d** Bar graphs showing that the presence of transcellular AJAP1 significantly increased basal BRET levels (**b**, ****$p < 0.0001$), BRET changes induced by 10 µM GABA (**c**, *$p = 0.0251$), and BRET changes induced by 25 µM CGP54626 (**d**, *$p = 0.0459$) determined in experiments as in **a**. **e** Individual experiments are showing BRET changes between Gαo-RLuc and Gγ2-Venus in HEK293T cells expressing GB1a/2 exposed to naïve HEK293T cells (black) or HEK293T cells expressing PIANP (magenta) or PIANP-SDBM (light magenta). Note that in the presence of transcellular PIANP basal BRET levels increased, indicating elevated levels or reduced constitutive activity of transcellular GB1a/2 receptors. **f, g, h** Bar graphs showing that the presence of transcellular PIANP significantly increased basal BRET levels (**f**, *$p < 0.0196$), BRET changes induced by 10 µM GABA (**g**, ***$p = 0.0003$), and BRET changes induced by 25 µM CGP54626 (**h**, *$p = 0.0121$) determined in experiments as in **e**. **i** Left Individual experiments are showing BRET changes between Gαo-RLuc and Gγ2-Venus in HEK293T cells expressing GB1a/2 exposed to naïve HEK293T cells (black) or HEK293T cells expressing AJAP1 (blue) or AJAP1-SDBM (light blue). Administration of 4 µM CGP54626 blocks constitutive GB1a/2 receptor activity and leads to an increment of BRET above baseline. Right Bar graph showing a similar constitutive activity of GB1a/2 receptors exposed to naïve HEK293T cells (black) or HEK293T cells expressing AJAP1 (blue) or AJAP1-SDBM (light blue) determined in experiments as shown to the left. Note that the constitutive activity of GB1a/2 receptors in this system is small (about 10% increased to baseline). **j** Left Individual experiments showing BRET changes between Gαo-RLuc and Gγ2-Venus in HEK293T cells expressing GB1a/2 exposed to naïve HEK293T cells (black) or HEK293T cells expressing PIANP (magenta) or PIANP-SDBM (light magenta). Administration of 4 µM CGP54626 blocks constitutive GB1a/2 receptor activity and leads to an increment of BRET above baseline. Right Bar graph showing a similar constitutive activity of GB1a/2 receptors exposed to naïve HEK293T cells (black) or HEK293T cells expressing PIANP (magenta) or PIANP-SDBM (light magenta) determined in experiments as shown to the left. All data are means ± SEM. The number of independent experiments is indicated in the bar graphs. Statistical differences were analyzed by one-way ANOVA with Dunnett's multiple comparison test against GB1a/2.

8.3.6 AJAP1 and PIANP are negative allosteric modulators without affecting the maximum efficacy of transcellular GB1a/2 receptors.

Due to the GB1a/2 receptor-mediated accumulation of Luciferase over an extended period, the SRE-FLuc system mentioned above was used to elucidate the influence of AJAP1 and PIANP on the constitutive activity of GB1a/2 receptors *in trans*. Moreover, the SRE-FLuc system detects potential subtle allosteric properties exerted by AJAP1 and PIANP on transcellular GB1a/2 receptors. To ensure GB1a/2 receptor binding exclusively *in trans*, two pools of differentially transfected HEK293-Gαqi cells were mixed. The first pool of HEK293-Gαqi cells expressing GB1a/2 receptors together with the SRE-FLuc reporter was exposed to the second pool of HEK293-Gαqi cells expressing either AJAP1, AJAP1-SDBM, PIANP, or PIANP-SDBM. In the absence of GABA, HEK293-Gαqi cells expressing GB1a/2 receptors together with SRE-FLuc showed significantly reduced FLuc expression when exposed to HEK293-Gαqi cells expressing AJAP1 or PIANP, indicating reduced constitutive activity of transcellular GB1a/2 receptors (Fig. 8.7a & b). The FLuc expression in the absence of GABA was unchanged in co-cultures with naïve cells as well as with AJAP1-SDBM or PIANP-SDBM expressing HEK293-Gαqi cells, supporting that the interaction of AJAP1 and PIANP with GB1a/2 receptors *in trans* elicits the reduction of the constitutive receptor activity (Fig. 8.7a & b). At lower GABA concentrations, AJAP1 or PIANP attenuated transcellular GB1a/2 receptor-mediated FLuc expression resulting in a significant shift of the EC50 towards higher GABA concentrations (Fig. 8.7a & b). This finding is in line with the properties exerted by negative allosteric modulators, suggesting that AJAP1 or PIANP stabilizes the inactive conformation of transcellular GB1a/2 receptors. In contrast to negative allosteric modulators, GB1a/2 receptors interacting with AJAP1 or PIANP *in trans* showed a similar EMax (Fig. 8.7a & b). Elevated transcellular GB1a/2 receptor levels at cell surfaces due to AJAP1 or PIANP interaction imply an increment of the EMax. However, the negative allosteric effect of AJAP1 and PIANP on transcellular GB1a/2 receptors attenuates the EMax to similar levels detectable in the absence of AJAP1 or PIANP. A recent publication has claimed that a peptide comprising 17 amino acids of APP including the SD1 binding site induces GB1a/2 receptor activation (Rice et al., 2019). To elucidate whether the negative allosteric effects exerted by AJAP1 at transcellular GB1a/2 receptors require the anchorage of AJAP1 into the membranes of the exposed cells, I used a soluble version of AJAP1 (sAJAP1) and AJAP1-SDBM (sAJAP1-SDBM) containing only the extracellular part. Neither sAJAP1 nor sAJAP1-SDBM induced a change in basal activity, the EC50, or the EMax of transcellular GB1a/2 receptors, suggesting that anchorage of AJAP1 into the opposite cell membrane is required to exert its negative allosteric properties at transcellular GB1a/2 receptors (Fig. 8.7c). In line with the results above, the presence of AJAP1 significantly reduced the constitutive activity of transcellular GB1a/2 receptors and shifted the EC50 towards a higher GABA concentration without affecting the EMax (Fig. 8.7c). Hence, AJAP1 needs to be anchored into the opposite cell membrane, thereby inducing a conformational change stabilizing the inactive conformation of transcellular GB1a/2 receptors.

a

GB1a/2 — GB1a/2 + AJAP1 — GB1a/2 + AJAP1-SDBM
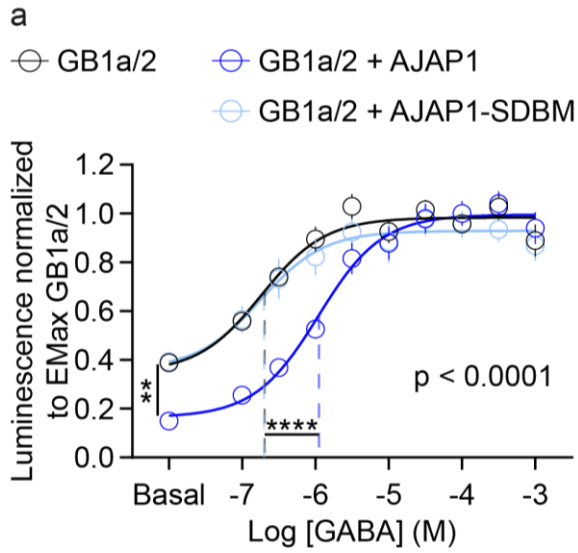
	Basal	EC50 μM	EMax	N
GB1a/2	0.35	0.18	0.98	8
GB1a/2 + AJAP1	0.16	1.10	1.00	8
GB1a/2 + AJAP1-SDBM	0.36	0.18	0.93	8

b

GB1a/2 — GB1a/2 + PIANP — GB1a/2 + PIANP-SDBM
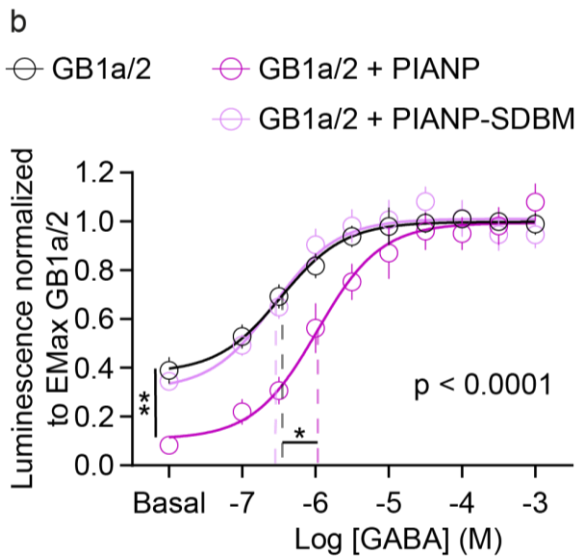
	Basal	EC50 μM	EMax	N
GB1a/2	0.38	0.34	1.00	9
GB1a/2 + PIANP	0.11	1.06	1.00	9
GB1a/2 + PIANP-SDBM	0.31	0.27	1.01	9

c

GB1a/2 — GB1a/2 + AJAP1 — GB1a/2 + sAJAP1 — GB1a/2 + sAJAP1-SDBM
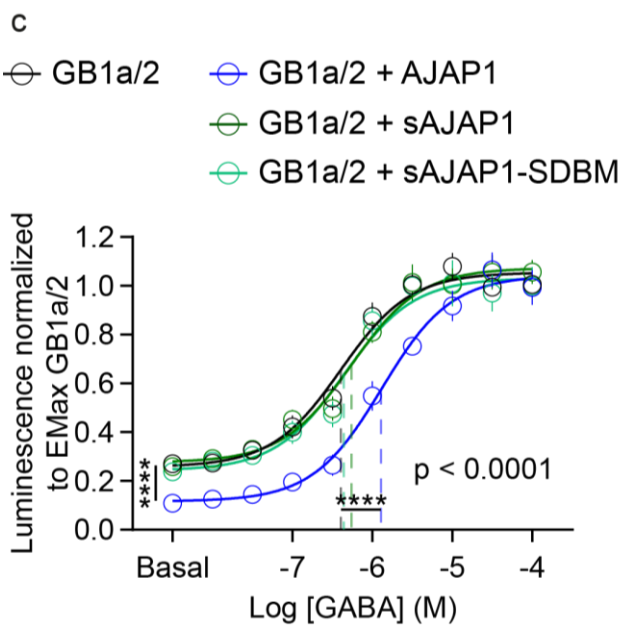
	Basal	EC50 μM	EMax	N
GB1a/2	0.28	0.40	1.06	8
GB1a/2 + AJAP1	0.12	1.31	1.04	8
GB1a/2 + sAJAP1	0.28	0.54	1.07	8
GB1a/2 + sAJAP1-SDBM	0.24	0.44	1.03	8

Figure 8.7 legend on next page

129

Figure 8.7 AJAP1 and PIANP exert negative allosteric effects at transcellular GB1a/2 receptors. **a,** *Left* Dose-response curves of GABA-induced FLuc activity in HEK-Gαqi cells expressing SRE-FLuc sensor together with GB1a/2 receptors exposed to naïve HEK-Gαqi cells (black) or HEK-Gαqi cells expressing AJAP1 (blue) or AJAP1-SDBM (light blue). A single curve does not fit all data sets ($p < 0.0001$). The presence of AJAP1 reduced constitutive activity ($p = 0.0071$) and potency (EC50 $p < 0.0001$) of transcellular GB1a/2 receptors without affecting the maximum efficacy (EMax). Note that AJAP1 increases the dynamic range of transcellular GB1a/2 receptors. *Right* Table showing the basal, EC50, and Emax values derived from the individual curve fits. **b** *Left* Dose-response curves of GABA-induced FLuc activity in HEK-Gαqi cells expressing SRE-FLuc sensor together with GB1a/2 receptors exposed to naïve HEK-Gαqi cells (black) or HEK-Gαqi cells expressing PIANP (magenta) or PIANP-SDBM (light magenta). A single curve does not fit all data sets ($p < 0.0001$). The presence of PIANP reduced the constitutive activity ($p = 0.0015$) and the potency (EC50 $p < 0.0295$) of transcellular GB1a/2 receptors without affecting the EMax. Note that PIANP increases the dynamic range of transcellular GB1a/2 receptors. *Right* Table showing the basal, EC50, and Emax values derived from the individual curve fits. **c** *Left* Dose-response curves of GABA-induced FLuc activity in HEK-Gαqi cells expressing SRE-FLuc sensor together with GB1a/2 receptors exposed to naïve HEK-Gαqi cells (black) or HEK-Gαqi cells expressing AJAP1 (blue), sAJAP1 (green), or sAJAP1-SDBM (light green). A single curve does not fit all data sets ($p < 0.0001$). Note that neither sAJAP1 nor sAJAP1-SDBM changed GB1a/2 receptor-mediated basal luciferase activity, EC50 or EMax values, indicating that anchorage of AJAP1 in the transcellular cell membrane is required to exert negative allosteric properties at transcellular GB1a/2 receptors. *Right* Table showing the basal, EC50, and Emax values derived from the individual curve fits. Data are presented as mean ± SEM with a non-linear regression curve fit of 8 (**a** & **c**) or 9 (**b**) independent experiments. Statistical differences were analyzed by the extra sum-of-squares F test.

8.4 Discussion

Presynaptic GB1a/2 receptors prevent neurotransmitter release in the brain. Their alteration in function and level has been associated with various diseases (Gassmann and Bettler, 2012; Heaney and Kinney, 2016; Kasten and Boehm, 2015; Kumar et al., 2013). A proteomic approach revealed several proteins in complex with GBRs (Schwenk et al., 2016). APP, AJAP1, and PIANP interact with SD1 of GB1a via a conserved WG motif but bind with different affinity in the rank order AJAP1>PIANP>>APP (Dinamarca et al., 2019). APP links SD1 of GB1a to the kinesin motor and is responsible for trafficking GB1a/2 receptors to cell surfaces (Dinamarca et al., 2019). AJAP1 and PIANP are associated with adherence junctions and are not involved in GB1a/2 receptor trafficking. In this report, I show that AJAP1 and PIANP recruit and cluster GB1a/2 receptors *in trans*. By binding GB1a/2 receptors *in trans*, AJAP1 or PIANP stabilize and exert negative allosteric effects at transcellular GB1a/2 receptors and represent the first negative allosteric modulators binding outside of the 7TMD. The exertion of the negative allosteric effects requires anchorage at the opposite cell membrane. My results strengthen the model that GB1a/2 receptors are trafficked to cell surfaces by APP, where they are transferred to AJAP1 and PIANP, precisely localizing GB1a/2 receptors proximal to the active zone. Furthermore, the disruption of SD1 binding might cause the pathophysiology of diseases associated with altered GB1a/2 receptor levels and function.

GBRs show a diversity of signaling and physiology regulated by distinct subunit compositions (Gassmann and Bettler, 2012). KCTDs are auxiliary subunits of GBRs and determine the pharmacology and response of the receptor (Schwenk et al., 2010). A plethora of constituents has been identified to form a complex with GBRs (Schwenk et al., 2016). Constituents binding the SD1 of GB1a include APP, AJAP1, and PIANP. APP, AJAP1, and PIANP share a six amino acid stretch comprising a conserved WG motif that mediates the interaction with SD1 of GB1a. The deletion or mutation to alanine of the corresponding amino acids within APP or AJAP1, respectively, abrogated the interaction with SD1. My findings that the mutation to alanine of the corresponding amino acids within PIANP results in a loss of SD1 interaction support that all three proteins share the same SD1 binding motif, as previously suggested (Dinamarca et al., 2019). Sharing the same binding site implies that APP, AJAP1, and PIANP compete for SD1 interaction. This assumption is in line with the finding that they form distinct complexes with GB1a/2 receptors (Schwenk et al., 2016), suggesting different functions for the receptor-associated proteins. APP has been reported to link GB1a/2 receptors to the kinesin motor and to mediate trafficking of GB1a/2 receptors to presynaptic sites while AJAP1 and PIANP are not involved in receptor trafficking (Dinamarca et al., 2019). At the cell surface, GB1a/2 receptors are stabilized through interaction with APP (Dinamarca et al., 2019). My results showing that basal BRET levels and the magnitude of GB1a/2 receptor-mediated G protein activation are unaltered in the presence of AJAP1 or PIANP *in cis* rule out a similar stabilizing effect. My finding that AJAP1 or PIANP do not influence basal GB1a/2 receptor-induced FLuc accumulation further supports the absence of a GB1a/2 receptor stabilizing effect of AJAP1 or PIANP *in cis*. However, my data point towards an effect of AJAP1 and PIANP on the FLuc accumulation independent of GB1a/2 receptor binding but dependent on GB1a/2 receptor activity. It has been shown that AJAP1 affects gene transcription by binding directly to the promotor (Zeng et al., 2014b) and by attenuating β-catenin reporter activity (Han et al., 2017). Hence, AJAP1 may interfere with the PLC pathway that is artificially coupled to GB1a/2 receptor activity and mediates SRE-FLuc transcription. Up to date, there is no evidence that PIANP is involved in regulating gene transcription, but due to the homology with AJAP1, it is conceivable that it could interfere with the PLC pathway as well.

The observation that AJAP1 and PIANP are expressed in dendritic compartments and that the genetic loss of AJAP1 or PIANP results in a depletion of presynaptic GB1a/2 receptors implies a GB1a/2 receptor interaction *in trans*. Considering the higher affinity of AJAP1 and PIANP for binding to SD1, it is conceivable that APP traffics GB1a/2 receptors to the synapse and AJAP1 and PIANP mediate precise localization of the receptor therein. My data shows that AJAP1 and PIANP recruit and cluster GB1a/2 receptors *in trans* and suggest that APP transfers GB1a/2 receptors to AJAP1 or PIANP. Similarly, the postsynaptic adhesion molecules ELFN1 and ELFN2 have been reported to recruit and cluster presynaptic group III

mGluRs (Dunn et al., 2019; Tomioka et al., 2014), suggesting that the interaction *in trans* represents a conserved mechanism to precisely localize GPCRs at synapses. Mice lacking either AJAP1 or PIANP exert a deficit in presynaptic GB1a/2 receptor-mediated inhibition of neurotransmitter release (T. Lalanne personal communication)(Winkler et al., 2019), suggesting that presynaptic GB1a/2 receptors are incorrectly located and are incapable of blocking Cav channels in the absence of AJAP1 or PIANP. Cav channels are mostly found in complex with presynaptic GB1a/2 receptors and are blocked upon GB1a/2 receptor activation (Schwenk et al., 2016). The assembly of Cav with GB1a/2 receptors requires KCTD16 that also associates with Cav independent of GB1a/2 receptors (Schwenk et al., 2016). However, GB1a/2/KCTD16/Cav complex formation requires localizing GB1a/2 receptors to the site of Cav/KCTD16. AJAP1 and PIANP localize to E-cadherin positive adherens junctions in polarized cells (Bharti et al., 2004; Geraud et al., 2010). In the brain, adherens junctions are located in distinct regions bordering the mature active zone, where neurotransmitters are released (Uchida et al., 1996). Hence, dendritic AJAP1 and PIANP located at adherens junctions are probably the missing players localizing presynaptic GB1a/2 receptors next to the active zone allowing Cav/KCTD16 to assemble with GB1a/2 receptors.

GBR activation is induced by agonist binding to the orthosteric site within the VFTD of GB1, leading to a conformational change of the 7TMD of both subunits, which leads to the activation of G proteins pre-coupled to the GB2 subunit. Recently, in-depth structural analysis of heterodimeric GBRs has been performed (Papasergi-Scott et al., 2020; Park et al., 2020; Shaye et al., 2020). In the inactive state, the VFTDs of both subunits are open and only partially in contact with one another. Agonist binding to the orthosteric site induces closure of the VFTD of GB1. As a result, the VFTD of GB1 and GB2 get in closer contact, resulting in a conformational change within the 7TMDs of both subunits. Conformational changes leading to G protein activation can also occur in the absence of agonist, known as a constitutive activity. Inverse agonists binding to the orthosteric site block the constitutive GBR activity by stabilizing the inactive conformation of GBRs (Geng et al., 2013). The negative allosteric modulator (NAM) CLH304a blocks the constitutive activity of GBRs and represents the only NAM identified for GBRs so far (Sun et al., 2016). CLH304a binds to the 7TMD of GB2 and does not compete for the binding site with agonists and antagonists, representing two characteristics that all allosteric modulators of GBRs identified so far have in common. The interaction of AJAP1 and PIANP with SD1 of GB1a *in trans* does not compete for the orthosteric binding site and blocks the constitutive activity of GB1a/2 receptors. Similar to NAMs, AJAP1 and PIANP attenuate transcellular GB1a/2 receptor responses in the presence of agonists leading to a shift in the EC50 towards higher concentrations. In contrast to NAMs, the maximum response of GB1a/2 receptors is not changed when AJAP1 or PIANP bind SD1 *in trans*, most likely because this interaction also increases GB1a/2 receptor levels at the surface, as seen in my BRET experiments. Increased GB1a/2 receptor levels lead to a rise in the maximum response of GB1a/2 receptors, but due to the negative allosteric properties of AJAP1 and PIANP at transcellular GB1a/2 receptors, no change in the maximum response is present. Nevertheless, AJAP1 and PIANP increase the dynamic range of GB1a/2 receptors and represent the first NAMs that do not exert their properties by binding to the 7TMD of GB2. The mechanism by which AJAP1 and PIANP exert their negative allosteric properties at GB1a/2 receptors *in trans* relies most likely on tightening the SD1, thereby constraining the rotation of the VFTDs towards each other. The rotation of the VFTDs towards each other and the succeeding close contact of VFTDs is a hallmark of active GBRs (Geng et al., 2013). Furthermore, it has been shown that locking the close contact of VFTDs is sufficient to induce constitutive activity (Geng et al., 2013), supporting that blockade of constitutive activity can be achieved by preventing the close contact of VFTDs through SD1 binding. My finding that the GB1a/2 receptor-mediated activity is unchanged when SD1 interacts with sAJAP1 supports this mechanism because the VFTDs can move unobstructed in this condition. Hence, AJAP1 anchored within the opposite cell membrane stabilizes the transcellular GB1a/2 receptor in the inactive conformation by constraining the rotation of VFTDs toward each other.

In contrast to AJAP1 and PIANP, ELFN1 and ELFN2 induce constitutive activity of group III mGluR *in trans* (Dunn et al., 2018; Dunn et al., 2019). The ELFN1-induced constitutive activation of mGluR7 recruits somatostatin interneurons (Jason Stachniak et al., 2019) and

regulates the release probability of CA1/Interneuron synapses (Sylwestrak and Ghosh, 2012), indicating the importance of constitutive activity on the establishment of neuronal networks. Unsurprisingly, ELFN1-KO mice exerted increased seizures (Tomioka et al., 2014), and the genetic ablation of ELFN2 resulted in the manifestation of various neurological diseases (Dunn et al., 2019). Increased constitutive activity of GBRs induced by mutations within the GB2 subunit causes the pathophysiology of Rett syndrome and epileptic encephalopathies (Vuillaume et al., 2018; Yoo et al., 2017), demonstrating the importance of correctly regulated GBR activity. GB1a-KO mice exhibit several phenotypes, including but not limited to increased seizure susceptibility, deficits in long-term potentiation, and cognitive impairments (Kasten and Boehm, 2015), showing the importance of presynaptic GB1a/2 receptors for proper network activity. PIANP-KO mice exhibit a general autism-like behavior, including reduced spatial learning and memory (Winkler et al., 2019). Hence, the interaction of PIANP with GB1a/2 receptors is crucial for the control of neuronal activity, and its abrogation could contribute to the pathophysiology of disease associated with altered GBR levels and function, including but not limited to major depressive disorder (Fatemi et al., 2011), ASD (Fatemi et al., 2009; Oblak et al., 2010) or AD (Martin-Belmonte et al., 2020). So far, the information on the behavior of AJAP1-KO mice is scarce. However, in patients suffering from TLE and a mouse model of epilepsy both, AJAP1 and GB1 are downregulated (Zhang et al., 2020). In the epileptic mouse model, lentiviral induced expression of AJAP1 restored GB1 levels resulting in a reduction of SRS (Zhang et al., 2020). Epilepsy is associated with deficits in GBR-mediated inhibition, and GB1a-KO mice exhibit infrequent seizures (Vienne et al., 2010). Hence, the reduction of SRSs in the epileptic mouse model due to AJAP1 expression can be explained by restoring the natural presynaptic localization of GB1a. Recently, it has been shown that the interaction of APP with GB1a/2 receptors reduces Aβ formation, suggesting that stabilizing APP/GB1a/2 complex potentially ameliorates the symptoms in AD patients (Dinamarca et al., 2019). Although further studies elucidating the role of SD1 binding proteins in GBR-associated diseases are needed, complex formation of GB1a/2 receptors with APP, AJAP1, and PIANP seems to be crucial for the control of neuronal activity, and the abrogation of SD1 interaction presumably causes the pathophysiology of various neurological diseases.

9 Generation of PIANP-KO mice

PIANP shares the conserved SD1 binding motif with APP and AJAP1 but forms a distinct complex with GB1a/2 receptors (Dinamarca 2019). Experiments in transfected neurons suggested that PIANP, unlike APP, is not directly involved in GB1a/2 receptor trafficking (Dinamarca et al., 2019). In order to elucidate the physiological function of PIANP in the nervous system in the context of GB1a/2 receptors, I generated PIANP knockout mice using CRISPR/Cas9-mediated gene editing in collaboration with the Centre for Transgenic Models (CTM), University of Basel.

9.1 Introduction

Site-specific genomic DNA mutations or ablations in mice can be achieved by nucleases, such as zinc-finger nucleases (ZFNs) (Urnov et al., 2010), transcription activator-like effector nucleases (TALEN) (Sun and Zhao, 2013), and clustered regularly interspaced short palindromic repeats (CRISPR) / CRISPR-associated (Cas) (Barrangou, 2013). All three nucleases introduce site-specific DNA double-strand breaks (DSBs). Since the restricted affinity to bind target sites, the number of available target sites, the need to redesign the constructs for every target, and the size of the nucleases limit the usability of ZFNs and TALENs, the CRISPR/Cas system emerged as the most commonly used gene-editing tool (Devkota, 2018; Gupta and Musunuru, 2014). The CRISPR/Cas system was identified initially in bacteria (Ishino et al., 1987), serving as an adaptive immune system against bacteriophages (Bolotin et al., 2005; Mojica et al., 2005; Pourcel et al., 2005). Three different types of CRISPR/Cas systems have been identified, with CRISPR/Cas type II being the most commonly used for genome editing because it requires only one Cas protein, Cas9, and two RNA constituents (Bhaya et al., 2011). Since the CRISPR/Cas9 system was used for the generation of PIANP-KO mice, the acquisition of the adaptive immune system with CRISPR/Cas9 will be described.

The acquisition of the cellular memory results from the integration of short sequences of foreign DNA, termed spacers, into the CRISPR locus of bacteria (Barrangou et al., 2007). In the CRISPR locus, the separation of distinct spacers is established by repeat sequences. Upon the transcription of the CRISPR locus, a long RNA molecule containing repeat sequences and distinct spacer sequences in alternating order is generated, called pre-CRISPR RNA (crRNA) (Bhaya et al., 2011). Besides pre-crRNA transcription, the trans-activating CRISPR RNAs (tracrRNAs) are transcribed that are complementary to the repeat sequences (Deltcheva et al., 2011). Hence, the tracrRNA and pre-crRNA form a double-stranded RNA that is cleaved by RNaseIII, resulting in various tracrRNA/crRNA complexes that contain only one specific spacer sequence (Deltcheva et al., 2011). The tracrRNA/crRNA complexes interact with Cas9 proteins, forming ribonucleoprotein (RNP) complexes, and activate the endonuclease activity of Cas9 (Barrangou, 2013; Bhaya et al., 2011). In order to identify foreign DNA specifically, the complementary crRNA sequence requires to form a hybrid DNA/RNA double helix, and the Cas9 needs to interact with proto-space adjacent motifs (PAMs) located on the foreign DNA directly next to the complementary crRNA sequence (Barrangou, 2013; Bhaya et al., 2011). Upon site-specific DNA binding, Cas9 cleaves the DNA three base pairs upstream of the PAM site (Jinek et al., 2012). The induced DNA break is deleterious to the foreign DNA, resulting in the degradation and protection against the foreign DNA.
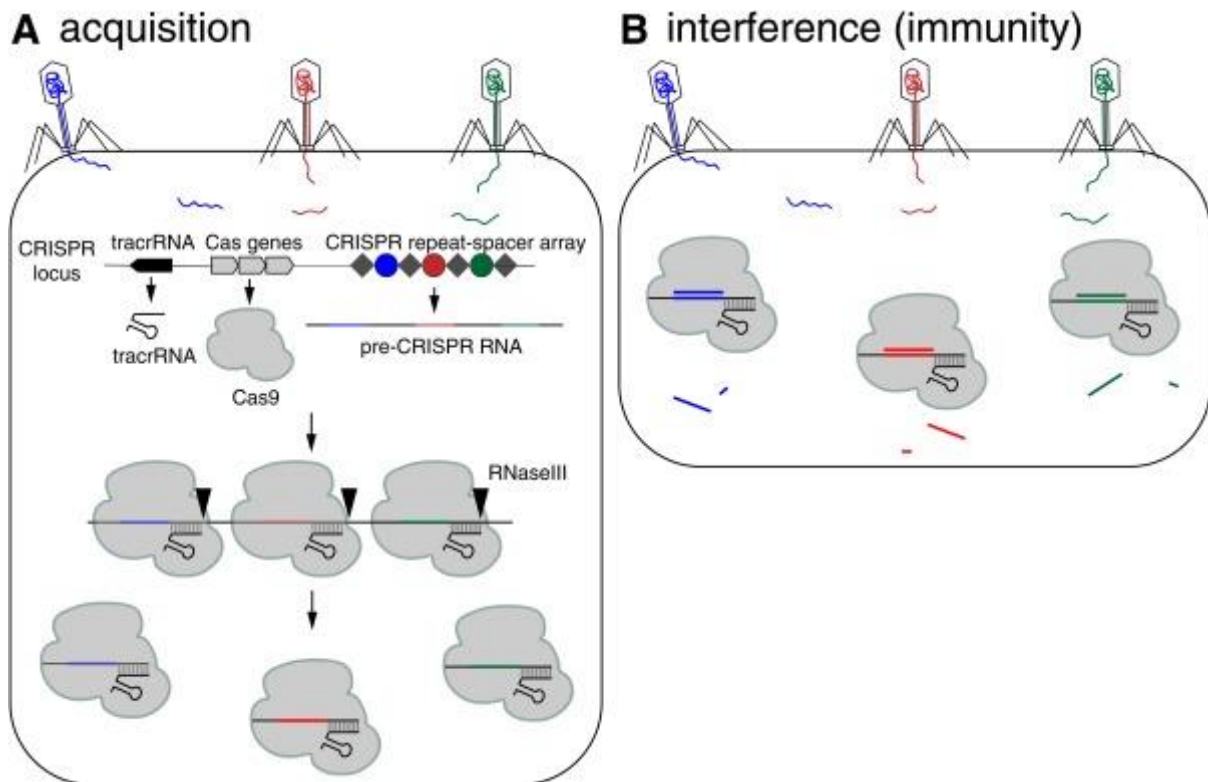
Figure 9.1 Scheme depicting CRISPR/Cas9-mediated adaptive immune system in bacteria. **a** Spacer sequences (colored circles) are integrated into the CRISPR locus and separated by repeat sequences (gray diamonds). CRISPR locus transcription generates tracrRNA, Cas9 protein and pre-crRNA. tracrRNA interacts with the repeat sequences of pre-crRNA. RNaseIII cleaves the pre-crRNA, resulting in tracrRNA/crRNA complex with only one spacer sequence. The tracrRNA/crRNA complex and Cas9 form the activated ribonucleoprotein (RNP). **b** Foreign DNA that is homologous to the crRNA sequence is bound by the RNP. Cas9 cleaves the foreign DNA that is subsequently degraded and protects the bacteria from foreign DNA. Figure is from (Thurtle-Schmidt and Lo, 2018).

The CRISPR/Cas9 defense mechanism can be adapted for gene editing in eukaryotes. In eukaryotic cells, Cas9 of the activated RNP cleaves both the complementary and the non-complementary DNA strand, resulting in a DSB. Since the DNA DSBs can result in the degradation of up to ten base pairs and thus in the loss of genetic information, eukaryotic cells respond to DNA DSBs either through the non-homologous end-joining (NHEJ) or homology-directed repair (HDR) system (Chapman et al., 2012; Devkota, 2018). The most predominant form of DNA DSB repair is the NHEJ, which exists in a canonical and an alternative pathway (c-NHEJ and a-NHEJ, respectively) (Devkota, 2018). In the c-NHEJ, the DNA ends are bound by the Ku complex, preventing further DNA degradation (Hefferin and Tomkinson, 2005). The Ku complex recruits the catalytic subunit of DNA protein kinase (DNA-PKCS) and together they form the DNA-dependent kinases (DNA-PKs), bridging the DNA ends (Dvir et al., 1992; Gottlieb and Jackson, 1993; Hefferin and Tomkinson, 2005). Upon DNA end bridging, the 5' endonuclease Artemis is recruited, and processes 3' single-stranded DNA (ssDNA) overhangs into blunt ends (Hefferin and Tomkinson, 2005). The blunt ends are ligated by the DNA ligase IV, terminating the NHEJ repair (Chen et al., 2000). Since the DNA DSB has been directly ligated, parts of the original DNA have been deleted. Instead of directly ligate the DNA DSB, DNA polymerases can be recruited prior to ligation, reconstituting the DNA sequence (Chiruvella et al., 2013; Devkota, 2018; Povirk, 2006). However, the inserted nucleotides are often incorrect due to the absence of a homologous template (Devkota, 2018). Compared to the c-NHEJ pathway, little is known for the a-NHEJ pathway. In the a-NHEJ repair pathway, some protein complexes are shared with the c-NHEJ, whereas other proteins are unique (Chiruvella et al., 2013). For example, the DNA ligase I and II mediate the DNA ligation in the a-NHEJ instead of the DNA ligase IV involved in the c-NHEJ (Chiruvella et al., 2013; Devkota, 2018). However, both NHEJ repair mechanisms are error-prone. Thus, the deletions or

136

insertions (indels) occurring during the NHEJ repair result in the mutation of the genomic DNA. Since indels frequently result in premature translation termination, the translated messenger RNA (mRNA) is eliminated by nonsense-mediated mRNA decay, resulting in the loss of the target protein (Kurosaki et al., 2019).

In the HDR pathway, the sister chromatid or the homologous chromosome is used to precisely repair the DNA DSBs (Capecchi, 1989; Devkota, 2018; Takata et al., 1998). Upon DNA DSBs, the MRN complex is recruited, preventing further DNA breaks (Devkota, 2018). The MRN complex recruits exonucleases that degrade nucleotides in 5'-3' direction, a process called resection, generating ssDNA overhangs (Devkota, 2018; Symington, 2014). The ssDNA overhangs interact with replication protein A (RPA), preventing cleavage by nucleases (Devkota, 2018). RPA is replaced by Rad51 recombinase in the next step, initiating the search for the repair template (Buisson et al., 2014). The template DNA unwinds and allows the interaction of the ssDNA overhangs with the corresponding strand, forming the displacement loop (D-loop) (Buisson et al., 2014). The DNA polymerase Δ attaches to the DNA and starts the replication process, forming Holliday junctions (Devkota, 2018; Jasin and Rothstein, 2013). The Holliday junctions are resolved by nickases that result in non-crossover or crossover of chromatids, depending on the cleavage site. Finally, ligase I joins the DNA ends, restoring the original DNA sequence and completing the HDR process (Liddiard et al., 2019). Since HDR uses homologous DNA for DSB repair, it is a beneficial tool for gene editing. In order to edit genomic DNA, a plasmid containing the homologous sequence with the desired mutations, insertions, or deletions is applied together with the CRISPR/Cas9 system.

Figure 9.2 Scheme depicting the DNA DSB-induced NHEJ and HDR pathways in eukaryotic cells. **a** Overview of the NHEJ pathway. Ku complex (blue) binds close to the DNA DSB to prevent further degradation, and recruits DNA-PK$_{CS}$ (light blue). Artemis (light magenta) generates ssDNA overhangs and in some cases, polymerases replicate the DNA. Ligase IV complexes finally ligate DNA breaks. The repaired DNA contains indels (red). **b** Overview of the HDR pathway. MRN complexes (gray) bind to the DNA upon DSBs and initiate the DNA resection. RPA (light brown) bind to the ssDNA overhangs and are replaced by Rad51 (dark brown). Rad51 initiates the invasion of homologous sister chromatid (green), forming D-loops. Polymerases replicate the DNA and ligases ligate the DNA, restoring the original DNA sequence. Figure was adapted from (Brandsma and Gent, 2012).
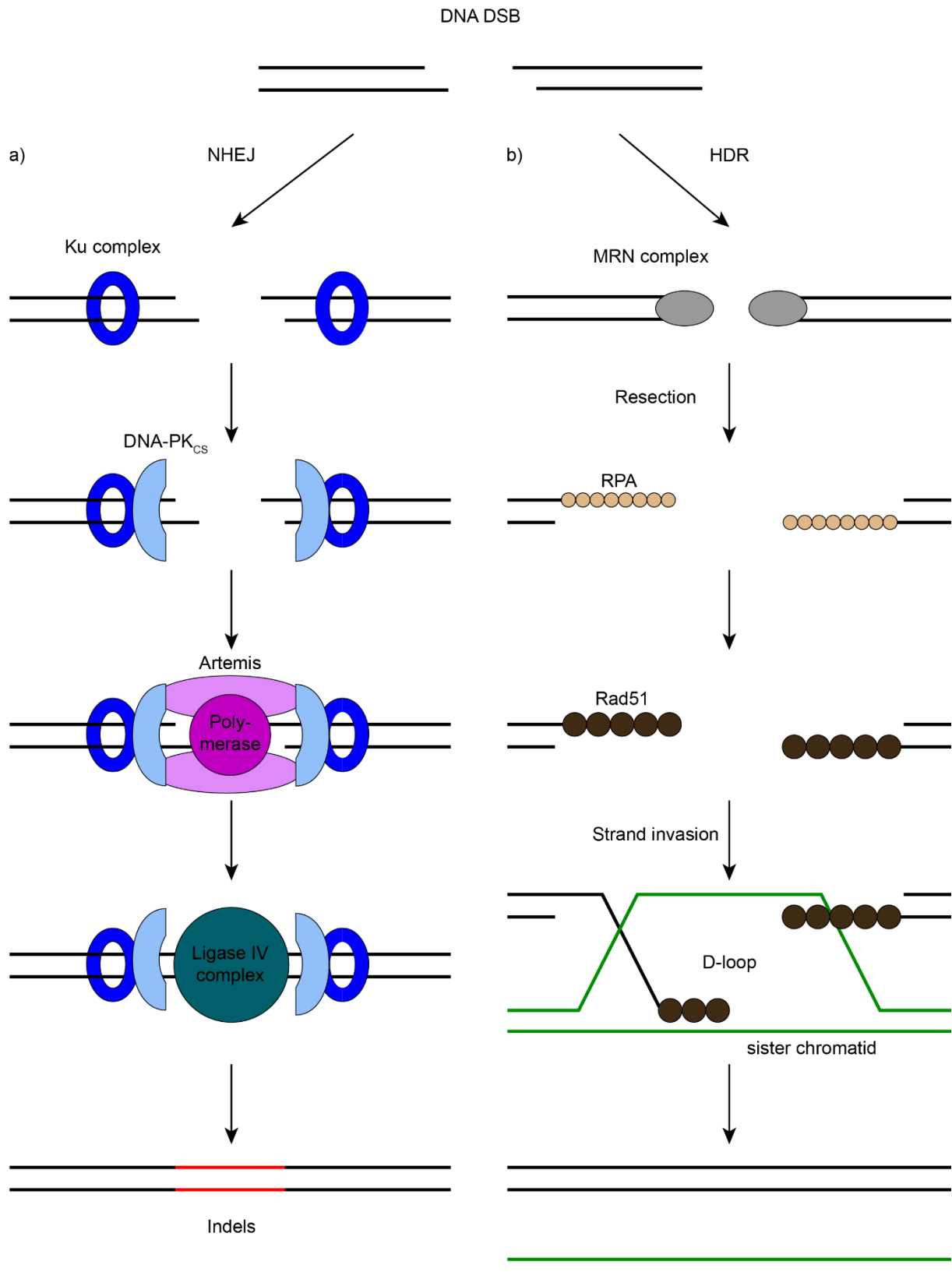
DNA DSB

a) NHEJ

Ku complex

DNA-PK$_{CS}$

Artemis

Poly-merase

Ligase IV complex

Indels

b) HDR

MRN complex

Resection

RPA

Rad51

Strand invasion

D-loop

sister chromatid

Figure 9.2 legend on previous page.

9.2 Material and Methods

9.2.1 Genomic PIANP sequence, crRNA, Cas9

The sequence of the PIANP gene (NC_000072.7 Reference GRCm39 C57BL/6J) was retrieved form NCBI (https://www.ncbi.nlm.nih.gov/gene/319352). CRISPOR (http://crispor.tefor.net) search algorithm was used to find crRNA sequences within the PIANP gene. The sequence 5'-GGCTGGTGGGGATCGATGGGAGG-3' (crRNA-1) and 5'-GACCCCACACTATAGCCCAAGGG-3' (crRNA-2) from the CRISPOR search list and the Alt-R® CRISPR-Cas9 tracrRNA were ordered at IDT (Leuven, BE). Cas9 was provided by the Centre for Transgenic Models, University of Basel.

9.2.2 Primers and PCR

Nested PCR was used to amplify the genomic PIANP sequence. The primers 5'-GACTCCTGGTGCAAACCTAC-3' (primer 1a) and 5'-GCAGATCATAGTCTTCAAGTCC-3' (primer 1b) were used for the initial PCR. The second PCR was performed with the primers 5'-CTACATGAGCCATCGCCTGG-3' (primer 2a) and 5'-CAATCCCTCACATCCCTACCAG-3' (primer 2b). Primers were ordered at Microsynth (St. Gallen, CH). The PCR was executed with fresh dNTP (Cat.No. U1511, Promega WI, US) and REDTaq® DNA-polymerase (Cat.No. D4309, Sigma-Aldrich, MO, US) with the following thermocycling conditions:

Temperature (°C)	Time (minutes)
94	2
94	1
55	1
72	1
72	5
4	pause

PCR products were purified using the NucleoSpin Gel & PCR clean-up kit (Cat. No. 740609, Macherey-Nagel, NRW, DE).

9.2.3 *In vitro* pre-validation, electroporation and biopsies

The *in vitro* pre-validation of crRNA-1 and crRNA-2, the electroporation of one cell embryos (C57BL/6), transfer of surviving embryos into pseudopregnant femals and biopsy sampling were performed by the Centre for Transgenic Models, University of Basel.

9.2.4 Genomic DNA extraction

Genomic DNA was extracted by dissolving biopsies in 200 µl NID-buffer (50mM KCl; 10mM Tris-HCl, pH 8.3; 2mM MgCl2; 0.1 mg/ml gelatin; 0.45% NP40; 0.45% Tween-20) with 1.5% Proteinase K (Cat.No, 3115879001, Roche, BS, CH) at 56°C on a shaker overnight. The reaction was inactivated by 96° for 10 minutes. Prior usage of genomic DNA extract, the sample was cooled down to RT and centrifuged for 2 minutes at 7,500 rpm.

9.2.5 Sequencing

PCR products of genomic DNA were sequenced by Microsynth (St. Gallen, CH) using primer- 2a. The sequencing results were analyzed using Clone Manager software (Sci Ed Software LLC).

9.2.6 Isolation of membrane-enriched fractions from mouse brains

The isolation of membrane-enriched fractions form adult WT and PIANP-KO mice was performed as described earlier (Fritzius et al., 2017).

9.3   Results

9.3.1   crRNA-1 and crRNA-2 sequence identification

In order to generate PIANP-KO mice using the CRISPR/Cas9 system, the target sequence has to be determined. For a holistic inhibition of PIANP translation, the crRNA sequence needs to target an exon that exists in all transcript variants of PIANP. In C57BL/6 mice, PIANP is encoded by six exons on chromosome 6. The start of the coding sequence is located at the end of exon two just four base pairs (bp) prior exon ending (Fig. 9.3a). Due to the possibility that the occurring indels are located in the succeeding intron, I excluded targeting exon two. Hence, I concentrated on identifying a crRNA sequence within exon three. Within exon three, the SD1 binding motif of PIANP is located. Due to the possibility that a small peptide could still be produced after CRISPR/Cas9-mediated indels, only the sequence in front of the SD1 binding motif was taken into consideration. Finally, CRISPR/Cas-9-mediated indels can be different on both alleles or only affect one allele, and thus, the separation of the distinct sequences for the determination of DNA alterations is required. To identify the CRISPR/Cas9-mediated changes within the target site, the target sites needs to contain a restriction site, which is lost upon DNA alteration. Using the CRISPOR search algorithm (http://crispor.tefor.net), crRNA sequences within the defined range were generated. Thorough analysis of the existing restriction sites, the predicted specificity, the GC content, and predicted efficiency, revealed the crRNA sequence 5'-GGCTGGTGGGGATCGATGGGAGG-3' (crRNA-1) and 5'-GACCCCACACTATAGCCCAAGGG-3' (crRNA-2) as the most promising candidates (Fig. 9.3a & b).

9.3.2   crRNA-2 targets endogenous PIANP DNA cleavage *in vitro*

The suitability of the identified crRNA to cleave the target DNA sequence is tested first *in vitro*. The *in vitro* pre-validation elucidates the eligibility of defined crRNAs to cleave the endogenous target DNA. I amplified the target DNA of PIANP by a nested PCR to improve the specificity and sensitivity of the PCR. For the nested PCR, I used the primer-1a (5'-GACTCCTGGTGCAAACCTAC-3') and primer-1b (5'-GCAGATCATAGTCTTCAAGTCC-3') for the initial PCR and primer-2a (5'- CTACATGAGCCATCGCCTGG-3') and primer-2b (5'-CAATCCCTCACATCCCTACCAG-3') for the second PCR (Fig. 9.3b). The final PCR product was purified using the NuceloSpin PCR clean-up Kit and transferred to the CTM at the University of Basel. Incubation of crRNA:tracrRNA/CRISPR/Cas9 complex, termed ribonucleoprotein (RNP), together with the PCR product of endogenous DNA of PIANP showed that only crRNA-2 cleaved the PCR product, yielding fragments with expected sizes (P. Pelczar, CTM personal communication). Hence, the team of CTM used only crRNA-2 for electroporation of the RNP into C57BL/6 one cell embryos. The CTM team further transferred the surviving embryos into pseudopregnant females and sampled biopsies from offspring.

9.3.3   Loss of endogenous PIANP upon crRNA-2-targeted DNA cleavage

The CRISPR/Cas9 system induces DNA double-strand breaks, activating the error-prone NHEJ DNA repair mechanism that frequently inserts or deletes nucleotides during the repair. To determine whether the repair of the DNA double-strand break guided by crRNA-2 resulted in nucleotide changes, I extracted and analyzed the genomic DNA from the biopsies of ten offspring. The aforementioned nested PCR was used to specifically amplify the genomic DNA targeted by the crRNA-2. Primer-2a was used for sequencing the PCR product (Microsynth). The sequencing results revealed that mice 2, 3, 5, and 6 did not show alterations compared to the genomic DNA of WT animals. The mice 1, 4, 9, and 10 showed a mixture of sequences after the crRNA-2 targeting site, indicating distinct alterations for the two alleles. The genomic DNA of mouse 7 showed mutations and the insertion of four novel base pairs at the crRNA-2 target region, causing a frameshift (Fig. 9.3c). In contrast, six base pairs were deleted in the genomic DNA of mouse 8 (Fig. 9.3c). However, the six base pair deletion did not result in a frameshift and premature termination of translation. Since both alleles of mouse 7 contain the same nucleotide changes, causing a frameshift and subsequent premature termination of translation, all mice but mouse 7 were excluded from further analysis. The frameshift in mouse 7 resulted in an altered amino acid sequence after P97 and a succeeding

premature termination of translation after I122 (Fig 9.3d). Premature termination of translation results in the elimination of the produced mRNA through the nonsense-mediated mRNA decay pathway and thus in the loss of PIANP protein (Kurosaki et al., 2019). Mouse 7 was backcrossed with a WT CL57B/6 mouse to clean-out undesired alterations within the genome induced by CRISPR/Cas9-mediated off-targeting. To ensure the loss of PIANP protein, membrane-enriched fractions of homozygous PIANP-KO mice brains were analyzed using western blots, which confirmed the absence of PIANP protein in the brain of PIANP-KO mice (Fig. 9.3e). Thus, PAINP-KO mice (B6-Pianp^{em1Bet}) were generated successfully, using the crRNA-2 as guide for the CRISPR/Cas9 system.

Figure 9.3 Endogenous PIANP is lost upon crRNA-2-targeted DNA cleavage. **a** Illustration depicting the non-coding and coding exons (squares) for PIANP on chromosome 6 in C57BL/6 mice. The coding sequence for PIANP (magenta) starts at the end of exon 2.The region encoding the SD1 binding motif (orange) is located in exon three. The corresponding sequence of crRNA-1 (red) and crRNA-2 (blue) are located on the negative strand within exon three. **b** *Top* Table of defined crRNA-1(red) and crRNA-2 (blue) sequences. *Bottom* Table of primer sequences used for nested PCR. **c** The genomic sequence after NHEJ repair induced by crRNA-2:tracrRNA/CRISPR/Cas9 complex in animal 7 (top) and animal 8 (bottom) shows a 4bp insertion together with four adjacent mutations and a 6bp deletion, respectively. Stars mark homologous bps in the sequence between WT and mouse 7 or WT and mouse 8. The line indicates a coding triplet used in WT PIANP translation. Note, only the insertions in mouse 7 result in a frameshift and premature termination of translation. **d** *Top* PIANP protein sequence in WT mice. P97 (red) and the SD1 binding motif (orange) are indicated. *Bottom* The frameshift in mouse 7 results in altered amino acid sequence (italic) after P97 (red) and a premature termination of translation. **e** Western blot analysis confirming the loss of PIANP protein in PIANP-KO mice. crRNA CRISPR RNA, bp base pair, WT wild type, KO knock-out

9.4   Discussion

Genetic knock-out models are pivotal in unravelling the physiological functions of proteins. Various tools exist to generate knock-out models but in the recent years, the CRISPR/Cas9 system gained popularity because it is fast, cheap, highly specific, and very efficient (Adli, 2018). In order to elucidate the physiological function of PIANP in general and with regards to GB1a/2 receptors, I successfully generated PIANP-KO mice in collaboration with the CTM at the University of Basel using the CRISPR/Cas9 system.

In order to efficiently generate a knock-out model using the CRISPR/Cas9 system, an specific and efficient guide RNA is crucial. After comprehensive sequence analysis and using the helpful CRISPOR search algorithm, I eventually identified two crRNAs that were fulfilling the defined criteria. Despite both crRNAs met the diverse criteria, only crRNA-2 cut the endogenous DNA *in vitro*. However, *in vitro* pre-validation does not always reflect the *in vivo* situation (P. Pelczar, CTM personal communication), leaving the utility of crRNA-1 *in vivo* conceivable.

Next to the *in vivo* efficiency of crRNAs, the effectiveness of the delivery system plays a crucial role in the utility of the CRISPR/Cas9 system to generate KO models (Alghadban et al., 2020). In the recent years, electroporation of RNPs composed of single guide RNA (sgRNA)/CRISPR/Cas9 developed into the standard delivery system (Alghadban et al., 2020). The delivery of RNP complexes shows reduced time until activity, increased mutagenesis efficiency and decreased mosaicism (Hashimoto et al., 2016; Wang et al., 2016). In our case, electroporation of RNPs induced DNA double-strand breaks in six out of ten animals, which is slightly lower than the reported efficiency of about 75% (Alghadban et al., 2020). The slightly reduced efficiency in mutagenesis upon RNP electroporation could be due to the usage of crRNA:tracrRNA instead of sgRNA. Four out of the six animals showed mosaicism, while two mice contained the same mutagenesis on both alleles. Out of these two mice, the introduced mutagenesis resulted in a frameshift and a premature termination codon in one mouse. Thus, the electroporation of RNPs containing our identified crRNA-2 was sufficient to generate PIANP-KO mice in the first attempt, making it a feasible and fast method to generate KO models.

The generation of complete gene KO mice using the CRISPR/Cas9 system depends on several steps (Lino et al., 2018). The crRNA guides the RNP to the DNA target site, resulting in the double-strand break. Next, the error-prone NHEJ-mediated repair randomly introduces indels during DNA double-strand repair, leading to a frameshift and a premature termination codon. Premature termination of translation leads to the elimination of mRNA through the nonsense mRNA decay pathway and the loss of endogenous protein (Kurosaki et al., 2019). In our case, DNA translation analysis revealed that the frameshift resulted in an altered peptide sequence after P97 and a premature termination of translation after I122. I could confirm the loss of PIANP protein in brains of PIANP-KO mice using western blot analysis. Thus, we successfully generated PIANP-KO mice that can be used to unravel the physiological functions of PIANP in general and with regards to GB1a/2 receptors.

9.5 Pianp deficiency links GABAB receptor signaling and hippocampal and cerebellar neuronal cell composition to autism-like behavior

Manuel Winkler, Siladitta Biswas, Stefan M. Berger, Moritz Küchler, Laurens Preisendörfer, Myeongjeong Choo, Simon Früh, <u>Pascal D. Rem</u>, Thomas Enkel, Bernd Arnold, Dorde Komljenovic, Carsten Sticht, Sergij Goerdt, Bernhard Bettler, Oliver von Bohlen Und Halbach, Dusan Bartsch, Cyrill Géraud

Personal contribution

I designed and validated the generation of PIANP-KO mice using CRISPR/Cas9-mediated gene editing in collaboration with the Center for Transgenic Models, University of Basel. My colleagues used the PIANP-KO mice for electrophysiological recordings (Fig. 2b, c & d).

ARTICLE

Pianp deficiency links GABA_B receptor signaling and hippocampal and cerebellar neuronal cell composition to autism-like behavior

Manuel Winkler [1] · Siladitta Biswas[1] · Stefan M. Berger[2] · Moritz Küchler[3] · Laurens Preisendörfer[3] · Myeongjeong Choo[4] · Simon Früh[4] · Pascal D. Rem[4] · Thomas Enkel[2] · Bernd Arnold[5] · Dorde Komljenovic[6] · Carsten Sticht[7] · Sergij Goerdt[1,8] · Bernhard Bettler[4] · Oliver von Bohlen und Halbach [3] · Dusan Bartsch[2] · Cyrill Géraud[1,8,9]

Abstract

Pianp (also known as Leda-1) is a type I transmembrane protein with preferential expression in the mammalian CNS. Its processing is characterized by proteolytic cleavage by a range of proteases including Adam10, Adam17, MMPs, and the γ-secretase complex. Pianp can interact with Pilrα and the GB1a subunit of the GABA_B receptor (GBR) complex. A recent case description of a boy with global developmental delay and homozygous nonsense variant in *PIANP* supports the hypothesis that PIANP is involved in the control of behavioral traits in mammals. To investigate the physiological functions of Pianp, constitutive, global knockout mice were generated and comprehensively analyzed. Broad assessment did not indicate malformation or malfunction of internal organs. In the brain, however, decreased sizes and altered cellular compositions of the dentate gyrus as well as the cerebellum, including a lower number of cerebellar Purkinje cells, were identified. Functionally, loss of *Pianp* led to impaired presynaptic GBR-mediated inhibition of glutamate release and altered gene expression in the cortex, hippocampus, amygdala, and hypothalamus including downregulation of *Erdr1*, a gene linked to autism-like behavior. Behavioral phenotyping revealed that *Pianp* deficiency leads to context-dependent enhanced anxiety and spatial learning deficits, an altered stress response, severely impaired social interaction, and enhanced repetitive behavior, which all represent characteristic features of an autism spectrum disorder-like phenotype. Altogether, *Pianp* represents a novel candidate gene involved in autism-like behavior, cerebellar and hippocampal pathology, and GBR signaling.

Introduction

Ajap1 and Pianp (initially described as Leda-1) constitute a family of type I transmembrane proteins preferentially expressed in the mammalian central nervous system (CNS) [1, 2]. *Ajap1*, contained in chromosomal region 1p36 [3],

These authors contributed equally: Manuel Winkler, Siladitta Biswas

Supplementary information The online version of this article (https://doi.org/10.1038/s41380-019-0519-9) contains supplementary material, which is available to authorized users.

✉ Cyrill Géraud
cyrill.geraud@umm.de

1 Department of Dermatology, Venereology, and Allergology, University Medical Center and Medical Faculty Mannheim, Heidelberg University, and Center of Excellence in Dermatology, Mannheim, Germany

2 Department of Molecular Biology, Central Institute of Mental Health and Medical Faculty Mannheim, Heidelberg University, Mannheim, Germany

3 Institute of Anatomy and Cell Biology, University Medicine Greifswald, Greifswald, Germany

4 Department of Biomedicine, Institute of Physiology, University of Basel, Basel, Switzerland

5 Division of Molecular Immunology, German Cancer Research Center (DKFZ), Heidelberg, Germany

6 Division of Medical Physics in Radiology, German Cancer Research Center (DKFZ), Heidelberg, Germany

7 Center for Medical Research, Medical Faculty Mannheim, Heidelberg University, Mannheim, Germany

8 European Center for Angioscience, Medical Faculty Mannheim, Heidelberg University, Mannheim, Germany

9 Section of Clinical and Molecular Dermatology, Medical Faculty Mannheim, Heidelberg University, Mannheim, Germany

was found to be frequently deleted in neuroblastoma and oligodendroglioma and thus represents a tumor suppressor gene in these tumors [4]. Notably, Isidor et al. [5] described a child with a complex constitutional subtelomeric 1p36.3 deletion/duplication that has intellectual disability (ID) and neonatal neuroblastoma indicating that *Ajap1* may have important functions in the brain beyond tumor suppression. In addition, *Ajap1* was identified as a new susceptibility locus for migraine [6] and as a novel candidate gene for the treatment response to risperidone in schizophrenia [7].

In contrast to Ajap1, Pianp is less well studied. Although most strongly expressed in the brain, Pianp was initially identified in rat liver sinusoidal endothelial cells [8]. Similar to Ajap1, Pianp also sorts to the basolateral domain of the plasma membrane and alters E-cadherin processing in polarized epithelial cells [8, 9]. Pianp itself also undergoes posttranslational proteolytic processing by Furin-like pro-protein convertases, Matrix-metalloproteinases (MMPs) as well as Adam10 or Adam17, and the γ-secretase complex [10, 11]. In addition, Pianp was shown to be expressed in lymphoid organs and bone marrow-derived macrophages of BALB/c mice [2]. In line with this, Pianp was identified as a ligand of immune inhibitory receptor Pilrα in vitro and it has been shown that glycosylation of Pianp is necessary for this interaction [1]. Pianp and Pilrα are counter regulated upon LPS stimulation of murine macrophages and MMPs are responsible for LPS-mediated downregulation of Pianp in these cells [2].

With regard to its putative functions in the brain, Anazi et al. [12] recently described a boy with a homozygous nonsense variant in *PIANP* upon performing an analysis of the morbid genome of human ID. This boy was 1 year and 8 months old, had dysmorphic facial and acral features, central hypotonia, and showed a delay of global development, as he was unable to walk and did not use simple words such as mama.

Autism spectrum disorders (ASD) represent a complex group of neurodevelopmental disorders that are characterized by impaired social behavior and communication as well as repetitive behavior and restricted interests. Although ID is not a prerequisite of ASD, both tend to be associated and correlate in their severity [13]. Interestingly, the cerebellum appears to be a key region affected by autism and Purkinje cells, GABAergic neurons located in the cerebellar cortex, have been shown to be reduced in number and density in ASD [14]. The role of Purkinje cells has also been underscored by the description of autism-like neuroanatomic alterations and behaviors in mice with Purkinje cell-specific deficiency of either *Tsc1* [15], *Tsc2* [16], or *Shank2* [17]. Although there is no uniform classification for endophenotypes of ASD, it was recently proposed that an ASD-associated gene cluster expressed in Purkinje cells correlated with ID-free ASD in comparison to an ASD-associated gene cluster expressed in the neocortex, which was related to ID-associated ASD [18].

Recently, it was shown that Pianp, Ajap1, and App form three distinct GABA$_B$ receptor (GBR) complexes by binding to the N-terminal sushi-domain of GB1a, a subunit of presynaptic GBRs [19, 20]. While App is necessary for axonal GBR expression, Ajap1 and Pianp are not required for axonal transport [20]. Lack of App results in a significant deficit in presynaptic inhibition of neurotransmitter release by the GBR agonist baclofen [20]. The role of Pianp in presynaptic GBR functioning has not been thoroughly analyzed yet. GBRs are key regulators of synaptic transmission in the brain [21]. Presynaptic GBRs inhibit the release of a variety of neurotransmitters, including glutamate and GABA [21]. GABAergic signaling is altered in a variety of diseases including neurodevelopmental disorders such as ASD [22, 23]. Despite the fact that GBRs are not yet described to be directly involved in ASD, they are shown to influence other neurodevelopmental disorders such as fragile X syndrome [24]. However, as Purkinje cells have emerged as key cells mediating ASD-like phenotypes in mice [14–17], and Purkinje cells represent the neuronal cell type with the highest levels of GBRs [25], involvement of GBR signaling in autism-like behavior appears reasonable. Although deficiency of the main subunits of GBRs in mice did not reveal autism-like behaviors [26], there is evidence that GABAergic signaling is functionally impaired in ASD despite normal GABA receptor availability [22, 23, 27]. Such impairment may be mediated by modifications of GABA receptor interactions with associated proteins.

In order to comprehensively analyze the physiological functions of Pianp in vivo, we generated *Pianp*-deficient (PianpKO) mice. PianpKO mice show neuroanatomical alterations including reduced thickness of the granule cell layer in the dentate gyrus (DG) and reduced numbers of Purkinje cells in the cerebellum. These alterations were accompanied by a significant deficit in presynaptic GBR-mediated inhibition of glutamate release, increased neuronal apoptosis, altered gene expression including reduced expression of ASD candidate gene *Erdr1* and autism-like behavior including enhanced anxiety, spatial learning deficits, repetitive behavior and severely impaired social interactions.

Results

Pianp is preferentially expressed by neurons and *Pianp*-deficient mice exhibit morphologic and cellular alterations in the hippocampus and cerebellum

Pianp was expressed in all brain regions indicating broad but variable expression throughout the whole brain
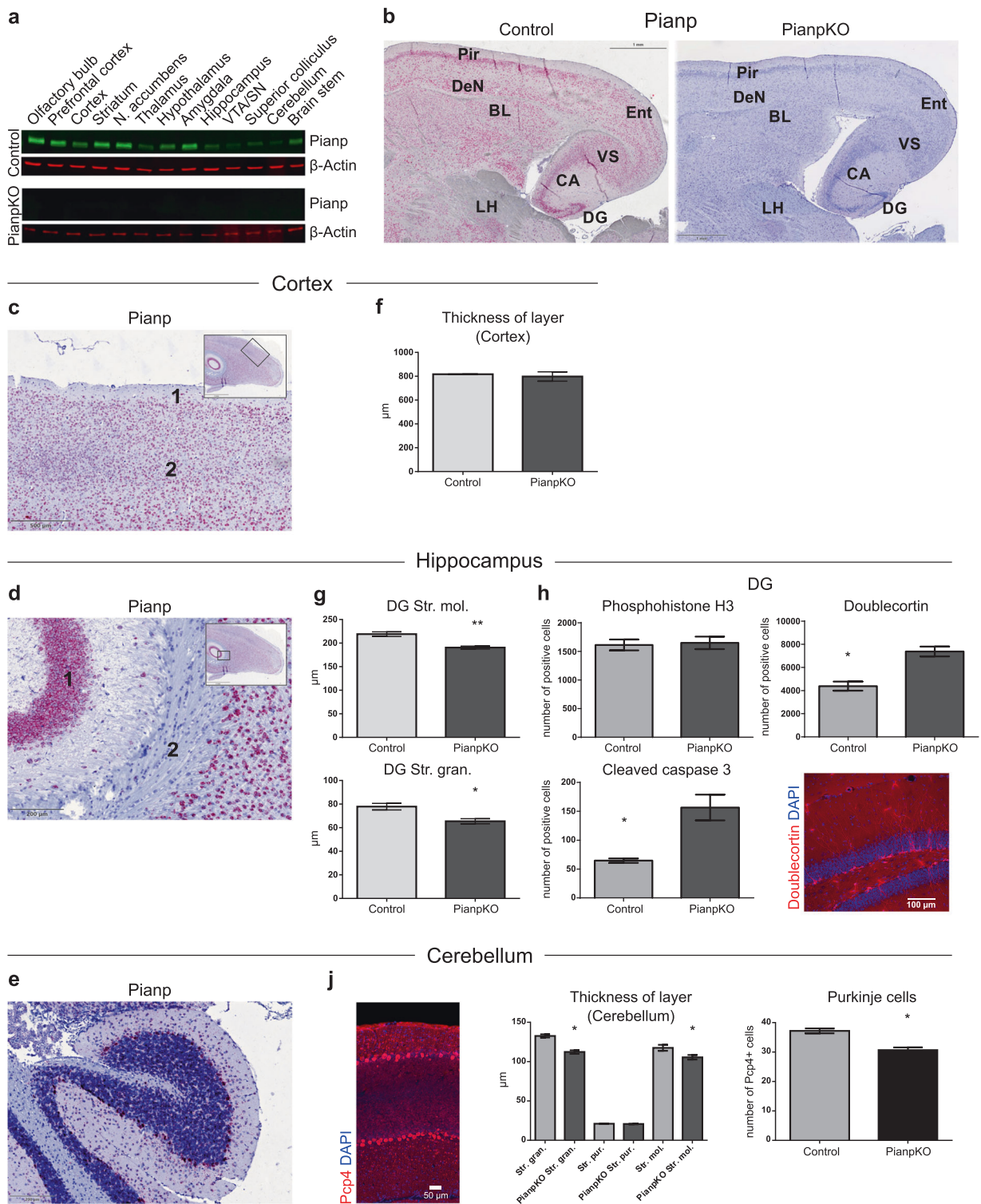
(Fig. 1a, b, and Supplementary Fig. 1A). On cellular level, in situ hybridization (ISH) confirmed *Pianp* expression in cortical layers II–VI (Fig. 1c), in hippocampal pyramidal neurons, in granule cells of the DG (Fig. 1d), and, within the cerebellum, especially in Purkinje cells (Fig. 1e). The pattern of expression indicated mostly neuronal expression as the fiber tracts of the hippocampus (Fig. 1d) and the cortex layer I were mostly negative (Fig. 1c). PianpKO mice did not show any Pianp expression in the brain (Fig. 1a) and ISH of the brain and liver using a probe

Fig. 1 *Pianp* is predominantly expressed in neuronal cells and its deficiency leads to increased numbers of immature neuronal cells and enhanced apoptosis in the hippocampus as well as reduced numbers of Purkinje cells in the cerebellum. **a** Western blots of whole protein lysates isolated from different brain regions of control and PianpKO mice with anti-Pianp and anti-β-Actin antibodies. **b** ISH for *Pianp* in the CNS showing basolateral amygdala (BL), CA1–CA3 fields of the hippocampus (CA), dorsoendopiriform nucleus (DeN), dentate gyrus (DG), entorhinal cortex (Ent), lateral hypothalamus (LH), piriform cortex (Pir), and ventral subiculum (VS). *Pianp* expression (in red) was observed with a neuronal expression pattern in most brain regions of control but not PianpKO mice. **c** In the cortex layer I (1), which is mostly composed of astrocytes, only minor *Pianp* expression (in red) was detected by ISH in control mice, while the deeper layers II to VI of the cortex (2), which are mostly composed of neuronal cells, displayed strong *Pianp* expression. **d** *Pianp* expression (in red) was detected by ISH in control mice in hippocampal pyramidal neurons (1) but not in fiber tracts (2) of the hippocampus, in which predominantly glia cells occur. **e** In the cerebellum of control mice *Pianp* expression (in red) was predominantly observed in Purkinje cells by ISH. **f** The thickness of the primary somatosensory cortex did not significantly differ ($p > 0.05$) between PianpKO and control mice ($n = 3$ per group). **g** Assessment of layer thicknesses of the DG in PianpKO and control mice. Stratum moleculare (Str. mol.) ($t(4) = 4.92$, $p < 0.01$) and stratum granulosum (Str. gran.) ($t(4) = 3.50$, $p < 0.05$) were significantly thinner in PianpKO than in control mice ($n = 3$ per group). **h** Adult hippocampal neurogenesis. No significant difference ($p = 0.6717$) between PianpKO and controls was seen in the number of proliferating cells (phosphohistone H3-positive) in the DG of adult mice ($n = 6$ per group). However, the numbers of immature neuronal cells (doublecortin-positive, +68%, $p = 0.0008$) and apoptotic cells (cleaved caspase 3-positive, +142%, $p = 0.0025$) were significantly higher in PianpKO compared with control mice ($n = 6$ per group). **j** Assessment of layer thicknesses and cellular composition of the cerebellum of PianpKO and control mice ($n = 3$ per group). A significant reduction in the thickness was noted in PianpKO mice in the stratum granulosum (Str. gran.) ($t(4) = 3.5$, $p < 0.05$) and the stratum moleculare (Str. mol.) ($t(4) = 4.92$, $p < 0.05$). The thickness of the Stratum purkinjense (Str. pur.), which only contains a single row of soma of Purkinje cells, was not altered, however, the density of Purkinje cells was significantly reduced in PianpKO mice as compared with their controls ($t(10) = 5.30$, $p < 0.05$, $n = 6$ per group). Bars indicate mean ± sem, *$p < 0.05$, **$p < 0.01$, two-tailed unpaired t test, thickness of layer (cerebellum): one-way ANOVA followed by the Sidak's multiple comparison test. All images are representative for $n \geq 3$

targeting the junction of exons 3 and 4 confirmed complete recombination and global inactivation (Fig. 1b and Supplementary Fig. 1B). PianpKO mice were viable, fertile, and survived at least 24 months. Grossly, these mice had no physical abnormalities. Blood plasma analyses (electrolytes, transaminases, cholinesterase, total protein, glucose, cholesterol, triglycerides, and urea) and routine staining of visceral organs did not reveal major abnormalities such as pathologic fibrosis or inflammation (Supplementary Figs. 2 and 3). The architecture and density of the vasculature of the liver appeared normal as shown by contrast-enhanced ultrasound (CEUS) and magnetic resonance imaging (MRI) (Supplementary Fig. 4). Mouse embryonic fibroblasts, that do not exhibit endogenous Pianp expression, were transfected with

empty vector (EV) and *Pianp*. While proliferation was not altered, adhesion, and transwell-migration were increased in MEF-Pianp in comparison to MEF-EV indicating that Pianp can be involved in adhesion and migration (Supplementary Fig. 5).

The overall brain volume was slightly larger in PianpKO mice compared with control mice with a trend towards statistical significance (Supplementary Fig. 6A). MRI volume measurements revealed a significantly lower volume of the prefrontal cortex in the PianpKO group compared with the controls while no differences were detected in the volume of the striatum and hippocampus (Supplementary Fig. 6B). Global size and structure as well as functional parameters derived from diffusion-weighted MR imaging of the brain appeared unaltered (Supplementary Fig. 6C). As MRI is not as sensitive as morphometric histologic measurements, neuroanatomic analyses of several brain regions were performed. While the thicknesses of the neocortex (Fig. 1f), the corpus callosum-alveus, and the external capsule were not altered in PianpKO mice (Supplementary Fig. 7A), layering and cellularity of the hippocampus and cerebellum differed in comparison to control mice. In the hippocampus decreased thicknesses of the stratum granulosum and the stratum moleculare of the DG (Fig. 1g) correlated with enhanced apoptosis of granule cells indicated by an increase of cleaved caspase 3 staining in PianpKO mice (Fig. 1h). On the other hand, the thicknesses of CA1 subregions stratum oriens, stratum pyramidale, stratum radiatum, and stratum lacunosum were unaltered (Supplementary Fig. 7A). Although proliferating phosphohistone H3-positive cells did not differ significantly in the DG of adult PianpKO and control mice (Fig. 1h), there was a notable and significant increase in the number of doublecortin-positive cells in the PianpKO mice, indicating enhanced abundance of newly formed, immature neuronal cells (Fig. 1h).

Measurements within the cerebellum demonstrated a significant reduction in the thicknesses of the granule cell layer and the molecular layer in PianpKO mice (Fig. 1j). Although the thickness of the Purkinje cell layer was not significantly altered, the density of Purkinje cells was significantly reduced in PianpKO mice (Fig. 1j).

Pianp localizes to axonal and dendritic neuronal processes and is involved in presynaptic GBR inhibition

To further elucidate neuronal Pianp functions, the distribution of ectopically expressed PIANP was assessed in cultured hippocampal neurons. PIANP-mCherry fusion was co-expressed with GFP for 6 h before cells were fixed and immunolabeled with neurite markers (Fig. 2a). In all cells analyzed, PIANP-mCherry was localized in
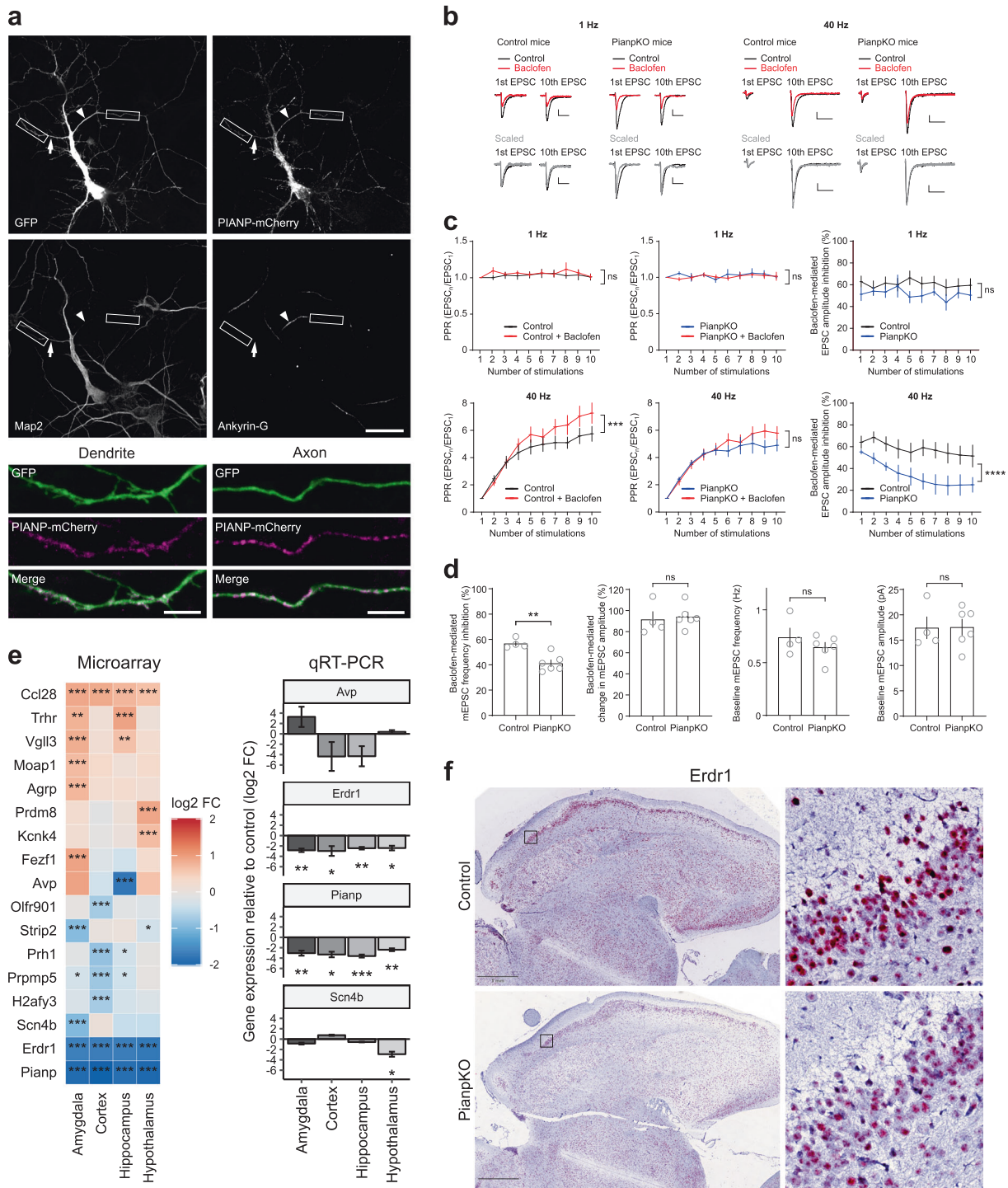
axons and somatodendritic compartments. Using GFP as a volume marker, the analysis of the normalized axon/dendrite ratio of PIANP-mCherry revealed a slight tendency toward a preferential axonal localization (Supplementary Fig. 7B).

Therefore, presynaptic GBR inhibition at CA3-to-CA1 synapses of PianpKO mice was tested under conditions of repetitive stimulation. While presynaptic inhibition by baclofen in PianpKO mice was normal with 1 Hz train stimulation (Fig. 2b, c), PianpKO but not control mice revealed a significant deficit in baclofen-mediated inhibition of glutamate release with 40 Hz train stimulation (Fig. 2b, c), a paradigm that induces short-term facilitation because of presynaptic Ca^{2+} accumulation. With 40 Hz stimulation,

Fig. 2 Pianp is sorted into axons and dendrites in neurons and controls presynaptic GBR inhibition as well as gene expression in the brain. **a** Overexpressed PIANP is sorted into axons and dendrites in cultured hippocampal neurons. At 7 days in vitro, PIANP-mCherry and GFP plasmids were transfected in wild-type hippocampal neurons and overexpressed for 6 h before fixation. GFP served as a volume marker. Representative co-transfected cell, demonstrating axonal and somato-dendritic localization of PIANP-mCherry. Higher magnification images of axonal and dendritic segments correspond to insets in overview image. Map2 was used as a marker of dendrites (arrow) and Ankyrin-G was used as a marker of the axon initial segment (arrowhead). Scale bars: 30 μm (overview images), 5 μm (high-magnification images). **b–d** Reduced presynaptic GBR-mediated inhibition in PianpKO mice. **b** Sample traces of evoked EPSCs from CA1 pyramidal neurons of PianpKO and control mice. EPSCs were evoked by train stimulation at 1 Hz or 40 Hz in the absence (black traces) and in the presence of 100 μM baclofen (red). The 1st EPSC in the presence of baclofen is scaled to that in the absence of baclofen (gray traces) to compare paired pulse ratios (PPR) of the 1st to the 10th EPSC. Scale bars, 50 ms and 50 pA. **c** Train stimulation at 40 Hz reveals a significant deficit in presynaptic GBR inhibition in PianpKO mice. Control (left: eight cells, three mice) and PianpKO (middle: nine cells, four mice) EPSCs are scaled to the 1st EPSC (Control 1 Hz, $p = 0.1737$; PianpKO 1 Hz, $p = 0.3836$; Control 40 Hz, $p = 0.0022$; PianpKO 40 Hz, $p = 0.0602$). Baclofen-mediated EPSC amplitude reduction is significantly decreased in PianpKO mice during 40 Hz train stimulation (right: 1 Hz, $p = 0.0705$; 40 Hz, $p < 0.0001$). **d** Impaired GBR-mediated inhibition of the mEPSC frequency in CA1 pyramidal neurons PianpKO mice ($p = 0.003$). The mEPSC amplitude remained unchanged ($p = 0.7576$). Basal mEPSC frequency ($p = 0.3304$) and amplitude ($p = 0.9653$) were unaltered. Data are from four cells from two control mice and seven cells from three PianpKO mice. **e** The heat map of significantly dysregulated genes identified by microarray transcriptome analysis of RNA isolated from amygdala, cortex, hippocampus, and hypothalamus of control and PianpKO mice ($n = 4$ for amygdala of control mice, $n = 5$ for each other group). QRT-PCR of amygdala, cortex, hippocampus, and hypothalamus of control and PianpKO mice for *Avp*, *Erdr1*, *Pianp* and *Scn4b* ($n = 5$ for each group). Bars indicate gene expression relative to control in log2 fold change (FC) normalized to *Actb*. **f** ISH for *Erdr1* in the CNS. *Erdr1* (in red) is broadly expressed in the cerebrum of control mice (upper panel) and its expression is reduced in the cerebrum of PianpKO mice (lower panel). Scale bars indicate 1 mm. Images are representative for $n ≥ 3$. Bars indicate mean ± SEM. $*p < 0.05$, $**p < 0.01$, $***p < 0.001$, $****p < 0.0001$, **c** two-way ANOVA, **d, e** two-tailed unpaired *t*-test

baclofen significantly increased the paired-pulse ratio (PPR) in control mice but not in PianpKO mice (Fig. 2b, c), which therefore exhibit a faster saturation of facilitation. In line with a deficit in presynaptic GBR-mediated inhibition in PianpKO mice, we observed a significantly reduced baclofen-mediated inhibition of the miniature excitatory postsynaptic current (mEPSC) frequency, without a change in mEPSC amplitude (Fig. 2d). Baseline mEPSC frequency and amplitude in PianpKO mice were unaltered (Fig. 2d).

Pianp regulates neuronal gene expression including autism-related gene *Erdr1*

Microarray gene expression analysis using whole-transcript arrays was performed with RNA isolated from

the cortex, hippocampus, amygdala, and hypothalamus of control and PianpKO mice. Thereby, 17 genes were identified that were significantly regulated with a log2 fold change (FC) of >0.7 or <0.7 (corresponding to a FC of approx. >1.6 and <0.6) and $p < 0.001$ (Fig. 2e). As expected, *Pianp* was the gene with the strongest reduction in all regions, while only two other genes, *Ccl28* and *Erdr1*, were dysregulated significantly in all four regions. Genes that were regulated with a FC > 2 or <0.5 were also assessed by qRT-PCR. Significant downregulation of *Erdr1* was confirmed in all four regions (Fig. 2e). By ISH *Erdr1* displayed a neuronal expression pattern that was weaker throughout the brain in PianpKO mice in comparison to control mice indicating that *Pianp* deficiency led to a global decrease of *Erdr1* expression in neurons (Fig. 2f).

To evaluate whether these molecular alterations also affected neurotransmitter abundance, the monoamines 5-hydroxyindoleacetic acid (5-HIAA), serotonin (5-HT), dopamine (DA), 3,4-dihydroxyphenylacetic acid (DOPAC), homovanillic acid (HVA), and noradrenaline (NA) were measured in the prefrontal cortex, hippocampus, amygdala, nucleus accumbens, striatum, ventral tegmental area/substantia nigra, and dorsal raphe nucleus of control and PianpKO mice. DA levels were slightly decreased in the amygdala of PianpKO mice in comparison to control mice (trend to significance, $p = 0.051$) while levels of all other neurotransmitters did not differ between the groups in the other regions (Supplementary Fig. 8). These data indicate that Pianp is likely not involved in the direct regulation of these neurotransmitters.

Pianp-deficient mice display endophenotypes associated with ASD

As the observed neuroanatomic alterations of the hippocampus and cerebellum and the impaired presynaptic GBR inhibition and altered neuronal expression pattern may impact on a wide range of neurological functions, PianpKO mice and control animals were subjected to a broad range of behavioral tests covering cognitive, affective, social, and motor domains. Motor functions were analyzed by grip strength assessment and the rotarod performance test. On the first experimental day, PianpKO mice showed a significantly higher grip strength and a higher latency to fall compared with the control mice (Supplementary Fig. 9A, B). As this difference could not be detected at the subsequent days, a motoric deficit seemed unlikely. In the startle and prepulse inhibition (PPI) test, a lower PPI was detected in PianpKO mice (Supplementary Fig. 9C). Post hoc analysis, however, revealed PPI deficits in PianpKO mice only at the prepulse levels 76 dB and 80 dB.

Exploratory and anxiety-like behavior in *Pianp*-deficient mice

The open field test (OFT) assesses general exploratory behavior as well as general motor functions. In the open field the total distance moved by PianpKO mice did not significantly differ from the control mice, neither at the habituation day (day 1) nor at the following day (day 2). Comparison of the two experimental days, however, revealed a difference in the distribution of the exploratory drive. PianpKO mice showed a bigger reduction in the distance moved in the first 5 min between day 1 (habituation day) and day 2 (test day) in comparison to control mice. This difference was also still observed between 6 and 10 min in PianpKO while it was absent in control mice (Fig. 3a). However, the enhanced movement on day 1 was likely the result of an enhaced temporary stress response of PianpKO mice toward the novel environment. As general locomotor activity was unaltered, these findings indicate that the general exploratory behavior of PianpKO mice is normal which is important for the interpretation of further behavioral tests.

The object exploration test (OET) assesses the exploratory behavior related to an unfamiliar object. A significantly lower distance to the object position after presentation of the object was only detected in control but not in PianpKO mice. Control mice were exploring the object much more than PianpKO mice in terms of a significantly higher time spent sniffing and lower distance to the object position. Moreover, PianpKO mice showed a significantly lower distance moved after presentation of the unfamiliar object. Grooming time, an indicator of repetitive behavior, however, was significantly higher in PianpKO than in control mice after object presentation (Fig. 3b).

The elevated plus maze test (EPM) assesses the exploratory behavior in an insecure area. Here PianpKO mice explored the open arms less frequently, spent less time there, and showed a higher latency to the open arm exploration than control mice. The distance moved, however, did not differ between the groups (Fig. 3c).

The novelty-induced hypophagia (NIH) test showed only a trend towards higher latency to consumption and lower consumption in the novel cage in PianpKO mice as compared with control mice (Supplementary Fig. 9D). Overall, these tests indicate context-dependent enhanced anxiety-like behavior.

Amphetamine challenge was performed including a 30 min habituation phase and saline injection as control. As observed in other experimental setups, PianpKO moved longer distances compared with control mice only during the first ten minutes of the habituation phase but neither in the later phases of habituation nor after saline injection. Thirty minutes after amphetamine injection PianpKO started to show increased movement in comparison to controls, however not reaching statistical significance (Supplementary Fig. 9E).

Stress response, emotionality, and autism-like behavior in *Pianp*-deficient mice

Tail suspension test (TST) and forced swim test (FST) were used to assess stress response [28, 29] and emotionality. In both tests PianpKO mice showed a significantly shorter time of immobility than control mice (Fig. 4a, b), indicating an increased stress response. The sucrose preference test did not show significant differences between the two groups (Supplementary Fig. 10A). Therefore, PianpKO mice did not exhibit features of a depression-like phenotype. In line with higher grooming times in OET (Fig. 3b), i.e. increased repetitive behavior, the nest building test (NBT) revealed significantly lower nesting scores in PianpKO mice compared with controls (Fig. 4c). These alterations suggest autism-like behavior.

Cognition in *Pianp*-deficient mice

In the novel object recognition test (ORT) PianpKO and control mice both showed higher preference ratios for the novel object while exploration times did not significantly differ (Fig. 4d and Supplementary Fig. 10B). Although total exploration times were higher for PianpKO mice in both comparisons, in the object relocation test (OLT), however, only control mice showed a preference for the relocated object, while PianpKO mice did not show this preference (Fig. 4e and Supplementary Fig. 10C). Contextual and cued fear conditioning was performed successfully in PianpKO and control mice. Cue presentation resulted in similar freezing times. In context recall, however, PianpKO showed significantly lower freezing times (Fig. 4f). Taken together, PianpKO mice showed a specific deficit in spatial, but not nonspatial memory.

Abnormal social behavior in *Pianp*-deficient mice

As similar cerebellar anomalies as found in PianpKO mice were also described in human patients with ASD [14] and murine models of the disease [15–17], social and repetitive autism-like behaviors were tested. In the social interaction test (SIT) control mice but not PianpKO mice showed a significantly different exploration time and preference for the social partner compared with the empty cage. Therefore, in contrast to control mice, PianpKO mice did not exhibit a normal preference for the chamber with a social partner. In comparing a known social partner (SP1) with a novel social partner (SP2) both PianpKO and control mice showed a preference for the novel social partner. However, the
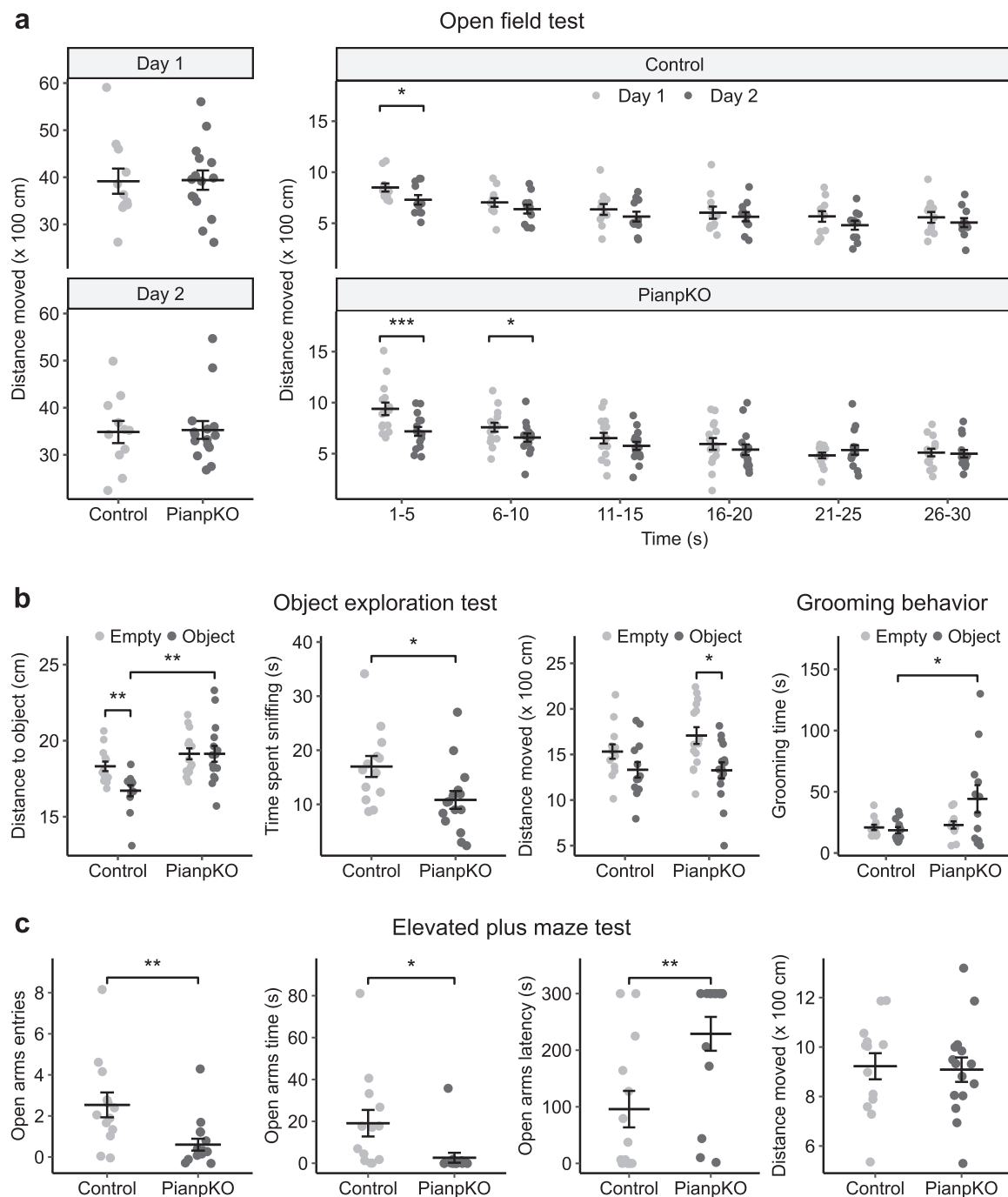
Fig. 3 *Pianp*-deficient mice show increased anxiety in novel and aversive settings. **a** The total distance moved in the open field test (OFT) was not significantly different between control ($n = 11$) and PianpKO mice ($n = 15$) at day 1 ($t(24) = 0.07$, $p > 0.05$) or day 2 ($t(24) = 0.14$, $p > 0.05$). However, a higher distance moved in the first 5 min at day 1 compared with day 2 was detected in PianpKO ($t(14) = 5.15$, $p > 0.001$) as well as in control mice ($t(10) = 2.83$, $p > 0.05$). Between 6 and 10 min PianpKO mice still showed higher distance moved ($t(14) = 2.16$, $p > 0.05$), while this difference could not be detected in the control mice ($t(10) = 1.68$, $p > 0.05$). **b** In the object exploration test (OET), control mice ($n = 13$) showed significantly less distance to the position of the object when it was present ($t(12) = 4.25$, $p < 0.01$). PianpKO mice ($n = 15$) did not show this difference ($t(14) = 0.01$, $p > 0.05$) and had a significantly larger distance to the object than the control mice ($t(26) = 3.70$, $p < 0.01$). The

time spent sniffing the object was significantly lower in PianpKO mice ($t(26) = 2.45$, $p < 0.05$). PianpKO mice moved significantly less when the object was present ($t(14) = 2.58$, $p < 0.05$) while this difference was not observed in control mice ($t(12) = 1.73$, $p > 0.05$). When the object was present, PianpKO mice ($n = 12$) showed a significantly longer time of grooming behavior compared with the controls ($n = 12$) ($t(22) = 2.24$, $p < 0.05$). **c** In the elevated plus maze test (EPM), PianpKO mice ($n = 15$) showed significantly less open arm entries ($t(26) = 3.02$, $p < 0.01$), a significantly shorter time spent on the open arms ($t(26) = 2.57$, $p < 0.05$), and a significantly higher latency to enter the open arms ($t(26) = 3.03$, $p < 0.01$) in comparison to control mice ($n = 13$). The total distance moved, however, did not differ significantly between the two groups ($t(26) = 0.19$, $p > 0.05$). Horizontal lines indicate mean ± SEM. *$p < 0.05$, **$p < 0.01$, ***$p < 0.001$, two-tailed unpaired or paired t-test
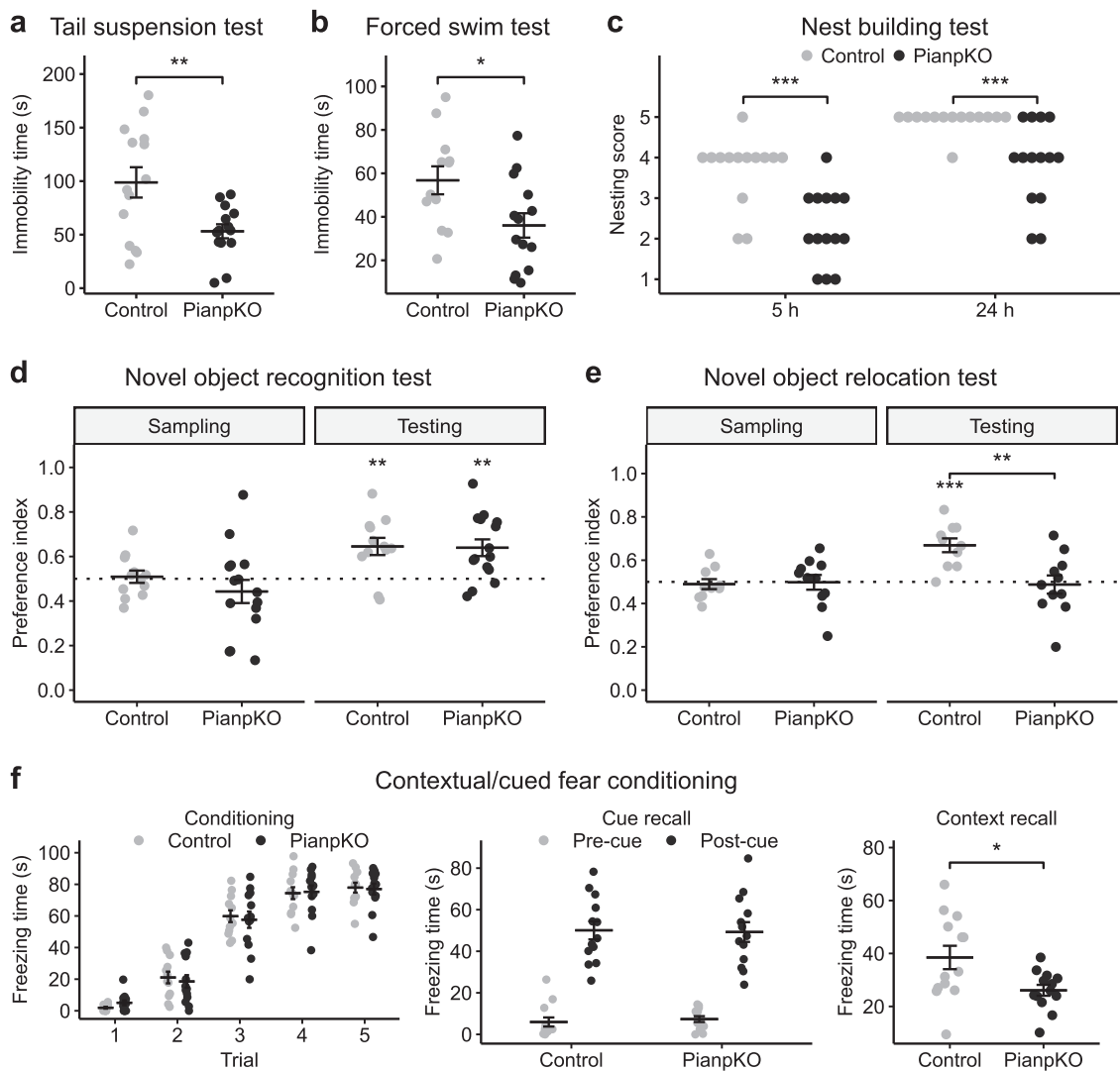
Fig. 4 *Pianp*-deficient mice show an increased response to acute stress, a lower nesting score, no preference for a relocated object, and a deficit in contextual fear conditioning. **a** In the tail suspension test (TST), PianpKO mice ($n = 14$) moved more and had a significantly shorter time of immobility ($t(26) = 2.93$, $p < 0.01$) compared with control mice ($n = 14$). **b** In the forced swim test (FST), PianpKO mice ($n = 14$) swam for a longer time and had a significantly shorter time of immobility ($t(24) = 2.44$, $p < 0.05$) compared with control mice ($n = 12$). **c** In the nest building test (NBT), PianpKO mice ($n = 14$) had significantly lower nesting scores compared with the controls ($n = 12$) in the nest building after 5 h ($U = 170.5$, $p < 0.001$) and 24 h ($U = 163$, $p < 0.001$). **d** In the novel object recognition test (ORT), PianpKO ($n = 15$) (sampling: $t(14) = 1.10$, $p > 0.05$; testing: $t(14) = 3.71$, $p < 0.01$) and control mice ($n = 12$) (sampling: $t(11) = 0.33$, $p > 0.05$; testing: $t(11) = 3.76$, $p < 0.01$) showed a similar preference for the novel object that did not differ between the two groups (sampling: $t(25) = 1.05$, $p > 0.05$, testing: $t(25) = 0.11$, $p > 0.05$). **e** In the object relocation test (ORL), control mice ($n = 10$) showed a preference for the relocated object (sampling: $t(9) = 0.45$, $p > 0.05$; testing: $t(9) = 5.30$, $p < 0.001$) while PianpKO ($n = 11$) did not show a preference for the relocated object (sampling: $t(10) = 0.06$, $p > 0.05$; testing: $t(10) = 0.29$, $p > 0.05$). The preference index differed significantly between the two groups in the testing phase (sampling: $t(19) = 0.20$, $p > 0.05$; testing: $t(19) = 3.38$, $p < 0.01$). **f** In the contextual and cued fear conditioning, PianpKO mice ($n = 12$) and control mice ($n = 13$) showed a successful conditioning and comparable cue recall ($t(24) = 0.13$, $p > 0.05$). In context recall, however, PianpKO had a significantly lower freezing time ($t(24) = 2.55$, $p < 0.05$). Horizontal lines indicate mean ± SEM. *$p < 0.05$, **$p < 0.01$, ***$p < 0.001$, **a**, **b** two-tailed unpaired *t*-test, **c** Mann–Whitney U test, **d**, **e** one sample or two-tailed unpaired *t*-test

exploration times at SP1 and SP2 differed significantly only in control mice, indicating reduced interest of PianpKO mice in novel social interaction (Fig. 5a). In the odor discrimination test a general deficit in the discrimination of nonsocial odors could not be detected. The difference detected in the very first solvent control can likely be attributed to the increased stress

response of PianpKO mice in novel settings. In the discrimination of social odors, PianpKO mice showed a significantly lower time sniffing at female urine, one of the strongest social cues, while sniffing time at water controls as well as at male urine did not significantly differ from control mice (Fig. 5b). Together, these results imply strong social
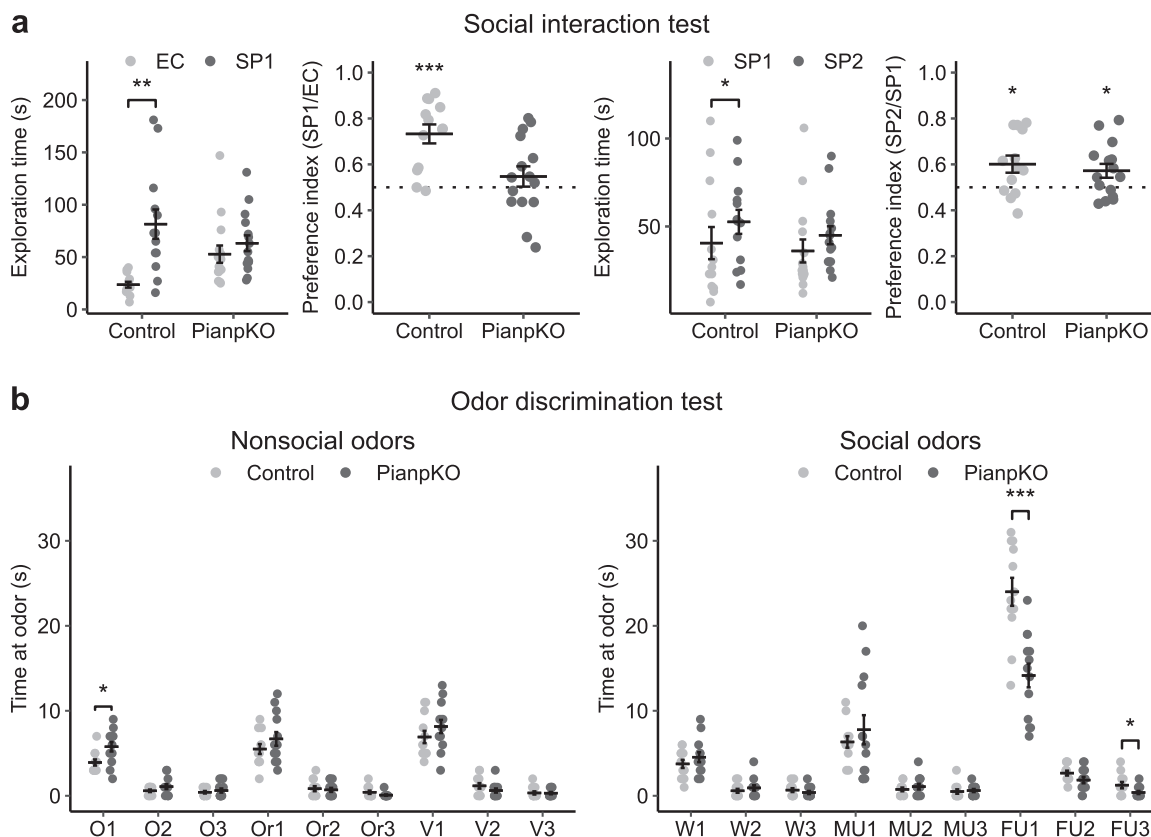
Fig. 5 *Pianp* deficiency impairs social interaction and social odor discrimination. **a** In the social interaction test (SIT), PianpKO mice ($n = 14$) showed equal exploration times at an empty cage (EC) and at a cage with an unknown mouse ($t(14) = 0.83$, $p > 0.05$), designated as social partner mouse 1 (SP1), while the controls ($n = 12$), showed a significantly higher exploration time at SP1 than at the EC ($t(12) = 4.08$, $p < 0.01$). Therefore control mice had a statistically significant preference for SP1 ($t(12) = 5.63$, $p < 0.001$) that was not present in PianpKO mice ($t(14) = 1.07$, $p > 0.05$). Subsequent exposure to the familiar SP1 and to another unknown mouse, designated as social partner mouse 2 (SP2), PianpKO mice ($t(14) = 2.38$, $p < 0.05$) and controls ($t(12) = 2.71$, $p < 0.05$) both showed a slight, but statistically significant, preference for unknown SP2. However, the exploration times at SP1 and SP2 did only differ statistically significant in the control group (control: $t(12) = 2.28$, $p < 0.05$; PianpKO: $t(14) = 1.58$, $p > 0.05$). **b** In the odor discrimination test, PianpKO mice ($n = 13$) did

not show a significant difference in the time spent sniffing the nonsocial odors oil (O2: $t(23) = 1.49$, $p > 0.05$; O3: $t(23) = 0.69$, $p > 0.05$), apart from the first round (O1: $t(23) = 2.75$, $p < 0.05$,), orange (Or1: $t(23) = 1.18$, $p > 0.05$; Or2: $t(23) = 0.37$, $p > 0.05$; Or3: $t(23) = 1.68$, $p > 0.05$), and vanilla (V1: $t(23) = 1.16$, $p > 0.05$; V2: $t(23) = 1.38$, $p > 0.05$; V3: $t(23) = 0.91$, $p > 0.05$) in comparison to the controls ($n = 12$). However, PianpKO mice spent a significantly shorter time sniffing female urine (FU1: $t(23) = 4.59$, $p < 0.001$; FU3: $t(23) = 2.15$, $p < 0.05$) compared with the controls ($n = 12$). However, FU2 did not differ significantly (FU2: $t(23) = 1.73$, $p > 0.05$). No significant difference between the groups could be detected for water (W1: $t(23) = 1.03$, $p > 0.05$; W2: $t(23) = 0.87$, $p > 0.05$; W3: $t(23) = 0.99$, $p > 0.05$) and male urine (MU1: $t(23) = 0.76$, $p > 0.05$; MU2: $t(23) = 0.81$, $p > 0.05$; MU3: $t(23) = 0.36$, $p > 0.05$). * $p < 0.05$, ** $p < 0.01$, *** $p < 0.001$, **a** one sample or two-tailed unpaired t-test, **b** two-tailed unpaired t-test

impairment which in synopsis with the other results, i.e. repetitive behavior and enhanced anxiety, can be interpreted as autism-like behavior.

Discussion

The global phenotype of PianpKO mice indicates that Pianp is primarily involved in the regulation of neuronal function and behavior as no major phenotypic or functional alterations were found in other organs beside the brain. Detailed phenotyping revealed that lack of Pianp affected a range of behavioral traits. Altogether, the results of OET and EPM

demonstrated heightened anxiety in PianpKO mice. As the NIH test did not indicate heightened anxiety, modulation of anxiety by Pianp may be context dependent. The trend to lower DA concentrations in the amygdala of PianpKO may suggest that altered dopaminergic signaling could be involved as DA signaling in the amygdala has been described to affect anxiety [30–39]. Anxiety-like behavior is also present in mice with Purkinje cell-specific deficiency of *Shank2* [40]. Thus, enhanced anxiety in PianpKO could be mediated by altered output signaling from the cerebellum.

Results from the ORT and OLT reveal a specific deficit in spatial, but not nonspatial memory in PianpKO mice. The comparably richer set of cues available in the ORT (e.g.

object shape, size, etc.) might be sufficient to provide the animal with enough information to recognize object novelty. With longer intervals (delays) between trials, however, a deficit in object novelty recognition might still become obvious. Hippocampus-independent auditory fear conditioning was normal, but PianpKO mice displayed significantly lower freezing in the hippocampus-dependent context recall. Taking these results together, a hippocampal deficit can be assumed in PianpKO mice. Regarding the hippocampus a decreased thickness of the stratum granulare and the stratum moleculare of the DG was observed. This is a result of altered adult neurogenesis and differentiation in this region. The number of doublecortin-positive, i.e. newly formed and immature neuronal cells was increased in PianpKO mice. However, also the rate of apoptotic cell death was strongly increased in PianpKO mice. These findings indicate altered differentiation of doublecortin-positive cells, which is likely delayed and may contribute to enhanced susceptibility to apoptosis. The observed imbalance of normal proliferation and enhanced apoptosis explains the net cell loss yielding a reduction in the thickness of the stratum granulosum and stratum moleculare of the DG. Using electrophysiology, a deficit in the baclofen-mediated inhibition of glutamate release was observed at CA3-to-CA1 synapses when recording mEPSCs or evoked EPSCs with 40 Hz train stimulation. The observed deficit in GBR-mediated presynaptic inhibition indicates that Pianp influences GBR regulation of synaptic transmission. The faster saturation of short-term synaptic plasticity observed with PianpKO mice likely influences information transfer in neuronal networks and contributes to the observed behavioral phenotypes. As GBR affects adult hippocampal neurogenesis [41] and is involved in learning and memory [22], it is likely that Pianp affects cellular composition and altered transmission in the hippocampus at least partially via interaction with GBR. As apoptosis can also be regulated by modulation of adhesion complexes [42, 43], alteration of these complexes by Pianp [8, 9] may also be involved in the observed phenotype.

PianpKO mice also displayed alterations in the composition of the cerebellum. The thickness of the stratum granulare and stratum moleculare as well as the density of Purkinje cells were significantly decreased in PianpKO mice. One of the main symptoms upon cerebellar dysfunction in humans is ataxia. PianpKO mice, however, did not show deficits in basic motor functions. In a mouse model of spinocerebellar ataxia these tests also revealed normal results [44]. Mice, as four-legged animals, might be less sensitive to cerebellar alterations in terms of motor functions. In addition, similar pathologic cerebellar features as observed in PianpKO are also seen in human patients with ASD [14] and murine models [15–17]. These murine models also exhibit normal basic motor functions

and only showed alterations in complex tasks of motor learning [17].

PianpKO mice did not show the typical preference for social vs. nonsocial exploration normally observed in mice indicating severe social impairment. In line with this, their interest for the strongest social cue (female urine) was also lower in comparison to controls. Given that exploration times in the social recognition stage of the SIT were comparable to control mice, PianpKO mice seem to exhibit a lack of social interest particularly in choice situations, one of the key symptoms seen in ASD. The described behavior of the boy with homozygous nonsense variant in *PIANP* [12] also indicates a lack in social interaction. In PianpKO mice, autism-like behavior is also supported by the higher grooming time in OET and lower nesting scores found in NBT [45–47]. Downregulation of *Erdr1* as seen in all brain regions of PianpKO mice has also been described in another genetic model of neurodevelopmental disorder with resemblance to autism [48]. Therefore, *Erdr1* is a potential mediator of this phenotype in both models. Context-dependent enhanced anxiety and learning can also be impaired in human ASD as well as murine models [15–17]. Therefore, behavioral analyses and pathologic features of PianpKO mice strongly indicated an ASD-like phenotype.

Although, it was already shown that Pianp is a constituent of the GBRs in the CNS [19, 20], we here provide the first experimental evidence that Pianp indeed alters GBR signaling in vivo. Although GBRs have not been reported to be directly involved in ASD [22, 23], several reports show that activation of GBRs by GBR agonist baclofen may improve ASD symptoms [49]. In the BTRB and C58 mouse models of autism, baclofen improves social deficits and repetitive behavior [49]. In constitutive NMDAR hypofunction, baclofen rescues behavioral deficits [50], and in 16p11.2 deletion mice, baclofen reverses cognitive deficits and improves social interactions [51]. These findings indicate that constitutive hypoactivation of GBRs may context-dependently contribute to the manifestation of autism-like behavioral traits. As Purkinje cells are recognized as key cells mediating autism-like phenotypes in mice [14–17] and Purkinje cells represent the neuronal cell type with the highest levels of GBRs [25] as well as high expression of Pianp, it appears reasonable that *Pianp* deficiency associated cerebellar alterations and Purkinje cell dysfunction contribute to autism-like behavior.

Overall, the behavioral phenotype of PianpKO mice including context dependent enhanced anxiety, learning deficits, altered stress coping, and impaired social interaction in synopsis with the neuroanatomic cerebellar alterations indicates an ASD-like phenotype with strong resemblance to several Purkinje cell-dependent models of this disease [15–17]. As the case

description of a boy with homozygous nonsense variant in *PIANP* showed global developmental delay including deficits in learning and social interaction, it appears likely that PIANP has conserved functions in mice and humans that involve global development, learning and social interaction. Therefore, these findings further strengthen the role of PIANP as an important mediator in these processes and identify *PIANP* as a novel candidate gene associated with ASD.

Future research to unravel how *PIANP* controls these diverse molecular and cellular alterations may further improve our understanding of the still enigmatic fields of ID as well as ASD and may therefore open new avenues for molecular diagnostic and therapeutic approaches.

Material and methods

Generation of *Pianp* knockout mice

Pianp[tm1a(KOMP)Wtsi] C57BL/6N-A[tm1Brd] mouse embryonic stem cells were obtained from the KOMP repository (No. CSD70665). After reconstitution these mice were crossed with B6N.Cg-Tg(ACTFLPe)9205Dym/CjDswJ mice (Jax No. 019100) to generate *Pianp* floxed mice. These mice were further bred with B6.C-Tg(CMV-cre)1Cgn/J mice (Jax No. 006054) to generate constitutive knockout mice, denoted as PianpKO. Western blotting, ISH, neuroanatomical, transcriptomic, and behavioral experiments were performed using male PianpKO and control (*Pianp* floxed) mice aged 8–48 weeks. For electrophysiology experiments P20-P27 B6-Pianp[em1Bet] mice [20], denoted as PianpKO and control (wild-type littermates) mice were used.

Brain microdissection

The whole brain was cut coronally using a cryostat (Leica Biosystems, Nussloch, Germany) and manually microdissected using brain punches. Paxinos' and Franklin's the Mouse Brain in Stereotaxic Coordinates [52] was used for identification of the different brain areas.

Western blotting

Dissected brain region tissue was lysed using RIPA buffer (Sigma-Aldrich, St. Louis, MO, USA). SDS-PAGE and immunoblotting were carried out as described previously [8]. Images were acquired with the Odyssey CLx imaging system (LI-COR Biosciences, Lincoln, NE, USA) and quantified using ImageJ 1.48i [53]. Primary antibodies: anti-Pianp (clone 9C7) [10], anti-beta-Actin (No. A2103, Sigma-Aldrich). Secondary antibodies coupled with IRDye680RD and IRDye800CW (LI-COR).

In situ hybridization (ISH)

ISH was conducted on coronal sections of formalin-fixed paraffin-embedded (FFPE) brains using RNAscope 2.5 HD and BaseScope assays in red [54] (Advanced Cell Diagnostics, Newark, CA, USA). The following probes were used for hybridization: BaseScope probe BA-Mm-*Pianp*-2EJ (No. 705741) and RNAscope probe Mm-*Erdr1* (No. 465101).

Thickness of layers, adult hippocampal neurogenesis, and Purkinje cell density

Thirty micrometers thick coronal sections were made using a VT1000 vibratome (Leica Biosystems). Immunofluorescence stainings were prepared using the following primary antibodies: forebrain: anti-CNPase (No. PA5-19551, Thermo Fisher Scientific, Waltham, MA, USA), cerebellum: anti-Pcp4 (No. sc-74816, Santa Cruz Biotechnology, Dallas, TX, USA). The thickness of different brain structures was measured on a series of six consecutive sections starting at Bregma −1.94 mm. To assess adult hippocampal neurogenesis the following antibodies were used: anti-phosphohistone H3 (No. sc-8656-R, Santa Cruz Biotechnology), anti-doublecortin (No. sc-8066, Santa Cruz Biotechnology), anti-cleaved caspase 3 (No. AB3623, Millipore, Merck, Darmstadt, Germany). To assess Purkinje cell density a region-of-interest of $600 \times 600\,\mu m$ was superimposed on the 6th cerebellar lobule (starting at ~ Bregma −6.6 mm) and the number of Purkinje cell profiles was determined. See supplementary information for a detailed description.

Immunocytochemistry and image analysis

Embryonic day 16.5 mouse hippocampi were dissected and dissociated. At 7 days in vitro, PIANP-mCherry and GFP plasmids were transfected in WT hippocampal neurons and overexpressed for 6 h before fixation. GFP served as a volume marker. See supplementary information for a detailed description.

Electrophysiology

Three-hundred micrometers thick hippocampal slices were prepared with a VT1200S vibratome (Leica Biosystems) and were incubated for 15 min at 32 °C in ACSF containing (in mM): 126 NaCl, 26 NaHCO$_3$, 2.5 KCl, 1.25 NaH$_2$PO$_4$, 2 CaCl$_2$, 1 MgCl$_2$, and 10 glucose. Slices were kept at room temperature until recording at 32 °C submerged in a recording chamber perfused with ACSF. CA1 pyramidal cells were visually identified using a 40x objective with a BX51WI microscope (Olympus, Tokyo, Japan). Cells were voltage-clamped at −60 mV with a

Multiclamp700B amplifier (Molecular Devices, San José, CA, USA). Spontaneous mEPSCs were recorded in the presence of 0.2 μM tetrodotoxin and 100 μM picrotoxin. EPSCs were evoked with extracellular monopolar current pulses generated by a custom made isolated current stimulator and applied via a patch-pipette filled with ACSF and positioned to activate the Schaeffer collaterals. All recordings were filtered at 4-10 kHz and digitized at 10–20 kHz with a Digidata 1550B digitizer (Molecular Devices).

Microarray transcriptome analysis

Total RNA was extracted from dissected brain region tissue using the RNeasy Mini Kit (Qiagen, Hilden, Germany). Gene expression profiling was performed using Affymetrix GeneChip Mouse Gene 2.0 ST Arrays (Thermo Fisher Scientific). A custom chip definition format version 21 with Entrez based gene definitions was used to annotate the arrays. The raw fluorescence intensity values were normalized applying quantile normalization. Differential gene expression was analyzed with ANOVA using JMP Genomics 13 (SAS Institute, Cary, NC, USA). A false positive rate of $\alpha = 0.05$ with false discovery rate correction was taken as the level of significance. The raw and normalized data have been deposited in NCBI's Gene Expression Omnibus and are accessible through GEO Series accession number GSE124791 (https://www.ncbi.nlm.nih.gov/geo/query/acc.cgi?acc=GSE124791).

Quantitative reverse-transcription PCR (qRT-PCR)

RevertAid H-Minus M-MuLV transcriptase (Thermo Fisher Scientific) was used for reverse transcription. QRT-PCR was performed in Stratagene Mx3005P system (Agilent, Santa Clara, CA, USA) using SYBR Green PCR Master-Mix (Thermo Fisher Scientific). Relative gene expression in relation to reference gene (*Actb*) was calculated using the $2^{-\Delta\Delta CT}$ method. See supplementary information for primer sequences.

Behavioral analysis

The experimental protocols used in this study complied with national and international ethical guidelines and were approved by the animal welfare commission of the Regierungspräsidium Karlsruhe (Karlsruhe, Germany). Housing conditions were as described previously [55]. All experiments were conducted during the dark period of the day, in the animals' active phase. Animals were allocated to the experimental groups according to their genotype and labeled with numbers without information on the genotype. Therefore, data acquisition was performed in blindfold manner. Animals were excluded from the analysis if certain quality parameters defined for every experiment were not met indicating failure of this animal in the experiment. OFT, EPM, TST, FST, OET, ORT, OLT, NBT, and ODT were conducted as described previously [55–59]. See supplementary information for a detailed description.

Social interaction test (SIT)

SIT was conducted according to Moy et al. [60]. Here, two phases, called sociability and preference for social novelty, were tested. In brief, in a three chamber test apparatus the test mouse was placed in the middle chamber. After a 5 min habituation phase, an unfamiliar male mouse (social partner 1) was placed into a wire cage in one of the side chambers, while the opposite side chamber contained an empty wire cage (sociability phase). In the second phase another unfamiliar male mouse (social partner 2) was placed into the empty wire cage to test preference for social novelty. See supplementary materials and methods for a detailed description.

Statistical analysis

Statistical analyses were performed using R 3.4.2 [61], SigmaPlot 11 (Systat Software, San Jose, CA, USA), Prism 6 (GraphPad Software, La Jolla, CA, USA), or Excel 2010 (Microsoft, Redmond, WA, USA). Sample size determination was performed separately for each experiment according to experience from previous experiments using an alpha level of 0.05 and a beta level of 0.20. Results are reported as mean ± SEM. For statistical testing two-tailed unpaired or paired *t*-test, one sample *t*-test, ANOVA, and Mann–Whitney *U*-test were used. The appropriate statistical test was chosen according to the requirements of each test (e.g. normal distribution or equal variance). Results were considered significantly different if $p < 0.05$.

Compliance with ethical standards

References

1. Kogure A, Shiratori I, Wang J, Lanier LL, Arase H. PANP is a novel O-glycosylated PILRα ligand expressed in neural tissues. Biochem Biophys Res Commun. 2011;405:428–33.

2. Biswas S, Adrian M, Evdokimov K, Schledzewski K, Weber J, Winkler M, et al. Counter-regulation of the ligand-receptor pair Leda-1/Pianp and Pilrα during the LPS-mediated immune response of murine macrophages. Biochem Biophys Res Commun. 2015;464:1078–83.

3. Lin N, Di C, Bortoff K, Fu J, Truszkowski P, Killela P, et al. Deletion or epigenetic silencing of AJAP1 on 1p36 in glioblastoma. Mol Cancer Res. 2012;10:208–17.

4. Zeng L, Fee BE, Rivas MV, Lin J, Adamson DC. Adherens junctional associated protein-1: a novel 1p36 tumor suppressor candidate in gliomas (Review). Int J Oncol. 2014;45:13–7.

5. Isidor B, Le Cunff M, Boceno M, Boisseau P, Thomas C, Rival J-M, et al. Complex constitutional subtelomeric 1p36.3 deletion/duplication in a mentally retarded child with neonatal neuroblastoma. Eur J Med Genet. 2008;51:679–84.

6. Anttila V, Winsvold BS, Gormley P, Kurth T, Bettella F, McMahon G, et al. Genome-wide meta-analysis identifies new susceptibility loci for migraine. Nat Genet. 2013;45:912–7.

7. Ikeda M, Tomita Y, Mouri A, Koga M, Okochi T, Yoshimura R, et al. Identification of novel candidate genes for treatment response to risperidone and susceptibility for schizophrenia: integrated analysis among pharmacogenomics, mouse expression, and genetic case-control association approaches. Biol Psychiatry. 2010;67:263–9.

8. Géraud C, Schledzewski K, Demory A, Klein D, Kaus M, Peyre F, et al. Liver sinusoidal endothelium: a microenvironment-dependent differentiation program in rat including the novel junctional protein liver endothelial differentiation-associated protein-1. Hepatology. 2010;52:313–26.

9. Evdokimov K, Biswas S, Schledzewski K, Winkler M, Gorzelanny C, Schneider SW, et al. Leda-1/Pianp is targeted to the basolateral plasma membrane by a distinct intracellular juxtamembrane region and modulates barrier properties and E-Cadherin processing. Biochem Biophys Res Commun. 2016;475:342–9.

10. Evdokimov K, Biswas S, Adrian M, Weber J, Schledzewski K, Winkler M, et al. Proteolytic cleavage of LEDA-1/PIANP by furin-like proprotein convertases precedes its plasma membrane localization. Biochem Biophys Res Commun. 2013; 434:22–7.

11. Biswas S, Adrian M, Weber J, Evdokimov K, Winkler M, Géraud C. Posttranslational proteolytic processing of Leda-1/Pianp involves cleavage by MMPs, ADAM10/17 and gamma-secretase. Biochem Biophys Res Commun. 2016;477:661–6.

12. Anazi S, Maddirevula S, Faqeih E, Alsedairy H, Alzahrani F, Shamseldin HE, et al. Clinical genomics expands the morbid genome of intellectual disability and offers a high diagnostic yield. Mol Psychiatry. 2017;22:615–24.

13. Matson JL, Shoemaker M. Intellectual disability and its relationship to autism spectrum disorders. Res Dev Disabil. 2009;30:1107–14.

14. Fatemi SH, Aldinger KA, Ashwood P, Bauman ML, Blaha CD, Blatt GJ, et al. Consensus paper: pathological role of the cerebellum in autism. Cerebellum. 2012;11:777–807.

15. Tsai PT, Hull C, Chu Y, Greene-Colozzi E, Sadowski AR, Leech JM, et al. Autistic-like behaviour and cerebellar dysfunction in Purkinje cell Tsc1 mutant mice. Nature. 2012;488:647–51.

16. Reith RM, McKenna J, Wu H, Hashmi SS, Cho S-H, Dash PK, et al. Loss of Tsc2 in Purkinje cells is associated with autistic-like behavior in a mouse model of tuberous sclerosis complex. Neurobiol Dis. 2013;51:93–103.

17. Peter S, Ten Brinke MM, Stedehouder J, Reinelt CM, Wu B, Zhou H, et al. Dysfunctional cerebellar Purkinje cells contribute to autism-like behaviour in Shank2-deficient mice. Nat Commun. 2016;7:12627.

18. Clifford H, Dulneva A, Ponting CP, Haerty W, Becker EBE. A gene expression signature in developing Purkinje cells predicts autism and intellectual disability co-morbidity status. Sci Rep. 2019;9:485.

19. Schwenk J, Pérez-Garci E, Schneider A, Kollewe A, Gauthier-Kemper A, Fritzius T, et al. Modular composition and dynamics of native GABAB receptors identified by high-resolution proteomics. Nat Neurosci. 2016;19:233–42.

20. Dinamarca MC, Raveh A, Schneider A, Fritzius T, Früh S, Rem PD, et al. Complex formation of APP with GABAB receptors links axonal trafficking to amyloidogenic processing. Nat Commun. 2019;10:1331.

21. Pin J-P, Bettler B. Organization and functions of mGlu and GABAB receptor complexes. Nature. 2016;540:60–8.

22. Heaney CF, Kinney JW. Role of GABA(B) receptors in learning and memory and neurological disorders. Neurosci Biobehav Rev. 2016;63:1–28.

23. Nelson SB, Valakh V. Excitatory/inhibitory balance and circuit homeostasis in autism spectrum disorders. Neuron. 2015;87:684–98.

24. Kang J-Y, Chadchankar J, Vien TN, Mighdoll MI, Hyde TM, Mather RJ, et al. Deficits in the activity of presynaptic γ-aminobutyric acid type B receptors contribute to altered neuronal excitability in fragile X syndrome. J Biol Chem. 2017;292:6621–32.

25. Luján R, Aguado C, Ciruela F, Cózar J, Kleindienst D, de la Ossa L, et al. Differential association of GABAB receptors with their effector ion channels in Purkinje cells. Brain Struct Funct. 2018;223:1565–87.

26. Gassmann M, Bettler B. Regulation of neuronal GABA(B) receptor functions by subunit composition. Nat Rev Neurosci. 2012;13:380–94.

27. Horder J, Andersson M, Mendez MA, Singh N, Tangen Ä, Lundberg J, et al. GABAA receptor availability is not altered in adults with autism spectrum disorder or in mouse models. Sci Transl Med. 2018;10:eaam8434.

28. Molendijk ML, de Kloet ER. Immobility in the forced swim test is adaptive and does not reflect depression. Psychoneuroendocrinology. 2015;62:389–91.

29. de Kloet ER, Molendijk ML. Coping with the forced swim stressor: towards understanding an adaptive mechanism. Neural Plast. 2016;2016:6503162.

30. Tebano MT, Martire A, Potenza RL, Grò C, Pepponi R, Armida M, et al. Adenosine A(2A) receptors are required for normal BDNF levels and BDNF-induced potentiation of synaptic transmission in the mouse hippocampus. J Neurochem. 2008;104:279–86.

31. Canas PM, Porciúncula LO, Cunha GMA, Silva CG, Machado NJ, Oliveira JMA, et al. Adenosine A2A receptor blockade

prevents synaptotoxicity and memory dysfunction caused by beta-amyloid peptides via p38 mitogen-activated protein kinase pathway. J Neurosci. 2009;29:14741–51.

32. Quarta D, Borycz J, Solinas M, Patkar K, Hockemeyer J, Ciruela F, et al. Adenosine receptor-mediated modulation of dopamine release in the nucleus accumbens depends on glutamate neurotransmission and N-methyl-D-aspartate receptor stimulation. J Neurochem. 2004;91:873–80.

33. Sahin B, Galdi S, Hendrick J, Greene RW, Snyder GL, Bibb JA. Evaluation of neuronal phosphoproteins as effectors of caffeine and mediators of striatal adenosine A2A receptor signaling. Brain Res. 2007;1129:1–14.

34. Wells L, Opacka-Juffry J, Fisher D, Ledent C, Hourani S, Kitchen I. In vivo dopaminergic and behavioral responses to acute cocaine are altered in adenosine A(2A) receptor knockout mice. Synapse. 2012;66:383–90.

35. Al-Hasani R, Foster JD, Metaxas A, Ledent C, Hourani SMO, Kitchen I, et al. Increased desensitization of dopamine D$_2$ receptor-mediated response in the ventral tegmental area in the absence of adenosine A(2A) receptors. Neuroscience. 2011;190:103–11.

36. Yamada K, Kobayashi M, Kanda T. Involvement of adenosine A2A receptors in depression and anxiety. Int Rev Neurobiol. 2014;119:373–93.

37. Correa M, Font L. Is there a major role for adenosine A2A receptors in anxiety? Front Biosci. 2008;13:4058–70.

38. Chen JF, Moratalla R, Impagnatiello F, Grandy DK, Cuellar B, Rubinstein M, et al. The role of the D(2) dopamine receptor (D(2)R) in A(2A) adenosine receptor (A(2A)R)-mediated behavioral and cellular responses as revealed by A(2A) and D(2) receptor knockout mice. Proc Natl Acad Sci USA. 2001;98:1970–5.

39. Deckert J, Brenner M, Durany N, Zöchling R, Paulus W, Ransmayr G, et al. Up-regulation of striatal adenosine A(2A) receptors in schizophrenia. Neuroreport. 2003;14:313–6.

40. Ha S, Lee D, Cho YS, Chung C, Yoo Y-E, Kim J, et al. Cerebellar Shank2 regulates excitatory synapse density, motor coordination, and specific repetitive and anxiety-like behaviors. J Neurosci. 2016;36:12129–43.

41. Giachino C, Barz M, Tchorz JS, Tome M, Gassmann M, Bischofberger J, et al. GABA suppresses neurogenesis in the adult hippocampus through GABAB receptors. Development. 2014;141:83–90.

42. Pfisterer U, Khodosevich K. Neuronal survival in the brain: neuron type-specific mechanisms. Cell Death Dis. 2017;8:e2643.

43. Lelièvre EC, Plestant C, Boscher C, Wolff E, Mège R-M, Birbes H. N-cadherin mediates neuronal cell survival through Bim down-regulation. PLoS ONE. 2012;7:e33206.

44. Hoxha E, Gabriele RMC, Balbo I, Ravera F, Masante L, Zambelli V, et al. Motor deficits and cerebellar atrophy in Elovl5 knock out mice. Front Cell Neurosci. 2017;11:343.

45. Silverman JL, Yang M, Lord C, Crawley JN. Behavioural phenotyping assays for mouse models of autism. Nat Rev Neurosci. 2010;11:490–502.

46. Kalueff AV, Stewart AM, Song C, Berridge KC, Graybiel AM, Fentress JC. Neurobiology of rodent self-grooming and its value for translational neuroscience. Nat Rev Neurosci. 2016;17:45–59.

47. Goorden SMI, van Woerden GM, van der Weerd L, Cheadle JP, Elgersma Y. Cognitive deficits in Tsc1+/− mice in the absence of cerebral lesions and seizures. Ann Neurol. 2007;62:648–55.

48. Trent S, Fry JP, Ojarikre OA, Davies W. Altered brain gene expression but not steroid biochemistry in a genetic mouse model of neurodevelopmental disorder. Mol Autism. 2014;5:21.

49. Silverman JL, Pride MC, Hayes JE, Puhger KR, Butler-Struben HM, Baker S, et al. GABAB receptor agonist R-baclofen reverses social deficits and reduces repetitive behavior in two mouse models of autism. Neuropsychopharmacology. 2015;40:2228–39.

50. Gandal MJ, Sisti J, Klook K, Ortinski PI, Leitman V, Liang Y, et al. GABAB-mediated rescue of altered excitatory-inhibitory balance, gamma synchrony and behavioral deficits following constitutive NMDAR-hypofunction. Transl Psychiatry. 2012;2:e142.

51. Stoppel LJ, Kazdoba TM, Schaffler MD, Preza AR, Heynen A, Crawley JN, et al. R-Baclofen reverses cognitive deficits and improves social interactions in two lines of 16p11.2 deletion mice. Neuropsychopharmacology. 2018;43:513–24.

52. Paxinos G, Franklin KBJ. The mouse brain in stereotaxic coordinates. 2nd ed. San Diego: Academic Press; 2001.

53. Schneider CA, Rasband WS, Eliceiri KW. NIH Image to ImageJ: 25 years of image analysis. Nat Methods. 2012;9:671–5.

54. Wang F, Flanagan J, Su N, Wang L-C, Bui S, Nielson A, et al. RNAscope: a novel in situ RNA analysis platform for formalin-fixed, paraffin-embedded tissues. J Mol Diagn. 2012;14:22–9.

55. Berger SM, Weber T, Perreau-Lenz S, Vogt MA, Gartside SE, Maser-Gluth C, et al. A functional Tph2 C1473G polymorphism causes an anxiety phenotype via compensatory changes in the serotonergic system. Neuropsychopharmacology. 2012;37:1986–98.

56. Deacon RMJ. Assessing nest building in mice. Nat Protoc. 2006;1:1117–9.

57. Zou J, Wang W, Pan Y-W, Lu S, Xia Z. Methods to measure olfactory behavior in mice. Curr Protoc Toxicol. 2015; 63:11.18.1–21.

58. Bevins RA, Besheer J. Object recognition in rats and mice: a one-trial non-matching-to-sample learning task to study 'recognition memory'. Nat Protoc. 2006;1:1306–11.

59. Blick MG, Puchalski BH, Bolanos VJ, Wolfe KM, Green MC, Ryan BC. Novel object exploration in the C58/J mouse model of autistic-like behavior. Behav Brain Res. 2015; 282:54–60.

60. Moy SS, Nadler JJ, Perez A, Barbaro RP, Johns JM, Magnuson TR, et al. Sociability and preference for social novelty in five inbred strains: an approach to assess autistic-like behavior in mice. Genes Brain Behav. 2004;3:287–302.

61. R Core Team. R: a language and environment for statistical computing. Vienna, Austria: R Foundation for Statistical Computing; 2017. https://www.R-project.org/
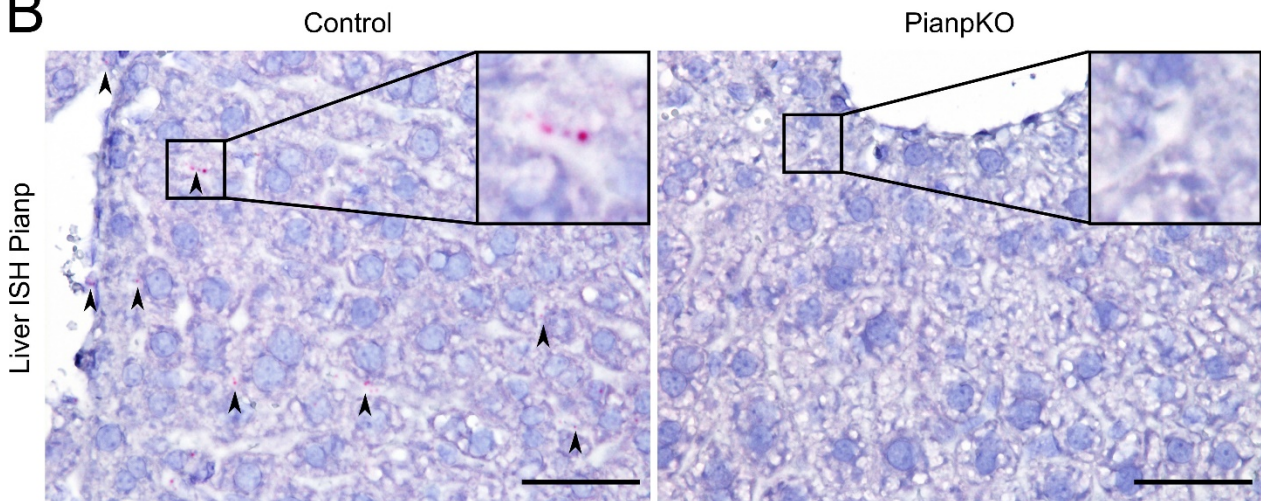
Supplementary Information

Supplementary Figures

A

B
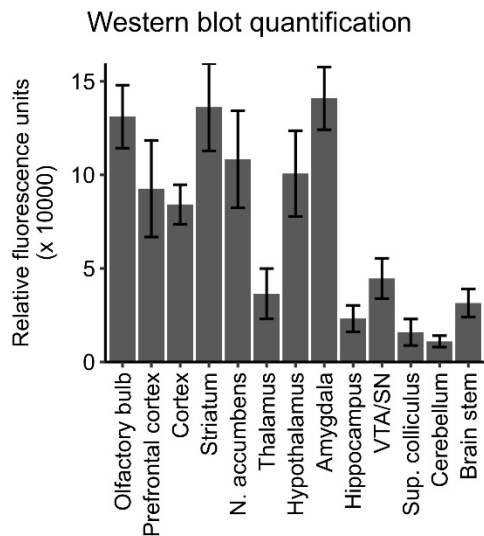
Supplementary Figure 1: Pianp expression in the brain and liver.

A) Quantification of the relative fluorescence of Pianp normalized to β-Actin in Western blots of different brain regions of control mice (n = 3). Bars indicate mean ± SEM.

B) In situ hybridization (ISH) for *Pianp* in the Liver. *Pianp* expression (in red, marked by black arrowheads) was observed in the liver predominantly in sinusoidal endothelial cells of control but not PianpKO mice. Scale bars: 50 μm. Images are representative for $n ≥ 3$.
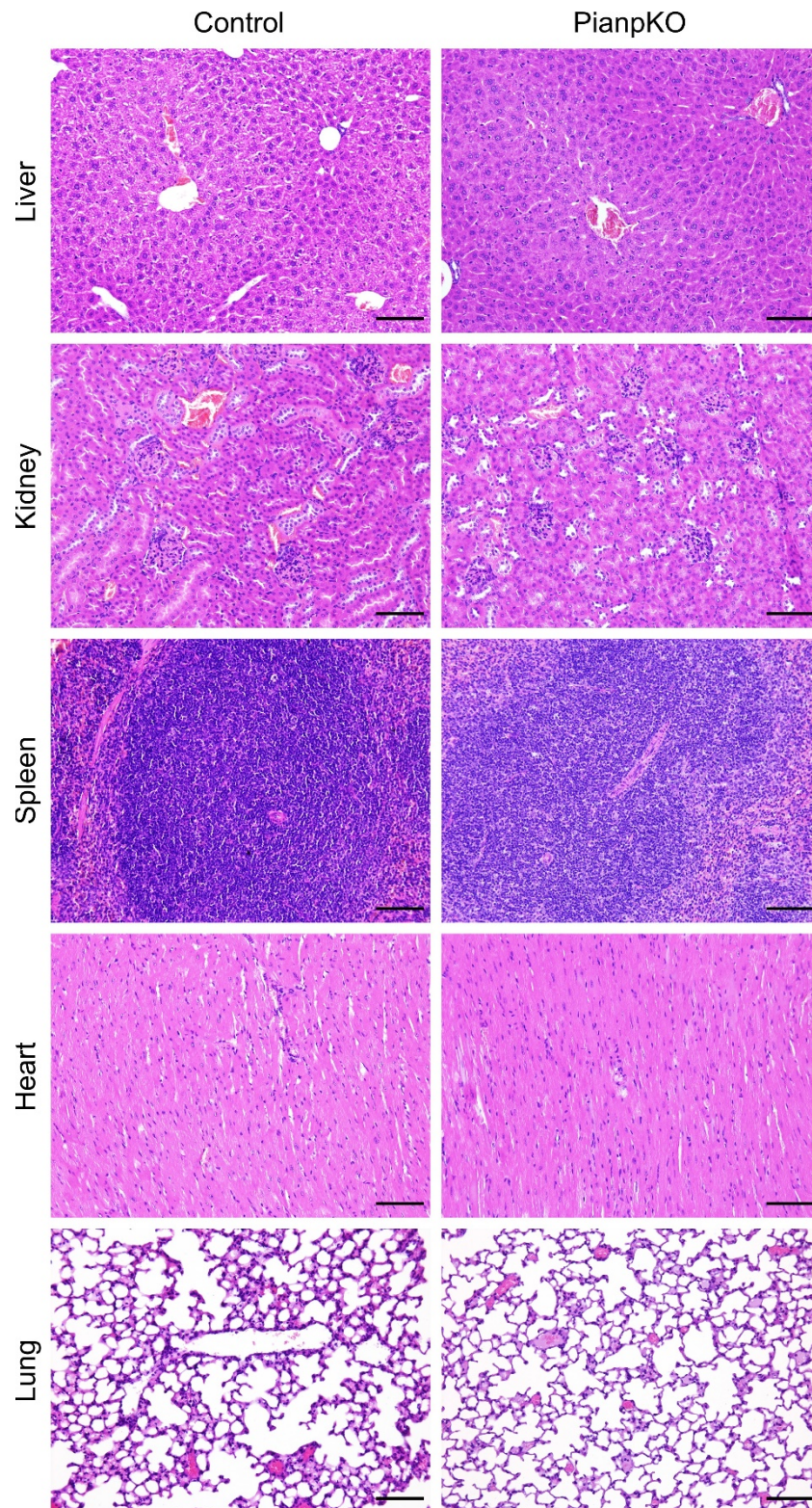
Supplementary Figure 2: H&E stains of the liver, kidney and spleen, heart, and lung revealed no obvious pathologies in PianpKO mice compared to controls. Scale bars: 100 μm. Images are representative for $n \geq 3$.
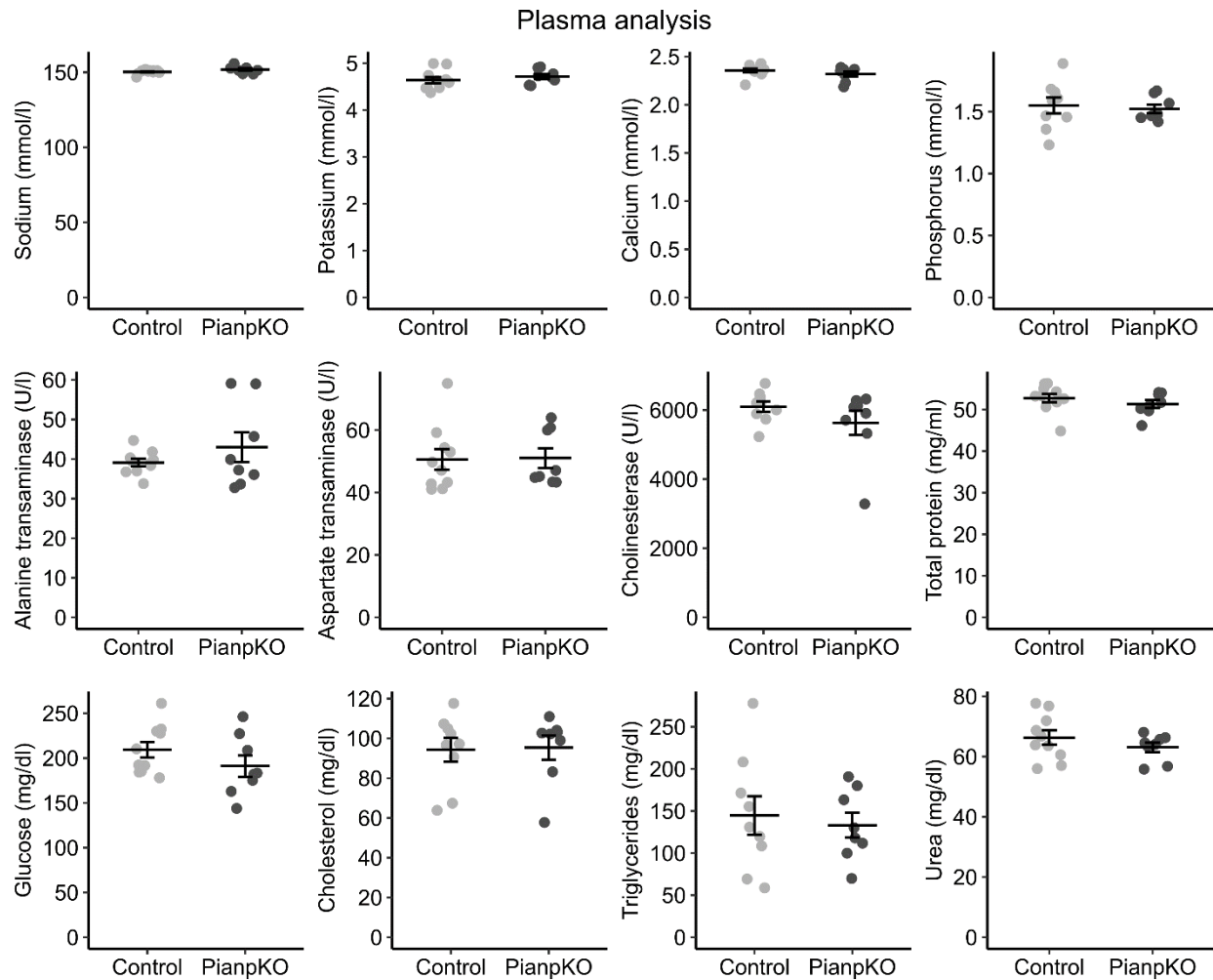
Supplementary Figure 3: Plasma analysis of blood samples taken from the ophthalmic venous sinus in PianpKO mice. No statistically significant differences between PianpKO mice and controls could be detected (n = 9 for each group). Horizontal lines indicate mean ± SEM.
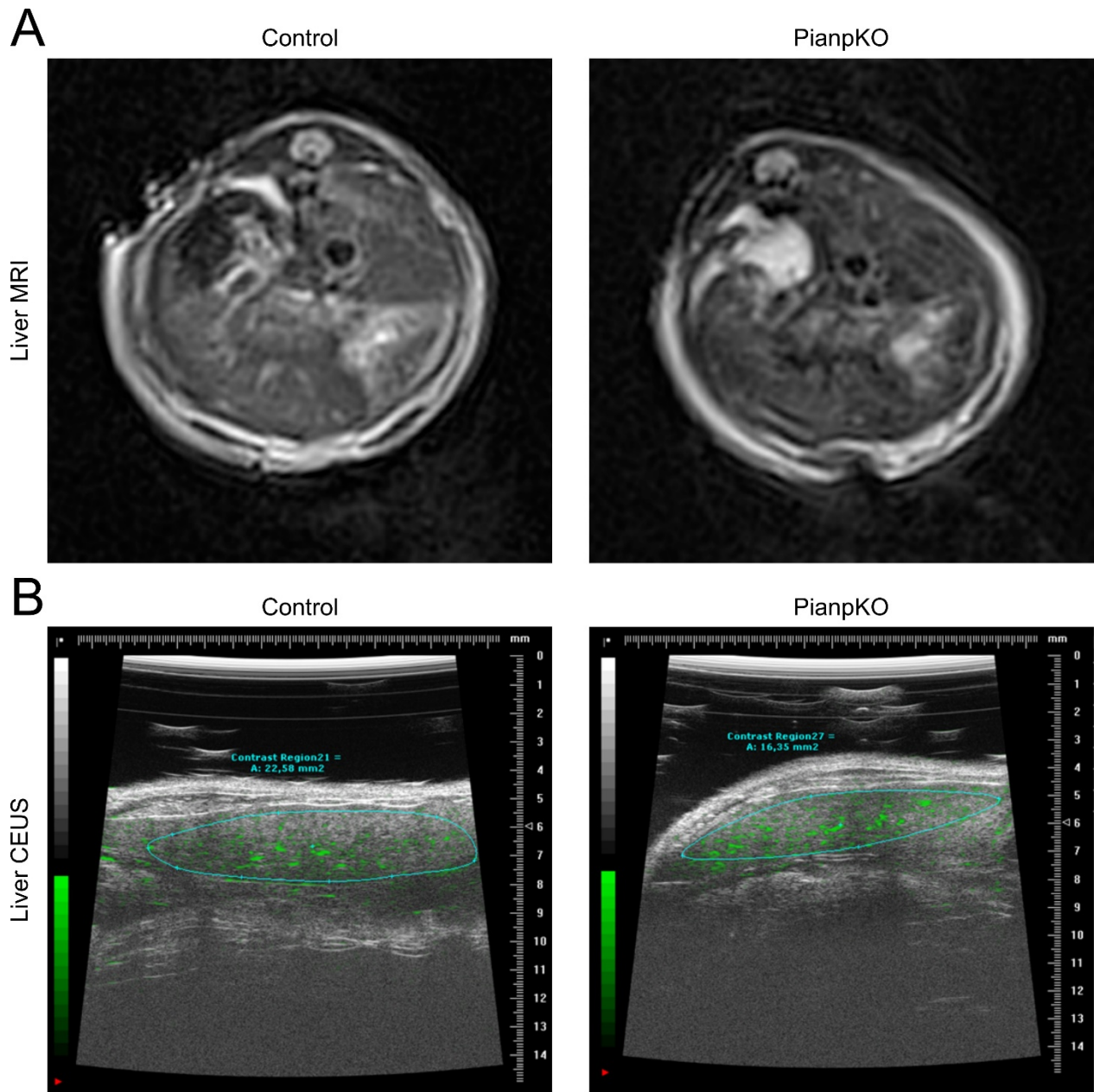
Supplementary Figure 4: Morphology and perfusion of the liver in Pianp-deficient mice.

A) 1.5 T magnetic resonance imaging (MRI) of the liver. No apparent morphological differences were detected between PianpKO mice and controls.
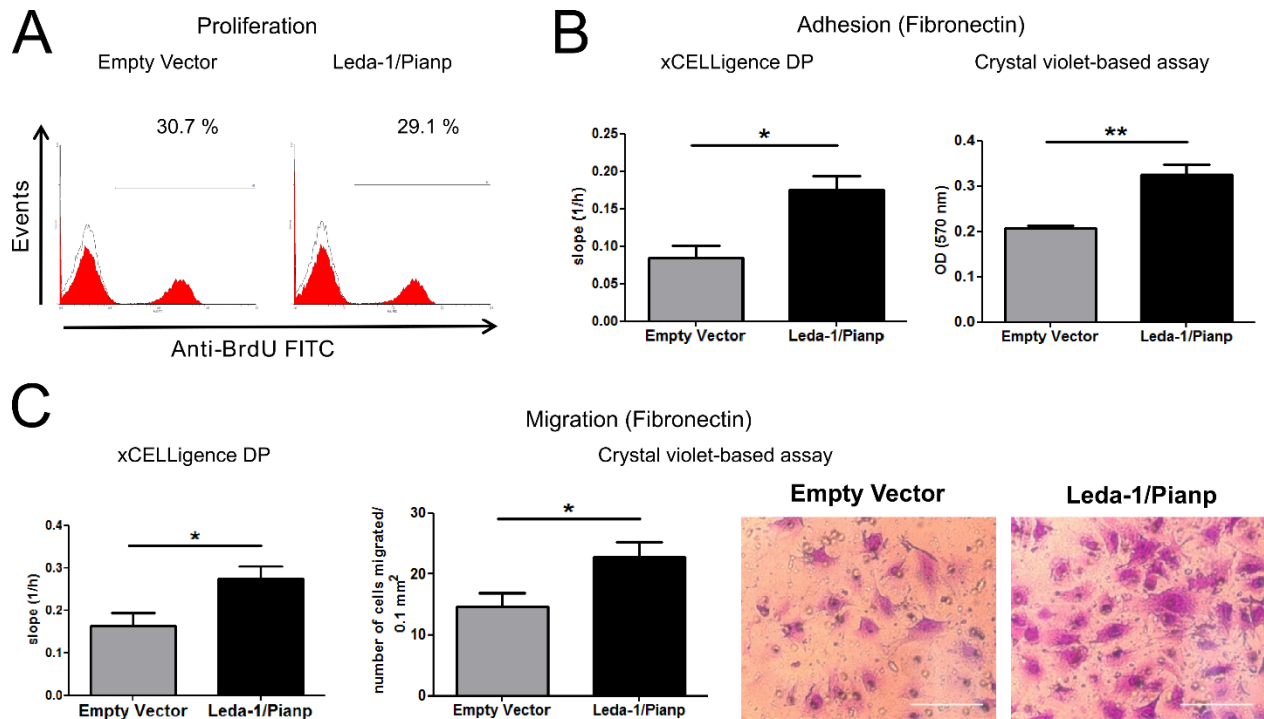
B) Contrast enhanced ultrasound (CEUS) imaging of the liver revealed no significant differences in liver perfusion between PianpKO mice and controls.

Images are representative for *n* ≥ 3.

Supplementary Figure 5: Pianp overexpression in mouse embryonic fibroblasts (MEF)

A) Flow cytometry based BrdU assay. No differences in proliferation between empty vector and Pianp transfected MEF cells were detected.

B) Fibronectin coating adhesion assay. Pianp transfected MEF cells showed higher adhesion rates than empty vector transfected MEF cells in both xCELLigence DP and Crystal violet-based assay.

C) Fibronectin coated transwell migration assay. Pianp transfected MEF cells migrated significantly more through fibronectin coated transwell plates than empty vector transfected MEF cells in both xCELLigence DP and Crystal violet-based assay. Scale bar: 100 μm. Images are representative for $n \geq 3$.

Bars indicate mean ± SEM.

A Brain volume and weight

brain volume

brain weight

B MRI volume measurement

C
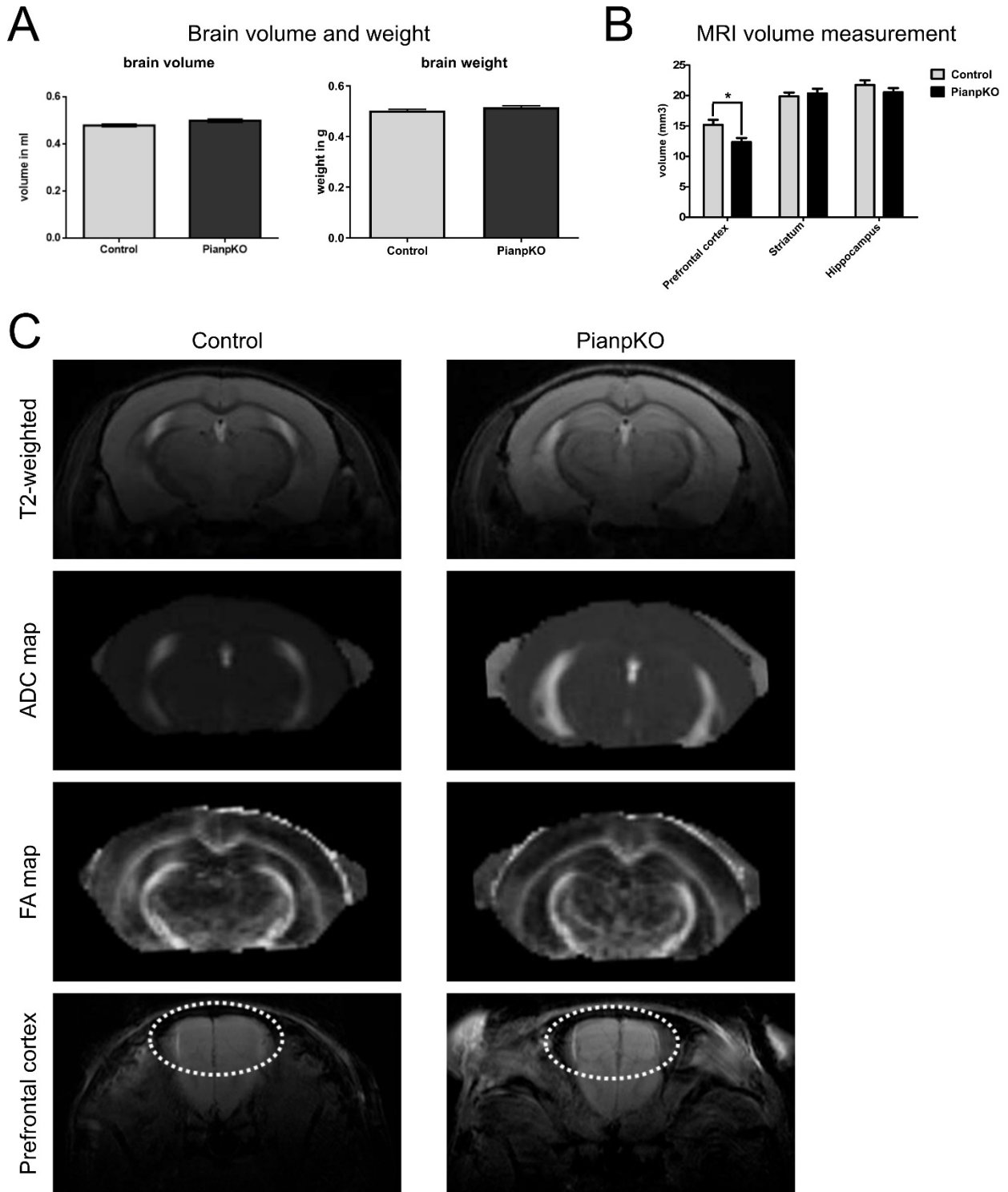
Supplementary Figure 6: Volume, weight and anatomic and functional MRI of the brain in Pianp-deficient mice.

A) Brain volume of PianpKO mice was slightly increased, but did not reach statistical significance (p = 0.0501, Control: n = 8; PianpKO: n = 9). Brain weight of PianpKO mice did not differ statistically significant from controls (p = 0.09, Control: n = 8, PianpKO: n = 9).

B) Measurement of the volume of different brain regions of PianpKO and control mice using T2-weighted 9.4 T MR imaging. The volume of the prefrontal cortex differed statistically significant between PianpKO and control mice (p = 0.015, Control: n = 9; PianpKO: n = 12). However in striatum and hippocampus volume no statistically significant difference was detected (p > 0.05).

C) Morphological T2-weighted 9.4 T MRI as well as diffusion weighted imaging (which is made sensitive to water molecule diffusion in the brain) and diffusion tensor imaging (relying on the three-dimensional shape of the diffusion) of the brain in PianpKO and corresponding control mice. Representative images of coronal T2-weighted images of the hippocampal region (upper panel) and corresponding apparent diffusion coefficient (ADC) maps (middle upper panel) and fractional anisotropy (FA) maps (middle lower panel) of PianpKO and control mouse brains (week 61). Additionally, representative images of the prefrontal regions for both groups (lower panel). No statistically significant differences in parameters derived from DWI and DTI were noted when comparing PianpKO and control mice (p > 0.05, Control: n = 9; PianpKO: n = 12).

Bars indicate mean ± SEM.

A
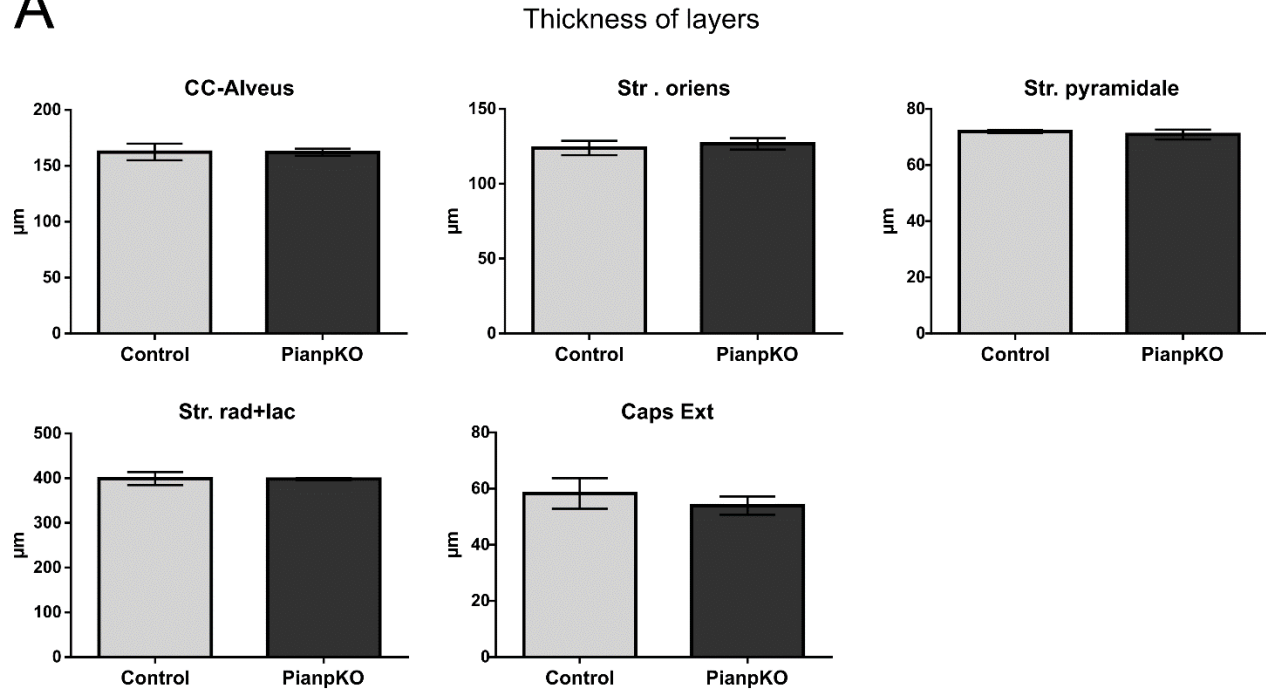
Thickness of layers
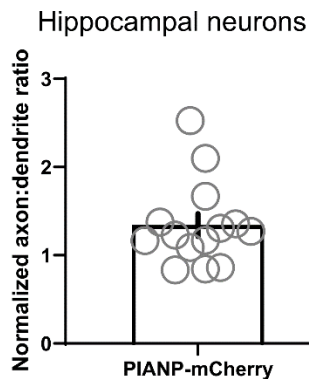
Supplementary Figure 7: Thickness of layers of fiber tracts in PianpKO mice and subcellular location of Pianp in hippocampal neurons.

A) PianpKO (*n* = 3) and control mice (*n* = 3) showed no differences in the layer width of the corpus callosum and alveus (CC-alveus), the stratum (str.) oriens, str. pyramidale, and str. radiatum (rad) plus lacunosum (lac) of the CA1 region of the hippocampus, and the external capsule (caps ext).

B) Quantification of PIANP-mCherry axon/dendrite ratio, normalized to GFP fluorescence in hippocampal neurons (*n* = 14 cells).

Bars indicate mean ± SEM.

Prefrontal cortex

Hippocampus

Amygdala

Nucleus accumbens

Striatum

Ventral tegmental area/substantia nigra

Dorsal raphe nucleus
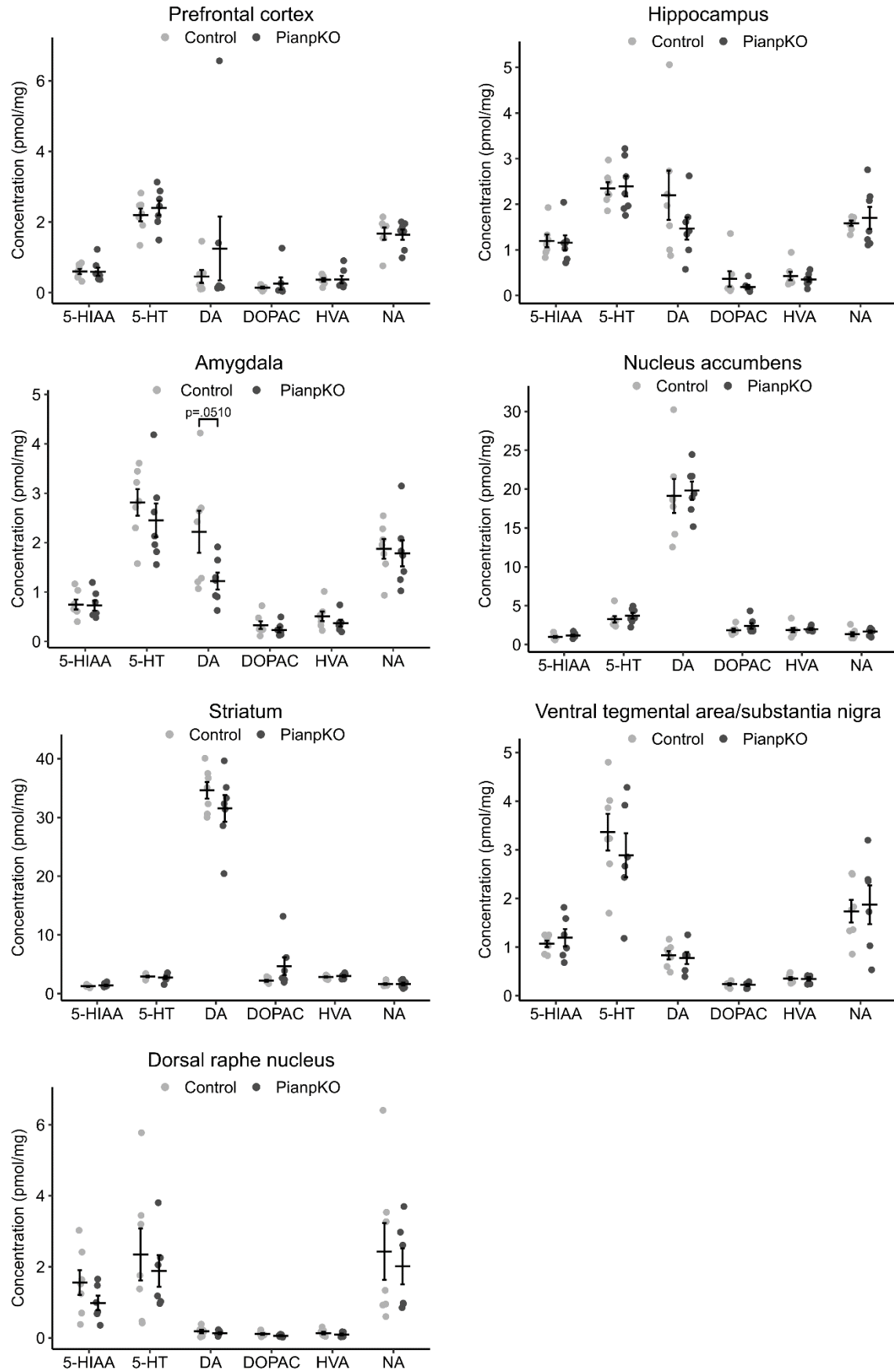
Supplementary Figure 8: Impact of Pianp on monoamine neurotransmitter concentration in the brain. High-performance liquid chromatography (HPLC) measurement of monoamine neurotransmitters in different brain regions. 5-hydroxyindoleacetic acid (5-HIAA), serotonin (5-HT), dopamine (DA), 3,4-dihydroxyphenylacetic acid (DOPAC), homovanillic acid (HVA), and noradrenaline (NA) did not significantly differ between control and PianpKO mice in the prefrontal cortex, the hippocampus, the amygdala, the nucleus accumbens, the striatum, the ventral tegmental area/substantia nigra and the dorsal raphe nucleus. However, a trend $(t(12) = 2.17, p = 0.051)$ towards reduced levels of Dopamine (DA) was observed in the Amygdala in PianpKO mice (n = 7 for each group). Horizontal lines indicate mean ± SEM.

A Grip strength

B Rotarod performance test

C Startle and PPI

D Novelty induced hypophagia test

E Amphetamine challenge
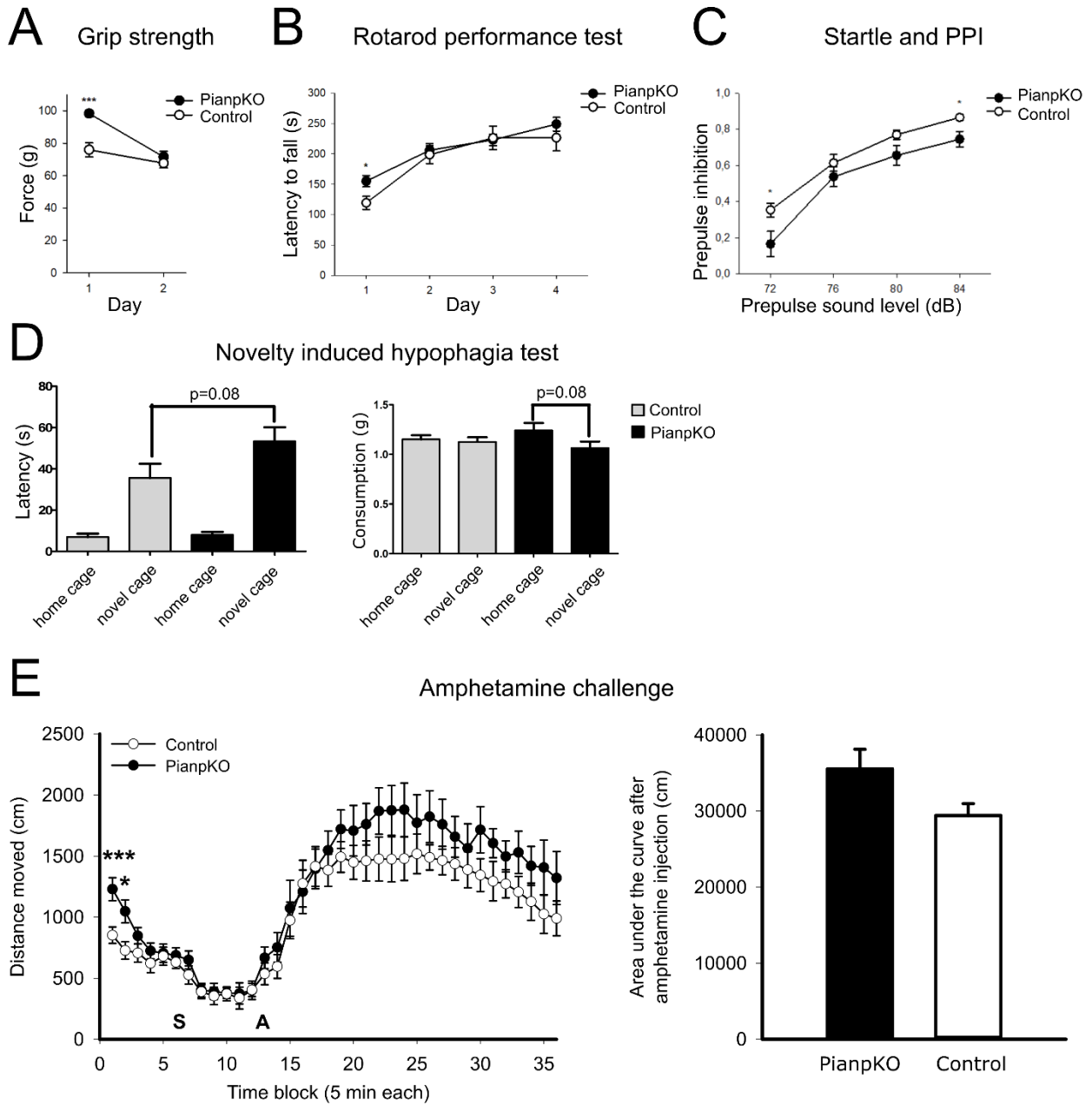
Supplementary Figure 9: Motor functions, startle response/prepulse inhibition, anxiety behavior and amphetamine challenge in Pianp-deficient mice.

A) At the experimental day 1 grip strength was significantly higher in PianpKO (n = 15) than in control mice (n = 13) ($t(26)$ = 4.87, p < 0.05). However on the following day 2, grip strength didn't differ significantly between the groups ($t(26)$ = 0.40, p > 0.05).
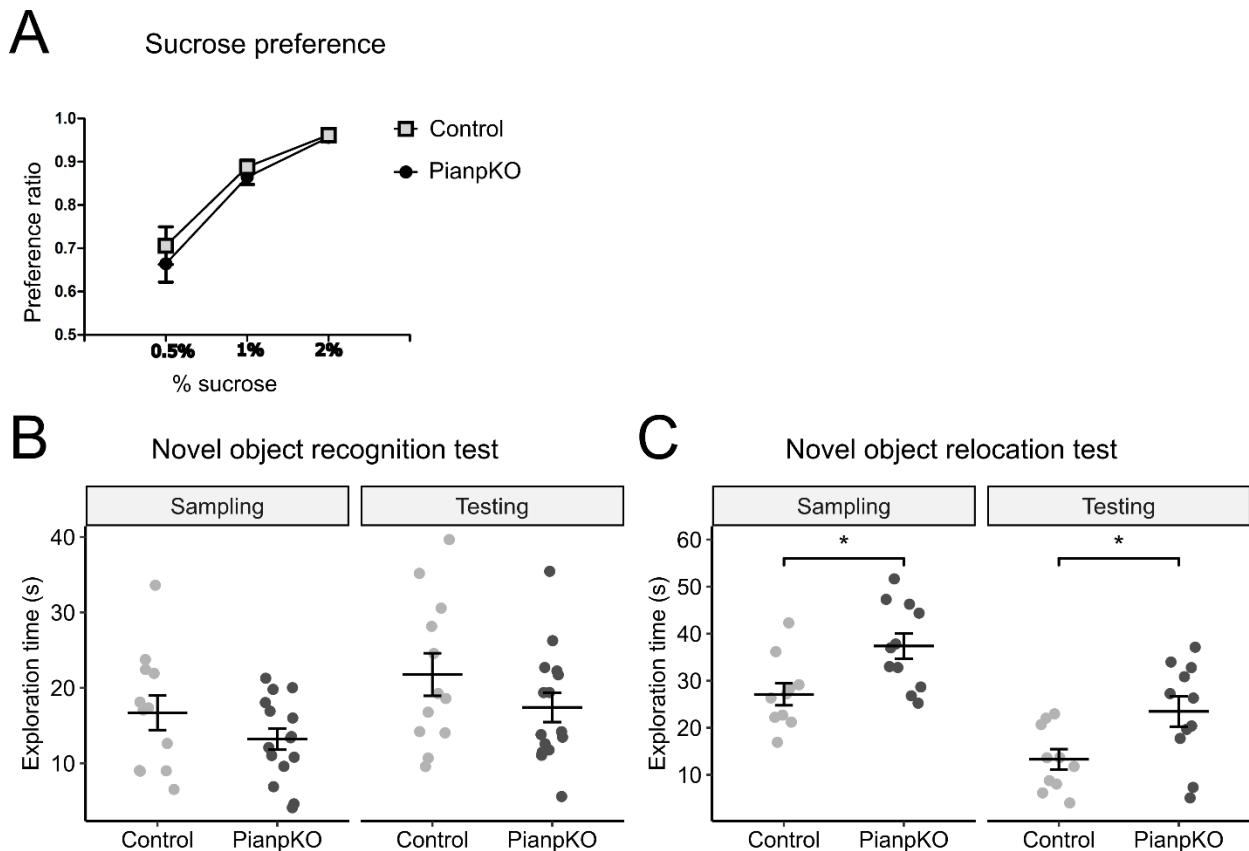
B) At the experimental day 1 of the rotarod performance test, PianpKO mice (n = 15) showed a significantly higher latency to fall than control mice (n = 13) ($t(26)$ = 2.52, p < 0.05). However on the following days 2 to 4 this difference was no longer observable (day 2: $t(26)$ = 0.68, p > 0.05, day 3: $t(26)$ = 0.49, p > 0.05, day 4: $t(26)$ = 0.35, p > 0.05).

C) In the startle and prepulse inhibition (PPI) test, PianpKO mice (n = 15) showed a significantly lower PPI in comparison to control mice (n = 13, two way ANOVA: genotype $F(1,78)$ = 5.16, p < 0.05, intensity $F(3,78)$ = 103.6, p < 0.0001, genotype x intensity $F(3,78)$ = 0.98, p > 0.05). Post hoc t-Tests however only revealed deficits at a sound level of 72 dB ($t(26)$ = 2.23, p < 0.05) and 84°dB ($t(26)$ = 2.66, p < 0.05) while 76 dB ($t(26)$ = 0.96, p > 0.05) and 80 dB ($t(26)$ = 1.95, p > 0.05) did not differ significantly between the two groups.

D) In the novelty induced hypophagia test, PianpKO mice (n = 14) showed a trend towards a higher latency to consumption in the novel cage in comparison to control mice (n = 11) ($t(23)$ = 1.82, p = 0.08), and a trend towards a lower consumption in the novel cage compared to the home cage ($t(26)$ = 1.80, p = 0.08).

E) Amphetamine challenge test with a 30 min habituation phase (time blocks 1–6 (5 min each)), a 30 min injection control phase (time blocks 7–12, S = saline injection) followed by the amphetamine challenge (time blocks 14–36, A = amphetamine injection). In the habituation phase differences could be detected in the first ($t(20)$ = 3.48, p < 0.001) and second ($t(20)$ = 2.81, p < 0.05) 5 min time blocks. In the amphetamine challenge test, PianpKO mice (n = 11) showed a trend towards a higher distance moved after amphetamine injection in comparison to control mice (n = 11) (two way repeated measures ANOVA: genotype $F(1,460)$ = 3.87, p = 0.063, time $F(23,460)$ = 8.59, p < 0.001, genotype x time $F(23,460)$ = 0.39, p > 0.05; area under the curve: $t(20)$ = 2.04, p = 0.055).

Dots/bars/horizontal lines indicate mean ± SEM. * p < 0.05, *** p < 0.001, A, B, D) two-tailed unpaired or paired t-Test, C) two way ANOVA followed by post hoc t-Tests

A
Sucrose preference

B
Novel object recognition test

C
Novel object relocation test

Supplementary Figure 10: Anhedonia and exploration time in novel object recognition and relocation tests in Pianp-deficient mice.

A) In the sucrose preference test for anhedonia no significant differences could be observed between PianpKO mice (n = 15) and control mice (n = 13) (0.5 % sucrose: $t(20)$ = 0.69, $p > 0.05$, 1 % sucrose: $t(20)$ = 1.01, $p > 0.05$, 2 % sucrose: $t(20)$ = 0.66, $p > 0.05$).

B) In the novel object recognition test, the exploration time did not differ significantly between the groups (sampling: $t(25)$ = 1.35, $p > 0.05$, testing: $t(25)$ = 1.31, $p > 0.05$).

C) In the novel object relocation test, the exploration time differed significantly between the groups in both phases (sampling: $t(19)$ = 2.86, $p < 0.05$, testing: $t(19)$ = 2.58, $p < 0.05$).

Dots/bars indicate mean ± SEM, * $p < 0.05$, two-tailed unpaired or paired t-Test.

Supplementary Material and Methods

Organ Histology

Organs were fixed in 10 % formalin (Carl Roth, Karlsruhe, Germany) at room temperature for 24 to 72 hours, followed by paraffin embedding according to standard protocols. Paraffin sections (3 to 5 µm) were deparaffinized, rehydrated and H&E stained according to standard protocols.

Blood Plasma Analysis

Blood samples were taken from the ophthalmic venous sinus. Plasma was separated (centrifugation at 2,000 g for 5 minutes at room temperature in Microvette 500 LH; Sarstedt, Nümbrecht, Germany) and analyzed for sodium, potassium, calcium, phosphorus, alanine aminotransferase (ALT), aspartate aminotransferase (AST), cholinesterase, total protein, glucose, triglycerides, cholesterol, and urea in a cobas c 311 Analyzer (F. Hoffmann-La Roche, Basel, Switzerland). Calibration and independent controls were used as recommended by the manufacturer.

Liver MRI

Animals were anesthetized with the mixture of isoflurane (1.5 %) and room air. T2-weighted imaging was performed using clinical 1.5 T MR scanner (Symphony, Siemens, Germany) equipped with a home-built coil for radiofrequency excitation and detection, using following parameters: turbo spin echo sequence, orientation axial, TR 3240 ms, TE 81 ms, resolution 0.4×0.4×1.5 mm, 3 averages, 15 images, scan time 3:40 min. MR images were post-processed using OsiriX software (Pixmeo, Bernex, Switzerland).

Liver CEUS

Animals were anesthetized with the mixture of isoflurane (1.5 %) and room air. Contrast-enhanced ultrasound imaging was performed on a pre-clinical ultrasound platform Vevo 770 (Fujifilm VisualSonics, Toronto, Canada) using a RMV-704 probe with a center frequency of 40 MHz. After the start of the acquisition, SonoVue ultrasound contrast agent (Bracco, Amsterdam, Netherlands) was injected through a tail vein (approx. 100 µl in 10 seconds). Vevo-LAB software (Fujifilm VisualSonics) was used for the post-processing of ultrasound data according to the instruction of the manufacturer.

Brain Volume and Weight Measurement

Brain volume was determined by using microvolumetry (µ-VM) as described previously[1]. In brief, a 5-ml syringe (probe container) was attached to a 1-ml syringe (measurement devise). 70 % ethanol was used as fluid. First, the fluid level was set to a specific marker on the probe container. Thereafter, the probe was put into the probe container. Finally, the 1-ml syringe was used to set the fluid level in the probe container back to its initial value.

Brain MRI

Animals were anesthetized by inhalation of the mixture of isoflurane (2.0 %) and room air and temperature held constant at 36°± 0.5°C using water heated cradle. Mice were placed in a prone position on a plate holder with an adjustable nose cone. A stereotactic device was utilized together with respiratory gating to minimize head movement. *In vivo* imaging was performed on a 9.4 T Biospec 94/20 USR (Bruker, Karlsruhe, Germany) small animal imaging system. T2-weighted images and diffusion tensor images were acquired using a cryogenic surface coil (transceiver, quadrature) and a dual resonator system composed of a transmit-only volume resonator and a receive-only surface coil at room temperature (Bruker). For T2-weighted (RARE) images, imaging parameters were set to: TE/TR 35/4000 ms, matrix 256×256, field of view 20×20 mm, slice thickness 0.5 mm, 2 averages, scan time 4:16 min. For DTI-EPI, imaging parameters were: TE/TR 22/7500 ms, matrix 128×128, gradient separations time 8.5 ms, flip angle 90 degrees, slice thickness 0.5 mm, 1 average, 30 diffusion directions with b = 1000 s/mm^2 and 5 unweighted b=0 s/mm^2 images, acquisition time 17:30 min. T2-weighted MR images were segmented using OsiriX software (Pixmeo). Segmentation was performed manually slice by slice, in the coronal plane view. Three regions of interest (prefrontal cortex, caudoputamen, and hippocampus) were outlined manually. The boundaries of these three structures were chosen by visually comparing the greyscale images to three online mouse atlases: MBL mouse brain atlas[2], CFA mouse brain atlas[3] and scalable Brain Atlas[4]. After segmentation, the volume was calculated based on the number of segmented voxels, for prefrontal cortex, caudoputamen, and hippocampus, respectively. The diffusion tensor imaging was analyzed using DSI Studio (http://dsi-studio.labsolver.org/).

Assessment of layer thickness of fiber tracts

30 µm thick coronal sections were made using a VT 1000 vibratome (Leica Biosystems, Nussloch, Germany) and collected in 20 % ethanol. Sections were mounted on SuperFrost slides (R. Langenbrinck, Emmendingen, Germany) and air-dried overnight. The next day, sections were rinsed three times in phosphate buffered saline (PBS).

In case of sections of the forebrain, sections were incubated in a solution containing antibodies directed against CNPase (No. PA5-19551, Thermo Fisher Scientific, Waltham, MA, USA) 1:300 in 3 % normal goat serum (NGS) and 0.1 % Triton-X100 (Serva, Heidelberg, Germany) in PBS) at 40 °C for 24 h. After rinsing in PBS (three times for 5 min at room temperature (RT)), sections were incubated in a solution containing Alexa Flour 488 conjugated goat anti-rabbit IgG (Dianova, Hamburg, Germany) 1:400 in 3 % NGS and 0.1 % Triton-X100 in PBS) for 2 h at RT. Sections were rinsed in PBS (three times for 5 min at RT) and afterward incubated in a solution containing Molecular Probes 4',6-diamidino-2-phenylindole (DAPI, Thermo Fisher Scientific) dissolved 1:10,000 in PBS in the presence of 0.1% Triton-X100. Thereafter, sections were rinsed three times and mounted in Mowiol fluorescent mounting medium (Merck, Darmstadt, Germany).

In case of sections from the cerebellum, sections were incubated in a solution containing antibodies directed against Purkinje-cell protein 4 (Pcp4, No. sc-74816, Santa Cruz Biotechnology, Dallas, TX, USA) as described previously in detail[5]. In brief, sections were incubated in a solution (0.1 Triton X-100 and 3% serum in PBS) containing Pcp4 antibodies over night at 4 °C. Visualization was done using Cy3-conjugated secondary antibodies (Jackson Immunoresearch, West Grove, PA, USA). Sections were counterstained with DAPI (1:10,000), washed and then coverslipped in Mowiol fluorescent mounting medium.

The thickness of different brain structures was measured on a series of serial sections. Sampling was started at Bregma -1.94 mm and six consecutive sections were sampled using an Olympus BX 63 (Olympus, Tokyo, Japan) and a DP80 camera (Olympus), connected to a personal computer. Measurements were done using the software cellSense 1.13 (Olympus). Per section the thickness of the different structures (primary somatosensory cortex, hippocampal area CA1 (stratum oriens, stratum pyramidale, stratum radiatum and lacunosum-moleculare), dentate gyrus (DG, stratum moleculare and stratum granulare) molecular-, Purkinje cell - and molecular layer of the cerebral cortex as well as the thickness of the corpus callosum, alveus and external capsule. For analysis, six consecutive sections were analyzed. In each section both hemispheres were analyzed and each structure was measured on three positions – thus individual 36 measurements per region and animal were made.

Analysis of adult hippocampal neurogenesis

To analyze cell proliferation within the dentate gyrus, phosphohistone H3 was used as a specific marker; doublecortin was used to label newly formed neurons (for details see e.g. Poser et al.[6]). For determination of apoptotic cells, we used antibodies directed against cleaved (activated) caspase 3[7]. Coronal sections of 30 µm thickness were cut using a vibratome. The following antibodies and substances were used: rabbit α-phosphohistone H3 (No. sc-8656-R, Santa Cruz Biotechnology), goat α-doublecortin (1:200; sc-8066, Santa Cruz Biotechnology), rabbit α-cleaved caspase 3 (1:250, AB3623, Millipore, Merck), biotinylated horse α-goat, (1:200; Vector Laboratories, Burlingame, CA, USA), biotinylated goat α-rabbit (1:200; Vector Laboratories); Cy3-conjugated streptavidin (1:1,000; Jackson Immunoresearch).

In case of phosphohistone H3 staining and cleaved caspase 3 staining, sections were mounted and air-dried over night. On the next day, sections were washed and then incubated in sodium citrate buffer (pH 6.0) for 20 min using a microwave oven (700 W) for antigen retrieval. After this, sections were washed in a solution containing 0.1 M PBS, 0.3 % Triton X-100, 3 % bovine serum albumin (BSA) for 1 h at RT. For doublecortin immunohistochemistry, free-floating sections were used. Sections were incubated for 1 h in a blocking solution containing 0.3% Triton X-100 and 3% BSA in PBS. Thereafter, sections were incubated in a solution (0.1 Triton X-100 and 3% BSA in PBS) containing antibodies directed either against phosphohistone H3, cleaved caspase 3 or doublecortin over night at 4 °C. Visualization was done using biotinylated secondary

antibodies and Cy3-conjugated streptavidin. Sections were counterstained with DAPI (1:10,000), washed and coverslipped in Mowiol fluorescent mounting medium.

To estimate the number of the labeled cells, cell counts were made using the serial sections. Countings were performed according to the Abercrombie's correction formula (starting at ~ Bregma −1.06 mm), since this method renders biases within the range of the optical disector by taking into account that the particles counted are small compared with the section thicknes[8]. No guard zones were used, since the use of guard zones can bias even optical disector counting[9]. The Linderstrom-Lang/Abercrombie (LLA) equation for estimating numerical neuronal densities is:

$$N = n * (t/(t + H)) \text{ or } N/n = f = t/(t + H)$$

N is an estimate of the number of objects in the defined region, n is the counted number of objects, t is the mean thickness of the virtual section, H is the mean height of the objects, and f is the conversion factor for converting n to N.

In a first step, n was quantified using an Olympus BX 63 microscope fitted for fluorescence. In a second step, H, the height of the cells in the z-axis, was estimated using a computer-driven motorized stage (Märzhäuser Wetzlar, Wetzlar, Germany) connected to the Axioplan 2 imaging microscope (Carl Zeiss Microscopy, Jena, Germany) under the control of Neurolucida software (MBF Bioscience, Williston, VT, USA).

Determination of Purkinje cell density

In 30 µm thick sections of the cerebellum Purkinje cells were visualized with Pcp4 (see above). A region-of-interest (ROI, dimension: 600 x 600 µm) was superimposed on 6th cerebellar lobule (starting at ~ Bregma -6.6 mm) and the number of Purkinje cell profiles was determined. Only profiles were counted that have a clear shape of a Pcp4 stained soma.

Immunocytochemistry and image analysis

Embryonic day 16.5 WT mouse hippocampi were dissected in ice-cold HBSS medium (No. 14170–088, Gibco, Thermo Fisher Scientific), digested with 0.25% trypsin (Invitrogen, Thermo Fisher Scientific) in HBSS medium for 13 min at 37 °C, dissociated by trituration and plated on glass coverslips coated with 0.2 mg / ml poly-L-lysine hydrobromide (Sigma-Aldrich) in 0.1 M borate buffer (boric acid / sodium tetraborate). Neurons were seeded at a density of ~550 cells / mm^2 in MEM medium (No. M4655, Sigma-Aldrich) containing 10% horse serum (Thermo Fisher Scientific, 26050070) and 0.6 % glucose (No. G8769, Sigma-Aldrich) and cultured at 37 °C in a humidified incubator (5% CO_2). After 2h, medium was replaced with Neurobasal medium (No. 21103-049, Gibco, Thermo Fisher Scientific) supplemented with B27 (No. 17504-044, Gibco, Thermo Fisher Scientific) and 1 mM L-glutamine (No. 25030-081, Gibco, Thermo Fisher Scientific). Cultured hippocampal neurons were transfected at 7 days in vitro using Lipofectamine 3000 (Thermo Fisher Scientific).

Cultured hippocampal neurons were fixed 6 h after transfection by immersion in phosphate buffered saline (PBS) containing 4% paraformaldehyde for 10 min at RT. After rinsing in PBS, cells were permeabilized with 0.2% Triton X-100 in PBS containing 10% NDS for 5 min at RT. Cell cultures were incubated with the following primary antibodies diluted in PBS containing 10% NDS for 2h at RT: Chicken anti-MAP2 (No. ab5392, Abcam, Cambridge, United Kingdom), mouse anti-Ankyrin G (No. 75-147, Antibodies Incorporated, Davis, CA, USA). After washing with PBS, cells were incubated with the following secondary antibodies for 45 min at RT: Donkey anti-chicken IgY Dylight 405 (No. 703-475-155, Jackson Immunoresearch Laboratories, West Grove, PA, USA), donkey anti-mouse IgG Alexa Fluor 647 (No. A31571, Thermo Fisher Scientific). Coverslips were mounted with Dako Fluorescence Mounting Medium (No. GM30411-2, Agilent, Santa Clara, CA, USA). Images were captured by confocal laser scanning microscopy (LSM 700, Carl Zeiss Microscopy, Jena, Germany) using a 40x objective with a numerical aperture of 1.3. For axon / dendrite ratio quantification, images were analyzed with ImageJ 1.48i[10] as described previously[11]. mCherry and GFP fluorescence intensity was measured in dendrite or axon segments at a distance of 100 μm from the cell soma. After background subtraction in both channels, mCherry intensity was normalized to GFP intensity and axon/dendrite ratios calculated.

Plasmids

Human PIANP (No. RC207868, Origene Technologies, Rockville, MD, USA) was C-terminally tagged with mCherry and subcloned into the pCI vector containing the human synapsin promoter. For GFP expression, plasmid pEGFP-N1 (Clontech Laboratories, Mountain View, CA, USA) was used.

Cloning and transfection of MEF cells

Cloning, transduction and preparation of MEF cells were preformed as described previously[12].

BrdU incorporation proliferation assay

To investigate the proliferation BrdU incorporation in DNA synthesizing cells was measured. Cells were seeded on 6-well plate (50000 cells/ well). Next day, the cells were serum starved for 16 h. BrdU (10 μM) was added to the cells in conditioned media and incubated for 1 h at 37°C. After the incubation the cells were harvested, transferred into FACS tube and centrifuged for 5 min at 1200 rpm. The supernatant was discarded. 10 μl of 70% Ethanol (pre-cooled at -20°C) was added drop wise to the cells while vortexing. The cells were incubated for 20 min at RT, washed with 1 ml washing buffer and centrifuged for 5 min at 1200 rpm. The supernatant was discarded, the cells were resuspended in 300 μl 2M HCl and incubated for 20 min at RT. The cells were washed with washing buffer and centrifuged for 5 min at 1200 rpm. The supernatant was discarded, the cells were resuspended in 1 ml 0.1 M sodium borate buffer ($Na_2B_4O_7$, 10 H_2O). The cells were incubated for 2 min at RT, washed with 1 ml washing buffer and centrifuged 5 min at 1200 rpm. BrdU FITC and mouse IgG FITC were diluted 1:20 with dilution buffer. 100 μl of the diluted antibodies were added into the cells and mixed by

vortexing. The cells were incubated for 25 min in the dark at RT, washed with 1 ml washing buffer and centrifuged for 5 min at 1200 rpm. The supernatant was discarded, cells were resuspended in 1 ml PBS and analyzed with BD FACSCanto II with BD FACSDiva 6.0 software.

xCELLigence DP-based adhesion assay

E-16 plates (Roche Diagnostics, Rotkreuz, Switzerland) were coated overnight at 4°C with Fibronectin at 5 µg/ml concentration. The wells were blocked by incubating for 30 min at RT with 1 % BSA. Transduced MEF cells which were grown in T75 flask of at least ~ 80 % confluency were detached with Trypsin/EDTA. However, the cells were allowed to regenerate cell surface proteins as the detached cells were incubated at 37°C for 2-3 h in a roller. E-16 plates were equilibrated at 37°C using the xCELLigence DP impedance-based cell analysis system (Roche Diagnostics). 10000 cells/ well of MEF cells were added. The plate was allowed to stay at RT for 30 min to let the suspended cells settle down. Immediately following that the experiment was started. As the cells start to adhere to the bottom surface of the wells the electrical impedance between the microelectrode changes resulting in a change of the Cell Index. Rate of change (slope in Cell Index/h) was calculated using the xCELLigence software (Roche Diagnostics).

Plate reader-based migration assay

96 well plate was coated overnight at 4°C with the Fibronectin at 5 µg/ml concentration. The wells were blocked by incubating for 30 min at RT with 1% BSA. Transduced MEF cells which were grown in T75 flask of at least ~80% confluency were detached with Trypsin/EDTA. However, the cells were allowed to regenerate cell surface proteins as the detached cells were incubated at 37°C for 2-3 in a roller. 50000 cells/ well of MEF cells were added. The plate was allowed to stay at RT for 30 min to let the suspended cells settle down. Immediately after that the plate was incubated at 37°C for 1 h. Non-adhered cells were removed by washing the plate thrice. 50 µl of crystal violet solution (0.5% crystal violet in 20% MeOH) was added and incubated for 15 min at room temperature in darkness. The plate was washed and air-dried overnight in darkness. Crystal violet was extracted by adding 100% MeOH and shaking the plate for 15 min at RT in darkness. Equal volume of crystal violet solution was transferred into a new clean 96 well plate. Absorbance values were measured at 570 nm using Tecan Infinite 200.

xCELLigence DP-based transwell migration assay

CIM-16 plates (Roche Diagnostics) were coated 1-2 h at RT with Fibronectin at 5 µg/ml concentration. The transwells were blocked by incubating for 30 min at RT with 1% BSA. Transduced MEF cells which were grown in T75 flask of at least ~80% confluency were detached with Trypsin/EDTA. However, the cells were allowed to regenerate cell surface proteins as the detached cells were incubated at 37°C for 2-3 h in a roller. CIM-16 plates were equilibrated at 37°C using the xCELLigence DP impedance-based cell analysis system (Roche Diagnostics). Serum containing medium were added to the lower wells of the transwells. The CIM-16 plate was assembled, i.e. the upper wells were inserted into the lower wells and were fixed together. 50000 cells/ well of MEF cells in serum free

media were added in the upper wells. The plate was allowed to stay at RT for 30 min to let the suspended cells settle down. Immediately following that the experiment was started. As the cells start to migrate from the upper surface to the bottom surface of the transwells the electrical impedance between the microelectrode changes resulting in a change of the Cell Index. Rate of change (slope in Cell Index/h) was calculated using the xCELLigence software (Roche Diagnostics).

Crystal violet-based transwell migration assay

BD transwell inserts for 6 well plate were coated for 1-2 h at RT with Fibronectin at 5 µg/ml concentration. The transwell inserts were blocked by incubating for 30 min at RT with 1 % BSA. Transduced MEF cells which were grown in T75 flask of at least ~80% confluency were detached with Trypsin/EDTA. However, the cells were allowed to regenerate cell surface proteins as the detached cells were incubated at 37°C for 2-3 h in a roller. After this the BD transwell inserts were placed in a special BD 6 well plate with low evaporation lid and serum containing medium were added per well of the 6 well plate. 50000 cells/ well of MEF cells in serum free media were added in the transwell inserts. The plate was allowed to stay at RT for 30 min to let the suspended cells settle down. Following this the cells were incubated at 37 °C for 6 h. Adherent cells in the upper surface of the transwell inserts were removed by using cotton swab. Cells migrated to the bottom surface of the transwell inserts were fixed using 4% PFA at RT for 10 min. The bottom surface was stained with crystal violet solution (0.5% crystal violet in 20% MeOH) for 15 min at RT in darkness. Crystal violet solution was removed and the surface was washed several times with distilled water and allowed to air-dry overnight or longer at RT in darkness. Pictures of the crystal violet stained cells on the bottom surface of the transwell inserts were taken using camera attached to the inverse microscope and quantified further.

Primers

The following primers were used for genotyping of PianpKO mice: forward primer: ACCTTGAGGCCCTTCCTGTTTGGA; reverse primer: CTGCGCCGCTTCTGGCTACGGT (Metabion, Planegg, Germany). The following primers were used for qRT-PCR: Avp-F CTCCGCTTGTTTCCTGAGCCT, Avp-R GGTCCGAAGCAGCGTCCT, Erdr1-F GGTCAAGATGTATGTGCCACC, Erdr1-R GCTTCTACGTGTGTGCTTTCG, Pianp-F CCCTTCCTGTTTGGAGGGCGT, Pianp-R CCGCTTCTGGCTACGGTCCCA, Scn4b-F AAAGGCCACCACCATCTACG, Scn4b-R TCCCGTCGATGAGAATCCTG, b-Actin-F ACCCGCGAGCACAGCTTCTTTG, b-Actin-R, CTTTGCACATGCCGGAGCCGTTG (Metabion).

Neurochemistry

Dissected brain regions were homogenized in an extraction solution (0.1 M perchloric acid, 1 mM EDTA) using a tissue homogenizer Mixer Mill (Qiagen, Hilden, Germany) and yielded solutions subsequently centrifuged at 15 000 g for 10 min at 4 °C. In all, 10 ml of the spun sample was loaded on a high-performance liquid chromatography (HPLC) system with electrochemical detection as described previously[13]. Brain region

specific accumulation of monoamine neurotransmitters was determined by normalizing the quantified neurotransmitter amounts to the respective weight of the tissue sample.

Open field test (OFT)

OFT was conducted as described previously[13]. Locomotor activity was quantified using the TruScan system (Coulbourn Instruments, Whitehall, PA, USA). Mice were individually placed into the center area of an open field chamber (26 x 26 x 38 cm, length x width x height), equipped with 2 banks of photobeam sensors to record both the horizontal and the vertical movement of the mouse. Each mouse was recorded for 30 min under red light illumination.

Elevated plus maze test (EPM)

EPM was conducted as described previously[13]. Mice were individually placed on the center square of the plus maze facing an enclosed arm, and allowed to freely explore the maze for 5 min. Their behavior was recorded and analyzed by the video tracking software EthoVision 3.0 (Noldus, Wageningen, Netherlands).

Tail suspension test (TST)

TST was conducted as described previously[13]. Within the 5 min of testing, all movements of the mice were automatically recorded by the video tracking software EthoVision 3.0.

Forced swim test (FST)

FST was conducted as described previously[13]. Within the testing period of 5 min, the activity of each mouse was recorded from the side by the video tracking software EthoVision 3.0. Immobility was defined as motionless floating in water, only allowing movements necessary for the animal to keep its head above the water.

Object exploration test (OET)

OET was conduted according to Blick et al[14]. Mice were habituated to the room and to the open field chamber for 30 min 1 day before the experiment. On the testing day, each mouse was placed in the testing arena, a clear plastic rectangular chamber (20 ×22 x 42 cm), without objects for 5 min immediately prior to testing for habituation. The mouse was then returned to the home cage, and an unfamiliar object was positioned in the center of the testing arena. After an inter-trial interval of 1 min, the mouse was placed in the testing arena with the object for 5 min. Behavior was recorded with a digital video camera and analyzed by the video tracking software EthoVision 3.0, and manually by a trained and blinded observer. Presented objects made from metal or glass were tested in previous experiments to be attractive for exploration. After every trial the container and objects were washed with soap and water and dried prior to being used again.

Novel object recognition (ORT) and Object relocation tests (OLT)

ORT and OLT were performed according to Bevins and Besheer[15]. Testing conditions and behavior evaluation were conducted as in the OET. Each mouse was placed in the testing arena containing two objects for 5 min for habituation (sampling period). The mouse was then returned to the home cage. For ORT, one object in the testing arena was replaced with a novel object. For OLT repositioned within the testing arena. After an intertrial interval of 30 min the mouse was placed in the testing arena for 5 min (testing period). The order and the side of the object replacement or repositioning were randomized.

Nest building test (NBT)

NBT was performed according to Deacon[16]. Mice were given a cotton nestlet (5 x 5 cm) in their home cage. As a natural behavior, mice form nests out of these cotton nestlets. The nature of the nest was graded from 1 to 5, 1 being only few scratches in the nestlet and 5 being a complete nest. The observation times were 5 and 24 h after giving the nestlet.

Odor discrimination test (ODT)

ODT was performed as described by Zou et al.[17] in two phases: nonsocial odor and social odor discrimination. A piece of cotton swab was glued to a weighing cup. Odors were presented to each mouse via fresh cotton swabs (10 µl/sample) for 2 min. During the test, mice were allowed to smell oil, vanilla, orange (diluted 1:20 in oil), water, male mice urine and female mice urine (diluted 1:20 in water).

Social Interaction Test

The social interaction test apparatus was a rectangular, three-chambered box where each chamber was 20 × 22 × 42 cm. Dividing walls were made from clear plastics with small rectangular openings connecting the chambers (7 cm × 10 cm). The test mouse was first placed in the middle chamber and allowed to explore for 5 min. The rectangular openings into the two side chambers were obstructed by plastic doors during this habituation phase. After the habituation period an unfamiliar C57BL/6N male (social partner 1), which had no prior contact with the subject mouse, was placed in one of the side chambers into a small, round wire cage (approximately 11 cm in height, with a bottom diameter of 10.5 cm), which allowed nose contact between the bars, but prevented any further interaction. An empty wired cage was placed into the opposite side chamber. The location of social partner 1 in the left vs. right side chamber was randomized between trials to avoid any side specific bias. For testing, both doors to the side chambers were then opened simultaneously and the test mouse was allowed to explore the entire chamber starting from the middle chamber for a 10 min session which is denoted as sociability test. At the end of the first 10 min, each test mouse was placed back into its home cage. Another second unfamiliar C57BL/6N male (social partner 2), which had no prior contact with the subject mouse, was placed into the empty wired cage side. Then the subject mouse was put back into the middle chamber for another 10 min session which is denoted as preference for social novelty test. The test sessions were recorded with the video tracking software EthoVision 3.0 (Noldus, Wageningen, Netherlands).

Grip Strength Assessment

Mice were allowed to grab a t-bar attached to a force meter with their forepaws. The mice were gently pulled away until they released the t-bar. The grip strength was measured in gram. The mean of 6 trials was used for analysis. Grip strength was assessed on 2 following days.

Rotarod Performance Test

Mice were placed on an immobile rotarod cylinder (TSE Systems, Bad Homburg, Germany) which was then accelerated for 3 min, from 2.5 to 25 rpm. The time until the mice fell off the rotating cylinder was recorded. The mean of 3 trials was used for analysis. The test was performed on 4 following days.

Light-Dark Box Test

Light-dark box test was conducted as described previously[13]. The test apparatus consisted of two plastic chambers, connected by a tunnel of 5 x 7 x 10 cm. The dark chamber made of black plastic (20 x 15 x 30 cm) and was covered by a lid. The lit compartment made of white plastic (30 x 15 x 30 cm). Before testing, mice were habituated with the experiment room for 30 min, illuminated from above with tubular fluorescent lamps (20 lux). During testing, the lit compartment was brightly illuminated from above with tubular fluorescent lamps (600–800 lux). At the beginning of the test, mice were individually placed into the dark compartment and their behavior was monitored by the video tracking software EthoVision 3.0 (Noldus, Wageningen, Netherlands) for 5 min.

Sucrose Preference Test

Sucrose preference test was conducted as described previously[13]. Mice were initially trained for 5 consecutive days to have access to two low seeping bottles for 1 h twice a day. During initial training, one bottle was filled with 7 % (w/v) sucrose solution; the other bottle contained tap water. To prevent any side preference of the mice the location of each choice bottle was randomized and the regular water bottle was positioned to the middle of the cage lid. After 5 successive days of training, the mice preference to sucrose solutions of different concentrations (0.5 %, 1 % or 2 %) was assessed for 3 consecutive days in a total of 3 conditions. Each condition was presented twice to the animals on the particular day in the identical way as during training. The consumption of each sucrose solutions was determined by the weight change of the respective bottles. Preference ratio was calculated as (sucrose solution consumed) / (sucrose solution consumed + tap water consumed).

Novelty Induced Hypophagia Test

Novelty induced hypophagia test was conducted as described previously[13]. Mice were first trained to consume sweetened condensed milk (1:3 dilution of Milchmädchen (Nestle, Vevey, Switzerland)) in their home cage once a day for 1 h. The latency to start consuming milk and the consumption of milk within the first 10 min and the entire

training session (60 min) were assessed for each individual mouse. Training was continued until the latency to start consuming milk was below 20 s. Following the training, the sweetened condensed milk was presented to each individual mouse within a novel environment (a new cage with a metal floor) for 10 min for a second assessment.

Fear Conditioning

Fear conditioning was conducted as described previously[18]. During the training day mice were placed in the testing chamber (25 x 25 x 25 cm, Coulbourn Instruments, Whitehall, PA, USA) and were allowed to freely explore it. The testing chamber was placed inside a soundproof chamber (67 x 53 x 55 cm, Coulbourn Instruments). 2 min after the start of the conditioning session, an auditory cue (80 dB) was presented for 2 min, that terminated by a scrambled foot-shock of 0.7 mA intensity for 2 s. This sequence was repeated in total 5 times before mice were removed from the testing chamber. Freezing behavior was recorded using Freezeframe software (Coulbourn Instruments) by which freezing was defined as lack of movement except that required for respiration. 24 h after conditioning, a contextual fear memory was assessed in the testing chamber for 5 min in the absence of any auditory cue. Approximately 3 h later cue-dependent fear memory (for the same set of mice) was quantified by placing the mouse into a novel chamber (59 x 19 x 24 cm, Coulbourn Instruments) for 4 min in total. After 2 min the auditory cue (80 dB) associated with the shock was presented for 2 min. Freezing was scored using time sampling (60 s interval).

Startle and PPI

Mice were placed into a SR-LAB startle response system (San Diego Instruments, Bilaney Consultants, Duesseldorf, Germany). After a 5 min habituation phase 45 trials were presented randomly a 40 ms acoustic pre-pulse of several pre-pulse levels (72, 76, 80, and 84 dB) followed by a 40 ms 115 dB acoustic startle pulse. At the beginning the startle pulse was presented 5 times for habituation. Control measurements were performed after the startle pulse without prepulse, the prepulse without a startle pulse and without any pulse. The mean interval between the different pulses was 30 sec.

Amphetamine Challenge

Mice were habituated to the experimental room for 30 min. Then the mice were placed in TruScan system open field chamber (27 cm x 27 cm x 39 cm, Coulbourn Instruments) individually and basal locomotor activities (moving episodes and time, total distance moved, speed and jumps) were measured for 30 min. Then, subject mice were intraperitoneally injected with 100 µl of 0.9 % NaCl solution and subsequently placed in open field chamber. Locomotor activities were measured for next 30 min to have the mock injection data (control). D-amphetamine hemisulfate (Merck) was dissolved in 0.9 % NaCl solution and intraperitoneally injected into the subject mice at the dose of 2.5 mg/kg. Locomotor activities were measured for next 120 min. Locomotor activities were measured using time sampling (5 min interval) by TruScan software (Coulbourn Instruments).

Supplementary References

1   Bracke A, Schäfer S, von Bohlen und Halbach V, Klempin F, Bente K, Bracke K *et al.* ATP6AP2 over-expression causes morphological alterations in the hippocampus and in hippocampus-related behaviour. *Brain Struct Funct* 2018; **223**: 2287–2302.

2   Sidman RL, Kosaras B, Misra B, Senft S. High Resolution Mouse Brain Atlas. http://www.hms.harvard.edu/research/brain/ (accessed 16 Jan2018).

3   Bai J, Trinh TLH, Chuang K-H, Qiu A. Atlas-based automatic mouse brain image segmentation revisited: model complexity vs. image registration. *Magn Reson Imaging* 2012; **30**: 789–798.

4   Bakker R, Tiesinga P, Kötter R. The Scalable Brain Atlas: Instant Web-Based Access to Public Brain Atlases and Related Content. *Neuroinformatics* 2015; **13**: 353–366.

5   Renelt M, von Bohlen und Halbach V, von Bohlen und Halbach O. Distribution of PCP4 protein in the forebrain of adult mice. *Acta Histochem* 2014; **116**: 1056–1061.

6   Poser R, Dokter M, von Bohlen und Halbach V, Berger SM, Busch R, Baldus M *et al.* Impact of a deletion of the full-length and short isoform of p75NTR on cholinergic innervation and the population of postmitotic doublecortin positive cells in the dentate gyrus. *Front Neuroanat* 2015; **9**: 63.

7   Freund M, Walther T, von Bohlen und Halbach O. Effects of the angiotensin-(1-7) receptor Mas on cell proliferation and on the population of doublecortin positive cells within the dentate gyrus and the piriform cortex. *Eur Neuropsychopharmacol* 2014; **24**: 302–308.

8   von Bartheld C. Counting particles in tissue sections: choices of methods and importance of calibration to minimize biases. *Histol Histopathol* 2002; **17**: 639–648.

9   Baryshnikova LM, von Bohlen und Halbach O, Kaplan S, von Bartheld CS. Two distinct events, section compression and loss of particles ('lost caps'), contribute to z-axis distortion and bias in optical disector counting. *Microsc Res Tech* 2006; **69**: 738–756.

10 Schneider CA, Rasband WS, Eliceiri KW. NIH Image to ImageJ: 25 years of image analysis. *Nat Methods* 2012; **9**: 671–675.

11 Biermann B, Ivankova-Susankova K, Bradaia A, Abdel Aziz S, Besseyrias V, Kapfhammer JP *et al.* The Sushi domains of GABAB receptors function as axonal targeting signals. *J Neurosci* 2010; **30**: 1385–1394.

12 Biswas S, Adrian M, Weber J, Evdokimov K, Winkler M, Géraud C. Posttranslational proteolytic processing of Leda-1/Pianp involves cleavage by MMPs, ADAM10/17 and gamma-secretase. *Biochem Biophys Res Commun* 2016; **477**: 661–666.

13 Berger SM, Weber T, Perreau-Lenz S, Vogt MA, Gartside SE, Maser-Gluth C *et al.* A functional Tph2 C1473G polymorphism causes an anxiety phenotype via compensatory changes in the serotonergic system. *Neuropsychopharmacology* 2012; **37**: 1986–1998.

14 Blick MG, Puchalski BH, Bolanos VJ, Wolfe KM, Green MC, Ryan BC. Novel object exploration in the C58/J mouse model of autistic-like behavior. *Behav Brain Res* 2015; **282**: 54–60.

15 Bevins RA, Besheer J. Object recognition in rats and mice: a one-trial non-matching-to-sample learning task to study 'recognition memory'. *Nat Protoc* 2006; **1**: 1306–1311.

16 Deacon RMJ. Assessing nest building in mice. *Nat Protoc* 2006; **1**: 1117–1119.

17 Zou J, Wang W, Pan Y-W, Lu S, Xia Z. Methods to measure olfactory behavior in mice. *Curr Protoc Toxicol* 2015; **63**: 11.18.1-21.

18 Strekalova T, Zörner B, Zacher C, Sadovska G, Herdegen T, Gass P. Memory retrieval after contextual fear conditioning induces c-Fos and JunB expression in CA1 hippocampus. *Genes Brain Behav* 2003; **2**: 3–10.

10 General discussion and perspectives

GBRs are key players in the control of synaptic transmission, and altered GBRs levels and functions are associated with various neurological diseases (Gassmann and Bettler, 2012; Heaney and Kinney, 2016; Kasten and Boehm, 2015; Kumar et al., 2013). Native GBRs show diverse responses that are dependent on the formation of distinct macromolecular complexes with a variety of different constituents. Pentameric KCTDs are the auxiliary subunits of GBRs and modulate the kinetics of Kir3 and Cav channel responses (Schwenk et al., 2010; Turecek et al., 2014). In my thesis, I showed that KCTD homo-and hetero-oligomers bind to G proteins, contributing to the understanding of the KCTD hetero-oligomer-induced desensitization and deactivation of GBR-mediated Kir3 currents observed by my colleagues (Fritzius et al., 2017). Additional constituents of native GBRs include effector channels, elements of the presynaptic release machinery, and SD1-interacting proteins (Dinamarca et al., 2019; Schwenk et al., 2016). My colleagues revealed that APP, AJAP1 and PIANP bind to SD1 of GB1a to form distinct complexes with GB1a/2 receptors (Dinamarca et al., 2019; Schwenk et al., 2016). I showed that GB1a/2 receptor activity does not affect the assembly and disassembly of APP/GB1a/2 complexes, and that co-expression of APP does not influence GB1a/2 receptor activity (Dinamarca et al., 2019). My colleagues further demonstrated that APP mediates axonal trafficking of presynaptic GB1a/2 receptors and that proteolytic processing of APP is reduced upon APP/GB1a/2 receptor complex formation (Dinamarca et al., 2019). Secreted sAPPα, a fragment generated by the proteolytic cleavage of APP, and a 17 residue long peptide composed of the APP sequence containing the SD1 binding motif, termed APP17, bind SD1 as well (Dinamarca et al., 2019; Rice et al., 2019). However, two independent publications reported controversial findings regarding the functional effects of sAPPα and APP17 on GB1a/2 receptor-mediated signaling. I performed an in-depth analysis of APP17 to study its influence on GB1a/2 receptor-mediated signaling *in vitro*, whereas my colleagues analyzed the effect of APP17 on GB1a/2 receptor-mediated signaling *in vivo*. Together we clearly showed that APP17 modulates neither recombinant nor native GB1a/2 receptor signaling (Rem et al. manuscript in preparation). In contrast to APP, my colleagues revealed that AJAP1 and PIANP are not involved in GB1a/2 receptor trafficking (Dinamarca et al., 2019). I demonstrated that AJAP1 and PIANP recruit and cluster GB1a/2 receptors *in trans* (unpublished). By interacting *in trans*, I further showed that AJAP1 and PIANP exerted negative allosteric effects at GB1a/2 receptors that are likely mediated by constraining the movement of VFTDs (unpublished). In order to gain further insights into the physiological function of PIANP, I generated PIANP KO mice using the CRISPR/Cas9 system in collaboration with the Centre for Transgenic Models, University of Basel. My colleagues observed impaired presynaptic GB1a/2 receptor-mediated neurotransmitter release and a deficit in spatial learning and memory in PIANP KO mice, indicating altered presynaptic GB1a/2 receptor localization and function (Winkler et al., 2019). Considering all this, I propose that APP mediates GB1a/2 receptor trafficking to presynaptic sites, where GB1a/2 receptors are transferred to postsynaptic AJAP1 and PIANP that precisely localize presynaptic GB1a/2 receptors at the synapse.

10.1 Implications of KCTD hetero-oligomers on the functional repertoire of GBRs

Native GBRs show a diversity in signaling that is not reproduced by cloned GBRs, suggesting the involvement of additional proteins (Cruz et al., 2004; Deisz et al., 1997; Kaupmann et al., 1997; Kaupmann et al., 1998). Proteomic analysis of native GBRs identified auxiliary subunits in complex with GBRs (Schwenk et al., 2010; Schwenk et al., 2016). KCTDs are the auxiliary subunits of GBRs, regulating the kinetics of GBR-mediated effector responses (Schwenk et al., 2010). While all KCTDs accelerate the effector response, only KCTD12 and 12b desensitize GBR-induced Kir3 currents and Cav inhibition by uncoupling Gβγ from the effector channel (Schwenk et al., 2010; Turecek et al., 2014). On the other hand, KCTD16 scaffolds Cav and HCN channels at GBRs. By scaffolding HCN channels at GBRs, GBR-

mediated Kir3 currents activate HCN channels that shorten receptor-induced IPSPs (Schwenk et al., 2016). Hence, KCTDs exert a dual role at GBRs by regulating the effector response and scaffolding effector channels. The observation of my colleagues that KCTD hetero-oligomers confer unique desensitizing and deactivation kinetics of GBR-mediated Kir3 currents indicates that KCTD hetero-oligomers further increase the functional repertoire of GBRs (Fritzius et al., 2017). Since the unique properties of KCTD hetero-oligomers on the Kir3 current activation and deactivation relies on the ability of KCTD12 and KCTD16 to retain their distinct regulatory properties, it is also conceivable that KCTD hetero-oligomers containing KCTD16 form GBR/KCTD/Cav and GBR/KCTD/HCN complexes, further increasing the functional repertoire of GBRs. The fine-tuning properties of KCTD hetero-oligomers on GBR-mediated Kir3 currents and the scaffolding properties of KCTD16 raise the question of whether the formation of GBRs with KCTD homo-and hetero-oligomers is regulated.

10.2 The involvement of APP, AJAP1 and PIANP on localizing presynaptic GB1a/2 receptor complexes

The interaction between KCTDs and GBRs takes place in the ER (Ivankova et al., 2013). Therefore, it is thinkable that GB1a/2/KCTD16/Cav complexes are formed in the ER, are trafficked to presynaptic sites, and are precisely located within the synapse. My colleagues revealed that APP mediates the axonal trafficking of GB1a/2 receptors (Dinamarca et al., 2019). APP belongs to the group of SD1 binding proteins identified in complex with native GB1a/2 receptors (Dinamarca et al., 2019; Schwenk et al., 2016). The SD1 binding protein group is further composed of AJAP1 and PIANP (Dinamarca et al., 2019; Schwenk et al., 2016). Unlike APP, AJAP1 and PIANP are not involved in GB1a/2 receptor trafficking (Dinamarca et al., 2019). I showed that AJAP1 and PIANP recruit and cluster presynaptic GB1a/2 receptors *in trans*. My colleagues further showed that AJAP1 KO and PIANP KO mice exhibit a deficit in presynaptic GB1a/2 receptor-mediated neurotransmitter release, supporting a function of AJAP1 and PIANP in the precise localization of presynaptic GB1a/2 receptors (T. Lalanne, personal communication)(Winkler et al., 2019). Since AJAP1 and PIANP are found at E-cadherin positive adherens junctions in epithelial cells, it is conceivable that AJAP1 and PIANP are also located to adherens junctions in the brain (Bharti et al., 2004; Geraud et al., 2010). Neuronal adherens junctions mediate the interaction between post- and presynaptic membranes and locate proximal to the active zone (Uchida et al., 1996). At the presynaptic site, GB1a/2 receptors inhibit Cav channels, which requires co-localization of GB1a/2 receptors and Cav channels (Gassmann and Bettler, 2012). Thus, it is conceivable that AJAP1 and PIANP precisely position presynaptic GB1a/2/KCTD16/Cav complexes at the active zone.

Recently, it has been shown that the regulation of presynaptic GB1a/2 receptor localization and function involves neurexins (Luo et al., 2021). However, neurexins have not been found in the proteome of native GBRs (Schwenk et al., 2016), suggesting the involvement of additional proteins. Neurexins are neuronal adhesion molecules that induce synaptogenesis by recruiting diverse scaffolding proteins, thereby promoting the formation of presynaptic terminals (Dean and Dresbach, 2006; Krueger et al., 2012). Presynaptic neurexins interact with postsynaptic neuroligins *in trans*. Neuroligins also induce the recruitment of additional scaffolding proteins, thereby establishing the formation of postsynaptic structures (Dean and Dresbach, 2006; Krueger et al., 2012). Since my data indicate that the precise localization of presynaptic GB1a/2 receptors is mediated by transcellular AJAP1 and PIANP, it is conceivable that neurexin/neuroligin complexes regulate presynaptic GB1a/2 receptor localization and function by inducing the recruitment of AJAP1 and PIANP. Because AJAP1 and PIANP presumably localize to cadherins in neurons and N-cadherin co-localizes with neuroligin-1 (Krueger et al., 2012), N-cadherin could scaffold AJAP1 and PIANP, resulting in presynaptic GB1a/2 receptor localization to newly formed synapses. However, whether AJAP1 and PIANP locate to cadherins in the brain remains elusive. In general, it is unclear whether AJAP1 and PIANP are expressed in different neurons in the brain. Because different cadherin subtypes are expressed specifically in excitatory or inhibitory neurons (Benson and Tanaka, 1998), and AJAP1 and PIANP are recruited to cadherins (Bharti et al., 2004; Geraud et al., 2010), distinct

localization of AJAP1 and PIANP to individual cadherins could define the localization of presynaptic GB1a/2 receptors to excitatory or inhibitory synapses.

10.3 Implications of AJAP1 and PIANP on presynaptic GB1a/2 receptor functions

Since AJAP1 and PIANP likely precisely position presynaptic GB1a/2 receptors, mice genetically lacking either AJAP1 or PIANP should uncover behavioral phenotypes similar to GB1a KO mice. My colleagues revealed that PIANP KO mice exhibit a deficit in spatial memory and learning, which is also observed in GB1a KO mice (Vigot et al., 2006; Winkler et al., 2019). Memory impairments are typical for AD, and in an AD animal model pre-and postsynaptic GB1 surface localization was decreased (Martin-Belmonte et al., 2020). Thus, PIANP presumably contributes to memory and learning by precisely localizing presynaptic GB1a/2 receptors. Since AJAP1 also precisely localizes presynaptic GB1a/2 receptors, mice genetically lacking AJAP1 should also exhibit deficits in memory and learning. GB1a KO mice further exhibit infrequent seizures (Vienne et al., 2010). In an animal model of absence seizures, GB1 expression and distribution were reduced, and the presynaptic GB1a/2 receptor function was diminished (Inaba et al., 2009; Merlo et al., 2007). Thus, AJAP1 KO mice could further exhibit seizures. In support of this, it has recently been shown that both AJAP1 and GB1 are downregulated in an epileptic mouse model that exerts spontaneous recurrent seizures (SRS) (Zhang et al., 2020). The exogenous expression of AJAP1 restored GB1 levels, resulting in reduced spontaneous recurrent seizures (SRS). Hence, the reduction in SRS due to the expression of AJAP1 possibly relies on restoring the natural presynaptic localization of GB1a/2 receptors.

10.4 New opportunities in drug discovery by targeting protein-protein interactions of GBR complexes

Despite the involvement of GBRs in various diseases, only two drugs targeting the GBRs are currently on the market. γ-hydroxybutyrate (GHB), a GABA metabolite, is used to treat narcolepsy, and the agonist baclofen is prescribed to treat spasticity (Fritzius and Bettler, 2019). The effectiveness of baclofen as treatment for alcohol abuse is still controversially discussed (Agabio and Leggio, 2018). However, the side effects observed with baclofen limit its usefulness for psychiatric indications (Kumar et al., 2013; Mugnaini and Corelli, 2016). Since pre-and postsynaptic GBRs play distinct roles in the pathophysiology of various diseases, and the current drugs lack the ability to discriminate between pre- and postsynaptic GBRs, a high demand for GB1 isoform-specific drugs exists. Therefore, directly targeting the protein-protein interactions relevant for diseases represents a meaningful approach to influence specific GBR functions (Fritzius and Bettler, 2019). Recently, a peptide highly potent to interfere with the GBR/KCTD complexes was developed (Sereikaite et al., 2019). Such a peptide could be used to displace KCTD12 from GBRs, resulting in increased and prolonged postsynaptic inhibition, which is expected to have anxiolytic effects (Fritzius and Bettler, 2019). GBR activation and inhibition contributes to the excitation-inhibition balance, whose alteration is associated with various neurological and neuropsychiatric disorders (Kato and Witkin, 2018). Since GBR antagonists enhance cognitive functions (Heaney and Kinney, 2016; Kumar et al., 2017; Kumar et al., 2013), the augmentation of neuronal excitability is a promising therapeutic strategy. In this context, small peptides containing the SD1 binding motif could displace the interaction of GB1a/2 receptors with APP, AJAP1, and PIANP, resulting in presynaptic GB1a/2 receptor internalization and increased glutamate release. Consequently, the neuronal excitability would be increased, resulting in enhanced cognitive functions. However, too little inhibition of presynaptic GB1a/2 receptor-mediated neurotransmitter release could result in seizures, as observed in GB1a KO animals (Vienne et al., 2010). Hence, further studies elucidating the therapeutic potential of peptides interfering with SD1-binding are required.

10.5 Similarities in complex formations of GBRs and mGluRs

GBRs and mGluRs share structural similarities (Pin and Bettler, 2016). mGluRs are divided into groups I, II, and III, with group I being postsynaptic, group II being pre-and postsynaptic, and group III being presynaptic (Kryszkowski and Boczek, 2021; Pin and Bettler, 2016). Group I mGluRs interact with the cytosolic Homer proteins that act as regulators and scaffolding proteins (Pin and Bettler, 2016) similar to the KCTDs. Hence, GBRs and mGluRs show analogous complex organization with proteins exerting similar functions. Despite similar functions of the associated proteins, they explicitly interact with distinct GPCRs because Homers have not been identified in complex with GBRs (Schwenk et al., 2016) and vice versa (Pin and Bettler, 2016). Likewise, the synaptic adhesion molecules ELFN1 and ELFN2 recruit and accumulate group III mGluRs *in trans* and modulate the activity of transcellular group III mGluRs, similar to what I observed with AJAP1 and PIANP (Dunn et al., 2018; Dunn et al., 2019; Tomioka et al., 2014). Compared to the negative allosteric properties of AJAP1 and PIANP at transcellular GB1a/2 receptors, ELFN1 and ELFN2 exerted positive allosteric properties at transcellular group III mGluRs. Furthermore, the postsynaptic orphan receptor GPR158 interacts with presynaptic glypican 4 (GPC4), and the genetic loss of GPR158 resulted in impaired synaptic transmission at mossy cell/CA3 synapses (Condomitti et al., 2018). Hence, within the Class C GPCR, the interaction *in trans* represents a conserved mechanism to localize GPCRs at synapses and modulate GPCR activity, however, with distinct modulatory properties. A characteristic of class C GPCRs is the large ECD that is shared by all members. Despite the similarities of the ECDs of GBRs and mGluRs (Kaupmann et al., 1997; Pin and Bettler, 2016), ELFN1 and ELFN2 were not identified in complex with GBRs (Schwenk et al., 2016), suggesting the evolution of distinct trans-interacting pairs. Thus, it is thinkable that all members of class C GPCRs form trans-interactions with distinct partners. In general, class C GPCRs presumably share analogy in the organization of macromolecular complexes and the regulation of functional receptors, however, with distinct proteins that exert similar functions.

11 References

Adelfinger, L., Turecek, R., Ivankova, K., Jensen, A.A., Moss, S.J., Gassmann, M., and Bettler, B. (2014). GABAB receptor phosphorylation regulates KCTD12-induced K(+) current desensitization. Biochem Pharmacol *91*, 369-379.

Adli, M. (2018). The CRISPR tool kit for genome editing and beyond. Nature communications *9*, 1911.

Agabio, R., and Leggio, L. (2018). Baclofen in the Treatment of Patients With Alcohol Use Disorder and Other Mental Health Disorders. Front Psychiatry *9*, 464.

Alexander, S.P.H., Christopoulos, A., Davenport, A.P., Kelly, E., Mathie, A., Peters, J.A., Veale, E.L., Armstrong, J.F., Faccenda, E., Harding, S.D.*, et al.* (2019). THE CONCISE GUIDE TO PHARMACOLOGY 2019/20: G protein-coupled receptors. Br J Pharmacol *176 Suppl 1*, S21-S141.

Alghadban, S., Bouchareb, A., Hinch, R., Hernandez-Pliego, P., Biggs, D., Preece, C., and Davies, B. (2020). Electroporation and genetic supply of Cas9 increase the generation efficiency of CRISPR/Cas9 knock-in alleles in C57BL/6J mouse zygotes. Scientific reports *10*, 17912.

Angelicheva, D., Tournev, I., Guergueltcheva, V., Mihaylova, V., Azmanov, D.N., Morar, B., Radionova, M., Smith, S.J., Zlatareva, D., Stevens, J.M.*, et al.* (2009). Partial epilepsy syndrome in a Gypsy family linked to 5q31.3-q32. Epilepsia *50*, 1679-1688.

Apelt, J., Schliebs, R., Beck, M., Rossner, S., and Bigl, V. (1997). Expression of amyloid precursor protein mRNA isoforms in rat brain is differentially regulated during postnatal maturation and by cholinergic activity. Int J Dev Neurosci *15*, 95-112.

Aydin, D., Filippov, M.A., Tschape, J.A., Gretz, N., Prinz, M., Eils, R., Brors, B., and Muller, U.C. (2011). Comparative transcriptome profiling of amyloid precursor protein family members in the adult cortex. BMC Genomics *12*, 160.

Ayoub, M.A., Damian, M., Gespach, C., Ferrandis, E., Lavergne, O., De Wever, O., Baneres, J.L., Pin, J.P., and Prevost, G.P. (2009). Inhibition of heterotrimeric G protein signaling by a small molecule acting on Galpha subunit. The Journal of biological chemistry *284*, 29136-29145.

Back, S., Haas, P., Tschape, J.A., Gruebl, T., Kirsch, J., Muller, U., Beyreuther, K., and Kins, S. (2007). beta-amyloid precursor protein can be transported independent of any sorting signal to the axonal and dendritic compartment. J Neurosci Res *85*, 2580-2590.

Balla, A., Nattini, M.E., Sershen, H., Lajtha, A., Dunlop, D.S., and Javitt, D.C. (2009). GABAB/NMDA receptor interaction in the regulation of extracellular dopamine levels in rodent prefrontal cortex and striatum. Neuropharmacology *56*, 915-921.

Barrangou, R. (2013). CRISPR-Cas systems and RNA-guided interference. Wiley Interdiscip Rev RNA *4*, 267-278.

Barrangou, R., Fremaux, C., Deveau, H., Richards, M., Boyaval, P., Moineau, S., Romero, D.A., and Horvath, P. (2007). CRISPR provides acquired resistance against viruses in prokaryotes. Science *315*, 1709-1712.

Baumkotter, F., Schmidt, N., Vargas, C., Schilling, S., Weber, R., Wagner, K., Fiedler, S., Klug, W., Radzimanowski, J., Nickolaus, S.*, et al.* (2014). Amyloid precursor protein dimerization and synaptogenic function depend on copper binding to the growth factor-like domain. The Journal of neuroscience : the official journal of the Society for Neuroscience *34*, 11159-11172.

Benes, F.M. (2010). Amygdalocortical circuitry in schizophrenia: from circuits to molecules. Neuropsychopharmacology : official publication of the American College of Neuropsychopharmacology *35*, 239-257.

Benson, D.L., and Tanaka, H. (1998). N-cadherin redistribution during synaptogenesis in hippocampal neurons. The Journal of neuroscience : the official journal of the Society for Neuroscience *18*, 6892-6904.

Bettler, B., Kaupmann, K., Mosbacher, J., and Gassmann, M. (2004). Molecular structure and physiological functions of GABA(B) receptors. Physiol Rev *84*, 835-867.

Bharti, S., Handrow-Metzmacher, H., Zickenheiner, S., Zeitvogel, A., Baumann, R., and Starzinski-Powitz, A. (2004). Novel membrane protein shrew-1 targets to cadherin-mediated junctions in polarized epithelial cells. Molecular biology of the cell *15*, 397-406.

Bhaya, D., Davison, M., and Barrangou, R. (2011). CRISPR-Cas systems in bacteria and archaea: versatile small RNAs for adaptive defense and regulation. Annu Rev Genet *45*, 273-297.

Biermann, B., Ivankova-Susankova, K., Bradaia, A., Abdel Aziz, S., Besseyrias, V., Kapfhammer, J.P., Missler, M., Gassmann, M., and Bettler, B. (2010). The Sushi domains of GABAB receptors function as axonal targeting signals. The Journal of neuroscience : the official journal of the Society for Neuroscience *30*, 1385-1394.

Billinton, A., Baird, V.H., Thom, M., Duncan, J.S., Upton, N., and Bowery, N.G. (2001). GABA(B) receptor autoradiography in hippocampal sclerosis associated with human temporal lobe epilepsy. Br J Pharmacol *132*, 475-480.

Biswas, S., Adrian, M., Weber, J., Evdokimov, K., Winkler, M., and Geraud, C. (2016). Posttranslational proteolytic processing of Leda-1/Pianp involves cleavage by MMPs, ADAM10/17 and gamma-secretase. Biochemical and biophysical research communications *477*, 661-666.

Bjarnadottir, T.K., Gloriam, D.E., Hellstrand, S.H., Kristiansson, H., Fredriksson, R., and Schioth, H.B. (2006). Comprehensive repertoire and phylogenetic analysis of the G protein-coupled receptors in human and mouse. Genomics *88*, 263-273.

Bolotin, A., Quinquis, B., Sorokin, A., and Ehrlich, S.D. (2005). Clustered regularly interspaced short palindrome repeats (CRISPRs) have spacers of extrachromosomal origin. Microbiology (Reading) *151*, 2551-2561.

Bour, A., Little, S., Dodart, J.C., Kelche, C., and Mathis, C. (2004). A secreted form of the beta-amyloid precursor protein (sAPP695) improves spatial recognition memory in OF1 mice. Neurobiol Learn Mem *81*, 27-38.

Brandsma, I., and Gent, D.C. (2012). Pathway choice in DNA double strand break repair: observations of a balancing act. Genome Integr *3*, 9.

Buisson, R., Niraj, J., Pauty, J., Maity, R., Zhao, W., Coulombe, Y., Sung, P., and Masson, J.Y. (2014). Breast cancer proteins PALB2 and BRCA2 stimulate polymerase eta in recombination-associated DNA synthesis at blocked replication forks. Cell reports *6*, 553-564.

Calon, F., Morissette, M., Goulet, M., Grondin, R., Blanchet, P.J., Bedard, P.J., and Di Paolo, T. (2000). 125I-CGP 64213 binding to GABA(B) receptors in the brain of monkeys: effect of MPTP and dopaminomimetic treatments. Exp Neurol *163*, 191-199.

Cao, X., and Sudhof, T.C. (2001). A transcriptionally [correction of transcriptively] active complex of APP with Fe65 and histone acetyltransferase Tip60. Science *293*, 115-120.

Capecchi, M.R. (1989). Altering the genome by homologous recombination. Science *244*, 1288-1292.

Casanova, E., Guetg, N., Vigot, R., Seddik, R., Julio-Pieper, M., Hyland, N.P., Cryan, J.F., Gassmann, M., and Bettler, B. (2009). A mouse model for visualization of GABA(B) receptors. Genesis *47*, 595-602.

Cathomas, F., Sigrist, H., Schmid, L., Seifritz, E., Gassmann, M., Bettler, B., and Pryce, C.R. (2017). Behavioural endophenotypes in mice lacking the auxiliary GABAB receptor subunit KCTD16. Behavioural brain research *317*, 393-400.

Cathomas, F., Stegen, M., Sigrist, H., Schmid, L., Seifritz, E., Gassmann, M., Bettler, B., and Pryce, C.R. (2015). Altered emotionality and neuronal excitability in mice lacking KCTD12, an auxiliary subunit of GABAB receptors associated with mood disorders. Transl Psychiatry *5*, e510.

Chalifoux, J.R., and Carter, A.G. (2010). GABAB receptors modulate NMDA receptor calcium signals in dendritic spines. Neuron *66*, 101-113.

Chalifoux, J.R., and Carter, A.G. (2011). GABAB receptor modulation of voltage-sensitive calcium channels in spines and dendrites. The Journal of neuroscience : the official journal of the Society for Neuroscience *31*, 4221-4232.

Chapman, J.R., Taylor, M.R., and Boulton, S.J. (2012). Playing the end game: DNA double-strand break repair pathway choice. Mol Cell *47*, 497-510.

Chen, L., Trujillo, K., Sung, P., and Tomkinson, A.E. (2000). Interactions of the DNA ligase IV-XRCC4 complex with DNA ends and the DNA-dependent protein kinase. The Journal of biological chemistry *275*, 26196-26205.

Chen, L.H., Sun, B., Zhang, Y., Xu, T.J., Xia, Z.X., Liu, J.F., and Nan, F.J. (2014). Discovery of a Negative Allosteric Modulator of GABAB Receptors. ACS Med Chem Lett *5*, 742-747.

Cheng, Z., Garvin, D., Paguio, A., Stecha, P., Wood, K., and Fan, F. (2010). Luciferase Reporter Assay System for Deciphering GPCR Pathways. Curr Chem Genomics *4*, 84-91.

Chiruvella, K.K., Liang, Z., and Wilson, T.E. (2013). Repair of double-strand breaks by end joining. Cold Spring Harb Perspect Biol *5*, a012757.

Chu, D.C., Penney, J.B., Jr., and Young, A.B. (1987a). Cortical GABAB and GABAA receptors in Alzheimer's disease: a quantitative autoradiographic study. Neurology *37*, 1454-1459.

Chu, D.C., Penney, J.B., Jr., and Young, A.B. (1987b). Quantitative autoradiography of hippocampal GABAB and GABAA receptor changes in Alzheimer's disease. Neuroscience letters *82*, 246-252.

Claasen, A.M., Guevremont, D., Mason-Parker, S.E., Bourne, K., Tate, W.P., Abraham, W.C., and Williams, J.M. (2009). Secreted amyloid precursor protein-alpha upregulates synaptic protein synthesis by a protein kinase G-dependent mechanism. Neuroscience letters *460*, 92-96.

Coburger, I., Hoefgen, S., and Than, M.E. (2014). The structural biology of the amyloid precursor protein APP - a complex puzzle reveals its multi-domain architecture. Biol Chem *395*, 485-498.

Cole, A.E., and Nicoll, R.A. (1984). The pharmacology of cholinergic excitatory responses in hippocampal pyramidal cells. Brain research *305*, 283-290.

Condomitti, G., Wierda, K.D., Schroeder, A., Rubio, S.E., Vennekens, K.M., Orlandi, C., Martemyanov, K.A., Gounko, N.V., Savas, J.N., and de Wit, J. (2018). An Input-Specific Orphan Receptor GPR158-HSPG Interaction Organizes Hippocampal Mossy Fiber-CA3 Synapses. Neuron *100*, 201-215 e209.

Conklin, B.R., Farfel, Z., Lustig, K.D., Julius, D., and Bourne, H.R. (1993). Substitution of three amino acids switches receptor specificity of Gq alpha to that of Gi alpha. Nature *363*, 274-276.

Cousins, S.L., Hoey, S.E., Anne Stephenson, F., and Perkinton, M.S. (2009). Amyloid precursor protein 695 associates with assembled NR2A- and NR2B-containing NMDA receptors to result in the enhancement of their cell surface delivery. Journal of neurochemistry *111*, 1501-1513.

Cruz, H.G., Ivanova, T., Lunn, M.L., Stoffel, M., Slesinger, P.A., and Luscher, C. (2004). Bi-directional effects of GABA(B) receptor agonists on the mesolimbic dopamine system. Nature neuroscience *7*, 153-159.

Cryan, J.F., and Slattery, D.A. (2010). GABAB receptors and depression. Current status. Advances in pharmacology *58*, 427-451.

Dawson, G.R., Seabrook, G.R., Zheng, H., Smith, D.W., Graham, S., O'Dowd, G., Bowery, B.J., Boyce, S., Trumbauer, M.E., Chen, H.Y.*, et al.* (1999). Age-related cognitive deficits, impaired long-term potentiation and reduction in synaptic marker density in mice lacking the beta-amyloid precursor protein. Neuroscience *90*, 1-13.

Dean, C., and Dresbach, T. (2006). Neuroligins and neurexins: linking cell adhesion, synapse formation and cognitive function. Trends in neurosciences *29*, 21-29.

Deisz, R.A., Billard, J.M., and Zieglgansberger, W. (1997). Presynaptic and postsynaptic GABAB receptors of neocortical neurons of the rat in vitro: differences in pharmacology and ionic mechanisms. Synapse *25*, 62-72.

Deltcheva, E., Chylinski, K., Sharma, C.M., Gonzales, K., Chao, Y., Pirzada, Z.A., Eckert, M.R., Vogel, J., and Charpentier, E. (2011). CRISPR RNA maturation by trans-encoded small RNA and host factor RNase III. Nature *471*, 602-607.

Deng, P.Y., Xiao, Z., Yang, C., Rojanathammanee, L., Grisanti, L., Watt, J., Geiger, J.D., Liu, R., Porter, J.E., and Lei, S. (2009). GABA(B) receptor activation inhibits neuronal excitability and spatial learning in the entorhinal cortex by activating TREK-2 K+ channels. Neuron *63*, 230-243.

Devkota, S. (2018). The road less traveled: strategies to enhance the frequency of homology-directed repair (HDR) for increased efficiency of CRISPR/Cas-mediated transgenesis. BMB Rep *51*, 437-443.

Deyts, C., Vetrivel, K.S., Das, S., Shepherd, Y.M., Dupre, D.J., Thinakaran, G., and Parent, A.T. (2012). Novel GalphaS-protein signaling associated with membrane-tethered amyloid precursor protein intracellular domain. The Journal of neuroscience : the official journal of the Society for Neuroscience *32*, 1714-1729.

Dinamarca, M.C., Raveh, A., Schneider, A., Fritzius, T., Fruh, S., Rem, P.D., Stawarski, M., Lalanne, T., Turecek, R., Choo, M.*, et al.* (2019). Complex formation of APP with GABAB receptors links axonal trafficking to amyloidogenic processing. Nature communications *10*, 1331.

Dunn, H.A., Patil, D.N., Cao, Y., Orlandi, C., and Martemyanov, K.A. (2018). Synaptic adhesion protein ELFN1 is a selective allosteric modulator of group III metabotropic glutamate receptors in trans. Proceedings of the National Academy of Sciences of the United States of America *115*, 5022-5027.

Dunn, H.A., Zucca, S., Dao, M., Orlandi, C., and Martemyanov, K.A. (2019). ELFN2 is a postsynaptic cell adhesion molecule with essential roles in controlling group III mGluRs in the brain and neuropsychiatric behavior. Molecular psychiatry.

Dvir, A., Peterson, S.R., Knuth, M.W., Lu, H., and Dynan, W.S. (1992). Ku autoantigen is the regulatory component of a template-associated protein kinase that phosphorylates RNA polymerase II. Proceedings of the National Academy of Sciences of the United States of America *89*, 11920-11924.

Ellaithy, A., Gonzalez-Maeso, J., Logothetis, D.A., and Levitz, J. (2020). Structural and Biophysical Mechanisms of Class C G Protein-Coupled Receptor Function. Trends Biochem Sci *45*, 1049-1064.

Enna, S.J., and Bowery, N.G. (2004). GABA(B) receptor alterations as indicators of physiological and pharmacological function. Biochem Pharmacol *68*, 1541-1548.

Evdokimov, K., Biswas, S., Adrian, M., Weber, J., Schledzewski, K., Winkler, M., Goerdt, S., and Geraud, C. (2013). Proteolytic cleavage of LEDA-1/PIANP by furin-like proprotein convertases precedes its plasma membrane localization. Biochemical and biophysical research communications *434*, 22-27.

Evdokimov, K., Biswas, S., Schledzewski, K., Winkler, M., Gorzelanny, C., Schneider, S.W., Goerdt, S., and Geraud, C. (2016). Leda-1/Pianp is targeted to the basolateral plasma membrane by a distinct intracellular juxtamembrane region and modulates barrier properties and E-Cadherin processing. Biochemical and biophysical research communications *475*, 342-349.

Evenseth, L.S.M., Gabrielsen, M., and Sylte, I. (2020). The GABAB Receptor-Structure, Ligand Binding and Drug Development. Molecules *25*.

Fatemi, S.H., Folsom, T.D., Reutiman, T.J., and Thuras, P.D. (2009). Expression of GABA(B) receptors is altered in brains of subjects with autism. Cerebellum *8*, 64-69.

Fatemi, S.H., Folsom, T.D., and Thuras, P.D. (2011). Deficits in GABA(B) receptor system in schizophrenia and mood disorders: a postmortem study. Schizophrenia research *128*, 37-43.

Fogel, H., Frere, S., Segev, O., Bharill, S., Shapira, I., Gazit, N., O'Malley, T., Slomowitz, E., Berdichevsky, Y., Walsh, D.M.*, et al.* (2014). APP homodimers transduce an amyloid-beta-mediated increase in release probability at excitatory synapses. Cell reports *7*, 1560-1576.

Foord, S.M., Bonner, T.I., Neubig, R.R., Rosser, E.M., Pin, J.P., Davenport, A.P., Spedding, M., and Harmar, A.J. (2005). International Union of Pharmacology. XLVI. G protein-coupled receptor list. Pharmacological reviews *57*, 279-288.

Fredriksson, R., Lagerstrom, M.C., Lundin, L.G., and Schioth, H.B. (2003). The G-protein-coupled receptors in the human genome form five main families. Phylogenetic analysis, paralogon groups, and fingerprints. Mol Pharmacol *63*, 1256-1272.

Fritzius, T., and Bettler, B. (2019). The organizing principle of GABAB receptor complexes: Physiological and pharmacological implications. Basic Clin Pharmacol Toxicol.

Fritzius, T., Turecek, R., Seddik, R., Kobayashi, H., Tiao, J., Rem, P.D., Metz, M., Kralikova, M., Bouvier, M., Gassmann, M.*, et al.* (2017). KCTD Hetero-oligomers Confer Unique Kinetic Properties on Hippocampal GABAB Receptor-Induced K+ Currents. The Journal of neuroscience : the official journal of the Society for Neuroscience *37*, 1162-1175.

Froestl, W., Gallagher, M., Jenkins, H., Madrid, A., Melcher, T., Teichman, S., Mondadori, C.G., and Pearlman, R. (2004). SGS742: the first GABA(B) receptor antagonist in clinical trials. Biochem Pharmacol *68*, 1479-1487.

Fukui, M., Nakamichi, N., Yoneyama, M., Ozawa, S., Fujimori, S., Takahata, Y., Nakamura, N., Taniura, H., and Yoneda, Y. (2008). Modulation of cellular proliferation and differentiation through GABA(B) receptors expressed by undifferentiated neural progenitor cells isolated from fetal mouse brain. Journal of cellular physiology *216*, 507-519.

Galvan, A., Hu, X., Smith, Y., and Wichmann, T. (2011). Localization and pharmacological modulation of GABA-B receptors in the globus pallidus of parkinsonian monkeys. Exp Neurol *229*, 429-439.

Gassmann, M., and Bettler, B. (2012). Regulation of neuronal GABA(B) receptor functions by subunit composition. Nature reviews Neuroscience *13*, 380-394.

Geng, Y., Bush, M., Mosyak, L., Wang, F., and Fan, Q.R. (2013). Structural mechanism of ligand activation in human GABA(B) receptor. Nature *504*, 254-259.

Geng, Y., Xiong, D., Mosyak, L., Malito, D.L., Kniazeff, J., Chen, Y., Burmakina, S., Quick, M., Bush, M., Javitch, J.A.*, et al.* (2012). Structure and functional interaction of the extracellular domain of human GABA(B) receptor GBR2. Nature neuroscience *15*, 970-978.

Geraud, C., Schledzewski, K., Demory, A., Klein, D., Kaus, M., Peyre, F., Sticht, C., Evdokimov, K., Lu, S., Schmieder, A.*, et al.* (2010). Liver sinusoidal endothelium: a microenvironment-dependent differentiation program in rat including the novel junctional protein liver endothelial differentiation-associated protein-1. Hepatology *52*, 313-326.

Getova, D.P., and Bowery, N.G. (2001). Effects of high-affinity GABAB receptor antagonists on active and passive avoidance responding in rodents with gamma-hydroxybutyrolactone-induced absence syndrome. Psychopharmacology *157*, 89-95.

Goebbels, S., Bormuth, I., Bode, U., Hermanson, O., Schwab, M.H., and Nave, K.A. (2006). Genetic targeting of principal neurons in neocortex and hippocampus of NEX-Cre mice. Genesis *44*, 611-621.

Gottlieb, T.M., and Jackson, S.P. (1993). The DNA-dependent protein kinase: requirement for DNA ends and association with Ku antigen. Cell *72*, 131-142.

Gross, J.C., Schreiner, A., Engels, K., and Starzinski-Powitz, A. (2009). E-cadherin surface levels in epithelial growth factor-stimulated cells depend on adherens junction protein shrew-1. Molecular biology of the cell *20*, 3598-3607.

Grunewald, S., Schupp, B.J., Ikeda, S.R., Kuner, R., Steigerwald, F., Kornau, H.C., and Kohr, G. (2002). Importance of the gamma-aminobutyric acid(B) receptor C-termini for G-protein coupling. Mol Pharmacol *61*, 1070-1080.

Gupta, R.M., and Musunuru, K. (2014). Expanding the genetic editing tool kit: ZFNs, TALENs, and CRISPR-Cas9. J Clin Invest *124*, 4154-4161.

Haass, C., and Willem, M. (2019). Secreted APP Modulates Synaptic Activity: A Novel Target for Therapeutic Intervention? Neuron *101*, 557-559.

Han, J., Xie, C., Pei, T., Wang, J., Lan, Y., Huang, K., Cui, Y., Wang, F., Zhang, J., Pan, S.*, et al.* (2017). Deregulated AJAP1/beta-catenin/ZEB1 signaling promotes hepatocellular carcinoma carcinogenesis and metastasis. Cell Death Dis *8*, e2736.

Hannan, S., Wilkins, M.E., and Smart, T.G. (2012). Sushi domains confer distinct trafficking profiles on GABAB receptors. Proceedings of the National Academy of Sciences of the United States of America *109*, 12171-12176.

Hashimoto, M., Yamashita, Y., and Takemoto, T. (2016). Electroporation of Cas9 protein/sgRNA into early pronuclear zygotes generates non-mosaic mutants in the mouse. Dev Biol *418*, 1-9.

Hawrot, E., Xiao, Y., Shi, Q.L., Norman, D., Kirkitadze, M., and Barlow, P.N. (1998). Demonstration of a tandem pair of complement protein modules in GABA(B) receptor 1a. FEBS letters *432*, 103-108.

Heaney, C.F., and Kinney, J.W. (2016). Role of GABA(B) receptors in learning and memory and neurological disorders. Neurosci Biobehav Rev *63*, 1-28.

Hefferin, M.L., and Tomkinson, A.E. (2005). Mechanism of DNA double-strand break repair by non-homologous end joining. DNA Repair (Amst) *4*, 639-648.

Henderson, C., Wijetunge, L., Kinoshita, M.N., Shumway, M., Hammond, R.S., Postma, F.R., Brynczka, C., Rush, R., Thomas, A., Paylor, R.*, et al.* (2012). Reversal of disease-related pathologies in the fragile X mouse model by selective activation of GABAB receptors with arbaclofen. Sci Transl Med *4*, 152ra128.

Hick, M., Herrmann, U., Weyer, S.W., Mallm, J.P., Tschape, J.A., Borgers, M., Mercken, M., Roth, F.C., Draguhn, A., Slomianka, L.*, et al.* (2015). Acute function of secreted amyloid precursor protein fragment APPsalpha in synaptic plasticity. Acta Neuropathol *129*, 21-37.

Hu, G.M., Mai, T.L., and Chen, C.M. (2017). Visualizing the GPCR Network: Classification and Evolution. Scientific reports *7*, 15495.

Huang, Y., and Mucke, L. (2012). Alzheimer mechanisms and therapeutic strategies. Cell *148*, 1204-1222.

Inaba, Y., D'Antuono, M., Bertazzoni, G., Biagini, G., and Avoli, M. (2009). Diminished presynaptic GABA(B) receptor function in the neocortex of a genetic model of absence epilepsy. Neurosignals *17*, 121-131.

Ishida, A., Furukawa, K., Keller, J.N., and Mattson, M.P. (1997). Secreted form of beta-amyloid precursor protein shifts the frequency dependency for induction of LTD, and enhances LTP in hippocampal slices. Neuroreport *8*, 2133-2137.

Ishikawa, M., Mizukami, K., Iwakiri, M., and Asada, T. (2005). Immunohistochemical and immunoblot analysis of gamma-aminobutyric acid B receptor in the prefrontal cortex of subjects with schizophrenia and bipolar disorder. Neuroscience letters *383*, 272-277.

Ishino, Y., Shinagawa, H., Makino, K., Amemura, M., and Nakata, A. (1987). Nucleotide sequence of the iap gene, responsible for alkaline phosphatase isozyme conversion in Escherichia coli, and identification of the gene product. J Bacteriol *169*, 5429-5433.

Ivankova, K., Turecek, R., Fritzius, T., Seddik, R., Prezeau, L., Comps-Agrar, L., Pin, J.P., Fakler, B., Besseyrias, V., Gassmann, M.*, et al.* (2013). Up-regulation of GABA(B) receptor signaling by constitutive assembly with the K+ channel tetramerization domain-containing protein 12 (KCTD12). The Journal of biological chemistry *288*, 24848-24856.

Iwakiri, M., Mizukami, K., Ikonomovic, M.D., Ishikawa, M., Hidaka, S., Abrahamson, E.E., DeKosky, S.T., and Asada, T. (2005). Changes in hippocampal GABABR1 subunit expression in Alzheimer's patients: association with Braak staging. Acta Neuropathol *109*, 467-474.

Jakob, V., Schreiner, A., Tikkanen, R., and Starzinski-Powitz, A. (2006). Targeting of transmembrane protein shrew-1 to adherens junctions is controlled by cytoplasmic sorting motifs. Molecular biology of the cell *17*, 3397-3408.

Jasin, M., and Rothstein, R. (2013). Repair of strand breaks by homologous recombination. Cold Spring Harb Perspect Biol *5*, a012740.

Jason Stachniak, T., Lauren Sylwestrak, E., Scheiffele, P., Hall, B.J., and Ghosh, A. (2019). Elfn1-induced constitutive activation of mGluR7 determines frequency-dependent recruitment of SOM interneurons. The Journal of neuroscience : the official journal of the Society for Neuroscience.

Javitt, D.C., Hashim, A., and Sershen, H. (2005). Modulation of striatal dopamine release by glycine transport inhibitors. Neuropsychopharmacology : official publication of the American College of Neuropsychopharmacology *30*, 649-656.

Jinek, M., Chylinski, K., Fonfara, I., Hauer, M., Doudna, J.A., and Charpentier, E. (2012). A programmable dual-RNA-guided DNA endonuclease in adaptive bacterial immunity. Science *337*, 816-821.

Johnston, T., and Duty, S. (2003). Changes in GABA(B) receptor mRNA expression in the rodent basal ganglia and thalamus following lesion of the nigrostriatal pathway. Neuroscience *120*, 1027-1035.

Kasten, C.R., and Boehm, S.L., 2nd (2015). Identifying the role of pre-and postsynaptic GABA(B) receptors in behavior. Neurosci Biobehav Rev *57*, 70-87.

Kato, A.S., and Witkin, J.M. (2018). Protein complexes as psychiatric and neurological drug targets. Biochem Pharmacol *151*, 263-281.

Kaupmann, K., Huggel, K., Heid, J., Flor, P.J., Bischoff, S., Mickel, S.J., McMaster, G., Angst, C., Bittiger, H., Froestl, W.*, et al.* (1997). Expression cloning of GABA(B) receptors uncovers similarity to metabotropic glutamate receptors. Nature *386*, 239-246.

Kaupmann, K., Malitschek, B., Schuler, V., Heid, J., Froestl, W., Beck, P., Mosbacher, J., Bischoff, S., Kulik, A., Shigemoto, R.*, et al.* (1998). GABA(B)-receptor subtypes assemble into functional heteromeric complexes. Nature *396*, 683-687.

Kim, Y., Jeong, E., Jeong, J.H., Kim, Y., and Cho, Y. (2020). Structural Basis for Activation of the Heterodimeric GABAB Receptor. J Mol Biol *432*, 5966-5984.

Kitaguchi, N., Takahashi, Y., Tokushima, Y., Shiojiri, S., and Ito, H. (1988). Novel precursor of Alzheimer's disease amyloid protein shows protease inhibitory activity. Nature *331*, 530-532.

Kogure, A., Shiratori, I., Wang, J., Lanier, L.L., and Arase, H. (2011). PANP is a novel O-glycosylated PILRalpha ligand expressed in neural tissues. Biochemical and biophysical research communications *405*, 428-433.

Korte, M. (2019). Neuronal function of Alzheimer's protein. Science *363*, 123-124.

Krueger, D.D., Tuffy, L.P., Papadopoulos, T., and Brose, N. (2012). The role of neurexins and neuroligins in the formation, maturation, and function of vertebrate synapses. Current opinion in neurobiology *22*, 412-422.

Kryszkowski, W., and Boczek, T. (2021). The G Protein-Coupled Glutamate Receptors as Novel Molecular Targets in Schizophrenia Treatment-A Narrative Review. J Clin Med *10*.

Kumar, K., Kaur, H., and Deshmukh, R. (2017). Neuroprotective role of GABAB receptor modulation against streptozotocin-induced behavioral and biochemical abnormalities in rats. Neuroscience.

Kumar, K., Sharma, S., Kumar, P., and Deshmukh, R. (2013). Therapeutic potential of GABA(B) receptor ligands in drug addiction, anxiety, depression and other CNS disorders. Pharmacol Biochem Behav *110*, 174-184.

Kurosaki, T., Popp, M.W., and Maquat, L.E. (2019). Quality and quantity control of gene expression by nonsense-mediated mRNA decay. Nat Rev Mol Cell Biol *20*, 406-420.

Lee, M.T., Chen, C.H., Lee, C.S., Chen, C.C., Chong, M.Y., Ouyang, W.C., Chiu, N.Y., Chuo, L.J., Chen, C.Y., Tan, H.K.*, et al.* (2011). Genome-wide association study of bipolar I disorder in the Han Chinese population. Molecular psychiatry *16*, 548-556.

Liddiard, K., Ruis, B., Kan, Y., Cleal, K., Ashelford, K.E., Hendrickson, E.A., and Baird, D.M. (2019). DNA Ligase 1 is an essential mediator of sister chromatid telomere fusions in G2 cell cycle phase. Nucleic acids research *47*, 2402-2424.

Lino, C.A., Harper, J.C., Carney, J.P., and Timlin, J.A. (2018). Delivering CRISPR: a review of the challenges and approaches. Drug Deliv *25*, 1234-1257.

Liu, J., Maurel, D., Etzol, S., Brabet, I., Ansanay, H., Pin, J.P., and Rondard, P. (2004). Molecular determinants involved in the allosteric control of agonist affinity in the GABAB receptor by the GABAB2 subunit. The Journal of biological chemistry *279*, 15824-15830.

Liu, Z., Xiang, Y., and Sun, G. (2013). The KCTD family of proteins: structure, function, disease relevance. Cell Biosci *3*, 45.

Luo, F., Sclip, A., Merrill, S., and Sudhof, T.C. (2021). Neurexins regulate presynaptic GABAB-receptors at central synapses. Nature communications *12*, 2380.

Madisen, L., Garner, A.R., Shimaoka, D., Chuong, A.S., Klapoetke, N.C., Li, L., van der Bourg, A., Niino, Y., Egolf, L., Monetti, C.*, et al.* (2015). Transgenic mice for intersectional targeting of neural sensors and effectors with high specificity and performance. Neuron *85*, 942-958.

Margeta-Mitrovic, M., Jan, Y.N., and Jan, L.Y. (2000). A trafficking checkpoint controls GABA(B) receptor heterodimerization. Neuron *27*, 97-106.

Martin-Belmonte, A., Aguado, C., Alfaro-Ruiz, R., Moreno-Martinez, A.E., de la Ossa, L., Martinez-Hernandez, J., Buisson, A., Fruh, S., Bettler, B., Shigemoto, R.*, et al.* (2020). Reduction in the neuronal surface of post and presynaptic GABAB receptors in the hippocampus in a mouse model of Alzheimer's disease. Brain Pathol *30*, 554-575.

Matsushita, S., Nakata, H., Kubo, Y., and Tateyama, M. (2010). Ligand-induced rearrangements of the GABA(B) receptor revealed by fluorescence resonance energy transfer. The Journal of biological chemistry *285*, 10291-10299.

McCudden, C.R., Hains, M.D., Kimple, R.J., Siderovski, D.P., and Willard, F.S. (2005). G-protein signaling: back to the future. Cell Mol Life Sci *62*, 551-577.

Merlo, D., Mollinari, C., Inaba, Y., Cardinale, A., Rinaldi, A.M., D'Antuono, M., D'Arcangelo, G., Tancredi, V., Ragsdale, D., and Avoli, M. (2007). Reduced GABAB receptor subunit expression and paired-pulse depression in a genetic model of absence seizures. Neurobiol Dis *25*, 631-641.

Metz, M., Gassmann, M., Fakler, B., Schaeren-Wiemers, N., and Bettler, B. (2011). Distribution of the auxiliary GABAB receptor subunits KCTD8, 12, 12b, and 16 in the mouse brain. The Journal of comparative neurology *519*, 1435-1454.

Mojica, F.J., Diez-Villasenor, C., Garcia-Martinez, J., and Soria, E. (2005). Intervening sequences of regularly spaced prokaryotic repeats derive from foreign genetic elements. J Mol Evol *60*, 174-182.

Mokrushin, A.A., Khama-Murad, A., Semenova, O.G., and Shalyapina, V.G. (2009). Electrophysiological characteristics of depressive states in rats with passive strategies of adaptive behavior. Neurosci Behav Physiol *39*, 275-280.

Mombereau, C., Kaupmann, K., Gassmann, M., Bettler, B., van der Putten, H., and Cryan, J.F. (2005). Altered anxiety and depression-related behaviour in mice lacking GABAB(2) receptor subunits. Neuroreport *16*, 307-310.

Monnier, C., Tu, H., Bourrier, E., Vol, C., Lamarque, L., Trinquet, E., Pin, J.P., and Rondard, P. (2011). Trans-activation between 7TM domains: implication in heterodimeric GABAB receptor activation. The EMBO journal *30*, 32-42.

Mott, D.D., and Lewis, D.V. (1994). The pharmacology and function of central GABAB receptors. Int Rev Neurobiol *36*, 97-223.

Mugnaini, C., and Corelli, F. (2016). The Allosteric Modulation of the GABAB Receptor: A Medicinal Chemistry Perspective. In GABAB Receptor, G. Colombo, ed. (Cham: Springer International Publishing), pp. 33-52.

Muller, U.C., Deller, T., and Korte, M. (2017). Not just amyloid: physiological functions of the amyloid precursor protein family. Nature reviews Neuroscience *18*, 281-298.

Neves, S.R., Ram, P.T., and Iyengar, R. (2002). G protein pathways. Science *296*, 1636-1639.

Niciu, M.J., Kelmendi, B., and Sanacora, G. (2012). Overview of glutamatergic neurotransmission in the nervous system. Pharmacol Biochem Behav *100*, 656-664.

Nicoletti, F., Bockaert, J., Collingridge, G.L., Conn, P.J., Ferraguti, F., Schoepp, D.D., Wroblewski, J.T., and Pin, J.P. (2011). Metabotropic glutamate receptors: from the workbench to the bedside. Neuropharmacology *60*, 1017-1041.

Niswender, C.M., and Conn, P.J. (2010). Metabotropic glutamate receptors: physiology, pharmacology, and disease. Annu Rev Pharmacol Toxicol *50*, 295-322.

Oblak, A.L., Gibbs, T.T., and Blatt, G.J. (2010). Decreased GABA(B) receptors in the cingulate cortex and fusiform gyrus in autism. Journal of neurochemistry *114*, 1414-1423.

Oldham, W.M., and Hamm, H.E. (2008). Heterotrimeric G protein activation by G-protein-coupled receptors. Nat Rev Mol Cell Biol *9*, 60-71.

Olpe, H.R., Karlsson, G., Pozza, M.F., Brugger, F., Steinmann, M., Van Riezen, H., Fagg, G., Hall, R.G., Froestl, W., and Bittiger, H. (1990). CGP 35348: a centrally active blocker of GABAB receptors. European journal of pharmacology *187*, 27-38.

Pagano, A., Rovelli, G., Mosbacher, J., Lohmann, T., Duthey, B., Stauffer, D., Ristig, D., Schuler, V., Meigel, I., Lampert, C.*, et al.* (2001). C-terminal interaction is essential for surface trafficking but not for heteromeric assembly of GABA(b) receptors. The Journal of neuroscience : the official journal of the Society for Neuroscience *21*, 1189-1202.

Papasergi-Scott, M.M., Robertson, M.J., Seven, A.B., Panova, O., Mathiesen, J.M., and Skiniotis, G. (2020). Structures of metabotropic GABAB receptor. Nature.

Park, J., Fu, Z., Frangaj, A., Liu, J., Mosyak, L., Shen, T., Slavkovich, V.N., Ray, K.M., Taura, J., Cao, B.*, et al.* (2020). Structure of human GABAB receptor in an inactive state. Nature.

Pasciuto, E., Ahmed, T., Wahle, T., Gardoni, F., D'Andrea, L., Pacini, L., Jacquemont, S., Tassone, F., Balschun, D., Dotti, C.G.*, et al.* (2015). Dysregulated ADAM10-Mediated Processing of APP during a Critical Time Window Leads to Synaptic Deficits in Fragile X Syndrome. Neuron *87*, 382-398.

Pin, J.P., and Bettler, B. (2016). Organization and functions of mGlu and GABAB receptor complexes. Nature *540*, 60-68.

Pin, J.P., and Prezeau, L. (2007). Allosteric modulators of GABA(B) receptors: mechanism of action and therapeutic perspective. Curr Neuropharmacol *5*, 195-201.

Pinkas, D.M., Sanvitale, C.E., Bufton, J.C., Sorrell, F.J., Solcan, N., Chalk, R., Doutch, J., and Bullock, A.N. (2017). Structural Complexity in the KCTD Family of Cullin3-Dependent E3 Ubiquitin Ligases. Biochem J.

Pourcel, C., Salvignol, G., and Vergnaud, G. (2005). CRISPR elements in Yersinia pestis acquire new repeats by preferential uptake of bacteriophage DNA, and provide additional tools for evolutionary studies. Microbiology (Reading) *151*, 653-663.

Povirk, L.F. (2006). Biochemical mechanisms of chromosomal translocations resulting from DNA double-strand breaks. DNA Repair (Amst) *5*, 1199-1212.

Rajalu, M., Fritzius, T., Adelfinger, L., Jacquier, V., Besseyrias, V., Gassmann, M., and Bettler, B. (2015). Pharmacological characterization of GABAB receptor subtypes assembled with auxiliary KCTD subunits. Neuropharmacology *88*, 145-154.

Rice, H.C., de Malmazet, D., Schreurs, A., Frere, S., Van Molle, I., Volkov, A.N., Creemers, E., Vertkin, I., Nys, J., Ranaivoson, F.M.*, et al.* (2019). Secreted amyloid-beta precursor protein functions as a GABABR1a ligand to modulate synaptic transmission. Science *363*.

Richter, M.C., Ludewig, S., Winschel, A., Abel, T., Bold, C., Salzburger, L.R., Klein, S., Han, K., Weyer, S.W., Fritz, A.K.*, et al.* (2018). Distinct in vivo roles of secreted APP ectodomain variants APPsalpha and APPsbeta in regulation of spine density, synaptic plasticity, and cognition. The EMBO journal *37*.

Ring, S., Weyer, S.W., Kilian, S.B., Waldron, E., Pietrzik, C.U., Filippov, M.A., Herms, J., Buchholz, C., Eckman, C.B., Korte, M.*, et al.* (2007). The secreted beta-amyloid precursor protein ectodomain APPs alpha is sufficient to rescue the anatomical, behavioral, and electrophysiological abnormalities of APP-deficient mice. The Journal of neuroscience : the official journal of the Society for Neuroscience *27*, 7817-7826.

Roenker, N.L., Gudelsky, G.A., Ahlbrand, R., Horn, P.S., and Richtand, N.M. (2012). Evidence for involvement of nitric oxide and GABA(B) receptors in MK-801- stimulated release of glutamate in rat prefrontal cortex. Neuropharmacology *63*, 575-581.

Ryan, M.M., Morris, G.P., Mockett, B.G., Bourne, K., Abraham, W.C., Tate, W.P., and Williams, J.M. (2013). Time-dependent changes in gene expression induced by secreted amyloid precursor protein-alpha in the rat hippocampus. BMC Genomics *14*, 376.

Sabbagh, M.N. (2009). Drug development for Alzheimer's disease: where are we now and where are we headed? Am J Geriatr Pharmacother *7*, 167-185.

Sandbrink, R., Masters, C.L., and Beyreuther, K. (1996). APP gene family. Alternative splicing generates functionally related isoforms. Ann N Y Acad Sci *777*, 281-287.

Schwenk, J., Metz, M., Zolles, G., Turecek, R., Fritzius, T., Bildl, W., Tarusawa, E., Kulik, A., Unger, A., Ivankova, K.*, et al.* (2010). Native GABA(B) receptors are heteromultimers with a family of auxiliary subunits. Nature *465*, 231-235.

Schwenk, J., Perez-Garci, E., Schneider, A., Kollewe, A., Gauthier-Kemper, A., Fritzius, T., Raveh, A., Dinamarca, M.C., Hanuschkin, A., Bildl, W.*, et al.* (2016). Modular composition and dynamics of native GABAB receptors identified by high-resolution proteomics. Nature neuroscience *19*, 233-242.

Schwirtlich, M., Emri, Z., Antal, K., Mate, Z., Katarova, Z., and Szabo, G. (2010). GABA(A) and GABA(B) receptors of distinct properties affect oppositely the proliferation of mouse embryonic stem cells through synergistic elevation of intracellular Ca(2+). FASEB journal : official publication of the Federation of American Societies for Experimental Biology *24*, 1218-1228.

Seddik, R., Jungblut, S.P., Silander, O.K., Rajalu, M., Fritzius, T., Besseyrias, V., Jacquier, V., Fakler, B., Gassmann, M., and Bettler, B. (2012). Opposite effects of KCTD subunit domains on GABA(B) receptor-mediated desensitization. The Journal of biological chemistry *287*, 39869-39877.

Selkoe, D.J., and Hardy, J. (2016). The amyloid hypothesis of Alzheimer's disease at 25 years. EMBO Mol Med *8*, 595-608.

Sereikaite, V., Fritzius, T., Kasaragod, V.B., Bader, N., Maric, H.M., Schindelin, H., Bettler, B., and Stromgaard, K. (2019). Targeting the gamma-Aminobutyric Acid Type B (GABAB) Receptor Complex: Development of Inhibitors Targeting the K(+) Channel Tetramerization Domain (KCTD) Containing Proteins/GABAB Receptor Protein-Protein Interaction. J Med Chem *62*, 8819-8830.

Shariati, S.A., and De Strooper, B. (2013). Redundancy and divergence in the amyloid precursor protein family. FEBS letters *587*, 2036-2045.

Shaye, H., Ishchenko, A., Lam, J.H., Han, G.W., Xue, L., Rondard, P., Pin, J.P., Katritch, V., Gati, C., and Cherezov, V. (2020). Structural basis of the activation of a metabotropic GABA receptor. Nature.

Sibille, E., Wang, Y., Joeyen-Waldorf, J., Gaiteri, C., Surget, A., Oh, S., Belzung, C., Tseng, G.C., and Lewis, D.A. (2009). A molecular signature of depression in the amygdala. Am J Psychiatry *166*, 1011-1024.

Silverman, J.L., Pride, M.C., Hayes, J.E., Puhger, K.R., Butler-Struben, H.M., Baker, S., and Crawley, J.N. (2015). GABAB Receptor Agonist R-Baclofen Reverses Social Deficits and Reduces Repetitive Behavior in Two Mouse Models of Autism. Neuropsychopharmacology : official publication of the American College of Neuropsychopharmacology *40*, 2228-2239.

Skoblov, M., Marakhonov, A., Marakasova, E., Guskova, A., Chandhoke, V., Birerdinc, A., and Baranova, A. (2013). Protein partners of KCTD proteins provide insights about their functional roles in cell differentiation and vertebrate development. Bioessays *35*, 586-596.

Slattery, D.A., Desrayaud, S., and Cryan, J.F. (2005). GABAB receptor antagonist-mediated antidepressant-like behavior is serotonin-dependent. J Pharmacol Exp Ther *312*, 290-296.

Smaldone, G., Pirone, L., Pedone, E., Marlovits, T., Vitagliano, L., and Ciccarelli, L. (2016). The BTB domains of the KCTD proteins prevalently assume pentameric states. FEBS letters.

Smrcka, A.V. (2008). G protein betagamma subunits: central mediators of G protein-coupled receptor signaling. Cell Mol Life Sci *65*, 2191-2214.

Sriram, K., and Insel, P.A. (2018). G Protein-Coupled Receptors as Targets for Approved Drugs: How Many Targets and How Many Drugs? Mol Pharmacol *93*, 251-258.

Stefan, E., Aquin, S., Berger, N., Landry, C.R., Nyfeler, B., Bouvier, M., and Michnick, S.W. (2007). Quantification of dynamic protein complexes using Renilla luciferase fragment complementation applied to protein kinase A activities in vivo. Proceedings of the National Academy of Sciences of the United States of America *104*, 16916-16921.

Steiger, J.L., Bandyopadhyay, S., Farb, D.H., and Russek, S.J. (2004). cAMP response element-binding protein, activating transcription factor-4, and upstream stimulatory

factor differentially control hippocampal GABABR1a and GABABR1b subunit gene expression through alternative promoters. The Journal of neuroscience : the official journal of the Society for Neuroscience *24*, 6115-6126.

Sun, B., Chen, L., Liu, L., Xia, Z., Pin, J.P., Nan, F., and Liu, J. (2016). A negative allosteric modulator modulates GABAB-receptor signalling through GB2 subunits. Biochem J *473*, 779-787.

Sun, N., and Zhao, H. (2013). Transcription activator-like effector nucleases (TALENs): a highly efficient and versatile tool for genome editing. Biotechnol Bioeng *110*, 1811-1821.

Sylwestrak, E.L., and Ghosh, A. (2012). Elfn1 regulates target-specific release probability at CA1-interneuron synapses. Science *338*, 536-540.

Symington, L.S. (2014). End resection at double-strand breaks: mechanism and regulation. Cold Spring Harb Perspect Biol *6*.

Takata, M., Sasaki, M.S., Sonoda, E., Morrison, C., Hashimoto, M., Utsumi, H., Yamaguchi-Iwai, Y., Shinohara, A., and Takeda, S. (1998). Homologous recombination and non-homologous end-joining pathways of DNA double-strand break repair have overlapping roles in the maintenance of chromosomal integrity in vertebrate cells. The EMBO journal *17*, 5497-5508.

Tang, B.L. (2019). Amyloid Precursor Protein (APP) and GABAergic Neurotransmission. Cells *8*.

Tanzi, R.E., McClatchey, A.I., Lamperti, E.D., Villa-Komaroff, L., Gusella, J.F., and Neve, R.L. (1988). Protease inhibitor domain encoded by an amyloid protein precursor mRNA associated with Alzheimer's disease. Nature *331*, 528-530.

Taylor, C.J., Ireland, D.R., Ballagh, I., Bourne, K., Marechal, N.M., Turner, P.R., Bilkey, D.K., Tate, W.P., and Abraham, W.C. (2008). Endogenous secreted amyloid precursor protein-alpha regulates hippocampal NMDA receptor function, long-term potentiation and spatial memory. Neurobiol Dis *31*, 250-260.

Thurtle-Schmidt, D.M., and Lo, T.W. (2018). Molecular biology at the cutting edge: A review on CRISPR/CAS9 gene editing for undergraduates. Biochem Mol Biol Educ *46*, 195-205.

Tomioka, N.H., Yasuda, H., Miyamoto, H., Hatayama, M., Morimura, N., Matsumoto, Y., Suzuki, T., Odagawa, M., Odaka, Y.S., Iwayama, Y.*, et al.* (2014). Elfn1 recruits presynaptic mGluR7 in trans and its loss results in seizures. Nature communications *5*, 4501.

Turecek, R., Schwenk, J., Fritzius, T., Ivankova, K., Zolles, G., Adelfinger, L., Jacquier, V., Besseyrias, V., Gassmann, M., Schulte, U.*, et al.* (2014). Auxiliary GABAB receptor subunits uncouple G protein betagamma subunits from effector channels to induce desensitization. Neuron *82*, 1032-1044.

Uchida, N., Honjo, Y., Johnson, K.R., Wheelock, M.J., and Takeichi, M. (1996). The catenin/cadherin adhesion system is localized in synaptic junctions bordering transmitter release zones. J Cell Biol *135*, 767-779.

Urnov, F.D., Rebar, E.J., Holmes, M.C., Zhang, H.S., and Gregory, P.D. (2010). Genome editing with engineered zinc finger nucleases. Nat Rev Genet *11*, 636-646.

Valdes, V., Valenzuela, J.I., Salas, D.A., Jaureguiberry-Bravo, M., Otero, C., Thiede, C., Schmidt, C.F., and Couve, A. (2012). Endoplasmic reticulum sorting and kinesin-1 command the targeting of axonal GABAB receptors. PloS one *7*, e44168.

Vienne, J., Bettler, B., Franken, P., and Tafti, M. (2010). Differential effects of GABAB receptor subtypes, {gamma}-hydroxybutyric Acid, and Baclofen on EEG activity and sleep regulation. The Journal of neuroscience : the official journal of the Society for Neuroscience *30*, 14194-14204.

Vigot, R., Barbieri, S., Brauner-Osborne, H., Turecek, R., Shigemoto, R., Zhang, Y.P., Lujan, R., Jacobson, L.H., Biermann, B., Fritschy, J.M.*, et al.* (2006). Differential compartmentalization and distinct functions of GABAB receptor variants. Neuron *50*, 589-601.

Vlachou, S., and Markou, A. (2010). GABAB receptors in reward processes. Advances in pharmacology *58*, 315-371.

Vuillaume, M.L., Jeanne, M., Xue, L., Blesson, S., Denomme-Pichon, A.S., Alirol, S., Brulard, C., Colin, E., Isidor, B., Gilbert-Dussardier, B.*, et al.* (2018). A novel mutation in the transmembrane 6 domain of GABBR2 leads to a Rett-like phenotype. Ann Neurol *83*, 437-439.

Wang, W., Kutny, P.M., Byers, S.L., Longstaff, C.J., DaCosta, M.J., Pang, C., Zhang, Y., Taft, R.A., Buaas, F.W., and Wang, H. (2016). Delivery of Cas9 Protein into Mouse Zygotes through a Series of Electroporation Dramatically Increases the Efficiency of Model Creation. J Genet Genomics *43*, 319-327.

Wang, Z., Wang, B., Yang, L., Guo, Q., Aithmitti, N., Songyang, Z., and Zheng, H. (2009). Presynaptic and postsynaptic interaction of the amyloid precursor protein promotes peripheral and central synaptogenesis. The Journal of neuroscience : the official journal of the Society for Neuroscience *29*, 10788-10801.

Wells, C.A., Zurawski, Z., Betke, K.M., Yim, Y.Y., Hyde, K., Rodriguez, S., Alford, S., and Hamm, H.E. (2012). Gbetagamma inhibits exocytosis via interaction with critical residues on soluble N-ethylmaleimide-sensitive factor attachment protein-25. Mol Pharmacol *82*, 1136-1149.

Wieronska, J.M., and Pilc, A. (2019). Depression and schizophrenia viewed from the perspective of amino acidergic neurotransmission: Antipodes of psychiatric disorders. Pharmacol Ther *193*, 75-82.

Winkler, M., Biswas, S., Berger, S.M., Kuchler, M., Preisendorfer, L., Choo, M., Fruh, S., Rem, P.D., Enkel, T., Arnold, B.*, et al.* (2019). Pianp deficiency links GABAB receptor signaling and hippocampal and cerebellar neuronal cell composition to autism-like behavior. Molecular psychiatry.

Wischmeyer, E., Doring, F., Wischmeyer, E., Spauschus, A., Thomzig, A., Veh, R., and Karschin, A. (1997). Subunit interactions in the assembly of neuronal Kir3.0 inwardly rectifying K+ channels. Molecular and cellular neurosciences *9*, 194-206.

Yamada, S., and Nelson, W.J. (2007). Synapses: sites of cell recognition, adhesion, and functional specification. Annu Rev Biochem *76*, 267-294.

Yates, D. (2019). Revealing a receptor for secreted APP. Nat Rev Neurosci *20*, 129.

Yoo, Y., Jung, J., Lee, Y.N., Lee, Y., Cho, H., Na, E., Hong, J., Kim, E., Lee, J.S., Lee, J.S.*, et al.* (2017). GABBR2 mutations determine phenotype in rett syndrome and epileptic encephalopathy. Ann Neurol *82*, 466-478.

Zeng, L., Fee, B.E., Rivas, M.V., Lin, J., and Adamson, D.C. (2014a). Adherens junctional associated protein-1: a novel 1p36 tumor suppressor candidate in gliomas (Review). International journal of oncology *45*, 13-17.

Zeng, L., Kang, C., Di, C., Fee, B.E., Rivas, M., Lin, J., and Adamson, D.C. (2014b). The adherens junction-associated protein 1 is a negative transcriptional regulator of MAGEA2, which potentiates temozolomide-induced apoptosis in GBM. International journal of oncology *44*, 1243-1251.

Zhang, M., Zhou, X., Jiang, W., Li, M., Zhou, R., and Zhou, S. (2020). AJAP1 affects behavioral changes and GABABR1 level in epileptic mice. Biochemical and biophysical research communications.

Zheng, S., Abreu, N., Levitz, J., and Kruse, A.C. (2019). Structural basis for KCTD-mediated rapid desensitization of GABAB signalling. Nature.

Zou, C., Crux, S., Marinesco, S., Montagna, E., Sgobio, C., Shi, Y., Shi, S., Zhu, K., Dorostkar, M.M., Muller, U.C.*, et al.* (2016). Amyloid precursor protein maintains constitutive and adaptive plasticity of dendritic spines in adult brain by regulating D-serine homeostasis. The EMBO journal *35*, 2213-2222.

Zuo, H., Glaaser, I., Zhao, Y., Kurinov, I., Mosyak, L., Wang, H., Liu, J., Park, J., Frangaj, A., Sturchler, E.*, et al.* (2019). Structural basis for auxiliary subunit KCTD16 regulation of the GABAB receptor. Proceedings of the National Academy of Sciences of the United States of America.

12 Acknowledgment